Battery fault diagnosis and energy management for embedded applications

Thèse de doctorat de l'université Paris-Saclay

École doctorale n° 575, Electrical, Optical, Bio: Physics and Engineering (EOBE)
Spécialité de doctorat: Génie électrique
Unité de recherche : Université Paris-Saclay, CentraleSupélec, CNRS, Laboratoire de Génie Electrique et Electronique de Paris, 91192, Gif-sur-Yvette, France.
Référent : Faculté des sciences d'Orsay

Thèse présentée et soutenue à Saint-Quentin-en-Yvelines, le 01/09/2020, par

Jianwen MENG

Composition du Jury

Emmanuel GODOY Professeur, CentraleSupélec, Université Paris-Saclay	Président
François AUGER Professeur, Université de Nantes	Rapporteur & Examinateur
Hamid GUALOUS Professeur, Université de Normandie	Rapporteur & Examinateur
Tarek RAISSI Professeur, Conservatoire National des Arts et Métiers	Examinateur
Moussa BOUKHNIFER Maître de Conférences, HDR, Université de Lorraine	Directeur de thèse
Demba DIALLO Professeur, Université Paris-Saclay	Co-encadrant & Examinateur
Harry Ramenah Maître de Conférences, HDR, IUT de Metz, Université de Lorraine	Invité

Thèse de doctorat

NNT : 2020UPAST003

Acknowledgment

First of all, I would like to express my sincere gratitude to my PhD supervisors, Prof. Demba DIALLO and Dr. Moussa BOUKHNIFER, for their instructive advice and useful suggestions on my thesis. They give me an independent working environment during this three-year doctoral study, and because of their continuous support, I have been very interested in this research topic.

Secondly, I would also like to express my gratitude to the members of my jury, Prof. François AUGER, Prof. Hamid GUALOUS, Prof. Emmanuel GODOY, Prof. Tarek RAISSI and Dr. Harry RAMENAH, for their presence for my PhD defense and their constructive comments on my work. I appreciate our fruitful discussion very much.

Besides, special thanks should go to my friends and colleagues in ESTACA, especially M. Antoine DURAND, M. Adriano CESCHIA and M. Abdelmoudjib BENTERKI. We have spent three years together, this journey was interesting because of you. In addition, I also would like to thank those who have helped me during this journey. I am extremely grateful to them.

Last but not least, I should express my gratitude to my family, especially my parents and my grandparents on my mother's side. Their support and love make me courageous.

Table of contents

General introduction

The energy crisis and environmental issues bring the greatest challenge for automobile industry and urge the necessity to develop alternative fuel-driven vehicles [1]. Hence, electric vehicles (EVs), including battery-driven EVs (BEVs), hybrid electric vehicles (HEVs) and plug-in HEVs(PHEVs), gain the ever booming development in recent years [2].

In view of their high energy/power density and extended life cycle, lithium-ion batteries (LIBs) are currently the state-of-the-art power sources for electrified powertrain systems [3]. Doubtlessly, the safety operation of LIBs is of vital importance for the development of EVs. However, LIBs have some potential safety issues that threat the reliable vehicle operation, and accidents happen occasionally due to battery faults.

As a typical type of electrochemical power source, LIBs undergo degradation in both energy capacity and internal resistance during their irreversible aging process [4]. Besides, according to the existing literature, overcharge, overdischarge, internal short circuit and external short circuit are four common electrical abuse conditions that may lead to battery thermal runaway [5–7]. And thermal runaway is a catastrophic failure of on-board batteries [8]. Although researchers have never ceased to explore the mechanisms of thermal runaway, deep insight is still premature [9–11].

From the perspective of automation, the reliable, efficient, and safe operation of on-board lithium-ion batteries requires monitoring, control and management. Monitoring refers to a continuous determination of battery states during operation. Control maintains the battery states within the safety ranges. Management, generalized from energy management and health management, means a health-conscious energy distribution strategy that decides the battery power flow. Instead of being independent from each other,these three parts are closely correlated. Among others, battery monitoring plays a primary role, because its output triggers the operating conditions.

Objective of this thesis

Since the aforementioned irreversible aging process and four common electrical abuse conditions can cause serious security problems for the embedded application, fault diagnosis around LIB is the main topic of this thesis. Although various research efforts have been invested for the LIBs because of their wide application, battery fault diagnosis remains challenging and problematic. The main reason is that the battery critical indicators, such as state of charge, state of health, cannot be measured directly. However, the energy management strategy, battery energy control and even battery useful life prediction are closely related to these unmeasurable indicators. Hence, battery fault diagnosis, namely the battery on-line monitoring, is of great importance for the follow-up works.

Therefore, this thesis tries to discuss and extend the battery on-line monitoring work from the perspective of control. Namely, taking advantage of the existing literature, including the experimentally validated battery model and published experimental information [12–14], we would like to make some new contributions for the battery state and parameter estimation and battery incipient short circuit fault diagnosis. The obtained results can become important supports for future work such as battery fault detection, fault tolerant control and the design of a health conscious energy management/battery charging strategy.

Outline of this thesis

This thesis is mainly structured in 3 chapters:

- **Chapter 1: Research background**

  The research background starts with a general review of different energy storage technologies, where proprieties of different energy storage systems are pointed out. Furthermore, considering the limitation of single energy storage technology for the EV application, hybrid energy storage system and its hybridization architecture are introduced. Besides, energy management strategy, as the high level supervisory control of hybrid energy storage systems, is also discussed. Moreover, as the main studied system in this thesis, the basics of LIB including its inevitable aging process and unforeseeable abuse conditions are presented in detail. Finally, this chapter ends with a real hybrid EV simulation example whose the main aim is to show the importance of battery state estimation and battery fault diagnosis.

- **Chapter 2: Battery state and parameter estimation**

  This chapter is dedicated to the battery aging monitoring based on the equivalent circuit model. In fact, the so-called battery monitoring process can be eventually converted to a classical state and parameter estimation problem. A usual method for estimating slowly varying unmeasureable parameters is to include them as the state variables with zero-time derivative condition. We can obtain the extended battery model. Hence, after deducing the necessary observability conditions for the nonlinear extended battery model, a new battery monitoring framework is proposed in this chapter. This extends the traditional battery monitoring frameworks, namely joint and dual estimation methods. The obtained results in this chapter provide an important theoretical support for the battery charge control design and battery on-line monitoring work.

- **Chapter 3: Battery incipient short circuit diagnosis**

  The problem of battery incipient short circuit diagnosis is discussed in this chapter. The slightly modified battery equivalent circuit model provides a new direction of battery fault diagnosis. Namely, the battery short circuit problem is addressed from the perspective of fault estimation. Considering the non-linear characteristic of the battery OCV (open circuit voltage)-SOC(state of charge) curve, a Takagi-Sugeno fuzzy non-linear observer that specialized for the battery short circuit estimation is proposed. Genetic algorithm has been used for the membership function tuning. In order to complete and improve the battery short circuit diagnosis work, the model-based short circuit estimation is combined with a statistical technique, namely Cumulative Sum, to detect the tiny change of the signal due to the incipient fault. Intensive simulation studies using real experimental data [13–15] have verified the effectiveness of the proposed diagnosis method.

Last but not least, the general conclusion and several perspectives will end this thesis. This PhD work has led to 3 journal papers and 5 international conference papers.

International journal papers:

1. Jianwen MENG, Moussa BOUKHNIFER and Demba DIALLO, *Incipient Short Circuit Fault Diagnosis of Lithium-Ion Batteries*, Journal of Energy Storage, vol. 31, 101658, 2020.

2. Jianwen MENG, Moussa BOUKHNIFER and Demba DIALLO, *Comparative study of lithium-ion battery open-circuit-voltage online estimation methods*, IET Electrical Systems in Transportation, vol. 10, pp. 162–169, 2020

3. Jianwen MENG, Moussa BOUKHNIFER, Demba DIALLO and Tianzhen WANG, *A New Cascaded Framework for Lithium-Ion Battery State and Parameter Estimation*, Applied Sciences, vol. 10, pp. 1–20, 2020.

International conference papers:

1. Jianwen MENG, Moussa BOUKHNIFER and Demba DIALLO, *Lithium-Ion Battery Monitoring and Observability Analysis with Extended Equivalent Circuit Model*, 28th IEEE Mediterranean Conference on Control and Automation (MED'2020), Saint-Raphaël, France.

2. Jianwen MENG, Moussa BOUKHNIFER, Demba DIALLO and Tianzhen WANG, *Short-Circuit Fault Diagnosis and State Estimation for Li-ion Battery using Weighting Function Self-Regulating Observer*, 2020 IEEE Prognostics and System Health Management Conference (PHM-Besançon), Besançon, France.

3. Jianwen MENG, Moussa BOUKHNIFER and Demba DIALLO, *On-line Model-based Short Circuit Diagnosis of Lithium-Ion Batteries for Electric Vehicle Application*, IECON 2019-45th Annual Conference of the IEEE Industrial Electronics Society, Lisbon, Portugal.

4. Jianwen MENG, Moussa BOUKHNIFER and Demba DIALLO, *A New Model-Based Lithium-Ion Battery Online Monitoring Structure*, 2019 IEEE Prognostics and System Health Management Conference (PHM-Paris), Paris, France. ***Best paper award***

5. Jianwen MENG, Moussa BOUKHNIFER and Demba DIALLO, *A Comparative Study of Open-Circuit-Voltage Estimation Algorithms for Lithium-Ion Batteries in Battery Management Systems*, 2019 6th IEEE International Conference on Control, Decision and Information Technologies, Paris, France.

List of Tables

List of Figures

List of abbreviations

AFC	Alkaline fuel cell
AH	Ampere-Hour
ARX	Auto regressive exogenous
AWG	Additive white Gaussian
BEV	Battery-driven electric vehicle
CO_2	Carbon dioxide
CAES	Compressed air energy storage
CUSUM	Cumulative Sum
DMFC	Direct methanol fuel cell
DOD	Depth of discharge
ECM	Equivalent circuit model
EKF	Extended Kalman Filter
EMS	Energy management strategy
EOL	End-of-lifetime
ESC	External short circuit
ESS	Energy storage system
EV	Electric vehicle
FC	Fuel cell
FDD	Fault detection and diagnosis
FES	Flywheel energy storage
Gt	Gigatons (1000 megatons = 10^9 metric tons)
HEV	Hybrid electric vehicle
ICE	Internal combustion engine
ISC	Internal short circuit

KF	Kalman filter
LIBs	Lithium-Ion batteries
LMI	linear-matrix-inequality
LTI	Linear time-invariant
MCFC	Molten carbonate fuel cell
NaS	Sodium sulfur
Ni–Cd	Nickel–cadmium
Ni–MH	Nickel–metal hydride
OC	Overcharge
OCV	Open circuit voltage
OD	Overdischarge
PAFC	Phosphoric acid fuel cell
PEMFC	Polymer electrolyte membrane fuel cell
PHEV	Plug-in HEV
PHS	Pumped hydro storage
PRBS	Pseudo random binary signal
RLS	Recursive least-squares
SC	Supercapacitor
SMES	Superconducting magnetic energy storage
SNR	Signal-to-noise ratio
SOC	State of charge
SOF	State of function
SOFC	Solid oxide fuel cell
SOH	State of health
SOP	State of power
SVM	Support Vector Machine

TR	Thermal runaway
TS	Takagi-Sugeno
UKF	Unscented Kalman Filter
UT	Unscented transformation
VRB	Vanadium redox battery
WLTC2	Class 2 worldwide harmonized light vehicles test procedures
ZnBr	Zinc bromine

Chapter 1

Research background

1.1 Introduction

Conventional energy sources, namely the fossil fuels like coal, oil and nature gas, have played an important role in the modernization and economic development of human society. However, the rapid depletion of fossil fuels and the global warming induced by greenhouse gases become the two main ecological threats for this century. Total global annual emissions of fossil CO_2 in gigatons (Gt) by sector from 1970 until 2018 are shown in Fig. 1.1. Since the beginning of the 21st century, global CO_2 emissions have grown in comparison to the three previous decades.

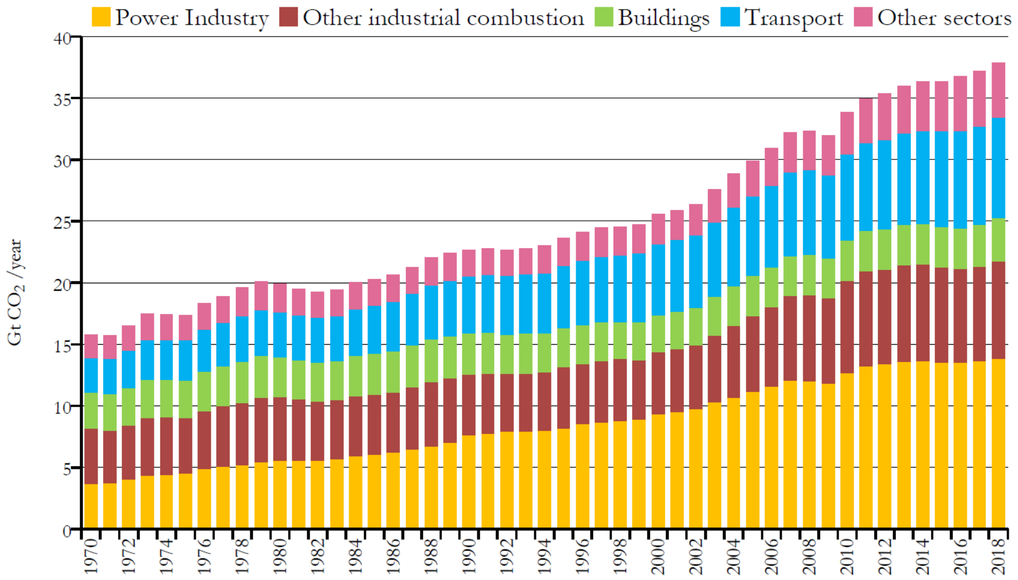

Figure 1.1: Global annual emissions of fossil CO_2 from 1970 until 2018 [16].

Nowadays, due to the enhancement of public environmental protection consciousness and the desire for CO_2-emission free power generation, more sustainable, eco-friendly, renewable-based energy sources are exploited. These energy sources, also named as distributed (renewable) energy sources, include solar, wind, ocean wave, tides, etc. And the corresponding electric power generation is termed as distributed generation [29]. Hence, the obtained electrical energy can be utilized, delivered, or stored into another form and converted back to electrical energy when needed.

1.1.1 Energy storage system

Energy storage system (ESS), which refers to an equipment that can perform both functions of storing and releasing energy at an adequate time, safely, efficiently and conveniently, plays a crucial role in the field of renewable energy technologies. Because electrical energy storage is indispensable and required in various applications:

- **Renewable power generation**

  As mentioned previously, researchers resort to renewable energy resources to tackle the climate change that international community is currently facing. However, the intermittent nature of many renewable energy resources, namely their dependency on environmental conditions like wind speed and solar irradiance, prevents a continuous power supply to the load. Therefore, their integration into power systems brings inherent variability and uncertainty. The power variation can even degrade the grid voltage stability due to the surplus or shortage of power [30]. Hence, these highly promising power generation technologies are always applied along with an ESS to constitute a hybrid energy system, whose aggregated output can be regulated to match the loads. The function of ESS is to smooth out the fluctuations and improve supply continuity and power quality [31].

- **Energy efficient buildings**

  The building sector is the largest energy consumer in the world [32]. Heating, lighting, ventilation and air conditioning are necessary for large residential or commercial buildings, such as office buildings, apartment buildings, supermarkets and hospitals. In order to reduce the greenhouse gas emissions in the building sector to a sustainable level, efforts to increase both energy efficiency and the share of renewable energies are required. Hence, reconstruction with better insulation and fenestration can doubtlessly reduce the energy losses from buildings. Additionally, application of combined heat and power (micro-cogeneration) systems, namely microgrid framework based on photovoltaic panels, micro-turbine and ESS, can also alleviate the situation by cutting the non-renewable energy demand [33]. The so-called microgrid can be connected to or islanded from the main electric grid. And ESS is an important element for microgrid in both of these two operation modes. In the connected mode, ESS can shave the load peaks, which make the microgrid has less harmful effect on the main electric grid. In the islanded mode, ESS should stabilize the microgrid [34].

- **Electrified transport**

> The energy crisis, environmental issues and even political concerns bring the greatest challenge for automobile industry and urge the necessity to develop alternative fuel-driven vehicles [1]. Hence, electric vehicles (EVs), including battery-driven EVs (BEVs), hybrid electric vehicles (HEVs) and plug-in HEVs (PHEVs), gain the ever booming development in recent years [2]. All these alternatives have in common that an internal combustion engine (ICE) is replaced or augmented by electric propulsion, because transportation electrification is seen as an effective way to substantially reduce the overall use of hydrocarbons [35]. ESS is one of the main elements in the powertrain. It should provide the power supply to the propulsion system, which determines both the driving mileage and the dynamic performance. Besides, energy efficiency also benefits from ESS. Considering the actual applications where vehicles operate frequently between static states and dynamic states, the braking energy is considerable during driving process. Instead of dissipating the braking energy in form of heat during driving process, ESS makes the reuse of regenerative energy from vehicle braking become feasible. Namely, during the deceleration process, the kinetic energy is converted into electric energy and stored; inversely, ESS can also send back the stored energy to the power system when the power demand is high such as hill climbing and accelerating. Except for the road transport, ESS is also applied in rail transport [36], maritime transport [37] and air transport [38].

In addition to the three specific examples above, ESS can also be used in uninterrupted power supply systems [39], aerospace engineering [40], military services [41], ocean engineering lifting system [42], etc. The main functions of ESS can be resumed in Fig. 1.2

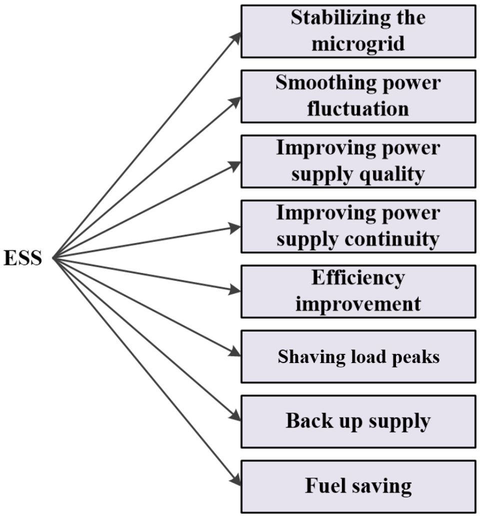

Figure 1.2: The main functions of ESS.

Electricity cannot be stored in electrical form in large-scale capacities. On the contrary, it can be easily stored in other forms [18,34]. Fig. 1.3 classifies different ESS technologies based on their primary source of energy, namely storage technologies for electricity can be classified in three categories regarding the type of the stored energy, including electrical, mechanical and chemical [43]. Although the electrical energy can also be stored in the form of thermal energy, it is technically developed but still not widely used [31]. Description of different ESSs in Fig. 1.3 is given briefly as follows.

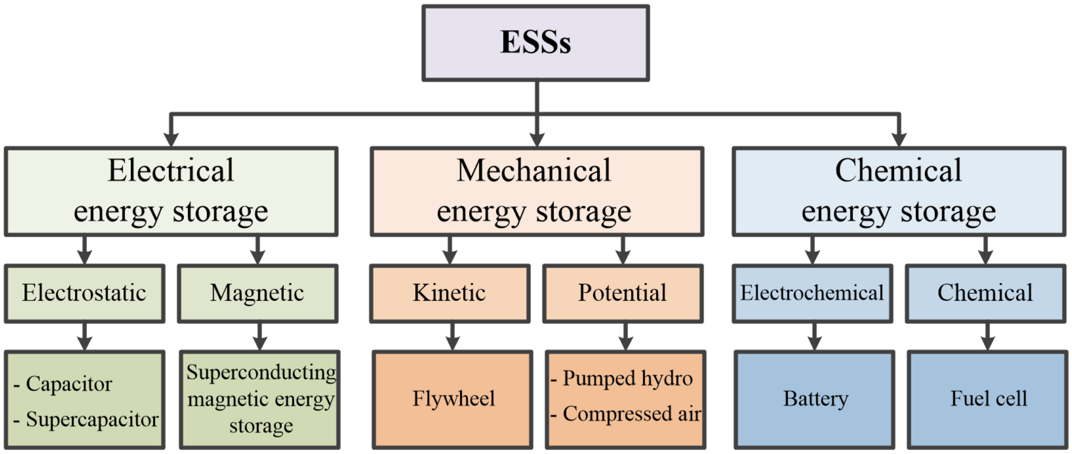

Figure 1.3: Energy storage technologies classification.

1.1.1.1 Capacitor/Supercapacitor

Conventional capacitors consist of two metal plates separated by a nonconducting layer which is termed as dielectric. When one plate is charged by a direct-current source, the other plate will be induced with charges of the opposite sign. Although capacitors can be charged quickly and cycled tens of thousands of times with a high efficiency, the main problem is the low energy density [18]. If a large capacity is required, the area of the dielectric must be very large, which prevents the application of the conventional capacitors.

Recently, great progress has been achieved in the capacitor storage technologies. Instead of the common arrangement of a solid dielectric between electrodes, an electrolyte solution is applied [31]. This is the so-called supercapacitor (SC) , which is also termed as ultracapacitor. A SC cell consists of two electrodes separated by an ion-permeable separator which is soaked in electrolyte [17]. The separator prevents the electrical contact between the electrodes. Fig. 1.4 illustrates the schematic diagram of SC's symmetric structure.

Depending on the different storage mechanisms or cell configuration, the SCs can be generally divided into three categories, namely electric double-layer capacitors,

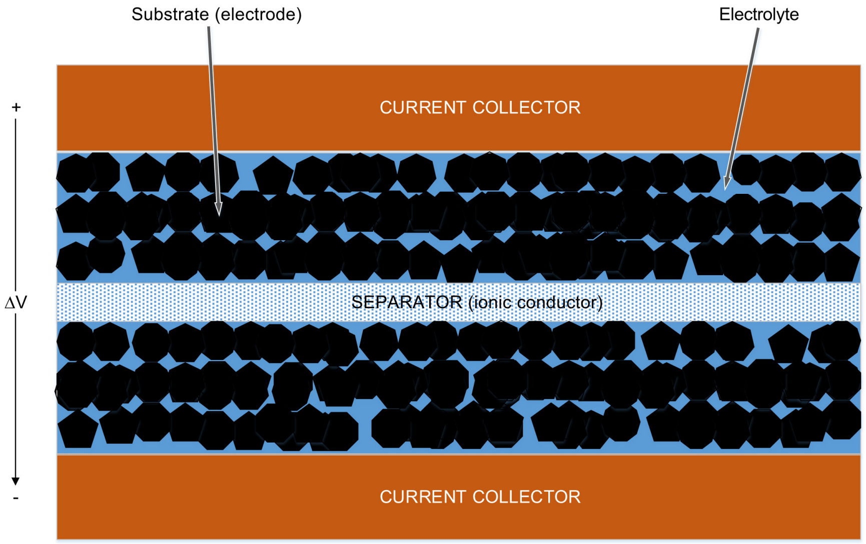

Figure 1.4: Schematic diagram of SC's symmetric structure [17].

pseudocapacitors and hybrid capacitors [17]. The electric double-layer capacitors are non-faradaic (electrostatic) because there are no chemical reactions, while the operation of pseudocapacitors is a faradaic process which involves the transfer of charge between electrodes and electrolyte such as oxidation-reduction reactions [44]. The hybrid capacitors, such as lithium-ion capacitors, are a combination of the two, including both faradaic and electrostatic processes [17, 44].

The SCs possess high specific power typically above 10 kW/kg but low specific energy, typically below 10 Wh/kg, also they are ESSs with very high life cycle typically above 500000 cycles [43]. Although they have greater energy storage capabilities than the conventional capacitors, short duration and high energy dissipation due to self-discharge losses are still the main concerns [44].

1.1.1.2 Superconducting magnetic energy storage

Superconducting magnetic energy storage (SMES) consists of superconductive coil, power conversion system and a cryostat which contains a refrigeration system and a vacuum-insulated vessel [18]. Schematic diagram of SMES is shown in Fig. 1.5. The operation principle of an SMES unit is that when a direct current voltage is applied across the terminals of a superconductive coil, energy will be stored in the magnetic field generated by direct electric current circulating through the superconductive coil [45]. Because of the extreme low resistance of the superconductor, the current in the coil can continue to flow even if the voltage source is interrupted.

SMES is the only known technology to store electrical energy into electric current [46]. The energy stored in the coil can be calculated by $E = 0.5LI^2$, where L is

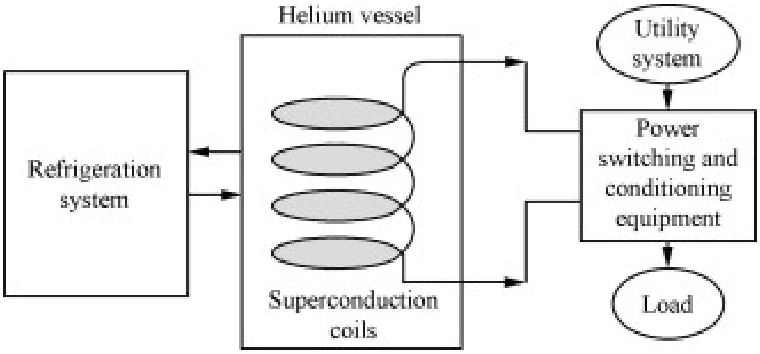

Figure 1.5: Schematic diagram of SMES [18].

the coil inductance and I the current [18]. In addition, the coil is maintained at low temperature considering the critical temperature of superconducting phenomenon. Therefore, SMESs are generally categorized in two main types, namely low temperature (around 5 Kelvin degree) and high temperature (around 70 Kelvin degree) [34].

Although it exhibits excellent characteristics in high energy storage efficiency (typically $>\sim 97\%$), high power density and high cycle life, necessity of the refrigeration mechanism is very costly and requires complex maintenance [18]. Besides, the superconductive coil is very sensitive to temperature changes. Up to now, only a few of them with small capacity are available for commercial use [31].

1.1.1.3 Flywheel energy storage

Flywheel is an ESS that stores the electrical energy in mechanical form. As shown in Fig. 1.6, a typical flywheel energy storage (FES) device consists of four main elements. Namely, a flywheel that spins at a very high velocity to achieve maximum storage of rotational kinetic energy within the given constraints, a containment system that provides a high vacuum environment to minimise windage losses and to protect the rotor assembly from external disturbance, a bearing assembly providing a very low loss support mechanism for the flywheel rotor, and a power conversion and control system for operating the flywheel for energy store or release [18, 19, 47].

During the charging process, the flywheel is accelerated to a very high speed by a motor. The energy is stored in the flywheel by keeping it at a constant speed. During the discharging process, the same motor acts as a generator in order to convert the rotational energy of the flywheel to electrical energy [31]. The total energy of a flywheel system is dependent on the size and speed of the rotor, and the power rating is dependent on the motor-generator [18]. The most utilized electrical machines in flywheel ESS are usually induction machine, doubly fed induction machine or permanent magnet synchronous machine [34].

Flywheel ESS can provide full charge-discharge cycles with little maintenance cost. Besides, high power density and high energy storage efficiency are also the advantages

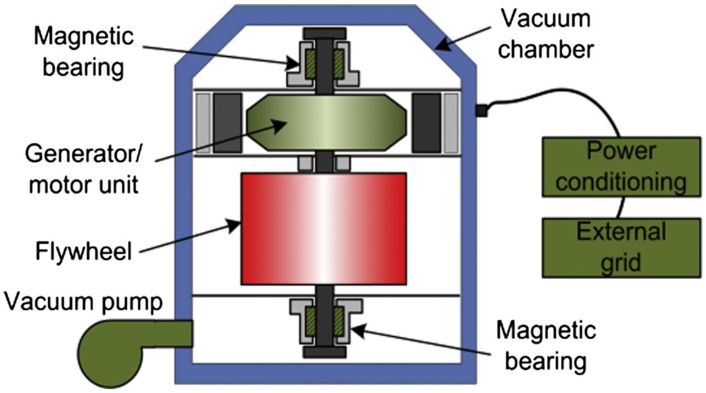

Figure 1.6: Schematic diagram of FES [19].

of this ESS. But compared with other ESSs, the relatively short duration, high frictional loss (high self-discharge loss) and low energy density restrain the flywheel ESS from the energy management application [18, 31, 47].

1.1.1.4 Pumped hydro storage

Pumped hydro storage (PHS) is the most widely implemented large-scale energy storage technology, which is technically mature and has been utilized worldwide for more than 70 years [43]. An example of modern conceptual PHS system with wind turbines is shown in Fig. 1.7.

A typical pumped hydraulic ESS normally consists of two reservoirs located at different elevations, a unit to pump water to the high elevation and a turbine to generate electricity with the water returning to the low elevation [20]. During off-peak hours, it pumps water to a reservoir at a higher altitude than the original one. This can be considered as a charging process, where the produced electrical energy is stored as the potential energy. Then, during peak periods, water from the upper reservoir is released and flows through hydro turbines that are connected to generators. Therefore, electrical energy is produced during this discharging process [20, 31]. To be short, the stored water is transferred between the two reservoirs, when electrical energy is required, the water flows to a lower height reservoir and the potential energy is converted to electrical energy. Clearly, the amount of stored energy is proportional to the height difference between the two reservoirs and the volume of water stored. Moreover, taking into account the evaporation and conversion losses, $\sim 70\%$ to $\sim 85\%$ of the electrical energy used to pump the water into the elevated reservoir can be regained [18].

However, geographical dependence of installation, high cost and environmental concerns (e.g. removing trees and vegetation from the large amounts of land prior to the reservoir being flooded) are the main drawbacks of the pumped hydraulic ESS [18, 43].

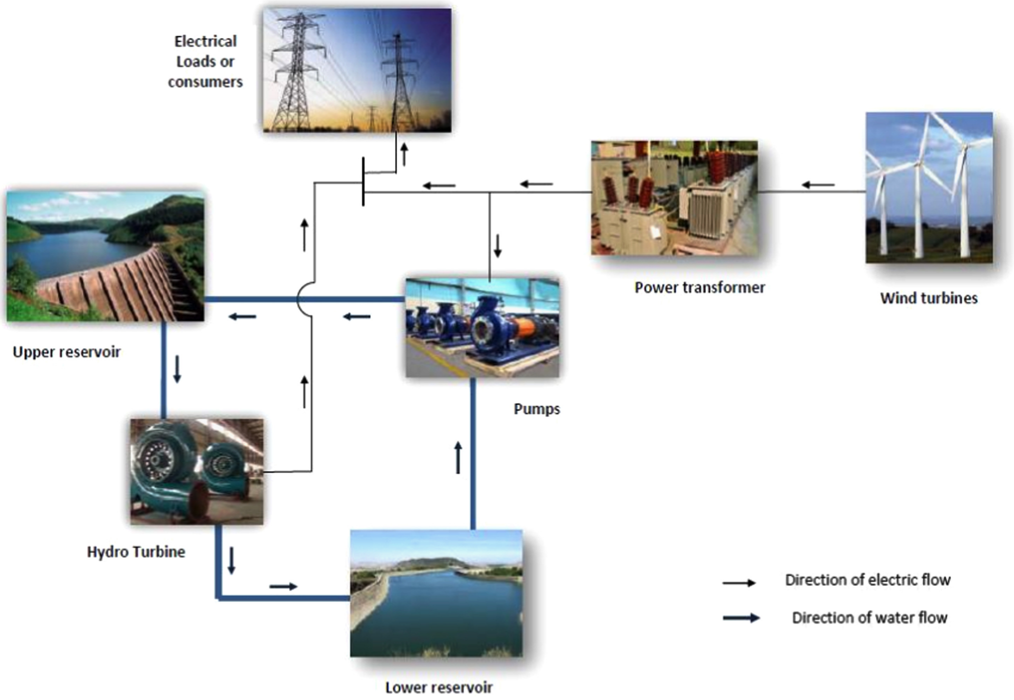

Figure 1.7: Conceptual PHS system with wind turbines [20].

1.1.1.5 Compressed air energy storage (CAES)

Except for the pumped hydraulic ESS, compressed air ESS is also a commercially available technology which is capable of providing very large energy storage capacity [18]. The idea of storing electrical energy by means of compressed air dates back to the early 1940s [21]. The world's first CAES plant was put into operation in 1978 near the northern German village of Huntorf with an output power of 290 MW [21]. An example of the machine hall of the Huntorf CAES plant is shown in Fig. 1.8.

The basic concept of CAES is simple, namely the storage is charged by the use of electrically-driven compressors which convert the electric energy into potential energy [21]. Generally, it consumes off-peak energy to compress air into underground cavities or surface vessel. To extract the stored energy, the compressed air is released and mixed with one of the conventional fuels, burned and expanded to drive a turbine generator to produce electricity [43].

CAES has a relatively long storage period due to very small self-discharge losses, which can be over a year [31]. However, the requirement of fossil fuels, the related contaminating emission, and the reliance on favourable geography render the CAES less attractive [18].

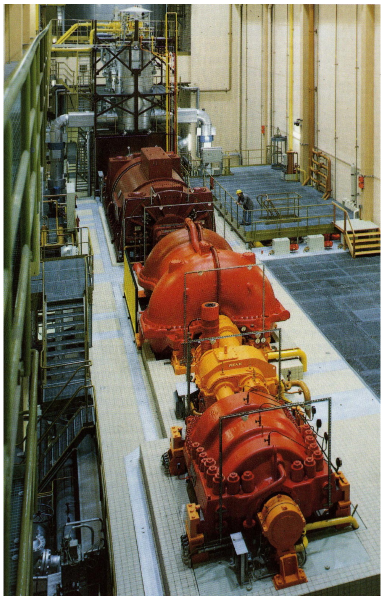

Figure 1.8: Example of the machine hall of the Huntorf CAES plant [21].

1.1.1.6 Battery

Battery, here refers to the rechargeable/secondary battery, is the most widely used ESS worldwide. It stores electricity in the form of chemical energy, and can be designed as high-power or high-energy ESS [48]. Each battery cell is made of a liquid, paste or solid electrolyte together with a positive electrode and a negative electrode [31]. During discharge process, electrochemical reactions occur at the two electrodes which generate a flow of electrons through an external circuit. The reactions are reversible, allowing the battery to be recharged by applying an external voltage across the electrodes [18]. Various types of secondary batteries have been developed for commercial use.

- **Lead-acid battery**

  Lead acid batteries, invented in 1859, are the oldest and most developed battery [18,49]. They are popular storage choice for power quality, uninterruptible power supply and some spinning reserve applications. However, their application for energy management is very limited due to their short life cycle and low energy density [18]. A typical lead-acid battery cell is composed of a sponge metallic lead anode, a lead-dioxide cathode and a sulfuric acid solution electrolyte [49]. It is by far the cheapest energy storage technology with regard to the cost of raw materials [50]. However, the use of heavy metal component is the main concern for this battery type as it makes them toxic and hazardous to the environment [49].

- **Nickel battery**

  Rechargeable nickel batteries are made of active material–nickelous hydroxide as the positive electrode [49]. Although there are various types of nickel based secondary battery, nickel–cadmium (Ni–Cd) battery and nickel–metal hydride (Ni–MH) battery are the most developed [50]. Ni–Cd batteries show a slightly higher energy density and a significantly higher power density than lead–acid batteries. However, Ni–Cd batteries have been banned because of their toxicity. Ni–MH batteries are the further development of Ni–Cd batteries, with the aim of creating a battery without toxic cadmium but with the advantages of nickel–cadmium batteries [50]. Even though Ni–Cd battery and Ni–MH battery are widely used in the market, they offer the lowest energy efficiency compared to others [49]. Besides, they also suffer form the memory effect and the strong lifespan dependence on cycle depth [31].

- **Sodium sulphur battery**

  Sodium sulfur (NaS) battery consists of liquid (molten) sulphur at the positive electrode and liquid (molten) sodium at the negative electrode as active materials separated by a solid beta alumina ceramic electrolyte [18]. It is the most developed type of high temperature battery. The battery should be maintained at 300∼350 °C [18, 49]. While NaS batteries not only have outstanding energy and power density, but also they have long life cycle of up to 15 years [18, 49]. These attributes made them attractive for large scale storage devices [49]. However, except for the high cost, the major drawback is that a heat source is required which uses the battery's own stored energy, partially reducing the battery performance [18].

- **Lithium battery**

  Lithium batteries, composed from lithium metal or lithium compounds at the anode, have the advantages such as light weight, high energy density and high power density [50]. Also the efficiency of lithium battery is almost 100%, which is another important advantage compared to other batteries [18]. The presence of lithium in its ionic rather than metallic state, in principle, overcomes the inherent drawback of lithium-metal cells, namely explosion hazards led by the uneven (dendritic) lithium growth [51]. Thus, various intercalation compounds, mostly studied and applied for the positive electrode, have spawned the diversity of lithium-ion battery family. Because of the increasing interest in EVs, the development of lithium-ion battery has received a significant boost in recent years.

- **Metal-air battery**

  Metal-air battery is the most compact and potentially the cheapest battery available in the market [18, 49]. Instead of an aqueous solution for electrolyte;

the battery uses ionic liquids [49]. Although other metal electrodes have higher theoretical energy density, the most advanced metal-air systems developed to date are the zinc-air and lithium-air batteries [49]. The high energy density and low cost of metal-air batteries make them ideal for many primary battery applications. However, the rechargeable metal-air batteries still need further development, because the current rechargeable metal-air batteries can only operate for a few hundred cycles and the efficiency is below 50% [18].

- **Flow battery**

  Furthermore, a promising capacity-oriented energy storage technology is the flow battery. The chemical energy is stored with the electrolyte solutions in two tanks outside the battery cell stacks [49]. Hence, the energy rating is determined by the quantity of electrolyte, while the power rating is dependent on the active area of the cell stack [18]. Compared to conventional batteries, the main advantage of flow battery is that it is possible to design the battery to have optimal power acceptance and delivery properties without needing to maximize the energy density [49]. The typical flow batteries are vanadium redox battery (VRB) and zinc bromine (ZnBr) battery [48]. The main studies on flow battery have focused on stationary applications [18].

Principle characteristics of the different battery technologies, namely energy density, power density, operating temperature and durability, are listed in table 1.1 [35, 52–54].

Table 1.1: Principle characteristics of different battery technologies

Battery technology	Energy density (Wh/kg)	Power density (W/kg)	Operating temperature	Durability (years)	Cost ($/kWh)
Lead-acid	30∼50	75∼300	-20∼50°C	10	200∼400
Ni-MH	30∼110	250∼2000	-20∼65°C	3∼15	800∼1500
Lithium-ion	75∼250	100∼5000	-20∼60°C	5∼20	600∼2500
NaS	150∼240	150∼230	300∼350°C	15	300∼500
VRB	10∼75	80∼150	-5∼50°C	10∼20	150∼1000
ZnBr	60∼85	50∼150	20∼50°C	5∼20	150∼1000
Zinc-air	110∼3000	∼100	0∼60°C	-	10∼60

1.1.1.7 Fuel cell

Fuel cell (FC) is an electrochemical energy conversion device that can generate electricity via oxidation-reduction reactions. It is actually a reversed electrolysis reaction [55]. The FC efficiently converts the chemical fuel into electrical energy at a continuous steady rate to provide extremely high energy density [43]. A schematic diagram of FC is shown in Fig. 1.9.

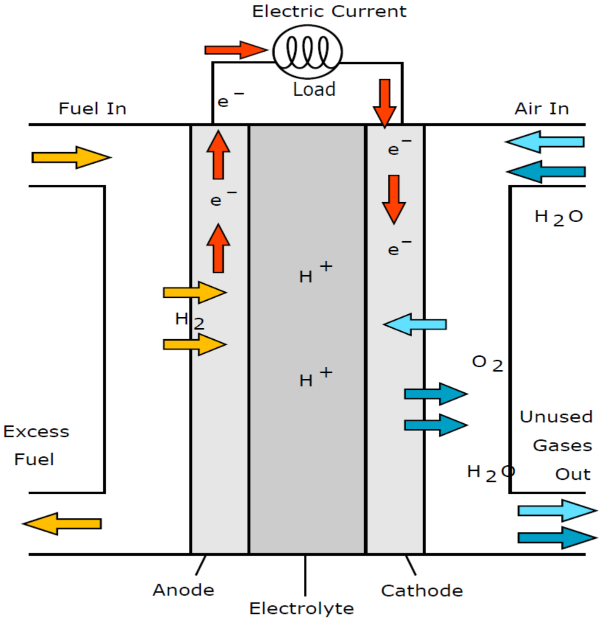

Figure 1.9: Schematic diagram of FC [1].

Although there are different types of FCs, they all operate with the same basic principles. Namely, they produce electricity from external supplies of fuel (anode side) and oxidant (cathode side), and the by-products are water and heat. Generally, a FC consists of four main parts, namely anode, cathode, electrolyte and the external circuit. The reactants flow in and reaction products flow out, while electrolyte remains in the cell [18]. Hydrogen is oxidized into protons and electrons at the anode, while oxygen is reduced to oxide species and reacts to form water at the cathode.

The main difference in various FC designs is the chemical characteristics of the electrolyte. Depending on the electrolyte, either protons or oxide ions are transported through an ion-conductor electron-insulating electrolyte while electrons travel through an external circuit to deliver electrical power [55]. Currently, six major different types of available fuel cells are polymer electrolyte membrane fuel cell (PEMFC), alkaline fuel cell (AFC), phosphoric acid fuel cell (PAFC), molten carbonate fuel cell (MCFC), solid oxide fuel cell (SOFC) and direct methanol fuel cell (DMFC) [56]. Comparison of these different FC technologies is shown in table 1.2.

1.1.1.8 Summary

In summary, ESS technologies have complementary characteristics in terms of power and energy density, life cycle, response rate, etc. The ideal ESS should offer fast access

Table 1.2: Comparison of different FC technologies

FC type	Electrolyte	Charge carrier	Fuel	Operating temperature	Cell voltage	Electrical efficiency	Application
PEMFC	Solid polymer membrane	H^+	Pure H_2	50∼100 °C	1.1 V	53-58%	Backup power, portable power, small distributed generation, transportation
AFC	Liquid solution	OH^-	Pure H_2	50∼200 °C	1.0 V	60%	Military, space
PAFC	Phosphoric acid	H^+	Pure H_2	∼200 °C	1.1 V	>40%	Distributed generation
MCFC	Lithium and potassium carbonate	CO_3^{-2}	H_2,CO, CH_4, other	∼650 °C	0.7-1.0 V	45-47%	Electric utility, large distributed generation
SOFC	Stabilized solid oxide electrolyte	O^{-2}	H_2,CO, CH_4, other	800∼1000 °C	0.8-1.0 V	35-43%	Auxiliary power, electric unity, large distributed generation
DMFC	Solid polymer membrane	H^+	CH_3OH	60∼200 °C	0.2-0.4 V	40%	Mobiles, computers and other portable devices

to power whenever needed, provides high energy capacity, has a long life expectancy and be available at a competitive cost. However, there is no energy storage technology currently available that can meet all these desirable characteristics simultaneously [48]. Furthermore, power density and energy density are two main characteristics of ESS, which are usually plotted in the same figure in order to compare the performance of different energy storage techniques. The obtained figure, as shown in Fig. 1.10, is the so-called Ragone plot. High power density means that the ESS can supply energy at very high rates, but characteristically for short time periods; alternatively, high energy density means that the ESS can supply energy for longer time periods. Besides, high power ESSs possess fast response rate, while high energy ESSs have slow response rate [43]. Hence, in analogy to data storage in computer engineering, a classification in terms of access and capacity orientation can be considered for ESS [48]. Table 1.3 categorizes ESS technologies based on this classification.

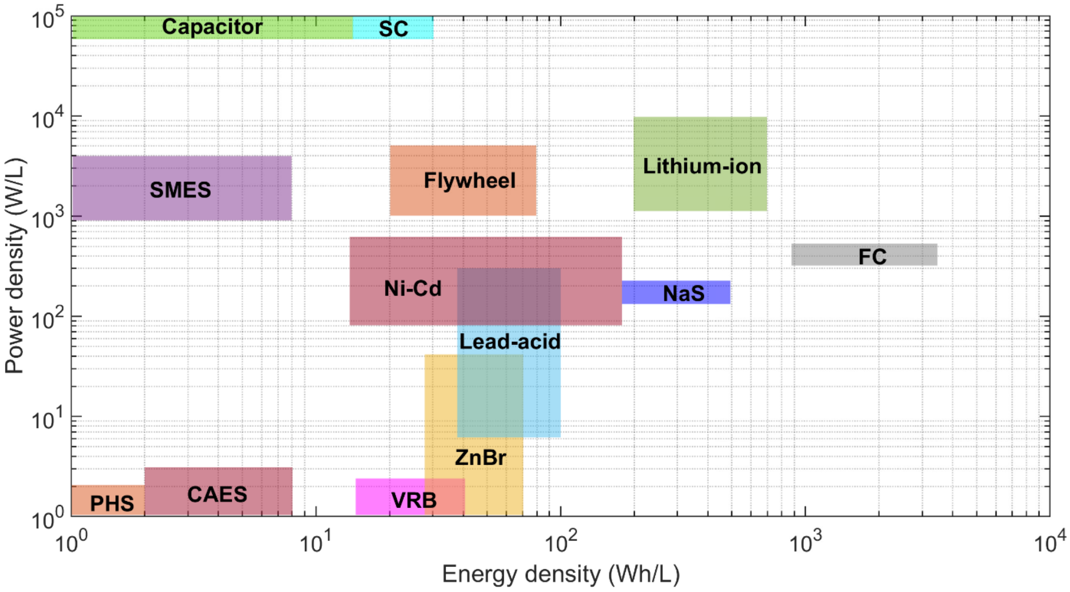

Figure 1.10: Ragone plot with different ESSs.

1.1.2 Hybrid energy storage system

Several ESS applications require a combination of energy and power rating, life cycle, and other specifications that cannot be fulfilled by a single ESS technology [43]. Hence, the idea of hybrid ESS lies on the fact that electronically combining the power output of two or more devices with complementary characteristics can increase the advantages that a single ESS technology can offer without fundamental development of the storage mechanism [43]. After coupling two or more ESS technologies together, namely combining the appropriate features of different technologies, the hybridization

Table 1.3: High power and high energy ESS technologies classification

High power devices (access-oriented)	High energy devices (capacity-oriented)
SC	Pumped hydro
SMES	CAES
Flywheel	FC
High-power battery	High-energy battery

can provide excellent characteristics not offered by a single ESS unit [57].

As it is shown in Fig. 1.11, the basic idea of hybrid ESS is to combine high energy devices with high power devices in order to yield a more functional ESS. The high power device should supply short term power needs, while the high energy device should meet long term energy needs. In other words, the access-oriented storage absorbs or delivers the transient and peak power, and the capacity-oriented storage fulfills the slowly varying and steady-state power demand [48]. Hence, based on this idea, the currently proposed hybrid ESS configurations are listed in table 1.4. Note that although a pumped hydro ESS is used as an energy supplier ESS unit, the relevant hybridization has not yet been proposed [43].

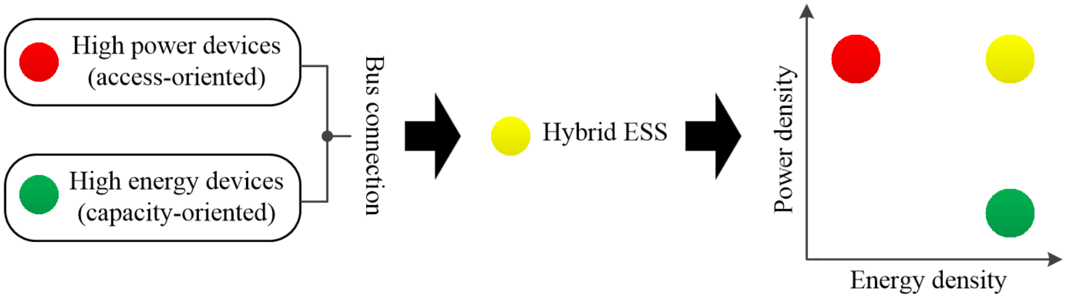

Figure 1.11: Basic idea of hybrid ESS.

Except for enhancing the dynamic performance of the energy storage, lifespan improvement is also a significant benefit of ESS hybridization. Especially in embedded application, where reliability is of vital importance. Embedded applications, such as EV, have strong requirement on reliability, energy efficiency and dynamic performance. Hence, EV is intended to be powered by a hybridized source. As our main topic is EV, in the following, we will focus on ESS suitable for this application.

Battery, SC and FC are the most studied energy storage devices in the electrified vehicle power train [58]. Especially the hybridization based on the PEMFC has received considerable research attention in recent years. Because PEMFC has

Table 1.4: Currently proposed hybrid ESS configurations

Energy supplier	Power supplier
Battery	SC SMES Flywheel
CAES	SC Flywheel
FC	SC SMES Battery

high power density, appropriate operating temperature and low corrosion compared to other types of FCs [3]. Thus, the vehicle all-electric range can be guaranteed by PEMFC. Additionally, one of the main concerns about EV application, namely the long charging time, can also be eliminated by the fast hydrogen filling process. Hence, hybrid ESS based on PEMFC and battery/SC is very promising for the next EV generation [1]. However, the lifetime of current PEMFC vehicle, evaluated only at 3900 hours in 2015, cannot satisfy the commercial use [22]. Because a 5000-hour's PEMFC lifetime requirement is requested for the light-duty EV market [3]. Owing to this, the advantage of using a hybrid ESS can be highlighted. The presence of battery/SC can meet the instantaneous power demand of the vehicle, which tries to improve the PEMFC power leveling. The less fluctuating power demanded from PEMFC will consequently prolong its lifespan. In turn, PEMFC will maintain the energy stored in the battery/SC at an adequate level, which will avoid frequent cyclic charging and discharging of battery/SC. Hence, the hybridization can prevent premature degradation of each component [1].

Moreover, reducing the weight, cost and fuel consumption are also relevant objectives for using hybrid ESS in EV application [59]. Results displayed in Fig. 1.12 shows that FC/battery-based hybrid ESS can achieve longer mileage with less weight, cost and fuel consumption compared with the corresponding single ESS system.

1.1.3 Hybridization architecture

Conditioning circuitry is required when combining two or more energy storage devices acting as a single power source. Numerous hybridization architectures have been proposed to achieve this aim ranging from simple to very flexible [35]. The presence of power electronic interfacing circuits brings more flexibility and scalability to the hybrid ESS. Thus, more choices in implementing control and energy management strategies have been proposed [48]. Besides, the complexity and cost of hybrid ESS

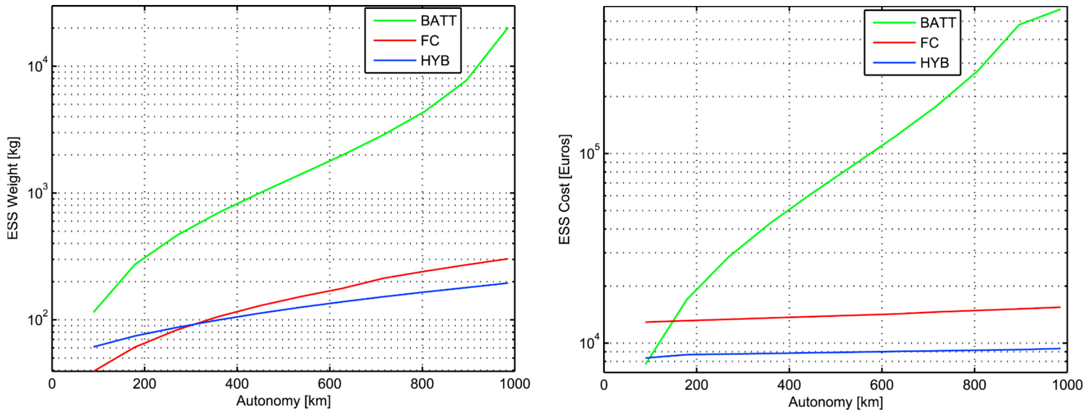

(a) Weight reduction (b) Cost reduction

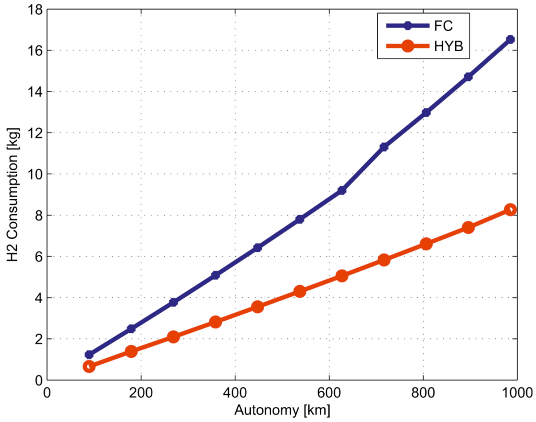

(c) Fuel consumption reduction

Figure 1.12: Example of hybrid ESS' interests in reducing weight, cost and fuel consumption (BATT refers to single battery ESS, FC refers to single FC ESS, HYB refers to hybrid ESS of FC/battery) [22].

have also increased. Generally, the connection principle between two energy storage devices can be grouped into three categories as shown in Fig. 1.13.

Fig. 1.13(a) shows direct parallel connection of two energy storage devices, which is also named as passive parallel architecture. It simply connects two ESS technologies together without any power electronic interfacing circuit. This kind of hybridization architecture is simple, but the output voltage of the two ESSs should be equal. Furthermore, the absence of power converter makes this architecture become the least expensive one. However, the major problem with this topology is that it cannot effectively utilize the energy stored in the ESSs, because the current distribution between ESSs is uncontrolled [60]. Namely, the range of power that is used from either energy source is limited by the voltage swing of the other, where individual maximum

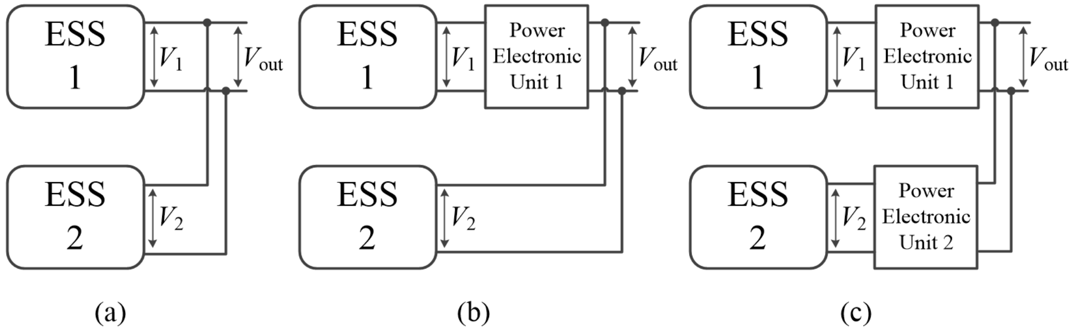

Figure 1.13: Hybridization architectures of hybrid ESS.

power point tracking is not possible for each source [35]. Besides, due to the direct connection of the two ESSs, this architecture has no fault tolerant ability. The faults occurring in one ESS will affect the other one, and will eventually induce malfunction at the system level [43].

Fig. 1.13(b) shows a more complex but flexible solution by combining two energy storage devices. A power converter is used to decouple the two power sources. Hence, it provides more flexibility for active energy management. The power converter controls the power output of ESS1, allowing its voltage to vary, while ESS2 delivers the remaining power requirement to the load [35]. Usually, the more sensitive ESS is operated as ESS1, because the power conditioning can protect it by adapting its power output. Hence, the lifetime of the overall system can be prolonged [43].

Fig. 1.13(c) shows the active parallel architecture. It has the highest level of flexibility, where each ESS unit has its own power converter. The converters are connected to the common output bus. Each power source can be controlled according to its specific voltage and power. Hence, this hybridization architecture not only allows to developing various energy management strategies, but also it makes the implementation of maximum power point tracking for each ESS possible [35]. In addition, this architecture has the highest level of fault tolerant ability, since the failure of one source does not affect the function of the other one [43, 60].

1.1.4 Energy management strategy

Energy management strategy (EMS) plays an important role for hybrid ESS. Because the basic objective of EMS is to meet the load power demand by determining the power reference for each ESS unit. In other words, EMS can be regarded as the high level supervisory control of hybrid ESS. However, a good EMS not only allows the hybrid ESS to delivering the load's power demand, but it can also increase the durability and reliability of the ESSs, maintain the global efficiency at its high level. Consequently, designing EMS comes with multiple objectives [1]. Generally, as shown in Fig. 1.14, EMSs can be categorized into rule-based and optimization-based strategies. In this

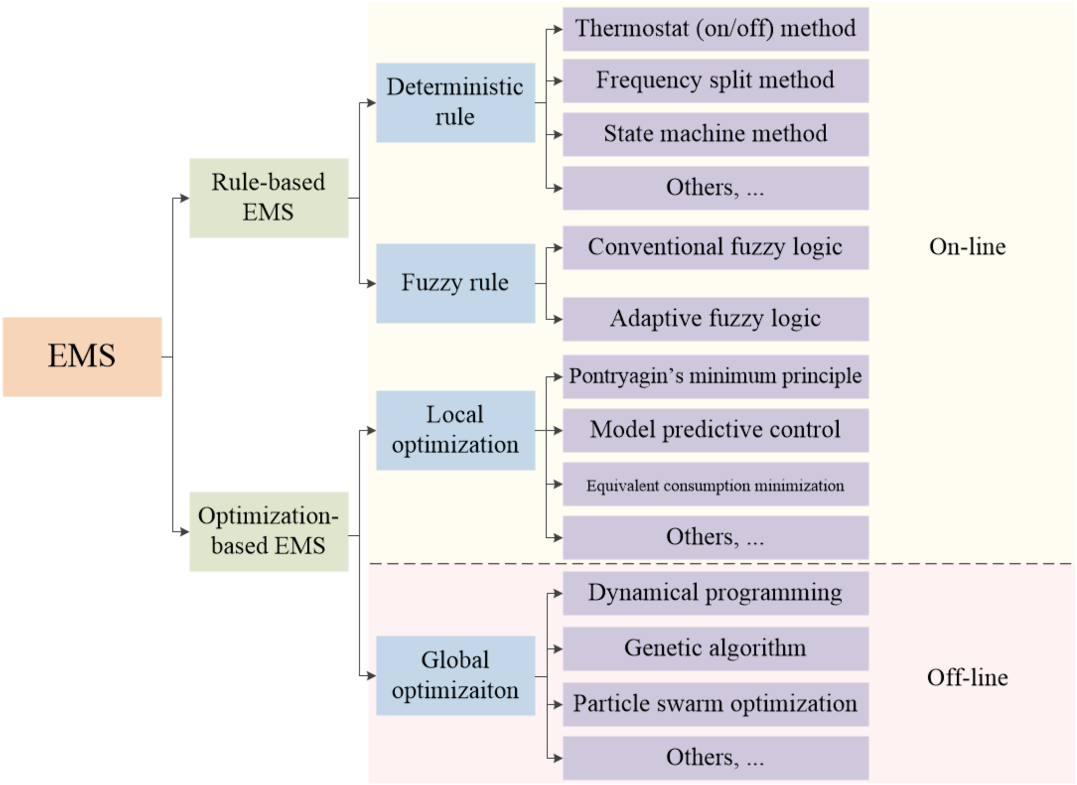

Figure 1.14: Classification of EMSs [1,3].

sub-section, different types of EMSs will be briefly presented without the details of design and implementation.

- **Rule-based EMSs**

The rule-based EMSs can be further divided into deterministic and fuzzy rules. They are usually designed based on human intelligence and experience and generally without prior knowledge of the drive cycle [1]. More advanced rule-based health-conscious EMSs are designed to find efficient operation points that mitigate the energy source degradation [3].

Deterministic rule-based strategies are mainly developed through look-up tables (not real-time data) and among which, thermostat (on/off) strategy, frequency split strategy and state machine strategy are mostly used [3]. Thermostat control strategy is a simple deterministic rule, which tries to operate the energy supplier at highest efficiency point to charge the power supplier when its energy is under the lower threshold. This EMS leads to frequent on and off (charging and discharging) on the energy storage devices, which results in the reduction of their lifetime [1]. Frequency split strategy divides power demand into low and high frequency components by low-pass filtering combined with load-leveling. Compared with the thermostat strategy, it can prevent the premature aging of the energy storage devices [61]. State machine strategy divides the hybrid ESS into several functional states according to the different energy state levels of power supplier. For every state, the energy supplier has it own power output decided by the load power. With this strategy, the overall efficiency and lifetime of energy storage devices can be improved [62]. To be short, deterministic rule-based strategies are simple and can be easily implemented in practice. Although optimal results are hardly reached, they are regarded as the most practical way to achieve multiple objectives [1].

Fuzzy rule-based EMSs can be considered as an extension of the deterministic rule-based EMSs. The basic idea is to formulate a collection of fuzzy "if-then" rules from human knowledge and reasoning, which offers a qualitative description of controlled system [61]. Contrary to the deterministic rule-based EMSs, fuzzy rule-based EMSs do not rely on precise system model. Hence, they are particularly suitable for nonlinear, uncertain and time varying systems [3]. Moreover, other advantages of fuzzy rule-based EMS are its robustness to measurement noise and component variability as well as its flexibility [61]. Fuzzy rule-based EMSs use fuzzy inference to transfer the deterministic inputs and outputs into linguistic ones. The fuzzy outputs are then defuzzyfied into precise control signals for the system. The "if-then" rules can be experience-based, which belongs to the conventional fuzzy logic [41]. While the membership functions can also be tuned by intelligent methods such as neural network algorithm, genetic algorithm. This constitutes the so-called adaptive fuzzy logic. The fuzzy inference technique solves the multi-objective problem by adding multiple inputs and designing proper rules [3].

- **Optimization-based EMSs**

Optimization-based EMSs, which can be further divided into local optimization and global optimization categories, have received more research interests recently because of their ability to reach optimal results [1]. Fuel economy, durability of power sources, energy cost can be included in an objective function, then the optimal results can be calculated after solving the optimization problem.

Global optimization strategies are carried out based on the overall driving cycle information, which cannot be applied in real-time applications unless the driving cycle could be predicted [61]. Dynamical programming, genetic algorithm, particle swarm optimization are widely used to cope with the global optimization problem. Although they cannot be implemented in real-time control, they can be a good benchmark for other EMSs and give insights for the development of simple and implementable strategies [1].

On the contrary, local optimization based strategy replaces the optimization period of the whole drive cycle for global optimization strategy into the instantaneous sampling time to calculate instantaneous optimal power split scheme among different power sources. Equivalent consumption minimization strategy, Pontryagin's minimum principle and model predictive control are usual [1, 59]. Especially the model predictive control, which can be regarded as a "look-ahead" strategy, is an attractive solution for multi-objective EMS design problem [63]. Because it can foresee dynamic changes before they happen and efficiently compute step-wise optimal input control to achieve a defined quadratic performance objective [64].

1.1.5 Summary

Hybrid ESS, combining the advantages of single ESS through power electronic interfacing circuits, can meet both static and dynamic power demand. In the meanwhile, EMS, as the high level supervisory control, is an essential topic for the hybrid ESS. Hence, fruitful research results about EMS have been made in recent years. However, information of the lower level, namely the real-time operating status of the single ESS, is the basis for designing the EMS. The detailed discussion about the monitoring task for the single ESS can not be ignored.

Therefore, in this thesis, the research efforts are focused on the battery monitoring and diagnosis. Because battery, especially the lithium-ion battery, is the most used ESS in EV application. The following sections are dedicated to lithium-ion battery.

1.2 Lithium-ion battery basics

Although the origin of the term "battery" dates back to 1749, the first real battery has been invented half a century later [65]. Since then, attempts to improve battery's energy density, power density, reliability, etc. have never ceased. Especially, resorting to lithium is suddenly making the news though it has been discovered for almost two centuries [66]. Features such as high energy/power density and extended life cycle, make lithium-ion batteries become currently the state-of-the-art energy storage devices [67]. In particular, lithium-ion batteries are widely used for electrified powertrain systems.

A lithium-ion battery cell mainly consists of four components, namely cathode (positive electrode), anode (negative electrode), electrolyte and a separator that prevents contact between cathode and anode [51, 68]. From a chemical point of view, lithium-ion batteries operate through reversible (and usually topotactic) insertion of lithium ions in the electrode materials structure while the electrolyte is ideally chemically inert and impregnates both electrodes and separator to enable ionic transport [69]. Fig. 1.15 illustrates the working principle of a lithium-ion battery cell. In brief, lithium ions (Li+) flow from the anode (negative electrode) to the cathode (positive electrode) via the electrolyte and separator diaphragm during a discharge process, and in opposite direction during charging process [23, 68].

The current main lithium-ion technologies for electrified powertrain are listed in table 1.5. The choice of electrode materials will determine the potential and

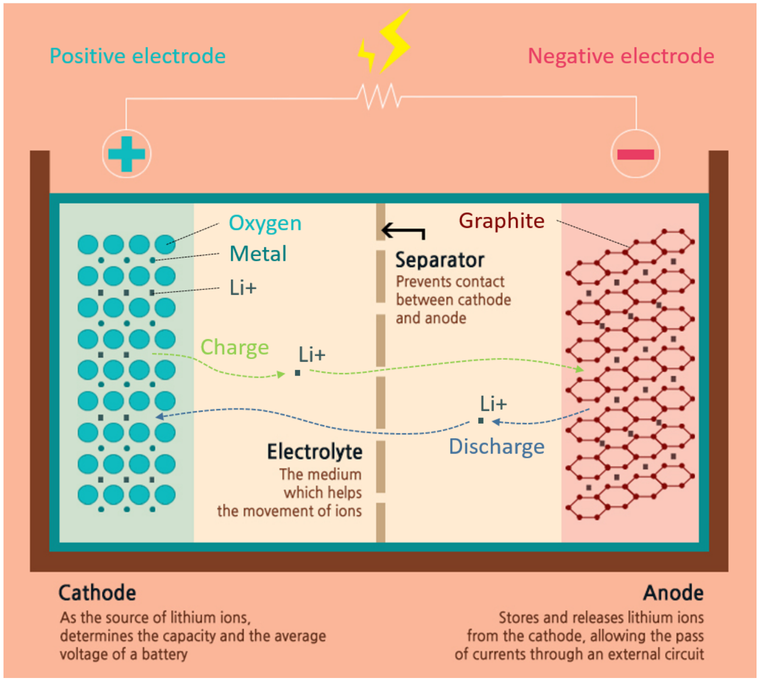

Figure 1.15: Working principle of a lithium-ion battery cell. (Redrawn with [23])

energy density of the cell [70]. As listed in table 1.5, the cathode is a lithium containing compound such as NMC ($LiNi_xMn_yCo_{1-x-y}O_2$), LFP ($LiFePO_4$), NCA ($LiNi_{0.8}Co_{0.15}Al_{0.05}O_2$), LMO ($LiMn_2O_4$) and LTO ($Li_4Ti_5O_{12}$) [71–73]; while the anode is of porous carbon, and the most commercially popular material is graphite [68]. Besides, as shown in Fig. 1.16, lithium-ion is expected to remain the technology of choice for the next decade. Other technology options are expected to become available after 2030 [2].

1.2.1 Glossary and technical terms

There are many important terms associated with lithium-ion battery. Hence, for the sake of having a better understanding on the follow-up discussion, the related glossary and technical terms will be explained firstly.

- **Capacity**

Battery capacity, usually expressed using ampere-hour (Ah) as unit, corresponds to the amount of charge that can be withdrawn from a battery until cut-off discharge voltage limit is reached when starting from a fully charged state [74].

However, a difference should be done between battery nominal capacity and battery actual capacity. The battery nominal capacity, usually indicated on the battery

Table 1.5: Current main lithium-ion technologies for electrified powertrain

Anode\Cathode	Cell nominal tension (V)	Eneregy density (Wh/kg)	Thermal runaway temperature (°C)	Cost ($/kWh)	Cycle life
Graphite\NMC	3.8~4.0	150~220	210	~420	1000~2000
Graphite\LFP	3.2~3.3	90~130	270	~580	1000~2000
Graphite\NCA	3.6~3.65	200~260	150	~350	500
LTO\LMO	2.3~2.5	50~85	safest	~1005	2000~25,000

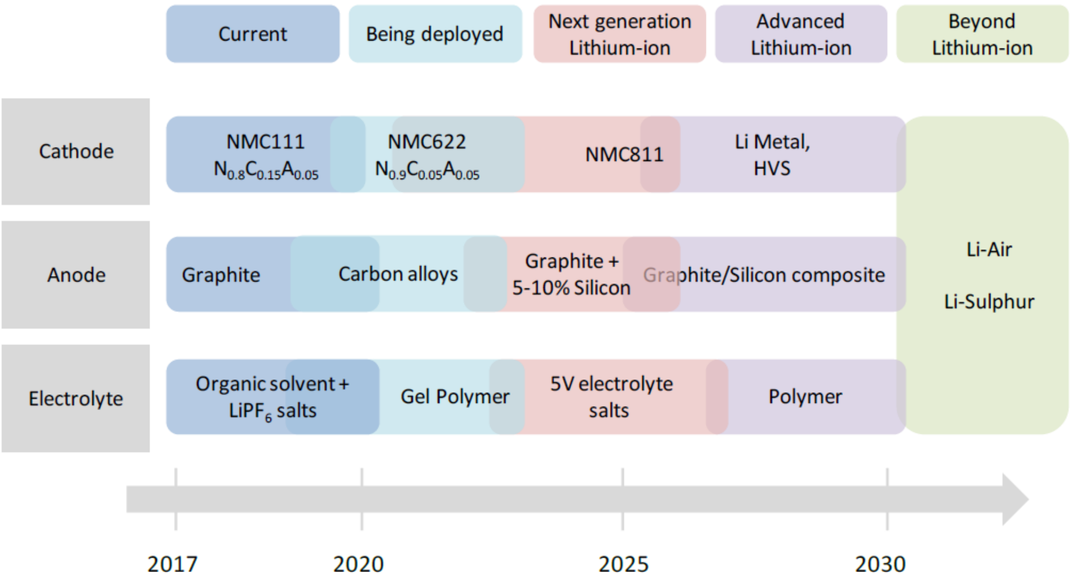

Figure 1.16: Expected battery technology commercialisation timeline [2].

itself, is given by the battery manufacturer and measured under certain conditions when it is new. This value is obtained with the specified standard discharge current under specified temperature [75]. Hence, the actual battery capacity varies significantly from the nominal one, since it not only depends strongly on the operating conditions such as temperature, discharging and charging current etc., but also it decays over the battery's lifetime due to aging processes [76].

- **C-rate**

C-rate is a measure of battery charge or discharge current rate, which is normalized against battery nominal capacity [72]. For instance, for a battery with nominal capacity of 20 Ah, 1 C's current is equal to 20 A, 2 C's current is equal to 40 A, 0.5 C's current is equal to 10 A.

- **State of charge**

State of charge (SOC) indicates the residual energy inside a battery cell. It is usually expressed by the ratio of the remaining capacity to the nominal capacity of the cell. The remaining capacity is the number of ampere-hours that can be drawn from the cell before it is fully discharged [24]. 100% means the battery is full charged, and 0% means the battery is empty. Fig. 1.17 shows the schematic diagram of SOC definition.

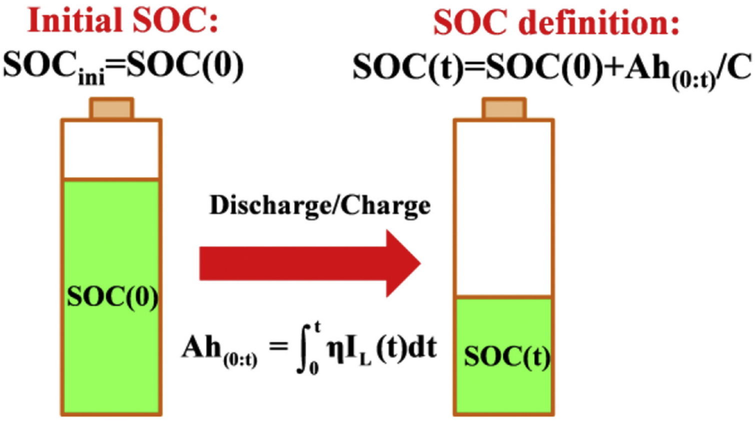

Figure 1.17: Schematic diagram of SOC definition for a single battery cell [24].

Generally, SOC is calculated based on current integration over charging/discharging time. Namely, the battery SOC $\in [0\%, 100\%]$ can be modeled by the classical Coulomb counting method:

$$soc(t) = soc(t_0) - \eta \int_{t_0}^{t} \frac{I_{\text{batt}}(\tau)}{\mathrm{C_n}} d\tau \tag{1.1}$$

where, the variable *soc* is the operator of SOC; η is the Columbic efficiency which is usually approximated to 1 for LIBs [72]; $\mathrm{C_n}$ (Ah) is the battery nominal capacity; $soc(t)$ is the required SOC at time point t based on its initial value $soc(t_0)$.

- **Depth of discharge**

Depth of discharge (DOD) is opposite to SOC (DOD=1-SOC). It describes how much a battery has been discharged [75]. For example, SOC of 20% means the DOD is up to 80%.

- **Internal resistance**

Internal resistance of a battery is defined as the opposition to the current flow within a battery [75]. It includes the resistance of contacts, electrodes, electrolyte as well as the related electrochemical reactions. The internal resistance of a battery depends on many factors such as C-rate of discharging/charging, battery temperature, SOC, etc. In general, due to the aging processes, the internal resistance tends to increase over the battery's lifetime [4].

- **State of health**

State of health (SOH), representing the health state of a battery, is an indicator that evaluates the battery performance reduction. Although there is still no consensus in the industry on what SOH is and how SOH should be determined, SOH is usually quantified by estimating the power fading or/and the capacity loss of a battery [75,77]. However, it can also be derived by other battery parameters like alternating current impedance, self-discharge rate and power density [77].

Although the assessment of SOH is arbitrary and may vary from one application to another, 80% decrease of battery actual capacity is commonly used as the threshold of end-of-lifetime (EOL) for the LIBs in BEVs and PHEVs due to the requirement of battery energy capability. Doubling of battery internal resistance is often defined as the EOL indicator for HEVs, where battery power capability plays the most important role [74].

- **Open circuit voltage**

Open circuit voltage (OCV) refers to the equilibrium state when battery enters the open circuit condition after charged or discharged. However, an accurate measurement of the OCV requires battery to stay in open-circuit condition for a sufficient long period of time which usually takes several hours [78]. In fact, this is because the so-called OCV relaxation process after the current interruption. To be short, when the battery is charging or discharging, its internal states (micro level) will be disturbed by the external excitation; while after the external current is interrupted, it will consequently take time for the battery to rebuild a new equilibrium state, which

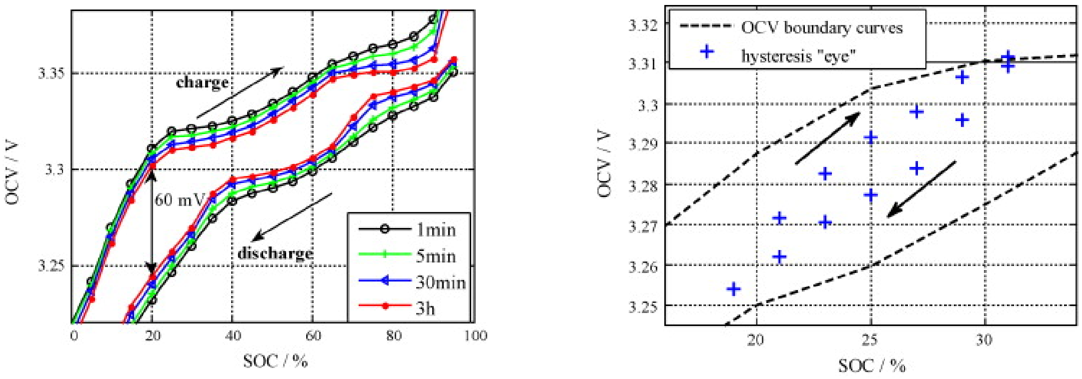

(a) OCV curves of the LFP-based cells measured after various rest periods at each step [81].

(b) Schematic illustration of the hysteresis “eye” phenomenon between OCV hysteresis boundaries [81].

Figure 1.18: Example of battery OCV.

is fixed as electromotive force (EMF) [79]. In other words, the OCV that usually appears in the literature is approximately the EMF in the equilibrium state after the OCV relaxation process.

Furthermore, the aforementioned relaxation process strongly depends on the short time previous usage history including the current value and the current direction, and the latter can cause the well-known OCV hysteresis phenomenon. Specifically, the OCV relaxation process is under the EMF if the battery is previously discharged; on the contrary, it is above the EMF if the battery is previously charged. However, even through there exist the relevant hysteresis models for the OCV, the battery will never operate along these two hysteresis curves in reality due to the more complicated hysteresis “eye” phenomenon (also called “minor loop”) [80]. Example of battery OCV curve is shown in Fig. 1.18. Moreover, other factors such as temperature, initial SOC and battery technology (e.g. the LIB with LFP cathode has serious hysteresis phenomenon) will also affect the OCV relaxation process [81].

- **Battery pack**

Different cell configurations such as cylindrical, prismatic or pouch, can be adopted considering the heat dissipation, production maturity, cost [68]. However, the capacity and voltage of a single lithium-ion battery cell are usually relatively small. Hence, cells are electrically connected in parallel to satisfy high capacity requirements and in series to provide the desired system voltage. In other words, a battery pack used in the electrical powertrain is a collection of modules, which are in turn made up of series/parallel combinations of individual cells [82].

1.2.2 Inevitable aging process

Aging is inevitable and ultimately rooted in chemical process over battery lifetime, which starts to emerge as soon as the cells are assembled [69, 83]. In fact, lithium-ion cells degrade as a result of their usage and exposure to environmental conditions [25]. Namely, cycling aging and calendar aging constitute the battery aging process, which exhibits a gradual effect on the cells' ability to store energy, meet power demands and, eventually, leads to their end of life [25, 69].

For automotive application, the battery aging extent is mostly determined by charge and discharge protocols, environment temperature and DOD [84]. Hence, in order to prevent the premature aging, lithium-ion batteries are usually requested to be used in a safe operating area. It is restricted by current, voltage and temperature ranges. The most significant boundaries are formed by maximum discharge current and maximum charge current, maximal and minimal voltages for each individual cell, and maximum and minimum operating temperature [4].

In addition, the degradation process of lithium-ion battery involves a large number of physical and chemical mechanisms and their interactions. Fig. 1.19 illustrates the degradation mechanisms in LIB cells. Moreover, most of these processes cannot be studied independently and occur at similar timescales, complicating the investigation of aging mechanisms [85]. Continuous and constant academic research on exploring their degradation mechanisms is triggered from a long time ago, nevertheless, a complete understanding of these synergistic effects is still lacking [69, 76].

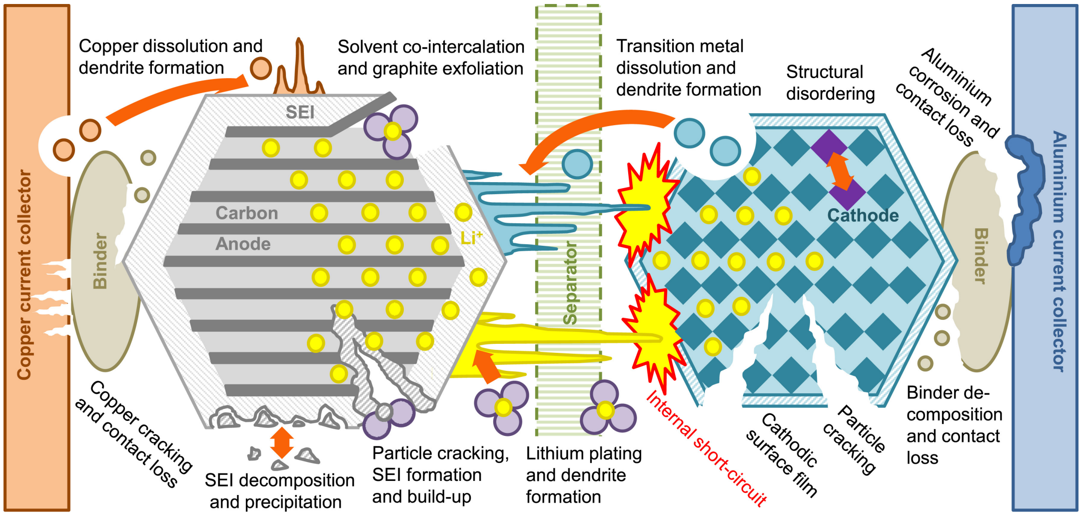

Figure 1.19: Degradation mechanisms in LIB cells [25].

However, one consensus has been reached recently, namely the most dominant aging mechanism is the formation and the growth of the solid electrolyte interphase (SEI) that take place on the electrode/electrolyte interface. It eventually results in three degradation modes, namely loss of lithium inventory, loss of active positive electrode material and loss of active negative electrode material [3,25,69,73,76,85,86]. Fig. 1.20 resumes the cause and effect of degradation mechanisms and associated degradation modes.

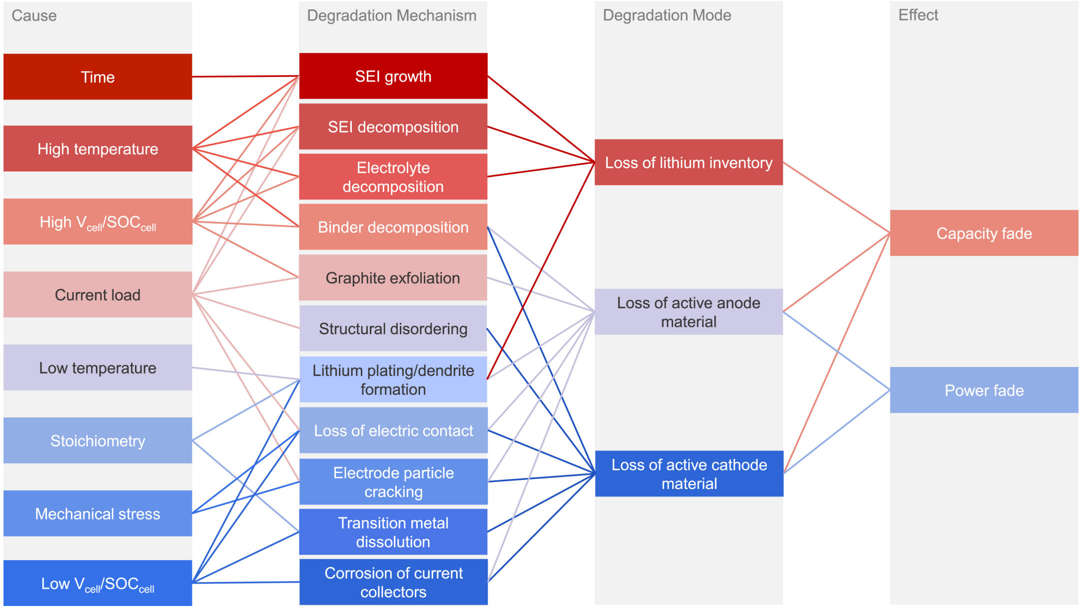

Figure 1.20: Cause and effect of degradation mechanisms and associated degradation modes [25].

1.2.3 Unforeseeable abuse conditions

Along with the battery slow aging process during the regular operation, lithium-ion batteries also have some potential safety issues that threat their reliability. Safety issue associated to the risk of thermal runaway is known to be a major problem of lithium-ion batteries [71].

Thermal runaway, which can induce serious safety problems such as smoke, fire and even explosion, is a catastrophic failure of on-board batteries [87]. Although the battery cells have to go through several compulsory test standards before their application in EV, accidents induced by thermal runaway happen occasionally [87]. It is mainly because of the unforeseeable abuse conditions, including mechanical abuse, electrical abuse, and thermal abuse [87, 88]. Deep insight of the mechanisms of battery thermal runaway is still premature [9–11]. However, as show in figure 1.21, a simple chain reaction-like relationship among the aforementioned three abuses can be deduced before the thermal hazard.

- **Mechanical abuse**

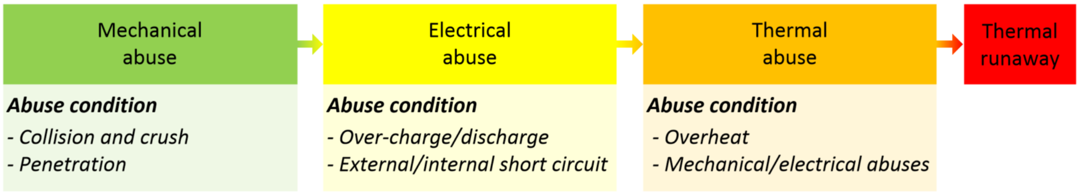

Figure 1.21: Chain reaction-like relationship among mechanical/electrical/thermal abuses.

Typical mechanical abuse conditions, such as vehicle collision and consequent crush or penetration of the battery pack, may result in the deformation of battery cell [87]. The electrode contact due to the cell separator failure will cause local internal short circuit and current flow, consequently, temperature increase induced by the heat generation will lead to spontaneous reactions and thermal runaway [73]. Worse still, the potential leakage of flammable electrolyte will deteriorate this bad situation.

- **Electrical abuse**

Overcharge, overdischarge, internal short circuit and external short circuit are four common electrical abuses that can cause irreversible battery damages, or even lead to battery thermal runaway [89]. Furthermore, as shown in figure 1.22, a general causal relationship among these four common battery electrical abuses can be concluded according to the literature.

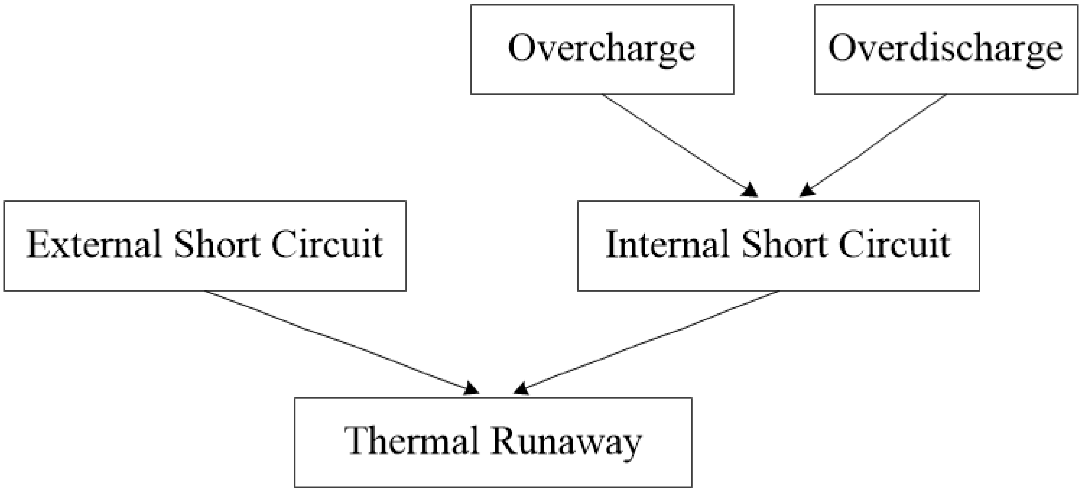

Figure 1.22: General causal relationship among the common battery electrical abuses

External short circuit, as indicated by its name, appears when the positive and negative electrodes are connected by conductors. Car collision, water immersion, contamination with conductors, electric shock during maintenance, etc., can lead to external short circuit [87]. The internal short circuit has been mentioned in the mechanical abuse, namely it mainly occurs when the battery cathode and anode contact with each other caused by the failure of the separator. Under the electrical abuse, dendrite growth induced by overcharge or overdischarge can pierce the battery separator [9, 10, 73, 77, 87, 90]. Besides, charging the battery at the low temperature has also been reported as one of the sources of internal short circuit [91]. Moreover, both external short circuit and internal short circuit can trigger thermal runaway if they are not treated correctly in time.

- **Thermal abuse**

Thermal abuse is the direct cause of battery thermal runaway. Except for the local overheat induced by mechanical or electrical abuse, loose contact of the metal cell connector is the main reason of thermal abuse [87]. The cells are connected through metal current connectors in the battery pack. However, the unavoidable vehicle vibration during its usage will lead to the connection loose, which will make the contact resistance increase [92]. As a result, intensive heat generation occurs when high current flows through the particular area, resulting in local overheat and consequent thermal runaway [87, 92].

1.2.4 Summary

Based on the former two subsections, it is necessary to point out that the main concerns regarding battery reliability and safety come from the following two aspects. Firstly, as a typical type of electrochemical power source, lithium-ion batteries undergo degradation in both energy capacity and internal resistance during their irreversible aging process. Secondly, thermal runaway, caused by the unforeseeable mechanical, electrical or thermal abuses, threats the confidence of applying lithium-ion batteries in the automotive industry.

Therefore, the reliable, efficient, and safe operation of on-board lithium-ion batteries require monitoring, control and management [93]. Monitoring refers to a continuous determination of battery states during operation [4]. Control maintains the battery states with the safety ranges. Management, generalized from energy management and health management, means a health-conscious energy distribution strategy that decides the battery power flow. Instead of being independent from each other, these three parts are closely correlated as shown in figure 1.23. Among others, battery monitoring plays a primary role, because its output triggers the operating conditions.

1.3 Battery management system

For automotive application, the aforementioned battery monitoring task is integrated in the so-called battery management system (BMS). BMS is not only composed of

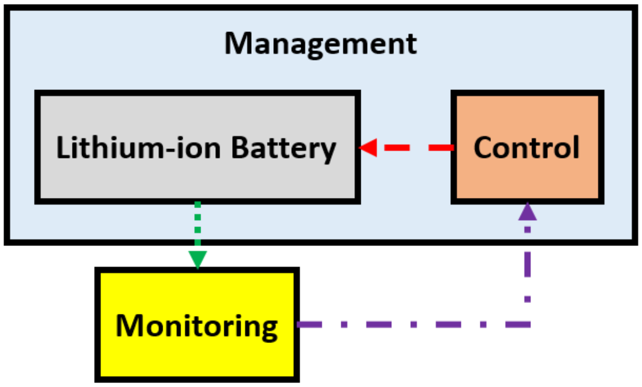

Figure 1.23: Schema of battery monitoring, control and management.

hardware, software also plays an important role. Namely for a battery pack, although there are electronic control circuits ranging from high and low voltages that are built around the battery cells, most of them are simple control units that only monitor current and voltage. Hence, they can be considered as protection units rather than BMS [94].

There is no doubt that data acquisition is the primary function of BMS, which collects the cell current, voltage and temperature at proper sampling frequency and precision [77]. While a smart BMS can not only control the operational conditions of the battery to guarantee its safety, but also it should possess the following main functions [77, 86, 94].

- **Accurate state estimation**

  From the perspective of control, one essential means for ensuring a reliable operation and prolonging the battery lifetime is to estimate the battery states continuously during the operation [95]. Here, the battery states mainly refers to the SOC and SOH. Although there are also battery states like state of power (SOP) and state of function (SOF), they can be easily retrieved from the SOC and SOH. Hence, an accurate determination of SOC and a reasonable assessment of SOH can make batteries work closer to their physical limits, and in turn guarantees their safety and lifetime with the more appropriate control input.

  However, the previously mentioned two crucial indicators cannot be measured directly during the battery operation, because only battery current, voltage and temperature are accessible for low-cost measurement [4]. Hence, indicators like SOC and SOH need to be inferred from these limited available measurements, which forms a challenging but interesting research topic. Especially for the battery SOC, because the SOC can be regarded as a replacement of the fuel gauge used in traditional vehicles. Therefore, the determination of the battery SOC is always a part of the BMS.

- **On-board diagnosis**

  Battery safety is not only guaranteed by an accurate state estimation module, on-board diagnosis is also important. As shown in section 1.2.3, the unforeseeable abuse conditions do have some potential safety issues that threat the reliable battery operation. Furthermore, from the chain reaction-like relationship among mechanical/electrical/thermal abuses in Fig. 1.21, how to diagnosis the electrical and thermal abuses is more meaningful. Because the mechanical abuse conditions are uncontrollable. On the contrary, an efficient on-board diagnosis for the electrical and thermal abuses can prevent further deterioration.

  Hence, BMS should detect the operating conditions that are harmful to both the battery and the users. Namely, overcharge, overdischarge, internal short circuit, external short circuit and abnormal abuse conditions are hazardous conditions that should be avoided as much as possible. Once the battery works under these conditions, the BMS should quickly make an on-line diagnosis. Especially for the four common electrical abuse conditions, on-board diagnosis is of great significance. Because this can interrupt their development and prevent from thermal runaway in time.

- **Cell balancing**

  The battery pack is made up of series and parallel combinations of individual cells. Hence, the imbalance of cells in battery systems is very usual. The sources of cell imbalance fall into two major categories, namely manufacturing variability and inhomogeneous working environment [24]. Manufacturing variability includes physical volume, internal impedance and capacity variance, and the consequent difference in self-discharge rate. While the inhomogeneous working environment is mainly caused by the uneven temperature distribution of the battery pack, namely the so-called thermal imbalance [77]. These small variations are inevitable and will further deteriorate with time due to non-uniform ageing of cells. In other words, this situation will deteriorate because of the tight coupling between cell imbalance and non-uniform aging, where a vicious cycle is formed: cell imbalance causes cell non-uniform ageing which in turn causes even more imbalance and so on. Hence, the weakest cell tends to have large voltage swings when charging and discharging. Namely, the cell with reduced capacity and high internal impedance has the potential to be over-discharged and over-charged. Furthermore, the performance of the battery pack may be severely affected due to the weakest cell, regardless of the SOH of other cells.

  Evidently, in order to prevent the potential electrical abuse conditions, the BMS should have effective equalization methods to make the SOC between cells as consistent as possible. Moreover, except for the electrical balancing, thermal balancing can also be considered as the task of cell balancing.

- **Thermal management**

As presented previously, improper temperature will induce the battery unexpected performance degradation and may even lead to the thermal runaway. Research works imply that either low ($< 15°\text{C}$) or high temperature ($> 50°\text{C}$) will progressively reduce the cycle life, and the threat of thermal runaway at a temperature higher than 70°C leads to cell thermal hazards [96]. The function of thermal management is therefore required in the BMS, which will maintain the batteries in the optimum operating temperature range.

Cooling and preheating are two primary aims of the thermal management. Battery cooling is used because of two major thermal problems. Firstly, the cell temperature can exceed the permissible levels during charge or discharge [97]. Secondly, uneven temperature distribution within the battery pack will lead to a localized deterioration [96]. As for the battery preheating, it is mainly used for the sub-zero climates. Hence, according to the temperature distribution within the battery pack and the requirements of charge or discharge, BMS decides whether to start preheating or cooling as well as heating power and cooling power [77].

- **Charge control**

  According to the applied batteries and the power level of the charger, BMS has the ability to control the charger to charge the batteries [77]. Furthermore, the used battery charging strategies largely affect the battery degradation. Normally, traditional but popular charging approaches integrated in the BMS are model-free. Namely, the charging profiles are determined by some predefined current and voltage limits irrespective of battery's actual internal states and chemical characteristics [98]. For example, constant current charging strategy, constant-voltage charging strategy, and constant current constant voltage charging strategy. Besides, these strategies are usually too conservative. Because the lifetime is a competing factor to the charging time [99].

  Hence, with the accurate estimation of battery SOC, SOH and temperature, optimal fast battery charging control is also one of the necessary features of BMS [94]. The battery can be charged from initial state to final SOC target value as fast as possible. Meanwhile, the optimal charging approaches can also protect batteries from overheating, prolong its durability and improve the capacity utilization [99].

In summary, the BMS is to lithium-ion batteries what medical care center is to human beings [69]. Online, real-time and reliable are the basic requirements for BMS [86].

1.4 Fault detection and diagnosis

The battery monitoring task is essentially supervisory control process, where fault detection and diagnosis (FDD) is the most important sub-component. Because EMS or the relevant control decisions cannot be designed without this module.

Generally, any unexpected behavior of a controlled process is termed as "fault" [100]. It can happen in actuator, sensor and process (component) itself. Furthermore, faults can also be classified according to their time-varying behavior. Namely, as shown in Fig. 1.24, a fault can be abrupt, intermittent or gradual [101].

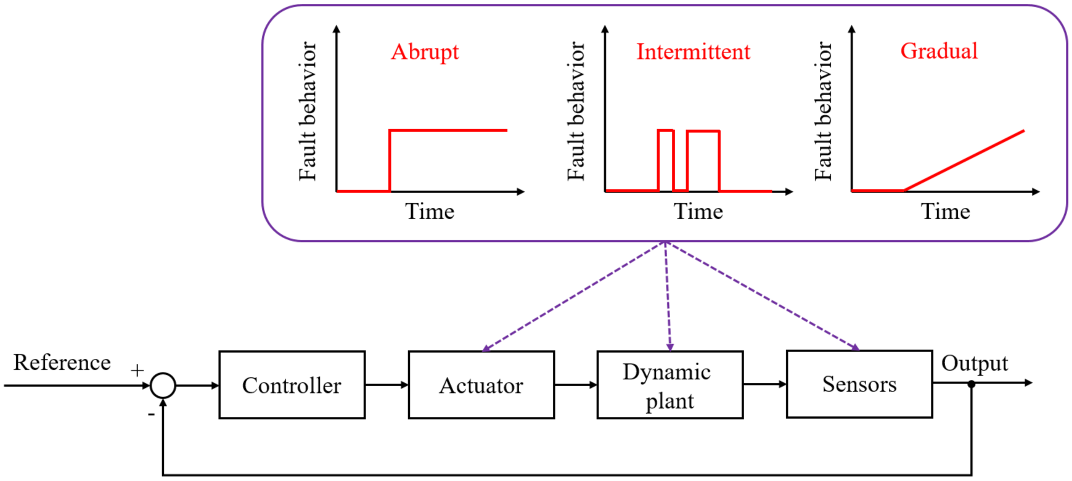

Figure 1.24: Classification of different faults.

Furthermore, if we suppose that the system performance can be simply projected into a 2D space as shown in Fig. 1.25, the difference between the terms fault and failure can be clearly illustrated. Namely, a fault causes a small process plant deviation, while a failure will induce undesired consequences such as functionality loss [100].

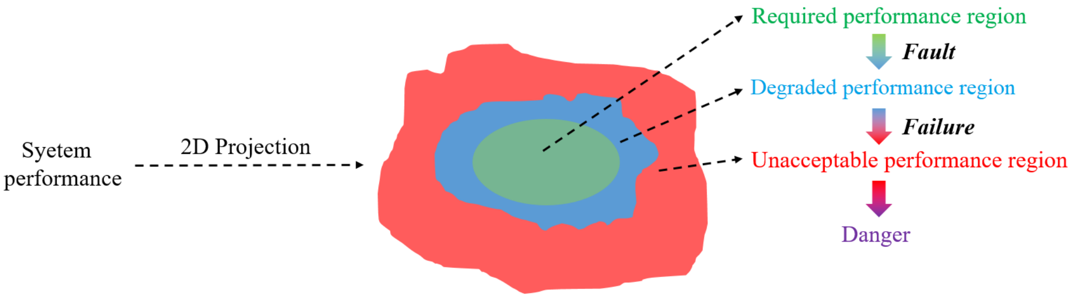

Figure 1.25: Illustration of the difference between fault and failure.

Faults in actuators, sensors and dynamic system itself are inevitable because of aging process, abuse operating conditions and many other causes. As illustrated in Fig. 1.25, faults can at least induce the malfunction of the dynamic system, and at worst threat the safety [100]. Hence, FDD is an important topic in process engineering [102], which will prevent further deterioration. It can even avoid the failing of the overall process by applying reconfiguration control mechanism, which forms the research direction of fault tolerant control [101]. Besides, it is also an important tool for system monitoring.

Comparing the consistency between the system's actual behavior and its nominal one is the main working principle of FDD [102]. In other words, FDD is executed by generating and analyzing the residual between the system's actual behavior and its nominal one. Hence, a redundancy of the system's nominal behavior is naturally required in order to check the consistency. Currently, the redundancy can be created through two ways, namely hardware redundancy or analytical redundancy [101]. The hardware redundancy directly uses a replication of hardware in order to compare the outputs of identical components. Although it is extremely reliable, this approach is expensive and cumbersome. Hence, its application is restricted to safety-critical process such as nuclear reactors and aeroplanes. On the contrary, analytical redundancy is more popular considering the cost, volumetric and gravimetric limitations. It has been a major area of research since three decades or more [100].

Additionally, as its name suggests, there are two main steps in a FDD process. Namely, the fault detection step alerts the existence of a fault, while fault diagnosis provides information about the fault such as location and amplitude. Furthermore, fault diagnosis is sometimes denoted as fault isolation and identification [103]. However, except for the actuator, sensor and process faults, there are also some unknown inputs in the control scheme such as measurement noises, unknown disturbances and model incertitude. These unknown factors can cause the deviation from the nominal behavior, and may further induce the inappropriate functioning of the FDD block which manifests itself by: "false alarms" and "missed faults" [103]. Hence, the challenge for any FDD module is to achieve high sensitivity with respect to incipient faults while being robust against the unknown inputs [100].

In general, FDD techniques can be classified into two categories, namely model-based methods and data-based methods [103]. Model-based methods, including quantitative (mathematical) and qualitative (knowledge based) model-based methods, use the concept of residual generation to perform FDD [101]. While data-based methods rely on feature extraction, where the features carry symptoms characterising the faults [100]. Comprehensive surveys of FDD methods are given in [102, 104–106]. Here, only the classification of the current main available FDD approaches is shown in Fig. 1.26. The main contributions of the present thesis for the battery monitoring work focus on the blue branch of the graphic.

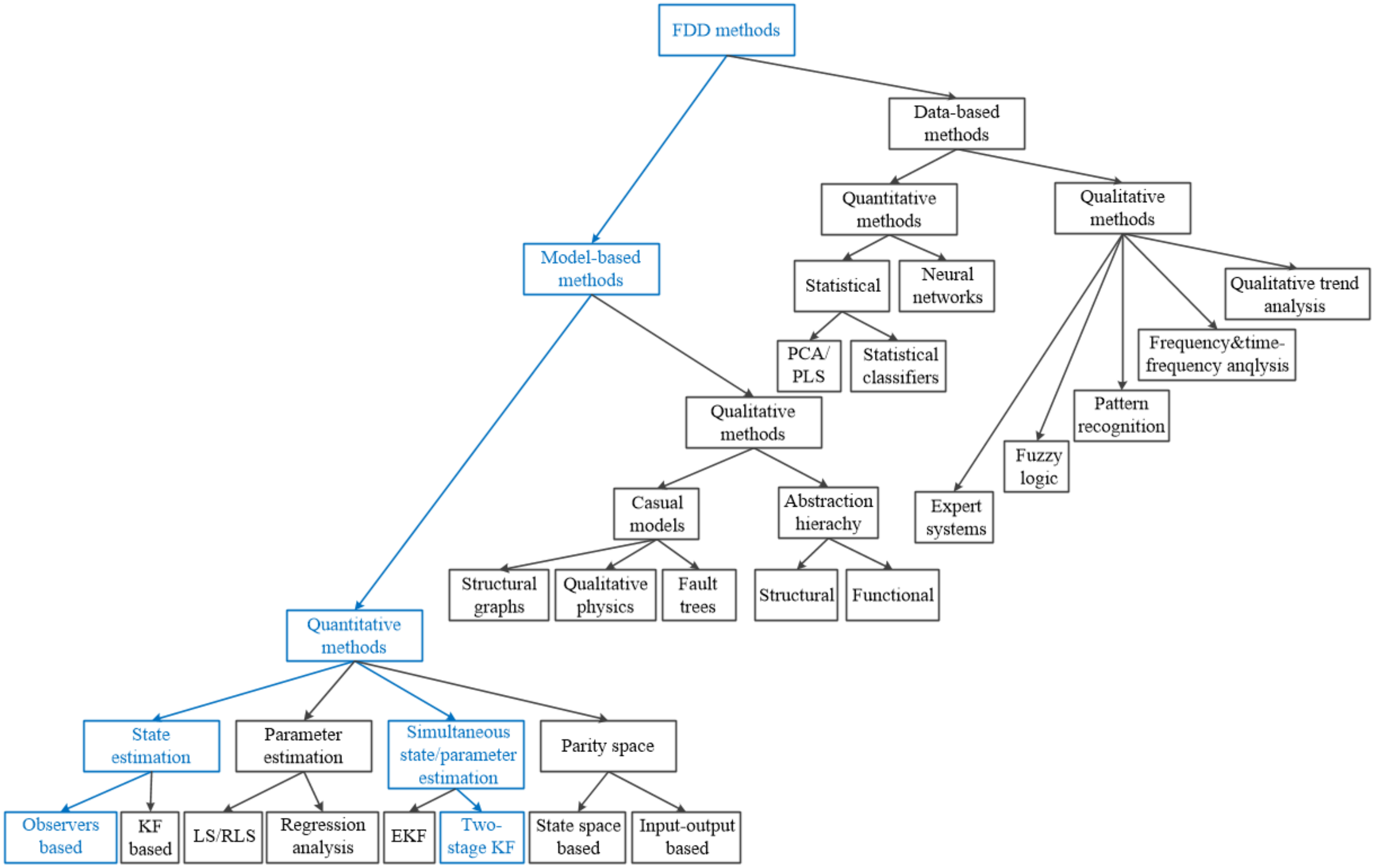

KF: Kalman filter, LS/RLS: Least squares/Recursive least squares, EKF: extended Kalman filter, PCA: Principal component analysis, PLS: Partial least squares

Figure 1.26: Classification of FDD methods.

1.5 Problem statement

The problem will be presented with extensive simulation examples in this section.

1.5.1 Example of FC/battery traction system

The considered example of FC/battery traction system is taken from the "IEEE VTS Motor Vehicles Challenge 2017 – Energy Management of a Fuel Cell/Battery Vehicle"[1], where a two driven-wheels HEV with maximum speed up to 85 km/h is studied.

The information about the studied HEV is given briefly as follows. As shown in Fig. 1.27, the traction subsystem is composed by a three-phase bidirectional converter connected to a 15 kW induction machine which is coupled to the driving wheels [26]. As for the energy storage subsystem, a 80 V- 40 Ah LFP battery pack is directly connected to the DC bus. While a 16 kW, 40-60 V, PEMFC is connected trough unidirectional DC-DC boost converter. Furthermore, the FC current and the vehicle speed are controlled by two PI controllers respectively [14]. The deterministic model of each subsystem of the vehicle is explained in detail in [14], so it will not be repeated here. The main advantage of this topology is the limited number of power converters, and then the weight, size and even the cost of the vehicle is reduced [14, 26].

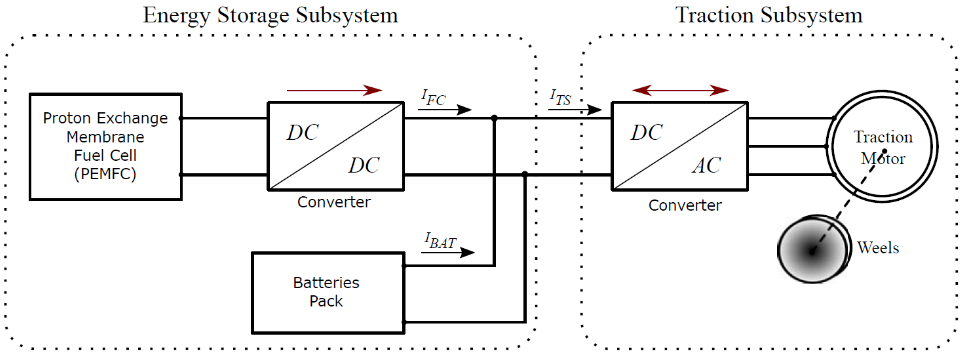

Figure 1.27: Considered example of FC/battery traction system [26].

Before discussing the simulation results,two key assumptions related to the battery pack should be pointed out as follows.

- The cell difference is not considered. Namely, the battery pack can be regarded as a huge battery cell with the corresponding electrical characteristics. Hence, difference in cell parameters, temperature distribution, cell aging process are not considered.

---

[1] http://www.uqtr.ca/VTSMotorVehiclesChallenge17

- The temperature is assumed to be constant and optimal for the battery working condition.

In fact, the aforementioned two points become true if the cell balancing and thermal management functions of BMS are supposed to be effective.

Furthermore, the following simulation is discussed with 10 cycles of class 2 worldwide harmonized light vehicles test procedures (WLTC2), which has been used since 2015 to harmonize the worldwide driving behavior [14]. One cycle's speed profile of WLTC2 is shown in Fig. 1.28 as an example.

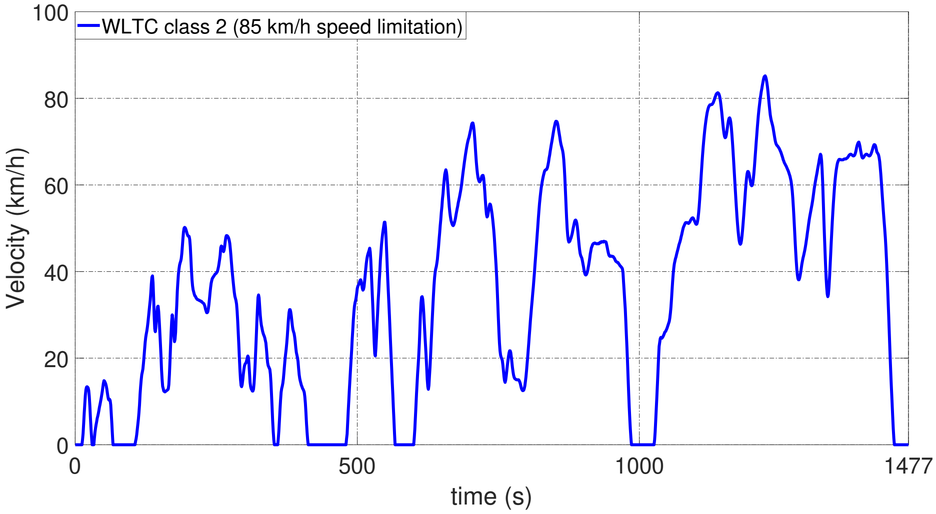

Figure 1.28: One cycle's speed profile of WLTC2.

In addition, a simple EMS (thermostat (on/off)) strategy is applied for the presented FC/battery hybrid system. Namely, the sum of output of FC and battery will meet the vehicle's power demand, while at the same time, the battery SOC is maintained by the FC within 40% $\sim$ 70% range.

1.5.1.1 Healthy case

Healthy case refers to the situation in which battery capacity equals its nominal value, 40 Ah, during the 10 test cycles. Hence, simulation results are discussed as follows.

The simulated vehicle velocity and the reference one are shown in Fig. 1.29, where the lower sub-figure indicates their difference. Undoubtedly, the FC/battery hybrid energy source can meet the vehicle dynamic performance.

The power demand and supply are shown in Fig. 1.30. The sum of the power output of battery and FC is used to meet the load demand. The dynamic behavior is mainly guaranteed by the battery, while the FC is applied to extend the driving range as well as charge the battery when needed.

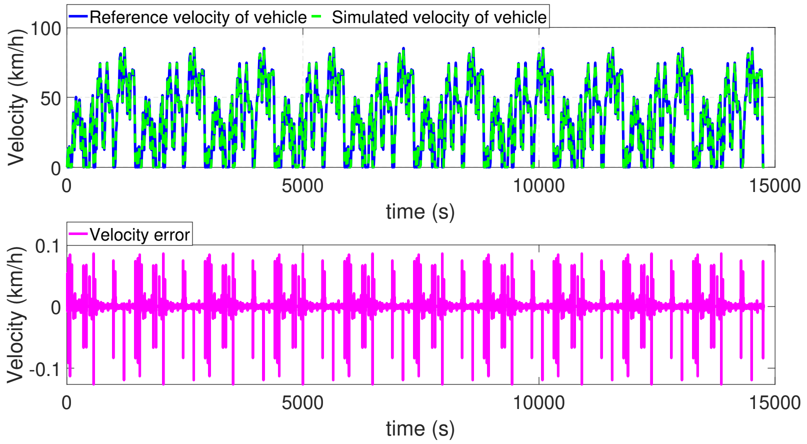

Figure 1.29: Vehicle velocity in the healthy case.

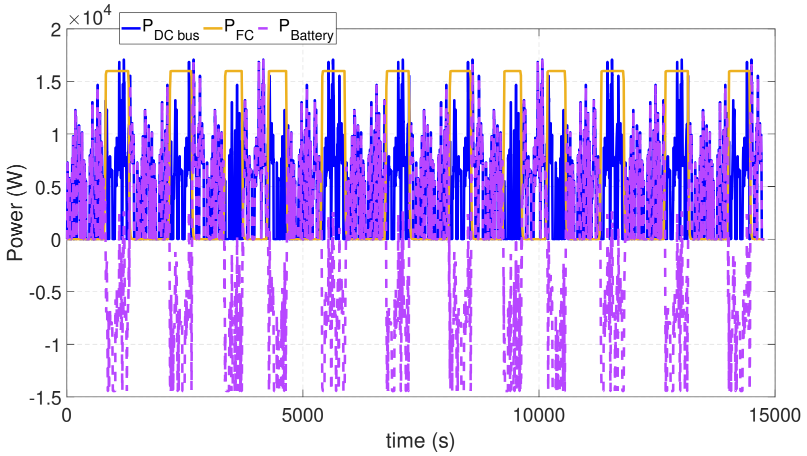

Figure 1.30: Power demand and supply in the healthy case.

The voltage of the FC/battery and the corresponding SOC in the healthy case are shown in Fig. 1.31 and Fig. 1.32 respectively. The initial value of battery SOC is 70%. As it can be seen from Fig. 1.32, the FC can effectively maintain the battery SOC within the required range thanks to the thermostat (on/off) strategy. In addition, analogous to the battery SOC, the SOC of the on-board hydrogen tank is also expressed [14].

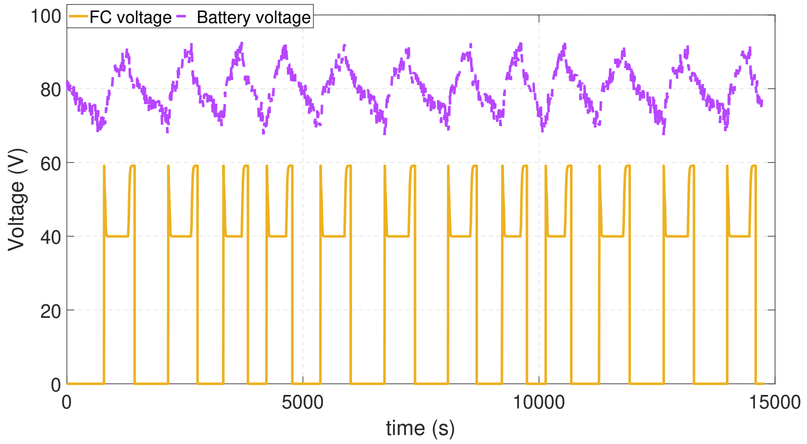

Figure 1.31: Voltage of FC/battery in the healthy case.

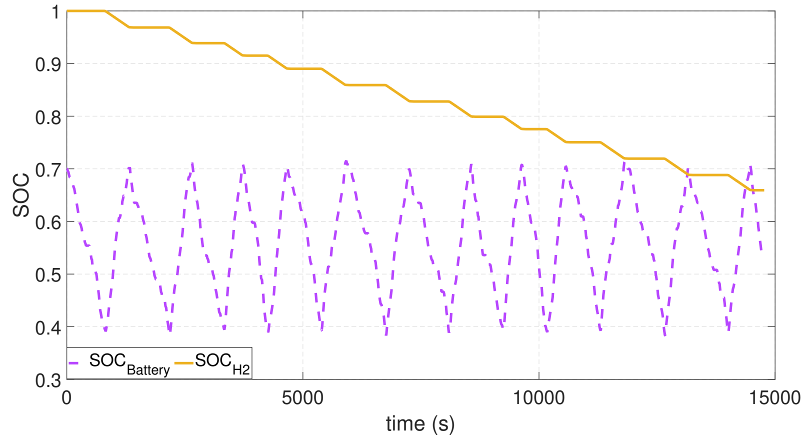

Figure 1.32: SOC of FC/battery in the healthy case..

1.5.1.2 Aging case

Aging refers to the case when battery capacity decreases to 70% of its nominal value in the middle of the simulation test. Note that in the reality, the battery capacity cannot decrease suddenly, it is a gradual fading process. However, in order to show the aging effect, a sudden change of the battery capacity is introduced from the 5th test cycle. The same simulation procedure can be found in [75]. Hence, simulation results are discussed as follows.

As shown in Fig. 1.33, the simulated vehicle velocity can still track the reference value. The decrease of the battery capacity does not emerge at the system level, namely the power demand of the battery does not change before and after the capacity fading as shown in Fig. 1.34. The sum of the FC and battery power output can still meet the load demand, however, the battery capacity decrease does exist.

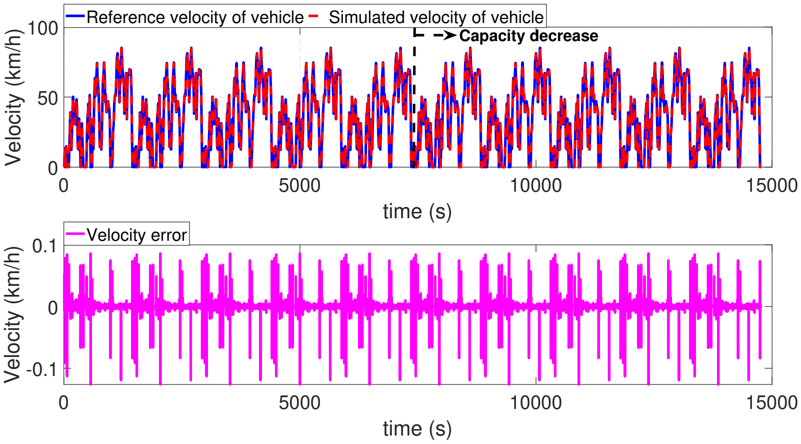

Figure 1.33: Vehicle velocity in the aging case.

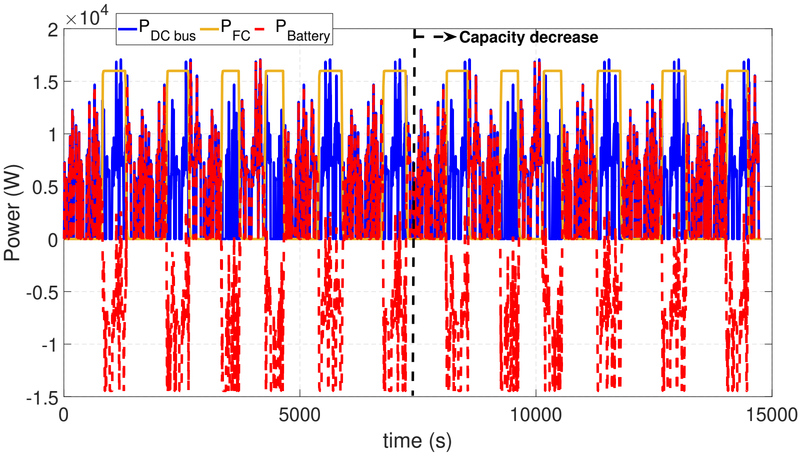

Figure 1.34: Power demand and supply in the aging case.

However, the battery capacity decrease reflects on its voltage, where a more fluctuating voltage profile can be observed in Fig. 1.35. The battery SOC, as shown in Fig. 1.36, is still maintained within the predefined range regardless the aging occurrence.

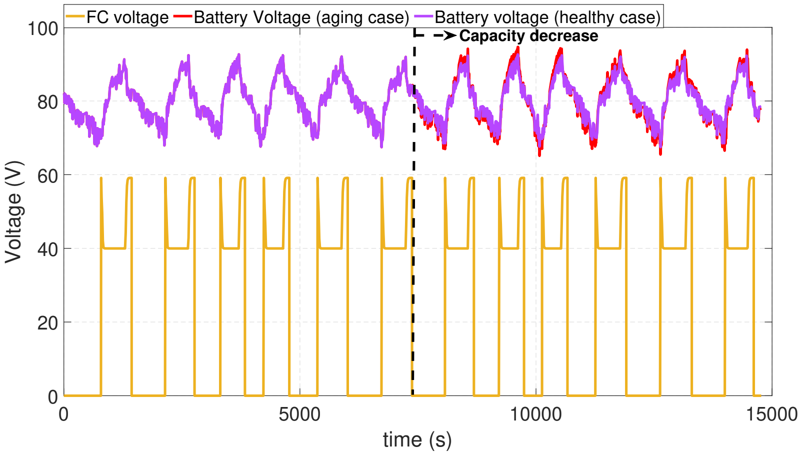

Figure 1.35: Voltage of FC/battery in the aging case.

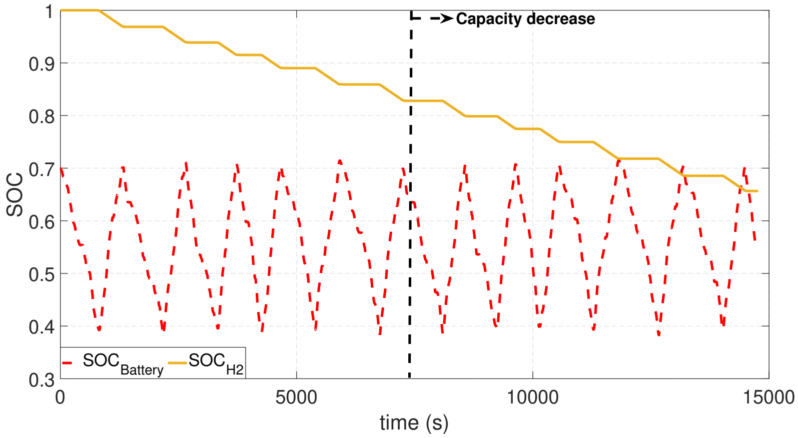

Figure 1.36: SOC of FC/battery in the aging case.

1.5.1.3 Soft short circuit case

Hard SC ($m\Omega$ magnitude of short resistance) will directly induce serious thermal hazard. Therefore, its detection results will be meaningless due to no time to take corresponding reaction. On the contrary, soft SC (short resistances of 100/10/1 Ω) needs time to evolve into thermal accidents [8]. Evidently, SC detection for the soft SC is more meaningful. Hence, the simulation test with 5 Ω's SC resistance is shown as an example as following.

The 5 Ω's external SC resistance is introduced to the battery pack from the 5th test cycle. As it can be seen from Fig. 1.37 and Fig. 1.38, the FC/battery hybrid energy source can still meet the power demand. However, due to soft SC, the FC is engaged earlier than in the healthy case.

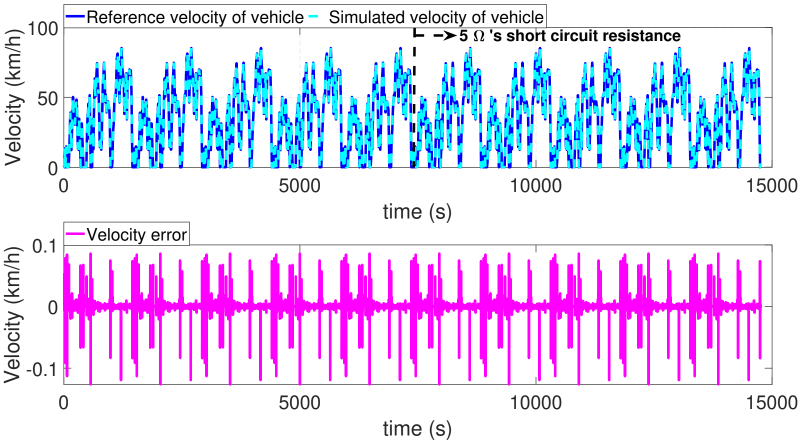

Figure 1.37: Vehicle velocity in the soft short circuit case.

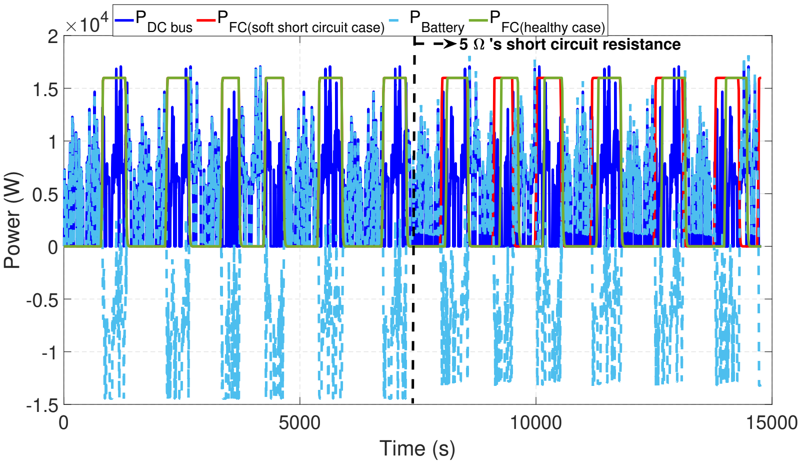

Figure 1.38: Power demand and supply in the soft short circuit case.

Fig. 1.39 and Fig. 1.40 show the voltage and SOC of FC/battery in the soft short circuit case. The battery voltage decreases more quickly than in the healthy case, while the FC tries to keep the battery SOC in the predefined range.

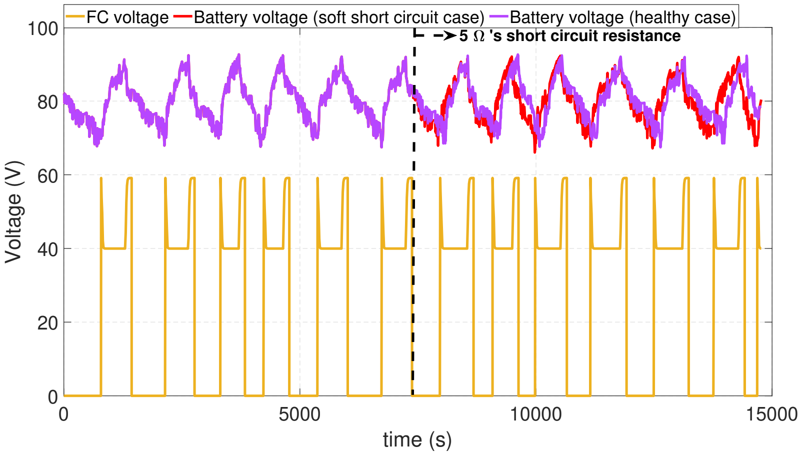

Figure 1.39: Voltage of FC/battery in the soft short circuit case.

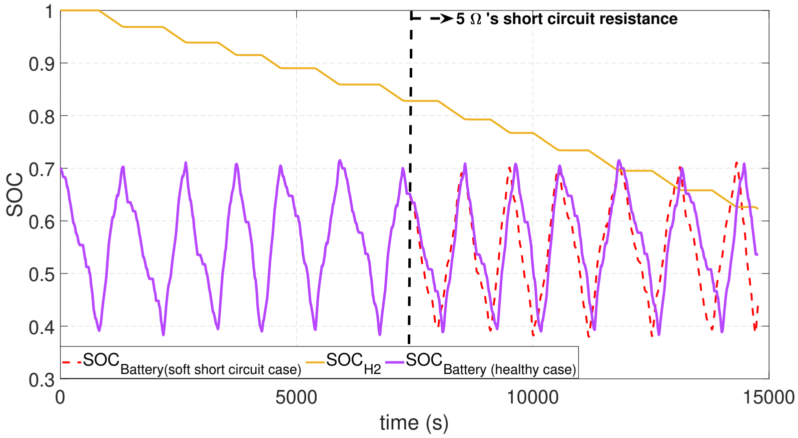

Figure 1.40: SOC of FC/battery in the soft short circuit case.

1.6 Conclusion

Especially for embedded application, although lithium-ion battery has been regarded as an efficient and eco-friendly ESS for power generation, low reliability and short lifetime are still the main concerns. Therefore, various intelligent energy management strategies that consider the battery health status have been proposed in recent years. However, most of these research works lack a detailed discussion focused on battery fault detection and diagnosis. In other words, easy-to-get assumptions about battery health status cannot replace the in-depth discussions about battery fault detection and diagnosis.

In this work, we focus on the fault related to battery cell. Specifically, battery aging and battery short circuit are considered as the faults. Because as introduced previously, the battery aging will induce the capacity decrease and power fading, and battery short circuit is an important stage before thermal runaway. Hence, battery aging diagnosis and short circuit detection are meaningful for preventing the serious failures, which can in turn make the energy management strategy engage the right mitigation strategies in the degraded mode.

CHAPTER 2

Battery state and parameter estimation

2.1 Introduction

Lithium-Ion batteries (LIBs), which can be deployed as the principal energy source in BEVs/ PHEVs or the auxiliary energy module in HEVs, have been massively used for on-board ESSs because of their relatively high power and energy density, eco-friendly characteristic and promising potential for cost reduction [4]. Various research works around LIBs have been carried out on a large scale; while from the perspective of control, LIB online monitoring, especially battery state and parameter estimation, is fundamental and necessary for the follow-up works such as battery fault diagnosis, battery health prognosis and energy management.

The battery state mainly refers to SOC. As a replacement for the fuel gauge used in traditional vehicles, battery SOC is a key indicator that should be determined during the operation. Because it will be used to design the battery EMS, and can further avoid the emergence of overcharge and overdischarge problems in LIBs. As for the other battery states such as SOH, SOP, SOF and even RUL, their determination can be eventually regarded as battery parameter estimation [107–111]. Because all of them are related to the battery parameters like actual capacity and internal resistance. However, these mentioned indicators cannot be measured directly, which form an interesting and independent research topic.

2.1.1 Battery SOC estimation

The traditional Ampere-Hour (AH) counting method, also named as Coulomb counting method as shown in eq. (1.1), is a classical real-time SOC estimation technique, where the required SOC can be determined by integrating the flowing current with the known battery capacity and an accurate initial SOC value. However, the open-loop mechanism will cause the AH counting method to have accumulated estimation errors over a long period of time. Indeed, this method is inevitably affected by the current noise, the uncertain initial SOC value as well as the rated actual battery capacity, which will change with various factors such as temperature, aging degree [72]. Therefore, in order to overcome this drawback, the AH counting method is usually combined with an OCV-based SOC estimation method, whose working principle is a voltage-look-up process based on the one-to-one relationship between battery OCV and SOC. The measured battery OCV can infer the corresponding SOC, which can be used as a periodic calibration for the AH counting method. Hence, the combination of these two methods constitutes an efficient approach for determining the battery SOC in EV [78].

However, the previously mentioned two conventional methods, namely AH counting method and OCV-based SOC estimation method, cannot satisfy the requirement of SOC real-time estimation due to the accumulative estimation errors and the long waiting time for battery OCV measurement. Hence, with the help of modern control theory, model-based SOC estimation using observers and various adaptive filter algorithms, has emerged and the real-time battery SOC determination through OCV-SOC look-up table becomes possible [72]. In addition, compared with the electrochemical models which usually have complicated mathematical expressions and numerous physical parameters, equivalent circuit models (ECMs) are more attractive because of their accuracy despite their simplicity [107, 112]. The common ECM composed of an OCV source connected in series with a resistor and one or more RC network(s) is widely used to reproduce the battery's electrical behavior, and to further accomplish the objective of SOC estimation. The SOC usually appears as a state variable derived by the common Coulomb counting method. Representative research works about the ECM-based battery SOC estimation are listed in table 2.1.

Furthermore, the artificial intelligence technology has become a hot topic in recent years and has been applied successfully in many fields, and there is no exception in the field of battery monitoring. Especially because of the improvement of embedded hardware performance, researchers attempt to promote the development of SOC estimation with the help of data-driven techniques such as artificial neural network, Support Vector Machine (SVM) and even Deep Learning [124]. The black box mechanism of these data-driven approaches can provide convenience for modeling, namely coping with the complex non-linear relationship between battery internal states and numerous stress factors such as time and temperature. Hence, the monitoring result could be very accurate depending on the training data [72]. For instance, in [125], a novel approach using deep feedforward neural networks is used for battery SOC estimation, where the intrinsic behavior of the battery at different ambient temperatures can be considered. In [126], an optimized SVM for regression is used to estimate SOC for EVs under diversified driving condition, where the proposed method can be scalable to integrate knowledge from indicators such as temperature, power, etc. In [127], neuro-fuzzy inference system, a combination of neural networks learning method and fuzzy inference system, is used to develop the SOC estimation model using six inputs including current, temperature, actual power loss, available and requested power, cooling air temperature and battery thermal factor. Besides, various optimization algorithms, such as genetic algorithm and particle swarm optimization algorithm, are applied in the data-driven methods in order to improve the accuracy and robustness

Table 2.1: Resume of ECM-based battery SOC estimation

Algorithm	Reference	Comment
Luenberger observer	[113]	Low computational complexity because of the off-line gain calculation.
Proportational-integral observer	[114]	An integral loop is introduced to the traditional Luenberger observer in order to cope with the model uncertainties.
Sliding mode observer	[115] [116]	Modeling errors and uncertainties caused by the simple model are compensated by sliding mode approach.
H∞ observer	[117]	SOC estimation accuracy is guaranteed by the robust H∞ control theory.
Kalman filter	[118]	Optimal SOC estimation technique for the linearized model if the statistical characteristics of the process and measurement noises are Gaussian and known.
Extended Kalman filter	[119]	Nonlinear version of the Kalman filter based on local linearization and Jacobian matrix. It is mainly used to cope with the nonlinearity of the OCV-SOC curve.
Unscented Kalman filter	[120]	Numerical approximation based on sigma points, which improves the nonlinear SOC estimation through a deterministic sampling technique known as the unscented transformation.
Improved Kalman filter	[121] [122]	Variant of estimation algorithms in the Kalman filter family. The main purpose is to cope with the mismatch between the statistical information of the process and measurement noises.
Particle filter	[123]	Numerical approximation based on a set of particles, which belongs to Monte Carlo algorithm under the Bayesian statistical inference framework.

of SOC estimation [124]. However, a critical concern about the data-driven techniques is that when the data availability is not satisfied, or the data is biased, the results can be imprecise or even entirely incorrect. In other words, data-driven methods are more sensitive to unexpected conditions and outliers [84].

2.1.2 Battery parameter estimation

Regarding the actual battery capacity and internal resistance estimation, especially the on-board determination, the existing methods are limited. The basic principle of almost all methods for on-board capacity estimation is based on the relationship between the ampere-hours charged or discharged from the battery and the voltage difference before and after the respective charging or discharging [4]. Namely, the battery voltage varies when it is being charged or discharged. In addition, the discharging or charging of a certain amount of ampere-hours creates a higher voltage change for a battery with a lower capacity than that for a battery of the same type but with a higher capacity [74]. The differences among the approaches consist in how the voltage change is measured and correlated with the charged or discharged ampere-hours.

For example, in [128], the voltage change is measured from the battery OCV before and after charging or discharging. Hence, the battery capacity is calculated based on the given OCV-SOC relationship. The advantage is that only the OCV-SOC relationship is used as a parameter, whose variation is small over the battery lifetime [4]. The disadvantage is that the OCV has to be measured at two very different SOC levels for accurate capacity estimation, where the long waiting time for OCV measurement is an obstacle. Therefore, in [129], the OCV is estimated based on the measured battery voltage under load in order to shorten the waiting time. Hence, the capacity can be estimated as long as the battery is sufficiently discharged or charged. However, an accurate battery model with parameters adaptable to the aging state of battery is required. Moreover, the online OCV estimation is further improved through the on-line parameter update framework, where extended model or auto regressive model is employed. Hence, adaptive estimation algorithms are used to simultaneously estimate the battery SOC (directly or indirectly through the estimation of the OCV) and model parameters [28, 130].

As for the battery resistance estimation, it can be traditionally estimated with the help of impedance spectroscopy in the frequency domain at various frequencies. In addition to academic publications, there are numbers of patents and patent applications that claim basic ideas for determination of the battery resistance by considering the change in the terminal current and voltage of the battery under load. However, the majority of on-board resistance estimation methods is based on updating the model parameters for the used electrical or electrochemical models [4].

2.1.3 Kalman filtering

As mentioned previously, estimation algorithm is essential in the topic of battery monitoring. Because the battery SOC and parameters cannot be directly measured, an appropriate state reconstruction technique is therefore necessary. Kalman filtering is an elegant and usual method for dynamic state estimation [131]. Except for the battery management domain, it has been applied in many fields such as target tracking, dynamic systems control, fault diagnosis, navigation and communication [44,131,132]. Hence, Kalman filtering, as the main tool used in this chapter will be introduced at first.

2.1.3.1 Linear Kalman Filter

Linear Kalman Filter (KF) has been recognized as an optimal state estimation technique for tracking the state of an uncertain dynamic system with Gaussian independent white noises [78].

Considering a general discrete linear time invariant state space model as:

$$\begin{cases} \boldsymbol{x}_{k+1} = \boldsymbol{A}\boldsymbol{x}_k + \boldsymbol{B}\boldsymbol{u}_k + \boldsymbol{\omega}_k \\ \boldsymbol{y}_k = \boldsymbol{C}\boldsymbol{x}_k + \boldsymbol{D}\boldsymbol{u}_k + \boldsymbol{\upsilon}_k \end{cases} \tag{2.1}$$

where: $\boldsymbol{x} \in \mathbb{R}^n$ is the dynamic system's state vector; $\boldsymbol{y} \in \mathbb{R}^m$ is the output of the system; $\boldsymbol{u} \in \mathbb{R}^p$ is the system's known input; the matrices $\boldsymbol{A} \in \mathbb{R}^{n\times n}$, $\boldsymbol{B} \in \mathbb{R}^{n\times p}$, $\boldsymbol{C} \in \mathbb{R}^{m\times n}$ and $\boldsymbol{D} \in \mathbb{R}^{m\times p}$ describe the dynamics of the system; k is the time index for the discrete time system; $\boldsymbol{\omega} \in \mathbb{R}^n$ and $\boldsymbol{\upsilon} \in \mathbb{R}^m$ are the stochastic process and measurement noises respectively. Furthermore, both $\boldsymbol{\omega}$ and $\boldsymbol{\upsilon}$ are assumed to be mutually uncorrelated white Gaussian random processes, which have zero mean and covariance matrices with known values $\boldsymbol{Q} \in \mathbb{R}^{n\times n}$ and $\boldsymbol{R} \in \mathbb{R}^{n\times n}$ respectively [131].

Hence, the linear KF algorithm is summarized as follows:

$$\begin{aligned} \text{1. Prediction:} \quad & \hat{\boldsymbol{x}}_k^- = \boldsymbol{A}\hat{\boldsymbol{x}}_{k-1} + \boldsymbol{B}u_{k-1} \\ & \boldsymbol{P}_k^- = \boldsymbol{A}\boldsymbol{P}_{k-1}\boldsymbol{A}' + \boldsymbol{Q} \\ \text{2. Gain computation:} \quad & \boldsymbol{K}_k = \boldsymbol{P}_k^-\boldsymbol{C}'[\boldsymbol{C}\boldsymbol{P}_k^-\boldsymbol{C}' + \boldsymbol{R}]^{-1} \\ \text{3.Update:} \quad & \hat{\boldsymbol{x}}_k = \hat{\boldsymbol{x}}_k^- + \boldsymbol{K}_k[\boldsymbol{y}_k - (\boldsymbol{C}\hat{\boldsymbol{x}}_k^- + \boldsymbol{D}u_k)] \\ & \boldsymbol{P}_k = (\boldsymbol{I} - \boldsymbol{K}_k\boldsymbol{C})\boldsymbol{P}_k^- \end{aligned}$$

where, $\hat{\boldsymbol{x}}_k^-$ and $\boldsymbol{P}_k^-$ are respectively the priori state and error covariance estimates; $\boldsymbol{K}_k$ is the feedback gain for the KF, which is recursively calculated at each time step forcing the estimator to converge faster; $\hat{\boldsymbol{x}}_k$ is the estimated state value; $\boldsymbol{P}_k$ is the estimation error covariance matrix [78, 131].

In fact, although there exist different explanations for the Kalman filtering process such as Bayesian inference and geometric interpretation, the essence of Kalman filtering process can be illustrated intuitively by the "prediction-correction" principle as shown in Fig. 2.1 [44, 78]. In Fig. 2.1, the estimation process of a state variable is given as an example, where the core is the sustained error correction mechanism that is composed by a correction gain $\boldsymbol{K}$ multiplied by the error between measurement and prediction, namely, $\boldsymbol{y}$ and $\hat{\boldsymbol{y}}$. Then, broadly speaking, estimation algorithms differ in how to calculate the gain $\boldsymbol{K}$ in order to guarantee the convergence of the estimated state $\hat{\boldsymbol{x}}$ knowing only the system input $\boldsymbol{u}$ and output $\boldsymbol{y}$.

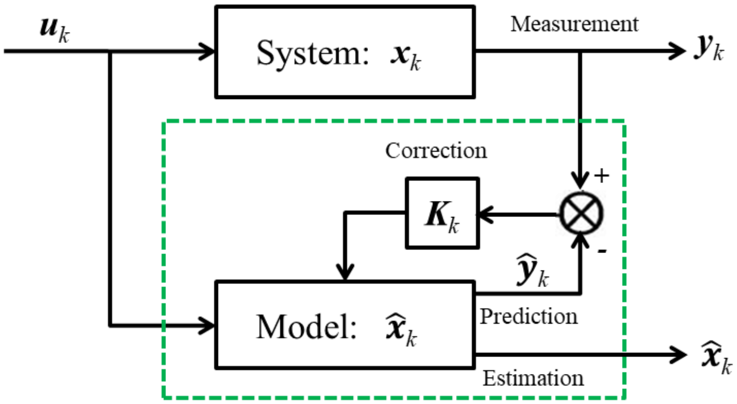

Figure 2.1: Schematic diagram of the “Prediction-correction” principle.

2.1.3.2 Extended Kalman Filter

As mentioned previously, the KF is the optimum state estimator for a linear system with Gaussian additive white noises on the state and measurement equations [131]. However, the nonliearity problem is inevitable in reality, hence various nonlinear KFs have been proposed. Extended Kalman Filter (EKF) is one of the most used nonlinear KF version. Although EKF is not necessarily optimal, it often works very well and has been used in many fields [131].

Considering a general nonlinear discrete system as:

$$\begin{cases} \boldsymbol{x}_{k+1} = f(\boldsymbol{x}_k, \boldsymbol{u}_k) + \boldsymbol{\omega}_k \\ \boldsymbol{y}_k = g(\boldsymbol{x}_k, \boldsymbol{u}_k) + \boldsymbol{v}_k \end{cases} \tag{2.2}$$

where: $\boldsymbol{x}$, $\boldsymbol{y}$, $\boldsymbol{u}$, $\boldsymbol{\omega}$ $\boldsymbol{v}$ and k have the same definitions as before. While $f(\cdot)$ and $g(\cdot)$ are the nonlinear functions that describe the system's dynamic behavior.

Hence, the algorithm of EKF is summarized as follows:

$$\begin{aligned}
\text{1. Prediction:}\quad \hat{\boldsymbol{x}}_k^- &= f(\hat{\boldsymbol{x}}_{k-1}, \boldsymbol{u}_{k-1}) \\
\boldsymbol{P}_k^- &= \boldsymbol{A}_{k-1}\boldsymbol{P}_{k-1}\boldsymbol{A}_{k-1}{}' + \boldsymbol{Q} \\
\text{2. Gain computation:}\quad \boldsymbol{K}_k &= \boldsymbol{P}_k^- \boldsymbol{C}_{\boldsymbol{k}}' [\boldsymbol{C}_{\boldsymbol{k}} \boldsymbol{P}_k^- \boldsymbol{C}_{\boldsymbol{k}}' + \boldsymbol{R}]^{-1} \\
\text{3.Update:}\quad \hat{\boldsymbol{x}}_k &= \hat{\boldsymbol{x}}_k^- + \boldsymbol{K}_k[\boldsymbol{y}_k - g(\hat{\boldsymbol{x}}_k^-, \boldsymbol{u}_k)] \\
\boldsymbol{P}_k &= (\boldsymbol{I} - \boldsymbol{K}_k \boldsymbol{C}_{\boldsymbol{k}})\boldsymbol{P}_k^-
\end{aligned}$$

where, $\hat{\boldsymbol{x}}_k^-$, $\boldsymbol{P}_k^-$, $\boldsymbol{K}_k$, $\hat{\boldsymbol{x}}_k$ and $\boldsymbol{P}_k$ have the same definitions as before. While $\boldsymbol{A}_k = \frac{\partial f(\boldsymbol{x}_k, \boldsymbol{u}_k)}{\partial \boldsymbol{x}_k}\Big|_{\boldsymbol{x}_k = \hat{\boldsymbol{x}}_k}$ and $\boldsymbol{C}_k = \frac{\partial g(\boldsymbol{x}_k, \boldsymbol{u}_k)}{\partial \boldsymbol{x}_k}\Big|_{\boldsymbol{x}_k = \hat{\boldsymbol{x}}_k^-}$ are the Jacobian matrices obtained after the first-order Taylor-series expansion for the nonlinear functions $f(\cdot)$ and $g(\cdot)$ respectively [131].

The EKF is probably the best known and most widely used nonlinear KF [131]. Its basic idea is to linearize the nonlinear function around the current estimation with the calculated Jacobian matrix at each time step. However, as the central and vital operation performed in the KF is the propagation of a Gaussian random variable through the system dynamics, the analytically approximation through the first-order linearization of the nonlinear system will introduce large errors in the true posterior mean and covariance [27].

2.1.3.3 Unscented Kalman filter

Unscented Kalman Filter (UKF) addresses the aforementioned problem through a deterministic sampling approach. Hence, there is no analytical linearization process for the nonlinear system. The state distribution is represented through a minimal set of carefully selected sample points, which are named as sigma points. These sample points completely capture the true mean and covariance of the Gaussian random variable, and can capture the posterior mean and covariance accurately to the 3rd order (Taylor series expansion) for any nonlinearity when propagated through the true nonlinear system [27]. A schematic diagram showing the key point of UKF, namely the unscented transformation (UT), is shown in Fig. 2.2. The superior performance of UT is clear. In Fig. 2.2, a 2-dimensional system is given as an example, where the left column illustrates the true mean and covariance propagation through Monte-Carlo sampling; the middle column shows the linearization approach as mentioned in EKF; the right column illustrates the UT where only 5 sigma points are required [27].

Hence, the algorithm of UKF is summarized as follows. Firstly, $2n+1$ sigma points and their weights w_i^c, w_i^m are respectively calculated by eq. (2.3) and eq. (2.4), where w_i^c represents the weight of the covariance and w_i^m stands for the weight of the mean.

$$(2n+1)\text{ sigma points:}\quad \begin{cases} \hat{\boldsymbol{x}}_k^0 = \hat{\boldsymbol{x}}_{k-1} \\ \hat{\boldsymbol{x}}_k^i = \hat{\boldsymbol{x}}_{k-1} + \left(\sqrt{(n+\lambda)\boldsymbol{P}_{k-1}}\right)_i, i = 1, 2, ..., n \\ \hat{\boldsymbol{x}}_k^i = \hat{\boldsymbol{x}}_{k-1} - \left(\sqrt{(n+\lambda)\boldsymbol{P}_{k-1}}\right)_{i-n}, i = n+1, ..., 2n \end{cases} \tag{2.3}$$

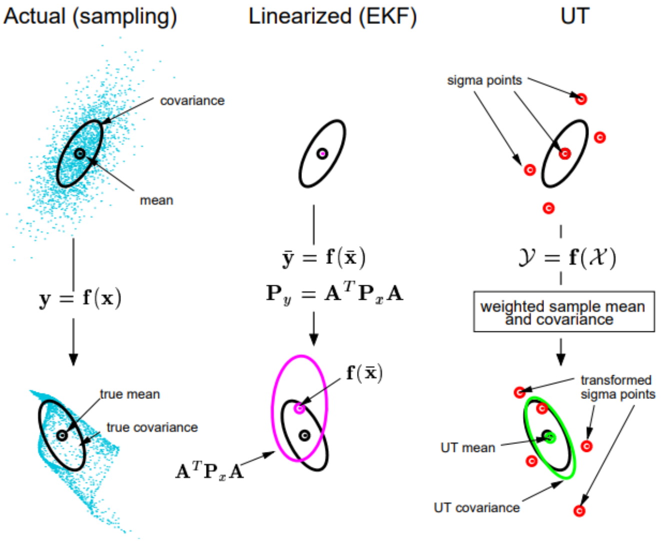

Figure 2.2: Schematic diagram of the unscented transformation for mean and covariance propagation [27]

$$\text{weights:} \quad \begin{cases} w_0^m = \frac{\lambda}{(n+\lambda)} \\ w_0^c = \frac{\lambda}{(n+\lambda)} + (1-\alpha^2+\beta) \\ w_i^m = w_i^c = \frac{1}{2(n+\lambda)}, i = 1, ..., 2n \end{cases} \tag{2.4}$$

where n is the dimension of the state vector $\boldsymbol{x}$; $\lambda = \alpha^2(n+\kappa)-n$ is a scaling parameter; α determines the spread of the sigma points around the mean and is usually set to a small positive value (e.g. 1×10^{-3}); κ is a secondary scaling parameter which is usually set to 0; β is used to incorporate prior knowledge of the distribution of random variable (for Gaussian distribution, $\beta = 2$ is optimal); $\left(\sqrt{(n+\lambda)\boldsymbol{P}_{k-1}}\right)_i$ is the ith row of the matrix square root; $\boldsymbol{P}$ has the same definition as before [27].

Then, each sigma point propagates through the nonlinear state model $f(\cdot)$, leading to the calculation of the mean and covariance of the state as in eq. (2.5):

$$\begin{cases} \hat{\boldsymbol{x}}_k^i = f(\hat{\boldsymbol{x}}_{k-1}^i, \boldsymbol{u}_{k-1}), i = 0, 1, 2, ..., 2n \\ \hat{\boldsymbol{x}}_k^- = \sum_{i=0}^{2n} (w_i^m \cdot \hat{\boldsymbol{x}}_k^i) \\ \boldsymbol{P}_k^- = \sum_{i=0}^{2n} \left[w_i^c \cdot (\hat{\boldsymbol{x}}_k^i - \hat{\boldsymbol{x}}_k^-) \cdot (\hat{\boldsymbol{x}}_k^i - \hat{\boldsymbol{x}}_k^-)' \right] + \boldsymbol{Q} \end{cases} \tag{2.5}$$

where $\hat{\boldsymbol{x}}^-$, $\boldsymbol{P}^-$ and $\boldsymbol{Q}$ have the same definition as before.

Similarly, each sigma point also propagates through the nonlinear measurement function $g(\cdot)$, then the mean, covariance of measurement and the cross covariance of the state and measurement are obtained by eq. (2.6):

$$\begin{cases} \hat{\boldsymbol{y}}_k^i = g(\hat{\boldsymbol{x}}_k^i, \boldsymbol{u}_k), i = 0, 1, 2, ..., 2n \\ \hat{\boldsymbol{y}}_k = \sum\limits_{i=0}^{2n} (w_i^m \cdot \hat{\boldsymbol{y}}_k^i) \\ \boldsymbol{P}_k^g = \sum\limits_{i=0}^{2n} \left[w_i^c \cdot (\hat{\boldsymbol{y}}_k^i - \hat{\boldsymbol{y}}_k) \cdot (\hat{\boldsymbol{y}}_k^i - \hat{\boldsymbol{y}}_k)' \right] + \boldsymbol{R} \\ \boldsymbol{P}_k^{fg} = \sum\limits_{i=0}^{2n} \left[w_i^c \cdot (\hat{\boldsymbol{x}}_k^i - \hat{\boldsymbol{x}}_k^-) \cdot (\hat{\boldsymbol{y}}_k^i - \hat{\boldsymbol{y}}_k)' \right] \end{cases} \tag{2.6}$$

where $\hat{\boldsymbol{y}}_k^i$ is the measurement respect to the sigma point at time step k; $\hat{\boldsymbol{y}}$ and $\boldsymbol{P}^g$ are the mean and covariance of $\hat{\boldsymbol{y}}^i$; $\boldsymbol{P}^{fg}$ is the cross covariance of the state $\hat{\boldsymbol{x}}^i$ and measurement $\hat{\boldsymbol{y}}^i$. $\boldsymbol{R}$ has the same definition as before.

Consequently, the Kalman gain, posterior mean and covariance are updated respectively by eq. (2.7).

$$\begin{cases} \boldsymbol{K}_k = \boldsymbol{P}_k^{fg} \left(\boldsymbol{P}_k^g \right)^{-1} \\ \hat{\boldsymbol{x}}_k = \hat{\boldsymbol{x}}_k^- + \boldsymbol{K}_k \left(\boldsymbol{y}_k - \hat{\boldsymbol{y}}_k \right) \\ \boldsymbol{P}_k = \boldsymbol{P}_k^- + \boldsymbol{K}_k \boldsymbol{P}_k^g (\boldsymbol{K}_k)' \end{cases} \tag{2.7}$$

2.1.4 Summary

So far, the most effective approach for battery monitoring is to apply advanced estimation algorithms based on ECMs [133]. Furthermore, a usual method for estimating slowly varying unmeasurable parameters is to include them in the state vector with zero time derivative condition. We can obtain the so-called battery extended ECM. Then, joint or dual estimation methods, mainly based on single or double observer(s) [119], can be applied to the battery extended ECM. Apart from enhancing the accuracy of state estimation, the estimated parameters can also be used to build other battery indicators such as SOH, SOP, SOF and RUL [134, 135].

On one hand, joint estimation method based on a single observer can cope with the battery monitoring problem in high-dimensional state space directly. For instance, single EKF is applied to the joint estimation structure for battery state and parameter estimation in [136]. Improvement of the battery monitoring performance with joint estimation method using UKF can be found in [120]. Furthermore, simultaneous battery OCV estimation is realized with adaptive EKF in the joint estimation framework in [130]. Recently, considering the model uncertainties in [137], H infinity EKF is introduced to the joint estimation structure in order to have a robust estimation of battery SOC, ohmic and polarization resistance simultaneously.

On the other hand, a more flexible estimation framework based on two observers is called dual estimation method. Double EKF [119], double UKF [120], double sliding mode observer [138], double H∞ observer [139] and double particle filter [140] are introduced to the dual estimation framework, where battery parameters and states can be estimated separately with different time scales. Additionally, merging the advantages of different filtering techniques is another objective of the dual estimation method. For example, UKF and H∞ observer are applied in the dual estimation framework in [134], in which H∞ observer is used to have a robust battery parameter estimation and more accurate SOC estimation is achieved with UKF.

Although various advanced estimation algorithms are applied to the joint estimation and dual estimation frameworks, the essence of these estimation frameworks has not been changed. Thus, the improvement of the battery monitoring result is limited. Therefore, this chapter is dedicated to the discussion of battery monitoring based on the battery extended ECM. The main contributions in this chapter are:

- An observability analysis for the battery extended model is conducted. It shows that the necessary conditions for the observability depend on the battery current, the initial value of the battery capacity and the square of the derivative of the OCV with respect to the SOC.

- The obtained observability analysis result becomes an important theoretical support to propose a new monitoring structure. Commonly used estimation algorithms, namely the KF, EKF, and UKF, are selected and employed for it. Apart from providing a simultaneous estimation of battery OCV, more rapid and less fluctuating battery capacity estimation are the main advantages of the new proposed monitoring structure.

2.2 Battery modelling

2.2.1 Overview of battery model

Several classifications about battery models can be found in the literature. Hence, an overview of various types of battery models will be given at first.

- Electrochemical battery model

Electrochemistry-based model has been recognized as the most precise model that can describe the physical phenomenon inside the battery [141]. However, it relies on complicated mathematical expressions often including partial differential equations along with required a priori knowledge [142]. Namely, a comprehensive understanding of the chemical reactions and physical phenomenon inside the battery is necessary. These two factors limit the application of electrochemical battery models for control-oriented objective. This kind of model is mainly used for the battery design and optimization [143].

- Empirical battery model

Empirical battery model attracts more and more researchers because of its conciseness and simplicity. Normally, several mathematical expressions, which usually include the exponential functions and polynomial functions, can describe the ageing process of the battery cell or the battery pack if necessary [144]. In fact, the employment of the exponential functions and polynomial functions is not casual. Considering the temperature factor during the usage of battery, the result of ageing process is in good accordance with Arrhenius law [145]. In other words, most of the aging model is based on the Arrhenius law. The empirical battery model is experiment-based, which means that the parameters should be obtained through ageing or accelerated ageing test [146]. However, there are two main shortcomings. Firstly, it requires stringent experimental conditions (representative environmental and operating conditions along with accurate measurements of eg. current, temperature, voltage, humidity, ...). Moreover, the experiment should last for several months or even several years. Secondly, the empirical model is built for a specific technology and a specific kind of battery. This of course limits the generalizability of the empirical model [144–146].

- Data-driven or numerical battery model

The third kind of battery model is the so-called data-driven or numerical model [143]. In fact, this kind of model is not a model in the traditional sense. With the help of artificial intelligence and database, this kind of model represents the “future” research methods and directions. The “future” means that the high performance processors in the future will help the on-line development of this numerical model. As mentioned previously, the black box mechanism can provide convenience for modeling the complex non-linear relationship between battery internal states and the numerous environmental stress factors. However, the data dependence is the main drawback of this modelling approach.

- Equivalent electrical circuit battery model

Electrical circuit model (ECM) is the most popular model in the battery research areas, especially for control-oriented research. Simplicity, flexibility, reliability, composability and practicability are the main advantages of this model.

1) Simplicity: the basic ECM is composed of several ideal components, namely, resistor, capacitor, inductor and RC networks [112]. The obtained electrical circuit can simulate the battery output voltage with the current as input. In fact, the ECM has been widely used in the field of ESS (Fuel Cell and supercapacitor) [3, 14, 44, 147] because of its simplicity.

2) Flexibility: according to the requirements of the researchers, the complexity of the ECM can be adjusted, which is mainly based on the specific application and the required accuracy of the model. Namely, the specific application will decide

"which kind of components will be used in the ECM ?". The battery is often used in the intermediate frequency range [44, 148], which means that the EMC is usually composed of a resistor in series connection with several RC networks [112]. However, if needed, the inductor which represents the performance in the low frequency and the constant phase element which simulates the phenomenon in the high frequency could be added to the basic ECM [143]. Furthermore, the required accuracy of the model will also answer to the question *"how much components will be used in the ECM ?"*: For example, increasing the number of RC networks in the ECM will increase the precision of the model; however, the computational burden will also be augmented at the same time [112]. Briefly, one more RC network will bring in one more state in the state-space equation, which means the observer's or controller's design will be more difficult.

3) Reliability: ECM has been used to study the battery for a long time, and many experimental validations have been carried out based on the battery ECM including optimization problem, controller design, state evaluation, etc. [12, 75, 80, 147] Therefore, we can reasonably consider that battery ECM has been validated.

4) Composability: different from the flexibility, which means the ECM can be altered in its own structure and number of components, the ECM can also be expanded by other models. The most common example of the composability is the battery multi-physical model [143]. Compared with the electrochemical battery models, the main drawback of the ECM is that the parameters of the ECM are usually constant. In other words, these parameters do not take into account the real use conditions such as current direction, temperature change, aging process. Therefore, in order to keep and take advantage of the ECM, thermal model or aging model can be merged with the basic ECM to simulate the parameter change as in real battery. As a result, the combined model constitutes the so-called battery multi-physics model. The composability allows the simulation of the battery electrical behaviour while including temperature and ageing effects [149, 150].

5) Practicability: this kind of model is suitable for online EMS calculation. Especially, when the OCV can be linearized, the ECM will degrade to a linear model, which can simplify the calculation process greatly. The practicability makes the ECM become a valuable tool for many engineers, researchers and even companies [80].

Based on the above analysis, the ECM is adopted in this thesis. Details will be presented later.

2.2.2 Dynamic equations of battery ECM

The considered battery ECM is shown in Fig. 2.3. It is one of the most widely used ECMs [13], and it includes a double RC-network which is a good trade-off between the error and the complexity of the model compared with single and triple-RC structures [149].

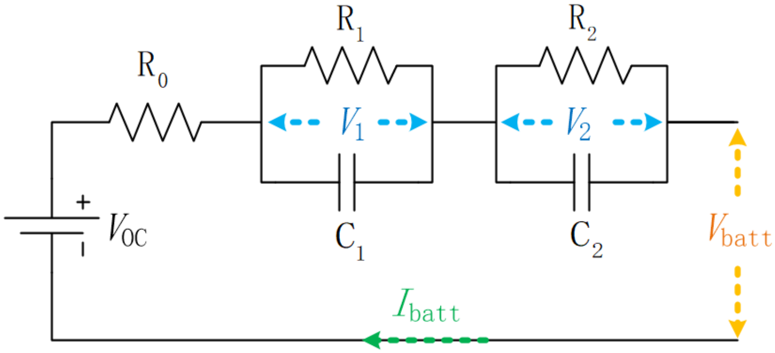

Figure 2.3: Battery ECM with double-RC network.

The resistor R_0 stands for Ohmic resistance which includes the resistance of contacts, electrodes as well as electrolytes [151]. The double pair RC captures the transient battery dynamics such as the charge transfer kinetics, the Lithium Ion diffusion, and solid/electrolyte interface dynamics [152].

The voltage source V_{OC} represents the OCV which mainly depends on the battery SOC [152]. As an example shown in Fig. 2.4, its average value, $V_{OC}(soc)$, is usually a monotonically increasing function of SOC [153]. In each SOC interval, it can be approximated by $V_{OCi}(soc) = a_i \cdot soc + b_i$ (a_i and b_i are constant in the i-th SOC interval). The nonlinearity of this curve is inevitable.

Furthermore, the battery SOC $\in [0\%, 100\%]$ can be modeled by the classical Coulomb counting method as given in eq. (1.1).

Therefore, the battery dynamic behavior can be described by the following state-space representation:

$$\begin{bmatrix} \frac{\mathrm{d}V_1(t)}{\mathrm{d}t} \\ \frac{\mathrm{d}V_2(t)}{\mathrm{d}t} \\ \frac{\mathrm{d}soc(t)}{\mathrm{d}t} \end{bmatrix} = \boldsymbol{M} \begin{bmatrix} V_1(t) \\ V_2(t) \\ soc(t) \end{bmatrix} + \boldsymbol{N} I_{\mathrm{batt}}(t) \qquad (2.8)$$

$$V_{\mathrm{batt}}(t) = V_{\mathrm{OC}}(soc) - V_1(t) - V_2(t) - \mathrm{R}_0 I_{\mathrm{batt}}(t)$$

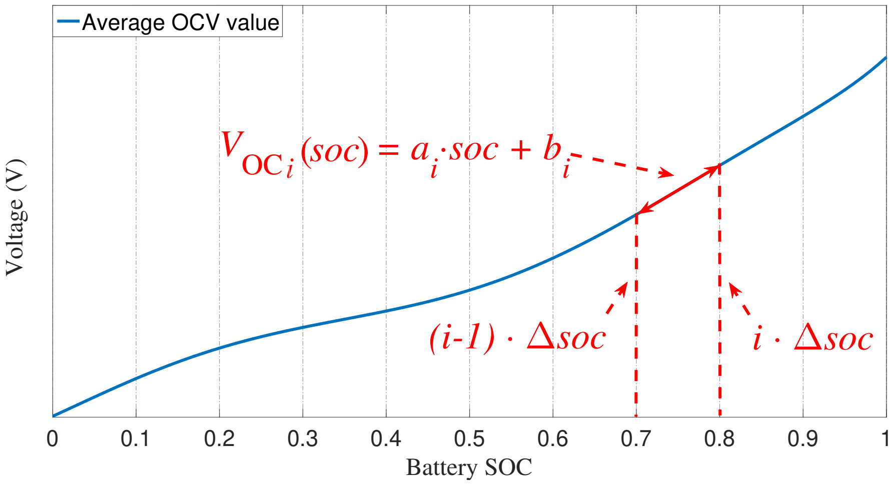

Figure 2.4: General shape of average OCV curve.

where:

$$\boldsymbol{M} = \begin{bmatrix} \frac{-1}{\mathrm{R_1C_1}} & 0 & 0 \\ 0 & \frac{-1}{\mathrm{R_2C_2}} & 0 \\ 0 & 0 & 0 \end{bmatrix}, \quad \boldsymbol{N} = \begin{bmatrix} \frac{1}{\mathrm{C_1}} \\ \frac{1}{\mathrm{C_2}} \\ \frac{-\eta}{\mathrm{C_n}} \end{bmatrix}$$

and V_{batt} is the battery output voltage, V_1 and V_2 are the voltages across the capacitors $\mathrm{C_1}$ and $\mathrm{C_2}$ respectively, I_{batt} is battery input current, according to its reference direction in the Fig. 2.3, “+” means discharging process, while “-” means charging process.

2.2.3 Dynamic equations of extended battery ECM

The battery monitoring framework not only refers to the battery SOC estimation, but the evolution of the physical parameters due to the aging process should also be tracked. Hence, as shown in Fig. 2.5, the battery parameters’ dynamic behavior should be described and integrated into eq. (2.8) to constitute the so-called extended battery model.

To take into account the parametric variation due to the aging process, the relationship $\frac{\mathrm{d}P}{\mathrm{d}t} \approx 0$ will be considered to build an extended battery ECM, where P is a general representation of the parameters such as $\mathrm{R_0}$, $\mathrm{R_1}$, $\mathrm{R_2}$, $\mathrm{C_1}$, $\mathrm{C_2}$ and $\mathrm{C_n}$. Considering the parameters P will change with temperature $Temp$, SOC and usage history H, the relationship $P = p(Temp, soc, H)$ can be analyzed, where $p(\cdot)$ is a nonlinear function [154]. Then, the differential of P with respect to time t is:

$$\frac{\mathrm{d}P}{\mathrm{d}t} = \frac{\partial p}{\partial Temp} \cdot \frac{\partial Temp}{\partial t} + \frac{\partial p}{\partial soc} \cdot \frac{\partial soc}{\partial t} + \frac{\partial p}{\partial H} \cdot \frac{\partial H}{\partial t} \tag{2.9}$$

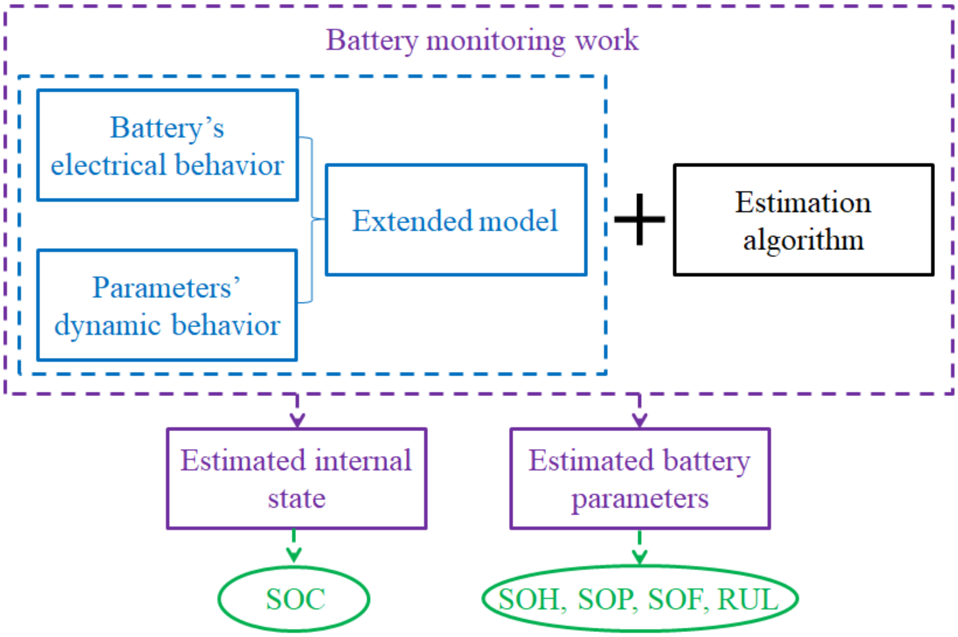

Figure 2.5: Schematic diagram of extended model based battery monitoring work

Equation (2.9) equals zero with the following assumptions [154]:

- Due to the battery cooling system, the LIBs' temperature changes slowly to avoid heavy thermal stress, then $\frac{\partial Temp}{\partial t} \approx 0$ becomes true consequently;
- A general example of city-EV given in [154] shows that $\frac{\partial soc}{\partial t} \approx -0.00028$, which means the battery energy is balanced, hence $\frac{\partial soc}{\partial t} \approx 0$;
- $\frac{\partial H}{\partial t} \approx 0$ definitely holds since the long usage history of LIB is considered.

It has been shown that the parameter variation of the second RC network during the aging process can be neglected [137]. Therefore, $\mathrm{R_2}$ and $\mathrm{C_2}$ are considered as constant. Hence, only the four parameters $\mathrm{R_0}$, $\mathrm{R_1}$, $\mathrm{C_1}$ and $\mathrm{C_n}$ are considered as additional state variables and will be estimated with the SOC. The updating of these variables will cancel or at least mitigate the battery aging effect or temperature variation on the monitoring [134]. Finally, the extended battery model is shown in eq. (2.10).

Obviously, the obtained extended battery ECM is nonlinear with seven states. The concept of observability is useful in reconstructing the unmeasurable state variables from the measurable signals. Therefore, assessing the observability for the used model before executing the state and parameter estimation is necessary. However, due to the numerous states and nonlinearity, observability analysis for the extended battery model (2.10) is challenging and usually overlooked by most of the research works. In [13], linear and nonlinear observability analysis methods are compared for battery SOC estimation with ECM. It is pointed out that the observability of a nonlinear dynamic system at a certain point is not the same as the observability of the system linearized around the point. The conclusion that constant input current cannot guarantee the observability for the extended battery ECM is given in [155]. However, a reference of private communication is presented as the proof for this conclusion. In [44], an additional pseudo random binary signal (PRBS) is added to the input current to ensure the observability of the extended model. Recently, the observability analysis for the extended ECM without extending the battery capacity is done in [137], where non-zero input battery current is deduced as the observability condition. However, the observability analysis for the extended battery model needs further discussion, which will be presented later.

$$\begin{cases} \frac{\mathrm{d}V_1(t)}{\mathrm{d}t} = \frac{-1}{\mathrm{R}_1(t)\mathrm{C}_1(t)}V_1(t) + \frac{1}{\mathrm{C}_1(t)}I_{\mathrm{batt}}(t) \\ \frac{\mathrm{d}V_2(t)}{\mathrm{d}t} = \frac{-1}{\mathrm{R}_2\mathrm{C}_2}V_2(t) + \frac{1}{\mathrm{C}_2}I_{\mathrm{batt}}(t) \\ \frac{\mathrm{d}soc(t)}{\mathrm{d}t} = \frac{-\eta I_{\mathrm{batt}}(t)}{\mathrm{C}_\mathrm{n}(t)} \\ \frac{\mathrm{dR}_0(t)}{\mathrm{d}t} \approx 0 \\ \frac{\mathrm{dR}_1(t)}{\mathrm{d}t} \approx 0 \\ \frac{\mathrm{dC}_1(t)}{\mathrm{d}t} \approx 0 \\ \frac{\mathrm{dC}_\mathrm{n}(t)}{\mathrm{d}t} \approx 0 \\ V_{\mathrm{batt}}(t) = V_{\mathrm{OC}}(soc) - V_1(t) - V_2(t) - \mathrm{R}_0(t) \cdot I_{\mathrm{batt}}(t) \end{cases} \tag{2.10}$$

2.3 Observability analysis

At first, the characteristic of the battery ECM is used to decompose the original ECM into two sub-models. Then, the nonlinear observability analysis method is applied for each extended sub-model. A schematic diagram of the proposed analysis method is shown in Fig. 2.6, where the arrows represent the analysis process.

2.3.1 Battery ECM decomposition

The previously presented modeling process shows that the SOC model (1.1) is integrated directly into the battery ECM state space representation (2.8). In addition, as it can be seen from the state transfer matrix $\boldsymbol{M}$, the diagonal form clearly means that there is no mutual coupling relationship between the battery states [116]. While the three battery states, namely V_1, V_2 and SOC, are only electrically coupled in the output function V_{batt}. Consequently, based on the output equation as shown in

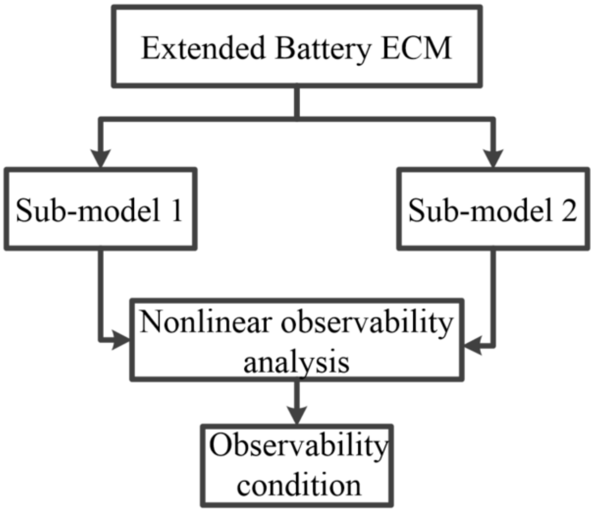

Figure 2.6: Schematic diagram of the analysis process.

eq. (2.8), the battery ECM can be mathematically decomposed into two sub-models which have two different outputs y_1 and y_2 respectively as shown in (2.11).

$$V_{\text{batt}}(t) = \underbrace{V_{\text{OC}}(soc)}_{y_2} + \underbrace{(-V_1(t) - V_2(t) - \mathrm{R}_0 I_{\text{batt}}(t))}_{y_1} \tag{2.11}$$

As given in eq. (2.12) and eq. (2.13), the sub-model 1 with output y_1 has two states, namely V_1 and V_2; while sub-model 2 has only one state. Besides, the consistency of the output between the original model and the sum of these two sub-models can be regarded as a reference to evaluate whether the decomposition is effective.

$$\text{Sub-model 1 :} \begin{cases} \begin{bmatrix} \frac{\mathrm{d}V_1(t)}{\mathrm{d}t} \\ \frac{\mathrm{d}V_2(t)}{\mathrm{d}t} \end{bmatrix} = \begin{bmatrix} \frac{-1}{\mathrm{R}_1\mathrm{C}_1} & 0 \\ 0 & \frac{-1}{\mathrm{R}_2\mathrm{C}_2} \end{bmatrix} \begin{bmatrix} V_1(t) \\ V_2(t) \end{bmatrix} + \begin{bmatrix} \frac{1}{\mathrm{C}_1} \\ \frac{1}{\mathrm{C}_2} \end{bmatrix} I_{\text{batt}}(t) \\ y_1(t) = -V_1(t) - V_2(t) - \mathrm{R}_0 \cdot I_{\text{batt}}(t) \end{cases} \tag{2.12}$$

$$\text{Sub-model 2 :} \begin{cases} \frac{\mathrm{d}soc(t)}{\mathrm{d}t} = \frac{-\eta}{\mathrm{C}_n} \cdot I_{\text{batt}}(t) \\ \\ y_2(t) = V_{\text{OC}}(soc) \end{cases} \tag{2.13}$$

Therefore, the same constant discharge current I_{batt} is introduced in the original battery ECM and the two sub-models. Simulation results with the same initial conditions are shown in Fig. 2.7. The output V_{batt} of the original model equals the sum of the two outputs y_1 and y_2 of the two sub-models. The battery SOC is also identical before and after decomposition.

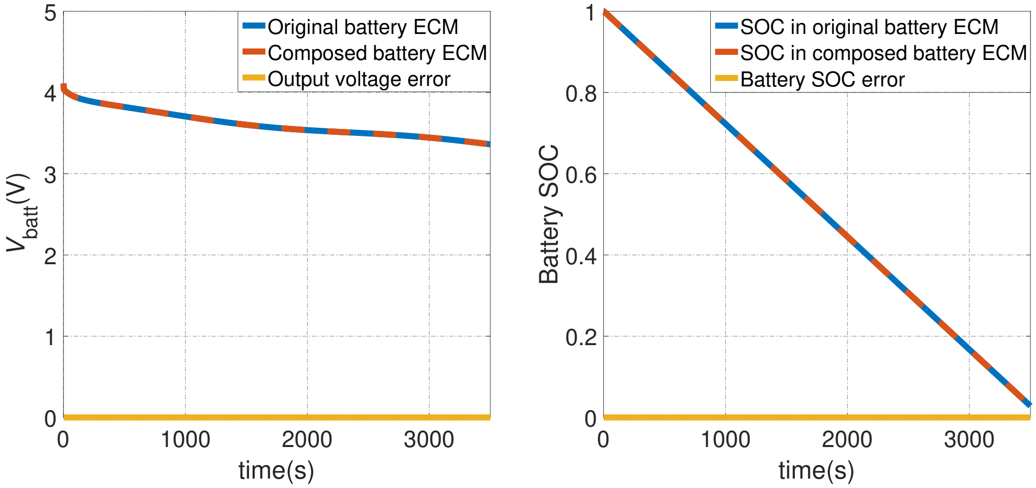

Figure 2.7: Validation of the consistency for the model decomposition.

2.3.2 Observability analysis for the extended sub-models

The observability for the sub-model with output y_1 has already been studied in [44]. Firstly, the model is extended with the zero-time derivative condition for the parameters as discussed in eq. (2.9). Then the nonlinear observability study is executed based on the obtained extended nonlinear model. However, the condition to determine the observability has a complex form depending on the states, the input current, the output voltage and their derivatives. Therefore, it is rather difficult to check the observability conditions for the obtained nonlinear extended model. Hence, a case-by-case demonstration with constant input signal, exponential input signal and sinusoidal input signal is proposed. The conclusion was that the time-varying behavior of current I_{batt} is of utmost importance to guarantee good observability conditions for the estimation of R_0, R_1, C_1.

Therefore, in our case, only the observability analysis for the the sub-model with output y_2 will be developed in the following. This sub-model can be extended as (2.14), where the battery capacity will be estimated along with the battery SOC.

$$\begin{cases} \frac{\mathrm{d}soc(t)}{\mathrm{d}t} = \frac{-\eta I_{\text{batt}}(t)}{\mathrm{C_n}(t)} \\ \frac{\mathrm{dC_n}(t)}{\mathrm{d}t} \approx 0 \end{cases} \tag{2.14}$$

$$y_2 = V_{\text{OC}}(soc)$$

Besides, let us recall the theorem for the observability of a nonlinear model $\begin{cases} \dot{\boldsymbol{x}} = f(\boldsymbol{x}, u) \\ y = h(\boldsymbol{x}, u) \end{cases}$, where $\boldsymbol{x}$ is an $n\times 1$ state vector; y is a scalar output; u is a scalar system input; $f(\cdot)$ and $h(\cdot)$ are nonlinear functions, at point x^0 [44]:

Theorem 2.3.1. *If the following Jacobian matrix $\boldsymbol{J}$ has full rank, then the nonlinear system is observable at x^0.*

$$\boldsymbol{J} = \frac{\partial \boldsymbol{Y}}{\partial \boldsymbol{x}} = \frac{\partial}{\partial \boldsymbol{x}} \begin{bmatrix} h(\boldsymbol{x}, u) \\ L_f(h)(\boldsymbol{x}, \boldsymbol{U}) \\ L_f(h_1)(\boldsymbol{x}, \boldsymbol{U}) \\ \vdots \\ L_f(h_{n-2})(\boldsymbol{x}, \boldsymbol{U}) \end{bmatrix} \tag{2.15}$$

where $\boldsymbol{Y} = [y, y', ..., y^{(n-1)}]^{\mathrm{T}}$, $\boldsymbol{U} = [u, u', ..., u^{(n-1)}]^{\mathrm{T}}$, and the i-th derivative of the scalar output y can be represented by Lie operator $L_f(h)$, which is the total differentiation of h:

$$\begin{aligned} y^{(i)} &= L_f(h_{i-1})(\boldsymbol{x}, \boldsymbol{U}) \\ &= \frac{\partial h_{i-1}}{\partial \boldsymbol{x}}(\boldsymbol{x}, \boldsymbol{U}) f(\boldsymbol{x}, u) + \frac{\partial h_{i-1}}{\partial u}(\boldsymbol{x}, \boldsymbol{U}) \frac{d\boldsymbol{U}}{dt} \end{aligned} \tag{2.16}$$

e.g. $y' = \frac{dy}{dt} = \frac{\partial h}{\partial \boldsymbol{x}} f + \frac{\partial h}{\partial u} u' = h_1(\boldsymbol{x}, u, u')$

Hence, according to **Theorem 2.3.1**, the Jacobian matrix $\boldsymbol{J}$ for the extended sub-model (2.14) is:

$$\boldsymbol{J} = \frac{\partial(y_2, \dot{y}_2)}{\partial(soc, \mathrm{C_n})} = \begin{bmatrix} \frac{\mathrm{d}V_{\mathrm{OC}}}{\mathrm{d}soc} & 0 \\ \Theta & \frac{\mathrm{d}V_{\mathrm{OC}}}{\mathrm{d}soc} \cdot (\frac{\eta I_{\mathrm{batt}}(t)}{\mathrm{C_n^2}(t)}) \end{bmatrix} \tag{2.17}$$

Note 1: $\dot{y}_2 = \frac{\mathrm{d}V_{\mathrm{OC}}(soc)}{\mathrm{d}t} = \frac{\mathrm{d}V_{\mathrm{OC}}}{\mathrm{d}soc} \cdot \frac{\mathrm{d}soc}{\mathrm{d}t} = \frac{\mathrm{d}V_{\mathrm{OC}}}{\mathrm{d}soc} \cdot (\frac{-\eta I_{\mathrm{batt}}(t)}{\mathrm{C_n}(t)})$

Note 2: Because of the zero in (2.17), Θ is just a symbol to represent the corresponding term in the 2×2 matrix, and it will have no effect on the determinant of $\boldsymbol{J}$.

Therefore, the observability condition for extended model (2.14) is defined by (2.18), where several interesting concluding remarks can be drawn.

$$\det(\boldsymbol{J}) = \left(\frac{\mathrm{d}V_{\mathrm{OC}}}{\mathrm{d}soc}\right)^2 \cdot (\frac{\eta I_{\mathrm{batt}}(t)}{\mathrm{C_n^2}(t)}) \neq 0 \tag{2.18}$$

1. The term $\left(\frac{\mathrm{d}V_{\mathrm{OC}}}{\mathrm{d}soc}\right)^2$ induces the inherent weaker observability environment for the battery capacity $\mathrm{C_n}$. Because $\frac{\mathrm{d}V_{\mathrm{OC}}}{\mathrm{d}soc}$ is smaller than one in most ranges of SOC, which means its square is usually smaller than itself.

2. The input I_{batt} appears in the numerator of $\det(\boldsymbol{J})$, which means the current value will also affect the observability condition. It has been indicated in [24] that a higher absolute value of the determinant will lead to a better observability. Hence, the larger the current is, the better is the observability condition.

3. As C_n^2 is in the denominator of $\det(\boldsymbol{J})$, then its impact cannot be ignored. A practical conclusion based on this point is that smaller initial value of the battery capacity will enhance the observability.

To summarize, a schematic resume of the obtained necessary observability conditions for the extended battery ECM is shown in Fig. 2.8.

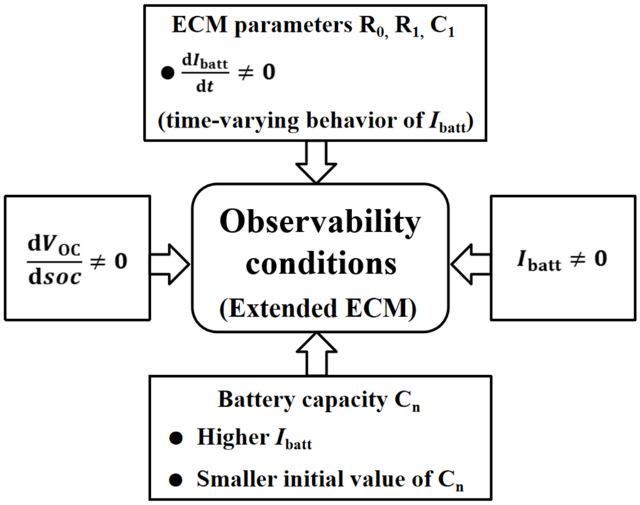

Figure 2.8: Schematic resume of the observability conditions for extended ECM.

Note that these observability conditions are necessary but not sufficient for battery monitoring. Because the observability of the model (2.10) will definitely be weaker than the observability of each sub-model. However, the proposed observability analysis method can avoid applying the nonlinear observability method directly to the extended battery model, which would be tricky.

2.4 New structure for battery state and parameter estimation

2.4.1 Battery model discretisation

Since the battery state and parameter estimation is usually carried out in discrete time domain inside BMS [156], the battery model discretisation process will be presented in this section firstly. The zero-order hold approximation is used in this thesis, details are shown as follows [157]. Consider a general expression of ordinary difference equations:

$$\frac{\mathrm{d}x(t)}{\mathrm{d}t} = ax(t) + bu(t) \Rightarrow \frac{\mathrm{d}x(t)}{\mathrm{d}t} - ax(t) = bu(t) \tag{2.19}$$

therefore, multiplying both sides of eq. (2.19) by e^{-at}, the following expression can be obtained:

$$\begin{gathered} \mathrm{e}^{-at}\left[\tfrac{\mathrm{d}x(t)}{\mathrm{d}t} - ax(t)\right] = \underline{\tfrac{\mathrm{d}}{\mathrm{d}t}\left[\mathrm{e}^{-at}x(t)\right]} = \mathrm{e}^{-at}bu(t) \\ \Downarrow \\ \overbrace{\int_0^t \frac{\mathrm{d}}{\mathrm{d}\tau}\left[\mathrm{e}^{-a\tau}x(\tau)\right]\mathrm{d}\tau = \mathrm{e}^{-at}x(t) - x(0) = \int_0^t \mathrm{e}^{-a\tau}bu(\tau)\mathrm{d}\tau} \end{gathered} \tag{2.20}$$

Besides, we wish to evaluate $x(t)$ at discrete times $x[k] = x(k\Delta t)$, where Δt is the sampling period [157]. Hence:

$$x[k+1] = x((k+1)\Delta t) = \mathrm{e}^{a(k+1)\Delta t}x(0) + \int_0^{(k+1)\Delta t} \mathrm{e}^{a((k+1)\Delta t - \tau)}bu(\tau)\mathrm{d}\tau \tag{2.21}$$

then, the integral in eq. (2.21) is split into two parts as following [157]:

$$\begin{aligned} x[k+1] &= \mathrm{e}^{a\Delta t}\mathrm{e}^{ak\Delta t}x(0) + \int_0^{k\Delta t} \mathrm{e}^{a((k+1)\Delta t-\tau)}bu(\tau)\mathrm{d}\tau + \int_{k\Delta t}^{(k+1)\Delta t} \mathrm{e}^{a((k+1)\Delta t-\tau)}bu(\tau)\mathrm{d}\tau \\ &= \mathrm{e}^{a\Delta t}\mathrm{e}^{ak\Delta t}x(0) + \int_0^{k\Delta t} \mathrm{e}^{a\Delta t}\mathrm{e}^{a(k\Delta t-\tau)}bu(\tau)\mathrm{d}\tau + \int_{k\Delta t}^{(k+1)\Delta t} \mathrm{e}^{a((k+1)\Delta t-\tau)}bu(\tau)\mathrm{d}\tau \\ &= \mathrm{e}^{a\Delta t}x(k\Delta t) + \int_{k\Delta t}^{(k+1)\Delta t} \mathrm{e}^{a((k+1)\Delta t-\tau)}bu(\tau)\mathrm{d}\tau \\ &= \mathrm{e}^{a\Delta t}x[k] + \int_{k\Delta t}^{(k+1)\Delta t} \mathrm{e}^{a((k+1)\Delta t-\tau)}bu(\tau)\mathrm{d}\tau \end{aligned}$$

Furthermore, $u(\tau)$ is assumed to be constant from $k\Delta t$ to $(k+1)\Delta t$, and equals to $u(k\Delta t)$ [157]. Hence:

$$\begin{aligned} x[k+1] &= \mathrm{e}^{a\Delta t}x[k] + \mathrm{e}^{a(k+1)\Delta t}\left(\int_{k\Delta t}^{(k+1)\Delta t} \mathrm{e}^{-a\tau}\mathrm{d}\tau\right)bu[k] \\ &= \mathrm{e}^{a\Delta t}x[k] + \mathrm{e}^{a(k+1)\Delta t}\left(-\frac{1}{a}\mathrm{e}^{-a\tau}\Big|_{k\Delta t}^{(k+1)\Delta t}\right)bu[k] \\ &= \mathrm{e}^{a\Delta t}x[k] + \frac{1}{a}\mathrm{e}^{a(k+1)\Delta t}\left(\mathrm{e}^{-ak\Delta t} - \mathrm{e}^{-a(k+1)\Delta t}\right)bu[k] \\ &= \mathrm{e}^{a\Delta t}x[k] + \frac{1}{a}\left(\mathrm{e}^{a\Delta t} - 1\right)bu[k] \end{aligned} \tag{2.22}$$

As a result, eq. (2.22) is used to deduce the discrete time model. For example, in our case, $x[k] = V_1[k]$, $a = \frac{-1}{\mathrm{R_1C_1}}$, $b = \frac{1}{\mathrm{C_1}}$ and $u[k] = I_{\mathrm{batt}}[k]$. Therefore, $V_1[k+1] = \mathrm{e}^{\frac{-1}{\mathrm{R_1C_1}}\Delta t}V_1[k] + \mathrm{R_1}\cdot(1-\mathrm{e}^{\frac{-1}{\mathrm{R_1C_1}}\Delta t})\cdot I_{\mathrm{batt}}[k]$. Finally, the discrete time version of model (2.8) is:

$$\begin{bmatrix} V_1(k+1) \\ V_2(k+1) \\ soc(k+1) \end{bmatrix} = \boldsymbol{A} \begin{bmatrix} V_1(k) \\ V_2(k) \\ soc(k) \end{bmatrix} + \boldsymbol{B} I_{\mathrm{batt}}(k) \tag{2.23}$$

$$V_{\mathrm{batt}}(k) = V_{\mathrm{OC}}(soc) - V_1(k) - V_2(k) - \mathrm{R_0} I_{\mathrm{batt}}(k)$$

where,

$$\boldsymbol{A} = \begin{bmatrix} \mathrm{e}^{\frac{-T}{\mathrm{R_1C_1}}} & 0 & 0 \\ 0 & \mathrm{e}^{\frac{-T}{\mathrm{R_2C_2}}} & 0 \\ 0 & 0 & 1 \end{bmatrix}, \quad \boldsymbol{B} = \begin{bmatrix} \mathrm{R_1}\cdot(1-\mathrm{e}^{\frac{-T}{\mathrm{R_1C_1}}}) \\ \mathrm{R_2}\cdot(1-\mathrm{e}^{\frac{-T}{\mathrm{R_2C_2}}}) \\ \frac{-\eta T}{\mathrm{C_n}} \end{bmatrix}$$

Note that we use "( )" to express the discrete time model instead of "[ ]" thereafter. k is the time index. The sampling period is T.

In addition, considering the uncertainty of the modeling and data acquisition process, stochastic model is employed instead of a deterministic one. Hence, $\omega_1, \omega_2, \omega_2$ are additive model errors. Using the common random walk model [137], $\omega_4, \omega_5, \omega_6, \omega_7$ are added to the slowly varying parameters and v is the measurement noise. It is assumed that all noises are additive white gaussian (AWG). Finally the extended discrete time model is given in eq. (2.24)

$$\begin{cases} V_1(k+1) = \mathrm{e}^{\frac{-T}{\mathrm{R_1}(k)\mathrm{C_1}(k)}} V_1(k) + \mathrm{R_1}(k)\cdot\left(1-\mathrm{e}^{\frac{-T}{\mathrm{R_1}(k)\mathrm{C_1}(k)}}\right)\cdot I_{\mathrm{batt}}(k) + \omega_1(k) \\ V_2(k+1) = \mathrm{e}^{\frac{-T}{\mathrm{R_2C_2}}} V_2(k) + \mathrm{R_2}\cdot\left(1-\mathrm{e}^{\frac{-T}{\mathrm{R_2C_2}}}\right)\cdot I_{\mathrm{batt}}(k) + \omega_2(k) \\ soc(k+1) = soc(k) - \frac{\eta T}{\mathrm{C_n}(k)}\cdot I_{\mathrm{batt}}(k) + \omega_3(k) \\ \mathrm{R_0}(k+1) = \mathrm{R_0}(k) + \omega_4(k) \\ \mathrm{R_1}(k+1) = \mathrm{R_1}(k) + \omega_5(k) \\ \mathrm{C_1}(k+1) = \mathrm{C_1}(k) + \omega_6(k) \\ \mathrm{C_n}(k+1) = \mathrm{C_n}(k) + \omega_7(k) \\ V_{\mathrm{batt}}(k) = V_{\mathrm{OC}}(soc) - V_1(k) - V_2(k) - \mathrm{R_0}(k)\cdot I_{\mathrm{batt}}(k) + v(k) \end{cases} \tag{2.24}$$

By the way, the classical estimation methods will be reviewed rapidly based on the discrete time model (2.24) before presenting the new cascaded estimation framework.

Based on (2.24), one way to execute the state and parameter estimation is to use a single observer, which is called joint estimation method. Another way that resorts to two parallel observers is named as dual estimation method, where parameter estimation can be isolated. Thus, it makes the multi-timescale estimation possible [120]. Although employing more advanced observers can improve the monitoring result based on these two classical estimation structures, the improvement is limited due to the incorrect parameter grouping.

The necessary observability conditions have shown that the battery usable capacity estimation has a higher demand for the observability condition. Especially, its inherent weak observability caused by the term $\left(\frac{\mathrm{d}V_{\mathrm{OC}}}{\mathrm{d}soc}\right)^2$ is challenging. It is better to estimate the battery usable capacity separately. Hence, the new proposed cascaded framework for battery state and parameter estimation is shown in Fig. 2.9, where $\hat{X}$ $(X = \mathrm{SOC}, \mathrm{R}_0, \mathrm{R}_1, \mathrm{C}_1, V_{\mathrm{OC}}, \mathrm{C}_{\mathrm{n}})$ stands for the estimated vector. Three estimation modules can be clearly observed from this schematic representation, namely, the battery capacity estimation, the battery OCV estimation and the battery SOC and ECM parameter estimation. Besides, the aforementioned three parts are connected together by some key state variables. Details for each part will be introduced in the following sections:

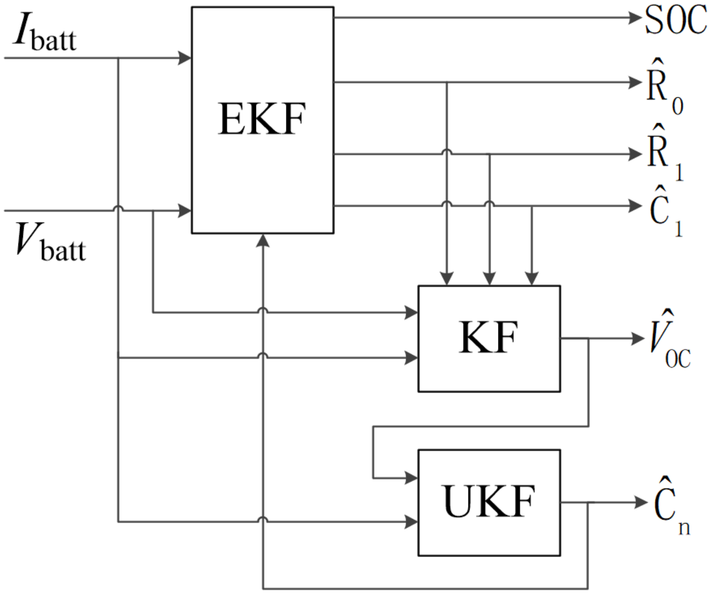

Figure 2.9: New proposed structure.

2.4.2 Battery actual capacity estimation

A novel method to separate and estimate the usable battery capacity $\mathrm{C_n}$ is introduced here, where the Coulomb counting model is reused. In addition, $V_{\mathrm{OC}}(soc)$ is used as the output model in this module because of its inherent relationship with SOC.

Hence, after adding $\mathrm{C_n}$ as an additional state, the on-line monitoring model prepared for the battery capacity is given in (2.25).

$$\begin{cases} soc(k+1) = soc(k) - \frac{\eta T}{\mathrm{C_n}(k)} I_{\mathrm{batt}}(k) + \gamma_1(k) \\ \mathrm{C_n}(k+1) = \mathrm{C_n}(k) + \gamma_2(k) \\ y_{\mathrm{O}}(k) = V_{\mathrm{OC}}(soc) + \delta(k) \end{cases} \tag{2.25}$$

where: the added noises $\gamma_{1,2}$ and δ are AWG.

Moreover, UKF, as a more powerful nonlinear observer, is selected for this two-state nonlinear model. This choice cannot only guarantee the estimation performance of $\mathrm{C_n}$, but also limits the increase of on-line calculation burden due to the separation.

However, the output equation y_{O} in (2.25) is the battery OCV, which cannot be measured during the battery operation. Hence, the prediction step in the UKF will be corrected by OCV estimation (introduced in the next section) used as an input for the battery usable capacity estimation.

2.4.3 Battery OCV estimation

The estimated battery OCV plays an important role in the new cascaded framework. As it can be noticed in Fig. 2.9, this module makes the connection between the estimated SOC and ECM parameters and the estimation of the battery usable capacity.

Broadly speaking, online OCV estimation techniques can be divided into two families, namely, observer-based and regression-based methods. For instance, in [130], EKF is employed to execute online parameter identification as well as OCV estimation. In [158], H_∞ filter is applied to obtain the OCV curve within 2s instead of using the traditional OCV tests such as incremental OCV or low-current OCV test which usually takes 3-5 days. On the other hand, the classical recursive least-squares (RLS) algorithm and its numerous variations can also realize OCV estimation. For example, in [133], multiple adaptive forgetting factors RLS, which can cope with the different varying rates of different parameters is proposed in order to distribute a forgetting factor to each parameter that needs to be estimated.

The models for observer-based and regression-based OCV estimation methods are described in section 2.4.3.1 and 2.4.3.2 respectively[1]. Firstly, based on Fig. 2.3, the battery model can be expressed as (2.26), which is obtained with the zero-order hold

---

[1] Detailed comparative study of OCV estimation methods has been published in: Jianwen MENG, Moussa BOUKHNIFER and Demba DIALLO, Comparative study of lithium-ion battery open-circuit-voltage online estimation methods, IET Electrical Systems in Transportation, vol. 10, pp. 162–169, 2020.

approximation introduced previously. However, at first, the V_{OC} is regarded as a constant term in order to deduce the desired model [78, 133, 158]

$$\begin{cases} \begin{bmatrix} V_1(k+1) \\ V_2(k+1) \end{bmatrix} = \boldsymbol{A} \begin{bmatrix} V_1(k) \\ V_2(k) \end{bmatrix} + \boldsymbol{B} I_{\text{batt}}(k) \\ V_{\text{batt}}(k) - V_{\text{OC}} = \boldsymbol{C} \begin{bmatrix} V_1(k) \\ V_2(k) \end{bmatrix} + D I_{\text{batt}}(k) \end{cases} \tag{2.26}$$

where,

$$\boldsymbol{A} = \begin{bmatrix} e^{\frac{-T}{\mathrm{R_1C_1}}} & 0 \\ 0 & e^{\frac{-T}{\mathrm{R_2C_2}}} \end{bmatrix} = \begin{bmatrix} \mathrm{a}_1 & 0 \\ 0 & \mathrm{a}_2 \end{bmatrix}$$

$$\boldsymbol{B} = \begin{bmatrix} \mathrm{R}_1(1 - e^{\frac{-T}{\mathrm{R_1C_1}}}) \\ \mathrm{R}_2(1 - e^{\frac{-T}{\mathrm{R_2C_2}}}) \end{bmatrix} = \begin{bmatrix} \mathrm{b}_1 \\ \mathrm{b}_2 \end{bmatrix}$$

$$\boldsymbol{C} = [-1, -1]$$

$$D = -\mathrm{R}_0$$

2.4.3.1 Auto regressive exogenous model for OCV estimation

For the purpose of applying the regression-based method, z-transform pairs for the discrete time model (2.26) between time-domain and frequency-domain is used to deduce the required auto regressive exogenous (ARX) model for estimating the battery OCV.

$$\begin{aligned} \frac{Y(z)}{U(z)} &= [\boldsymbol{C}(z\mathbf{I} - \boldsymbol{A})^{-1}\boldsymbol{B} + D] \\ \frac{V_{\text{batt}}(z) - V_{\text{OC}}}{I_{\text{batt}}(z)} &= \left[\frac{\mathrm{b}_1(\mathrm{a}_2 - z) + \mathrm{b}_2(\mathrm{a}_1 - z)}{(z - \mathrm{a}_1)(z - \mathrm{a}_2)} - \mathrm{R}_0\right] \end{aligned} \tag{2.27}$$

where, $\boldsymbol{A}$, $\boldsymbol{B}$, $\boldsymbol{C}$ and D are the corresponding matrixes and scalar of model (2.26); $\mathbf{I}$ is a unit matrix with corresponding dimension; $Y(z)$ and $U(z)$ are the output and input of eq. (2.26) in the z-domain corresponding to $V_{\text{batt}}(k) - V_{\text{OC}}$ and $I_{\text{batt}}(k)$ respectively in the time-domain; z is the z-transform operator. Note that V_{OC} is regarded as a constant during the transformation process.

Applying the inverse z-transform ($x[n-k] \Leftrightarrow z^{-k}x(z)$) for eq. (2.27), the following recurrent equation can be obtained after simplification and recombination [78]:

$$\begin{aligned} V_{\mathrm{batt}}(k) =& (\mathrm{a}_1 + \mathrm{a}_2)\mathrm{V}_{\mathrm{batt}}(k-1) \\ & - \mathrm{a}_1\mathrm{a}_2\mathrm{V}_{\mathrm{batt}}(k-2) - \mathrm{R}_0\mathrm{I}_{\mathrm{batt}}(k) \\ & + (\mathrm{R}_0\mathrm{a}_1 + \mathrm{R}_0\mathrm{a}_2 - \mathrm{b}_1 - \mathrm{b}_2)\mathrm{I}_{\mathrm{batt}}(k-1) \\ & + (\mathrm{b}_1\mathrm{a}_2 + \mathrm{b}_2\mathrm{a}_1 - \mathrm{R}_0\mathrm{a}_1\mathrm{a}_2)\mathrm{I}_{\mathrm{batt}}(k-2) \\ & + (1 - \mathrm{a}_1 - \mathrm{a}_2 + \mathrm{a}_1\mathrm{a}_2)V_{\mathrm{OC}} \end{aligned} \tag{2.28}$$

Consequently, the ARX model of the battery can be obtained by rewriting eq. (2.28) into the following form:

$$\mathrm{V}_{\mathrm{batt}}(k) = \boldsymbol{\varphi}'(k)\boldsymbol{\theta} \tag{2.29}$$

with $\boldsymbol{\varphi} = [\mathrm{V}_{\mathrm{batt}}(k-1), \mathrm{V}_{\mathrm{batt}}(k-2), \mathrm{I}_{\mathrm{batt}}(k), \mathrm{I}_{\mathrm{batt}}(k-1), \mathrm{I}_{\mathrm{batt}}(k-2), 1]'$; and $\boldsymbol{\theta} = [\theta_1, \theta_2, \theta_3, \theta_4, \theta_5, \theta_6]'$, where:

$$\begin{aligned} \theta_1 &= \mathrm{a}_1 + \mathrm{a}_2; \\ \theta_2 &= -\mathrm{a}_1\mathrm{a}_2; \\ \theta_3 &= -\mathrm{R}_0; \\ \theta_4 &= \mathrm{R}_0\mathrm{a}_1 + \mathrm{R}_0\mathrm{a}_2 - \mathrm{b}_1 - \mathrm{b}_2; \\ \theta_5 &= \mathrm{b}_1\mathrm{a}_2 + \mathrm{b}_2\mathrm{a}_1 - \mathrm{R}_0\mathrm{a}_1\mathrm{a}_2; \\ \theta_6 &= (1 - \mathrm{a}_1 - \mathrm{a}_2 + \mathrm{a}_1\mathrm{a}_2)V_{\mathrm{OC}}; \end{aligned} \tag{2.30}$$

and the battery OCV can be deduced as [78]:

$$V_{\mathrm{OC}} = \frac{\theta_6}{(1 - \mathrm{a}_1 - \mathrm{a}_2 + \mathrm{a}_1\mathrm{a}_2)} = \frac{\theta_6}{(1 - \theta_1 - \theta_2)} \tag{2.31}$$

In fact, eq. (2.29) is a simple linear mathematical model where $V_{\mathrm{batt}}(k)$ and $I_{\mathrm{batt}}(k)$ are the measurable signal, $\boldsymbol{\theta}$ is the parameter vector to be determined, the known vector $\boldsymbol{\varphi}(k)$ is called regression variables or regressors [78].

2.4.3.2 Extended battery ECM for OCV estimation

Thanks to the zero-time derivative condition, namely $\frac{\mathrm{dV_{OC}}}{\mathrm{d}t} \approx 0$, the estimation of the battery OCV can also be done similarly based on the model (2.32) which is extended based on (2.26) [130,158]. Furthermore, because the estimation of OCV is integrated in the new structure as shown in Fig. 2.9, the related parameters in the extended model (2.32) will be updated by the battery SOC and ECM parameter estimation module.

$$
\begin{aligned}
\begin{bmatrix} V_1(k+1) \\ V_2(k+1) \\ V_{\mathrm{OC}}(k+1) \end{bmatrix} &= \boldsymbol{F}(k+1) \begin{bmatrix} V_1(k) \\ V_2(k) \\ V_{\mathrm{OC}}(k) \end{bmatrix} + \boldsymbol{G}(k+1) I_{\mathrm{batt}}(k) + \begin{bmatrix} \varepsilon_1(k) \\ \varepsilon_2(k) \\ \varepsilon_3(k) \end{bmatrix} \\
V_{\mathrm{batt}}(k) &= \boldsymbol{H} \begin{bmatrix} V_1(k) \\ V_2(k) \\ V_{\mathrm{OC}}(k) \end{bmatrix} + J(k) I_{\mathrm{batt}}(k) + \psi(k)
\end{aligned}
\tag{2.32}
$$

where: the added noises $\varepsilon_{1\sim 3}$ and ψ are also AWG, and:

$$
\boldsymbol{F}(k) = \begin{bmatrix} \mathrm{e}^{\frac{-T}{\mathrm{R}_1(k)\mathrm{C}_1(k)}} & 0 & 0 \\ 0 & \mathrm{e}^{\frac{-T}{\mathrm{R}_2\mathrm{C}_2}} & 0 \\ 0 & 0 & 1 \end{bmatrix}, \qquad \boldsymbol{H} = [-1, -1, 1]
$$

$$
\boldsymbol{G}(k) = \begin{bmatrix} \mathrm{R}_1(k) \cdot (1 - \mathrm{e}^{\frac{-T}{\mathrm{R}_1(k)\mathrm{C}_1(k)}}) \\ \mathrm{R}_2 \cdot (1 - \mathrm{e}^{\frac{-T}{\mathrm{R}_2\mathrm{C}_2}}) \\ 0 \end{bmatrix}, J(k) = -\mathrm{R}_0(k)
$$

Obviously, the extended battery model (2.32) is linear, where the battery OCV could be estimated along with the other two battery states V_1 and V_2 during the operation. Note that there is no assumption on the linearity of the OCV-SOC curve during the battery modeling process. The linear model (2.32) is obtained with the assumption $\frac{\mathrm{dV}_{\mathrm{OC}}}{\mathrm{d}t} \approx 0$.

The comparative study between the observer-based and regression-based OCV estimation methods can be found in [78]. Although the regression-based OCV estimation algorithms can provide an independent OCV estimation, observer-based method exhibits better OCV estimation performance from the perspective of accuracy. Hence, observer-based OCV estimation is employed here in order to connect the other two modules.

Obviously, the full rank characteristic of the observability matrix of this linear model can be easily verified. Therefore, the classical linear Kalman Filter(KF) is used in this module as shown in Fig. 2.9.

2.4.4 Battery SOC and ECM parameter estimation

Due to the isolation of the battery usable capacity estimation, only the first six states of the state model in eq. (2.24) and its measurement model will be kept and used to estimate the battery SOC and ECM parameters. Hence, the battery SOC and ECM parameter estimation module in Fig. 2.9 is executed based on the extended model (2.33).

$$
\begin{cases}
V_1(k+1) = \mathrm{e}^{\frac{-T}{\mathrm{R}_1(k)\mathrm{C}_1(k)}} V_1(k) + \mathrm{R}_1(k) \cdot \left(1 - \mathrm{e}^{\frac{-T}{\mathrm{R}_1(k)\mathrm{C}_1(k)}}\right) \cdot I_{\mathrm{batt}}(k) + \omega_1(k) \\
V_2(k+1) = \mathrm{e}^{\frac{-T}{\mathrm{R}_2\mathrm{C}_2}} V_2(k) + \mathrm{R}_2 \cdot \left(1 - \mathrm{e}^{\frac{-T}{\mathrm{R}_2\mathrm{C}_2}}\right) \cdot I_{\mathrm{batt}}(k) + \omega_2(k) \\
soc(k+1) = soc(k) - \frac{\eta T}{\mathrm{C}_{\mathrm{n}}(k)} \cdot I_{\mathrm{batt}}(k) + \omega_3(k) \\
\mathrm{R}_0(k+1) = \mathrm{R}_0(k) + \omega_4(k) \\
\mathrm{R}_1(k+1) = \mathrm{R}_1(k) + \omega_5(k) \\
\mathrm{C}_1(k+1) = \mathrm{C}_1(k) + \omega_6(k) \\
V_{\mathrm{batt}}(k) = V_{\mathrm{OC}}(soc) - V_1(k) - V_2(k) - \mathrm{R}_0(k) \cdot I_{\mathrm{batt}}(k) + \upsilon(k)
\end{cases}
\tag{2.33}
$$

Note that repetition of the Coulomb counting model is inevitable, because the measured battery terminal voltage is an integral term, which cannot be divided into different components respectively.

Besides, EKF, as one of the most used observers, is selected for this module in order to cope with the nonlinear and high-dimension hyperspace. It should be pointed out that the battery capacity $\mathrm{C_n}$ is updated by the previously mentioned module. Thus, the combination of linear and different nonlinear state tracking methods can make the new structure maintain the on-line calculation burden as small as possible.

Moreover, for the battery OCV estimation module, the estimation of the polarization voltages V_1 and V_2 cannot be simply considered as done two times, i.e. during the estimation of SOC and parameters, as well as the estimation of OCV. Because in the kth step, the battery SOC and parameter estimation module uses the information of the (k-1)th step; while the state transfer matrix ***F(k)*** and the so-called control input matrix ***G(k)*** of (2.32) are calculated with the latest information of the kth step, namely the estimation is executed with the updated battery ECM parameters.

2.5 Numerical verification

2.5.1 Observability conditions' assessment

All the battery parameters used in this section, including the coefficients of a seventh-order polynomial OCV curve as shown in eq. (2.34), are taken from [12]. They are identified through the pulsed charge and discharge tests of a pouch cell LIB. The hardware-in-the-loop validation has been done in order to confirm the proposed model and parameters [12].

$$
\begin{aligned}
V_{\mathrm{OC}}(soc) = a_1 \cdot soc^7 + a_2 \cdot soc^6 + a_3 \cdot soc^5 + a_4 \cdot soc^4 ... \\
... + a_5 \cdot soc^3 + a_6 \cdot soc^2 + a_7 \cdot soc^1 + a_8
\end{aligned}
\tag{2.34}
$$

Firstly, as shown in Fig. 2.10, three special periodic input currents I_{batt} are considered. In one cycle (300s), the LIB is discharged and recharged by a dynamic current during a small time period at the beginning; then a constant discharge current is applied to the battery; and finally the battery will be idle until the next period. Besides, in order to verify whether the current value will affect the estimation of the battery capacity, three constant discharge values are selected, namely 10 A, 15 A and 20 A.

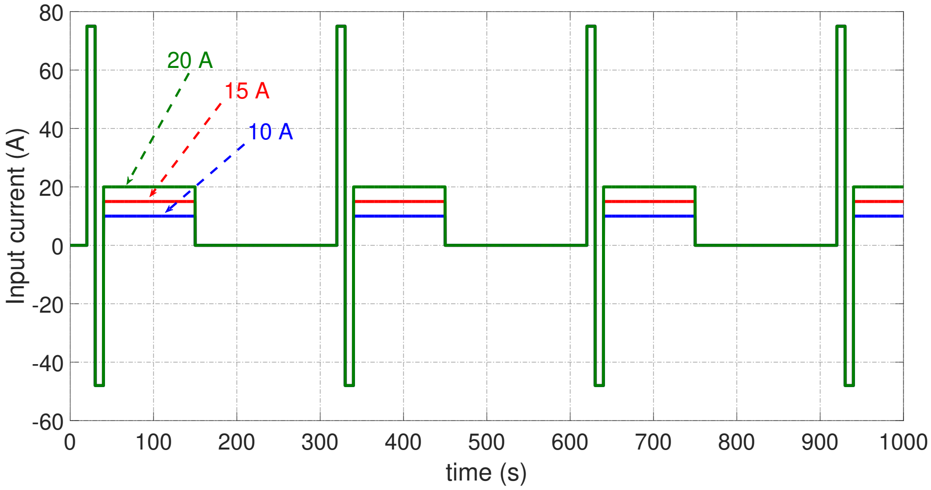

Figure 2.10: Three different input currents for the battery.

Note that the 20 A discharge current is the default value. The EKF is initialised with the vector $\boldsymbol{x_0}$=[V_1, V_2, SOC, R_0, R_1, C_1, C_n]=[0, 0, 0.8, 0.001 Ω, 0.0035 Ω, 17000 F, 18 Ah] in the simulation test if there is no further indication.

- $\frac{\mathrm{d}I_{\mathrm{batt}}}{\mathrm{d}t} \neq 0$ (variable battery input current)

Although there are three estimated ECM parameters, the estimation result of R_0 will be discussed as an example. Because the estimation of R_1 and C_1 are executed based on the same extended battery model with the same zero-time derivative condition. In order to verify the observability condition for the ECM parameter estimation, a simulation test is conducted in which R_0 will increase slowly in the battery model.

The estimation results are shown in Fig. 2.11, Fig. 2.12 and Fig. 2.13. In Fig. 2.11, the blue line is the estimation of R_0 by EKF. Fig. 2.12 shows the corresponding input current and Fig. 2.13 is the corresponding estimation error. From Fig. 2.11 and Fig. 2.13, we can deduce that the observer estimates efficiently the resistance only when the input current is variable. Besides, even when R_0 is constant in the first 1500s, the fluctuating characteristic of the estimated R_0 in Fig. 2.11 can be found evidently. This can be explained from the perspective of observability. The fluctuating characteristic of the estimated R_0 is due to the input current dynamics.

- Battery input current level

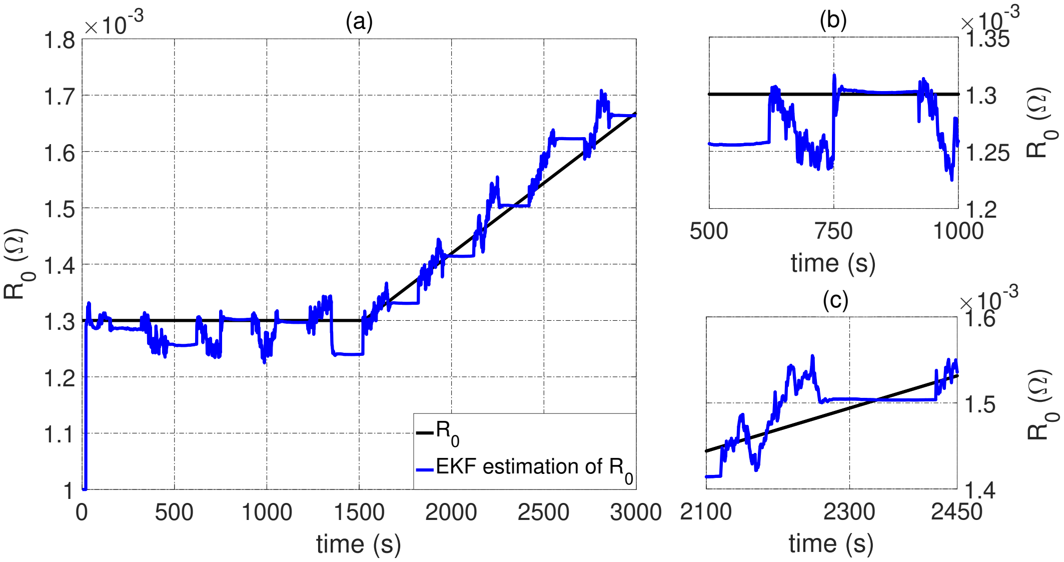

Figure 2.11: Verification of the time-varying behavior of I_{batt} on the estimation of ECM parameters.

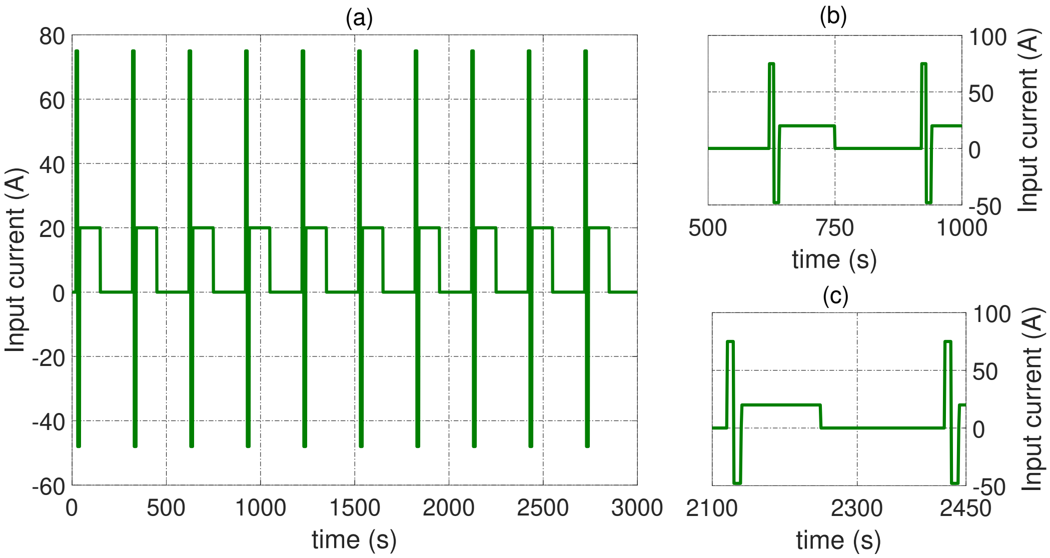

Figure 2.12: Corresponding input currents for the battery.

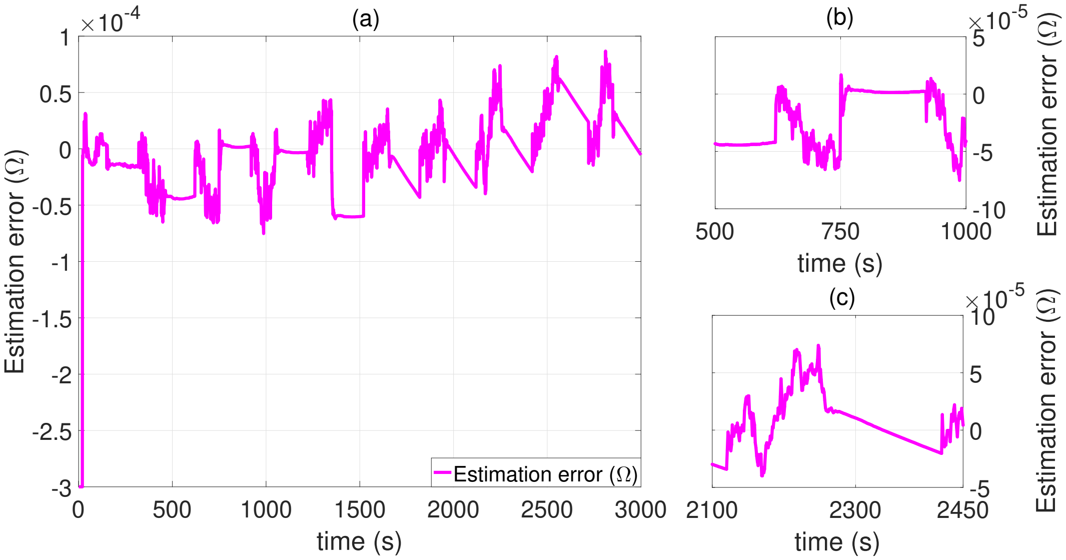

Figure 2.13: Estimation error of R_0.

On the other hand, three previously mentioned input currents are fed to the battery ECM in order to verify whether the input current value will influence the observability condition of battery capacity C_n estimation. Considering the effect of randomness in measurement noise, a simple quasi-Monte Carlo simulation test is conducted with 100 estimations. The estimation result based on eq. (2.24) is shown in Fig. 2.14. It confirms that a higher value of the battery input current improves the convergence speed of the battery capacity C_n estimation.

- Initial capacity value

In order to evaluate the effect of the battery capacity initial value, the estimator is initialised with three sets of different values, namely 17 Ah and 23 Ah, 18 Ah and 22 Ah, 19 Ah and 21 Ah. To minimize the randomness effect, the estimator is executed with 100 sets of synthetic data. The estimation result in Fig. 2.15 shows that a smaller initial value of C_n can guarantee a rapid convergence speed for tracking the reference value. This confirms the experimental results from [28] as shown in Fig. 2.16, where usable battery capacity estimation is executed with the extended battery model with joint/dual EKF estimation frameworks.

2.5.2 Evaluation of the new estimation structure

The effectiveness of the new structure will be verified in the following. Comparison with estimation results from the joint estimation frameworks composed of EKF or UKF respectively will be presented. Firstly, the characteristics of the noises are shown

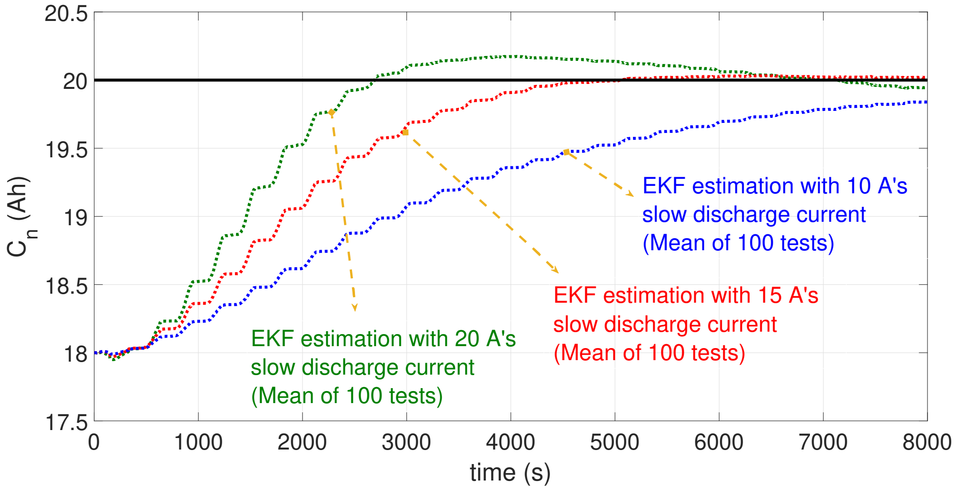

Figure 2.14: Battery input current level effect on battery capacity estimation.

in table 2.2, which are set according to the existing works and several tests. For the joint estimation frameworks based on eq. (2.24), the vector $\boldsymbol{x_0}$ will be used to initialise the EKF or UKF. In the new structure, the initial value of battery OCV is set to 3.5 V, and the other initial values are the same as in the vector $\boldsymbol{x}_0$.

First of all, as a specific term appeared in the new structure, the estimation result of OCV is shown in Fig. 2.17 and Fig. 2.18. Firstly, as it is shown in Fig. 2.17, the OCV estimation converges rapidly to the reference value, and can track the dynamic change of the battery OCV. Then, from the OCV estimation error in Fig. 2.18, KF is capable of providing an accurate estimation, which is important to connect the other two estimation modules based on EKF and UKF as shown in Fig. 2.9.

Then, the estimation results of the other parameters are shown in Fig. 2.19, Fig. 2.20, Fig. 2.21, Fig. 2.22 and Fig. 2.23. As it can be seen from Figs. 2.19, compared to joint EKF or joint UKF the main improvement with the new structure comes from the estimation of the battery capacity. Not only the convergence speed is more rapid, but also the estimation is less fluctuating and more accurate.

Furthermore, as for the computational cost, ten simulation tests are executed for these three monitoring algorithms. The current cycle duration for each test is 8500 s. The simulation was performed by using discrete-time model with a sampling period equal to 1 s, with Matlab/Simulink R2015b, on a desktop with an Intel Core i7-6700 CPU 3.4GHz and 8 Go RAM. The average calculation time of these ten simulation tests for each monitoring algorithm is listed in table 2.3.

However, this is only a general discussion of the computation load of the new proposed monitoring structure. Because the multi time-scale can also be introduced into the new structure, which means the sampling time period for the battery capacity can be extended to a larger value according to the application. For example, the

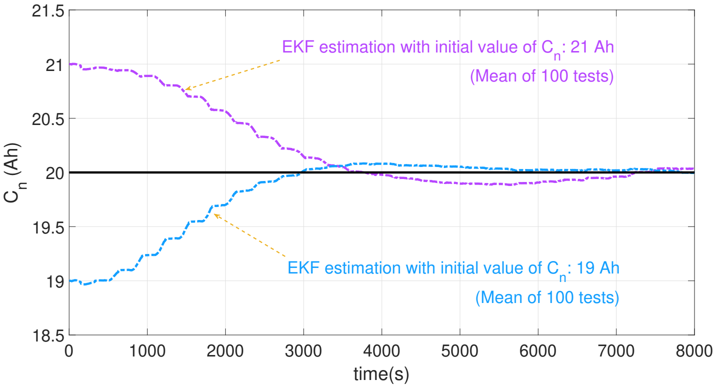

(a) Initial values of 19Ah and 21Ah

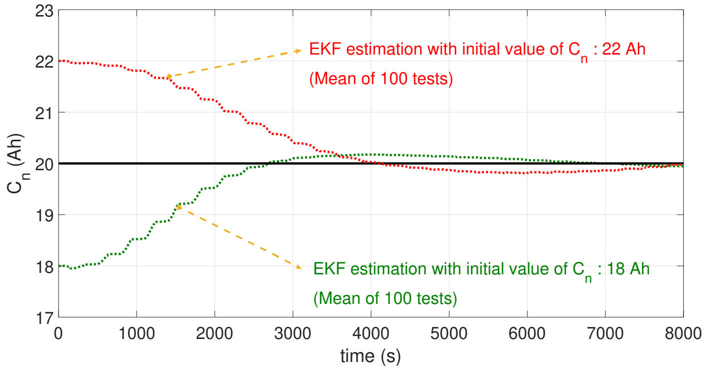

(b) Initial values of 18Ah and 22Ah

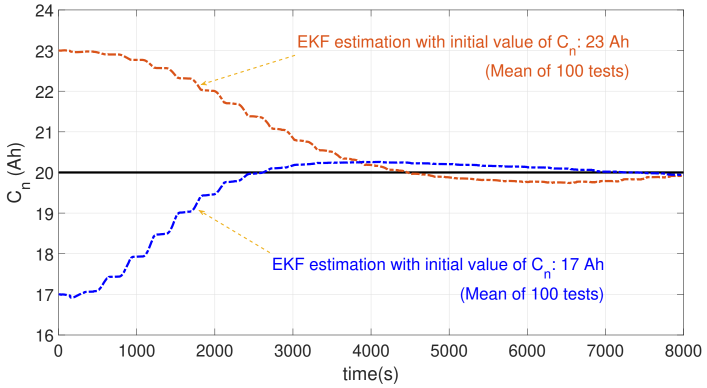

(c) Initial values of 17Ah and 23Ah

Figure 2.15: Initial capacity value effect on battery capacity estimation.

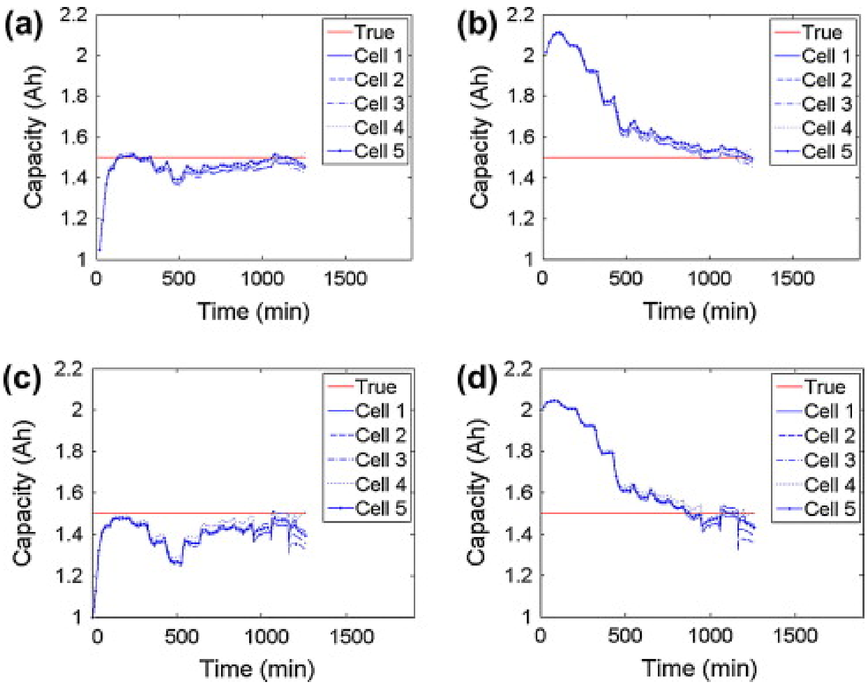

Figure 2.16: Experimental validation results of [28] for battery usable capacity estimation with the joint/dual estimation frameworks. (**a**),(**b**) are the capacity estimation result with dual estimation framework; (**c**),(**d**) are the capacity estimation result with joint estimation result. Both of these two experimental validations are tested with smaller (1 Ah) and larger (2 Ah) initial values in EKF than the true value of 1.5 Ah.

Table 2.2: Characteristics of the added noises

$\omega_1 \sim \mathrm{N}(0, 1 \times 10^{-8})$	$\gamma_1 \sim \mathrm{N}(0, 1 \times 10^{-7})$
$\omega_2 \sim \mathrm{N}(0, 1 \times 10^{-8})$	$\gamma_1 \sim \mathrm{N}(0, 1 \times 10^{-10})$
$\omega_3 \sim \mathrm{N}(0, 1 \times 10^{-9})$	$\delta \sim \mathrm{N}(0, 1 \times 10^{-4})$
$\omega_4 \sim \mathrm{N}(0, 1 \times 10^{-12})$	$\varepsilon_1 \sim \mathrm{N}(0, 1 \times 10^{-8})$
$\omega_5 \sim \mathrm{N}(0, 1 \times 10^{-10})$	$\varepsilon_2 \sim \mathrm{N}(0, 1 \times 10^{-8})$
$\omega_6 \sim \mathrm{N}(0, 1 \times 10^{-10})$	$\varepsilon_3 \sim \mathrm{N}(0, 1 \times 10^{-6})$
$\omega_7 \sim \mathrm{N}(0, 1 \times 10^{-10})$	$\psi \sim \mathrm{N}(0, 1 \times 10^{-6})$
$\upsilon \sim \mathrm{N}(0, 1 \times 10^{-6})$	

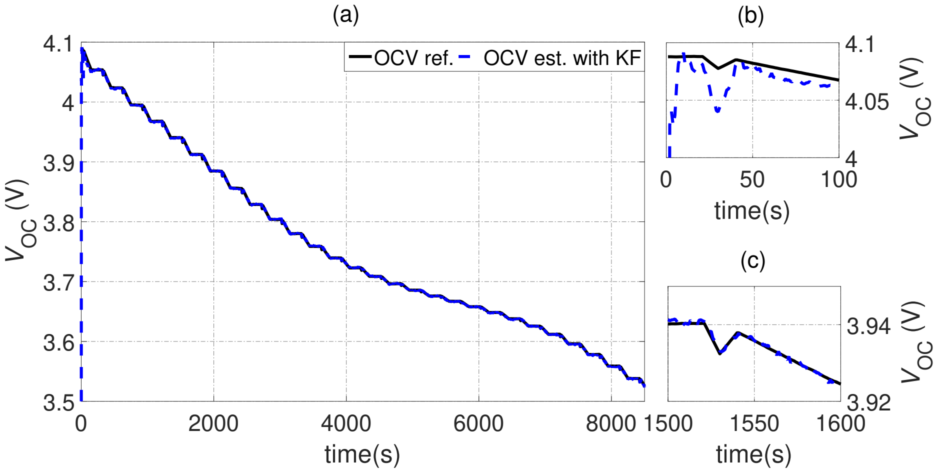

Figure 2.17: Estimation result of the battery OCV.

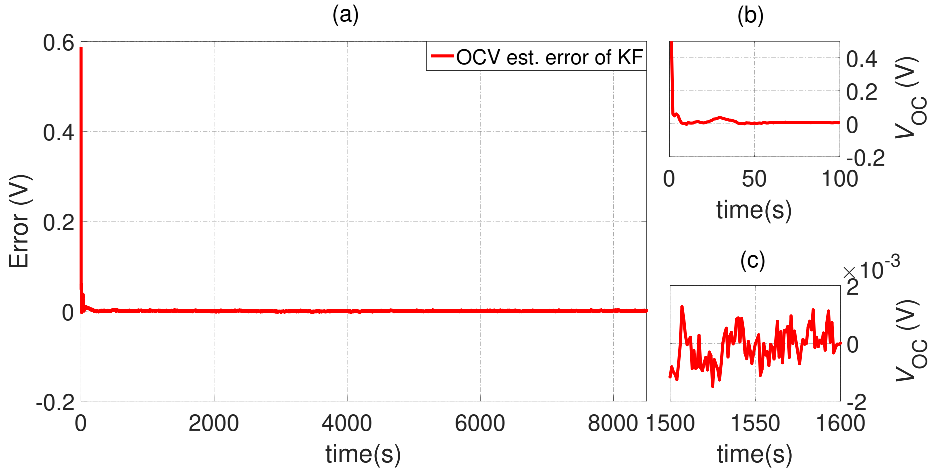

Figure 2.18: Estimation error of the battery OCV.

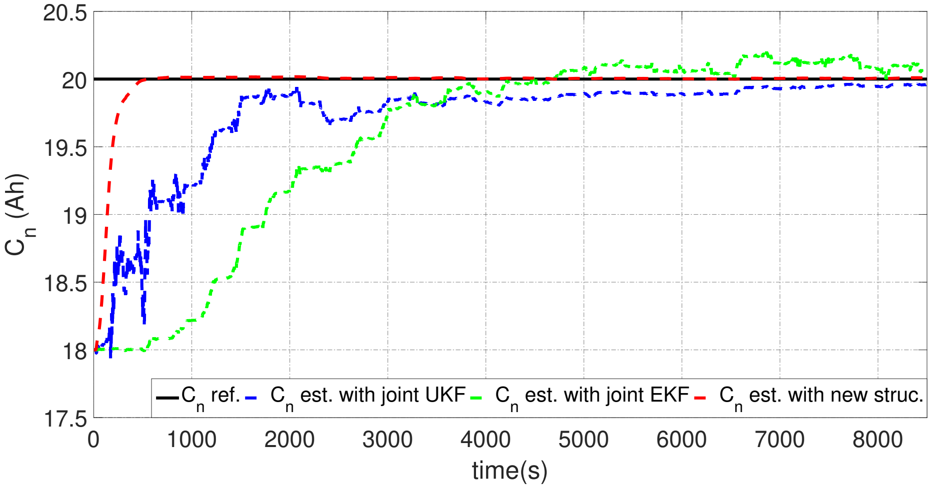

(a) Estimation result of $\mathrm{C_n}$

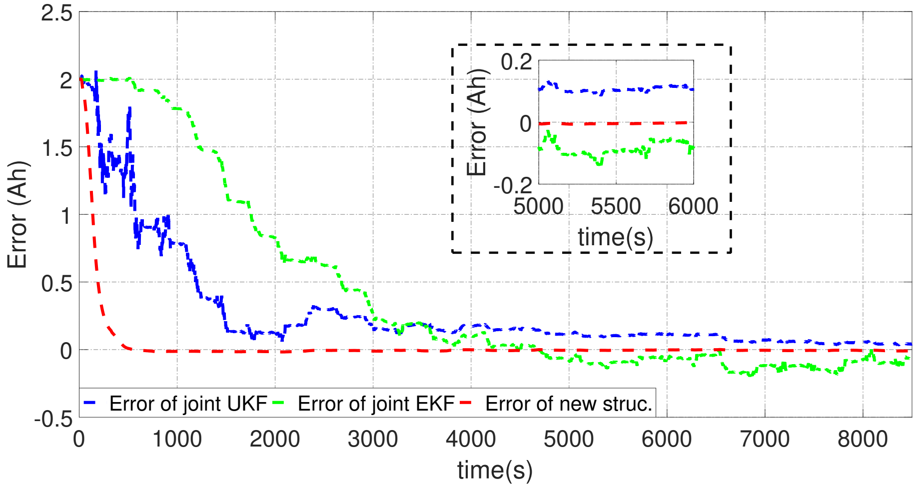

(b) Estimation error of $\mathrm{C_n}$

Figure 2.19: Comparison of estimation results with joint EKF, joint UKF and New structure ($\mathrm{C_n}$).

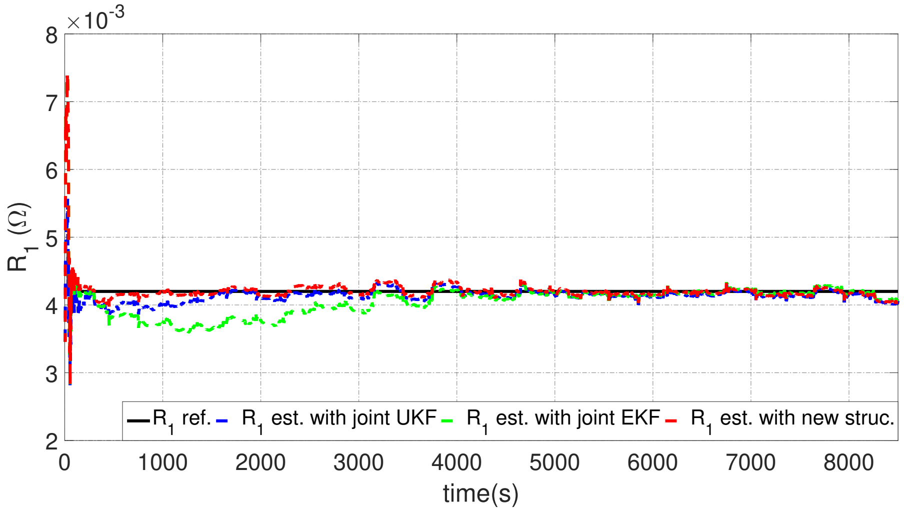

(a) Estimation result of R_1

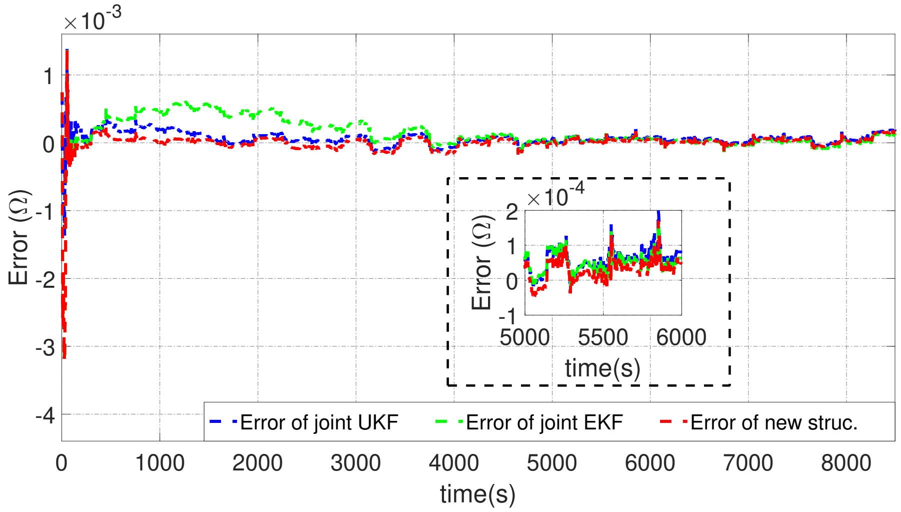

(b) Estimation error of R_1

Figure 2.20: Comparison of estimation results with joint EKF, joint UKF and New structure (R_1).

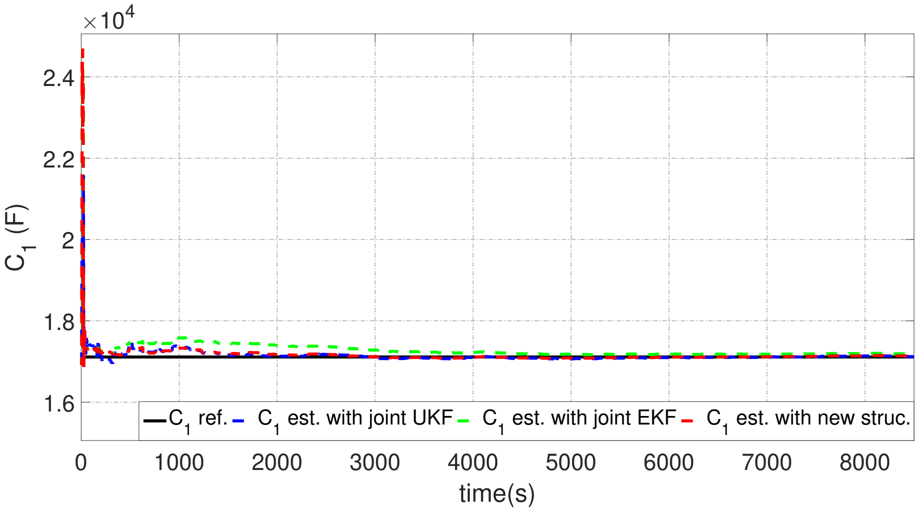

(a) Estimation result of C_1

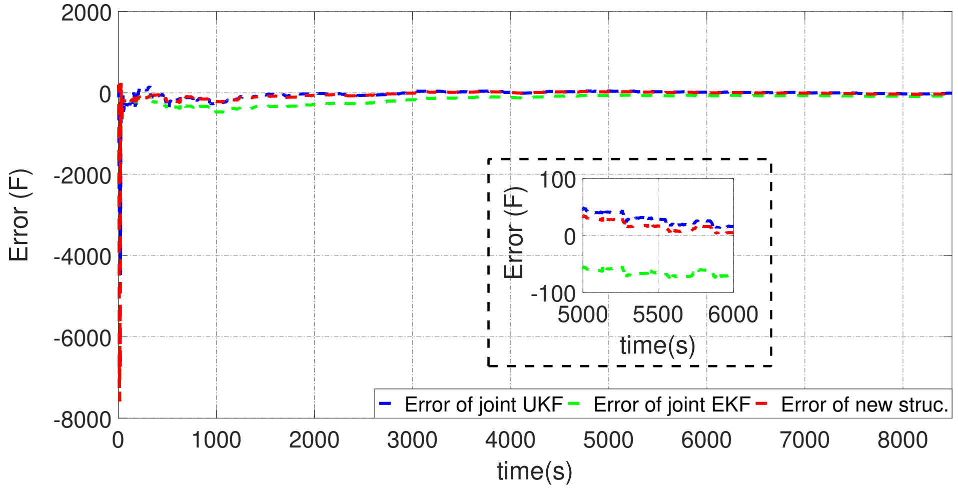

(b) Estimation error of C_1

Figure 2.21: Comparison of estimation results with joint EKF, joint UKF and New structure (C_1).

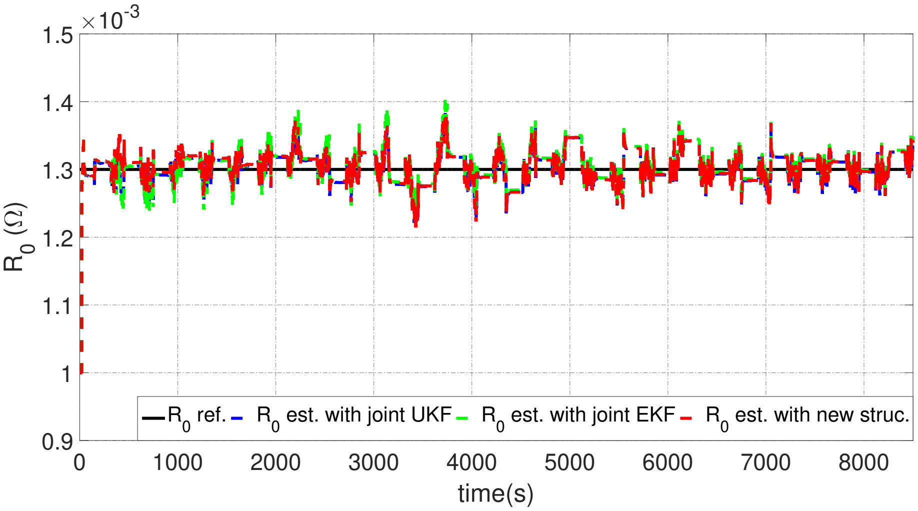

(a) Estimation result of R_0

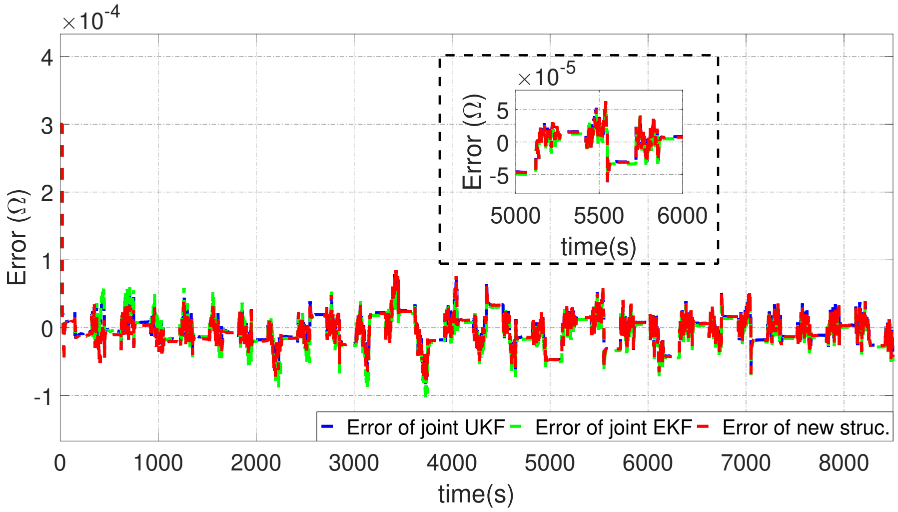

(b) Estimation error of R_0

Figure 2.22: Comparison of estimation results with joint EKF, joint UKF and New structure (R_0).

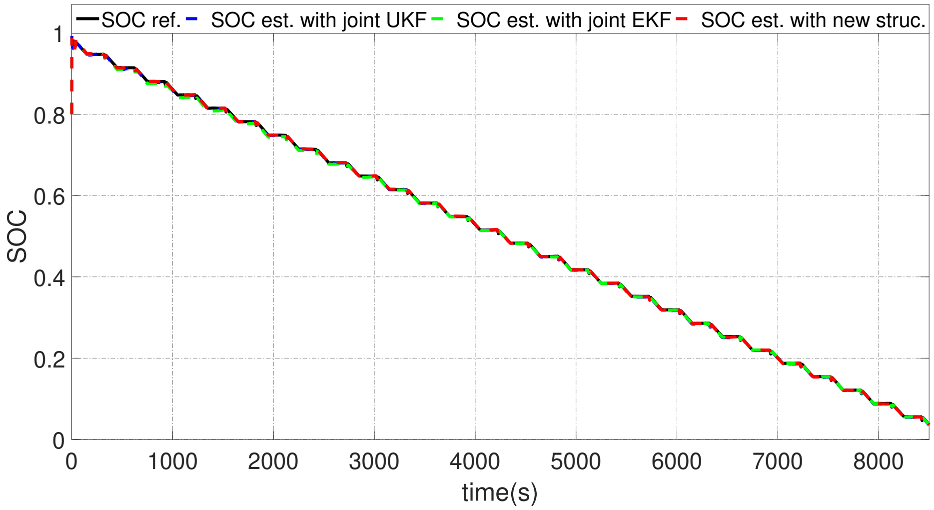

(a) Estimation result of SOC

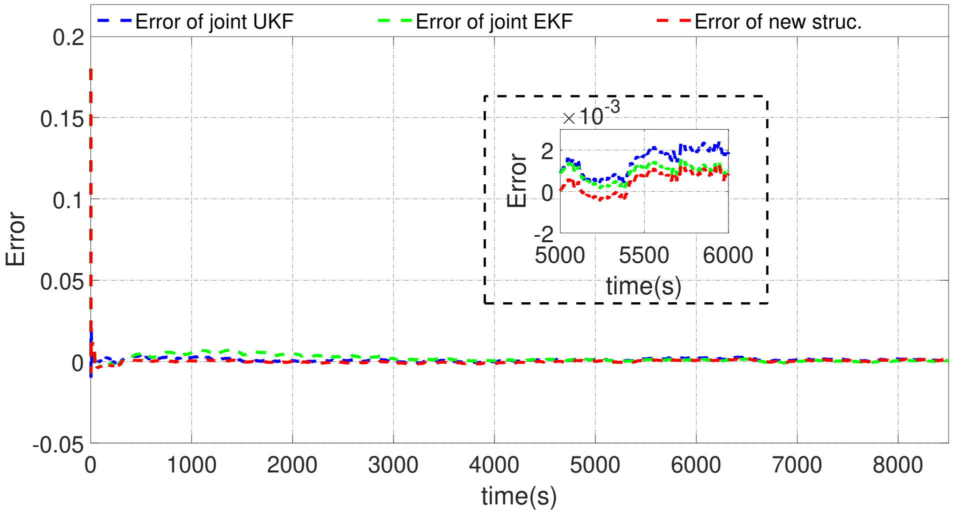

(b) Estimation error of SOC

Figure 2.23: Comparison of estimation results with joint EKF, joint UKF and New structure (SOC).

capacity estimation can even be performed quarterly or semiannually because of its slow time-varying property [135]. Thus, the new structure has similar computational loads than the traditional frameworks. Moreover, one potential advantage of the new structure should be pointed out. That is, working with multi time-scale, namely the usable battery capacity estimation part in Fig. 2.9 is executed with a longer sampling time, the battery ECM parameters can still be estimated and updated even when the battery capacity estimation is not activated.

Table 2.3: Computation efficiency of the new proposed monitoring structure.

	Joint EKF	Joint UKF	New structure
Average calculation time (s)	0.264	3.813	1.986

2.6 Conclusion

In this chapter, a new model-based battery monitoring framework is proposed. Firstly, the battery internal characteristic is fully used for the theoretical observability analysis. Namely, the independent characteristics of the battery states lead to a model decomposition. Thus, the original battery ECM has been decomposed into two sub-models. Each sub-model contains different battery states and parameters, hence each of them is extended in order to be analyzed. Therefore, after the nonlinear observability analysis, the necessary observability conditions are clearly listed for the battery ECM parameters and battery capacity.

Several key points for the battery state and parameter estimation based on the extended battery ECM are as: Firstly, the battery capacity estimation based on the extended ECM depends on $\left(\frac{\mathrm{d}V_{\mathrm{OC}}}{\mathrm{d}soc}\right)^2$, which induces the inherent weak observability. Secondly, smaller initial value of the battery capacity will guarantee a better local observability condition, which will consequently lead to a rapid convergence speed. Thirdly, the battery state and parameter estimation based on the extended ECM depend on the battery current, namely both the current amplitude and its time-varying behavior will affect the observability.

The proposed battery state and parameter estimation is still based on the extended battery model and well established estimation algorithms. The new proposed battery monitoring structure has extended the traditional battery diagnosis framework, namely joint estimation and dual estimation method. A new direction for the battery parameter grouping is proposed. Furthermore, the obtained battery parameter estimation conditions are important in practice, where a way of improving the battery state and parameter estimation is provided.

Chapter 3

Battery incipient short circuit diagnosis

3.1 Introduction

The safety operation of LIBs is of vital importance for the development of EVs. However, LIBs do have some potential safety issues that threat the reliable vehicle operation. As introduced previously, overcharge (OC), overdischarge (OD), internal short circuit (ISC) and external short circuit (ESC) are four common electrical abuse conditions that may lead to battery thermal runaway (TR) [5–7]. And TR is a catastrophic failure of on-board batteries [8]. Although researchers have never ceased to explore the mechanisms of TR, deep insight is still premature [9–11].

Therefore, the fault diagnosis and mitigation strategies for EVs' battery play a critical role. In other words, consistent effort is invested to prevent TR of on-board batteries. To this end, the EVs' battery, typically made with hundreds to thousands of cells, is completely controlled by a smart BMS. Monitoring and assessing the battery states such as SOC and SOH can not only essentially avoid the battery OC and OD, but also they can indirectly prevent the occurrence of thermal hazard [116, 135, 159].

Moreover, directly detecting the battery electrical abuse faults at an early stage can also prevent further deterioration. This is unfortunately challenging, because during the incubation period of TR, neither electrical nor thermal symptoms of the battery faulty conditions have significant difference from the normal one [5, 160]. Hence, the battery FDD has became a hotspot research topic in terms of BMS recently. In fact, short circuit (SC) under electrical abuse conditions, including both ESC and ISC, is an important stage before TR. While hard SC (mΩ magnitude of short resistances) will directly induce serious thermal hazard. Therefore, its detection results will be meaningless due to no time to take corresponding reaction [8]. On the contrary, soft SC (the value of the SC resistance should be evaluated with respective to the battery internal resistance, e.g. short resistances of 100/10/1 Ω) needs time to evolve into thermal accidents [8, 87]. Evidently, SC detection for the soft SC is more meaningful.

The SC detection can be, for instance, carried out by thermal analysis. In [161], a 3D electrochemical-thermal model is built to simulate various ISC scenarios and

ISC detection is addressed from a model parameterization and the parameter estimation perspective. In [162], residual-based battery thermal fault detection is achieved based on nonlinear observers and a two-state thermal model. However, from the aspect of security, the temperature-aware level fault often means that TR has been formed [160]. Hence, the battery SC diagnosis based on electrical signals, namely the measured battery current and voltage, is more popular. In [89,163], model-based ESC detection scheme is proposed using different models for faulty and healthy conditions, which are obtained from their conducted abuse experiments. In [164], a model-based switching model method is proposed to detect the ISC and quantitatively calculate the ISC resistance. In [160], soft SC diagnosis is executed with the help of remaining charging capacity variation inside battery pack. In [8], an ISC detection method for battery pack is proposed by identifying the parameters of cell difference model, where the voltage difference between each cell is described with a simplified ECM model. Furthermore, soft SC quantitative analysis is developed with the cell difference model and state estimation algorithm in [165].

Although the aforementioned research works have made remarkable progress in battery soft SC diagnosis and detection recently, more general solutions from the perspective of control-oriented work still need to be studied. That is, how to take advantage of the existing literature, including validated model and experimental information, to propose a general method of soft SC diagnosis is challenging.

To this end, this chapter is dedicated to battery soft SC detection, which is mainly carried out through a slightly modified battery ECM. The main contributions of this chapter are:

- Firstly, the traditional battery ECM is modified slightly by adding an equivalent SC resistance. Then, state-space representation for the battery SC model is introduced and used as a basis for applying a robust fault estimator, which is designed with linear-matrix-inequalities. Hence, the SC detection topic is converted to an estimation of the SC current flowing into the equivalent SC resistance.

- Furthermore, considering the nonlinear characteristic of the battery OCV curve, the concept of Takagi-Sugeno fuzzy model is introduced to propose a weighting function self-regulating observer for battery SC detection. The general idea is to use the robust observer design result for several different independent linear-time-invariant models. In addition, an optimization step for the membership function tuning is mandatory. Hence, genetic algorithm has been used for this optimization. The result is satisfying and the obtained membership functions are able to provide an optimal combination of the independent linear robust observers.

- Last but not least, considering the environment, modeling and measurement noise, accuracy of the SC estimation is a challenge. In other words, the fault signal is usually corrupted with noise, especially when the SC fault is at its earliest stage. For this typical challenge, the aforementioned model-based research work is combined with a method using statistical information. Namely, the obtained estimated SC current is treated as a time-series signal, and then, the Cumulative Sum method is used to detect the tiny change of the signal due to the incipient fault.

3.2 ECM with short circuit resistance

As shown in Fig. 3.1, both ISC and ESC can be described as a healthy battery ECM connected in parallel with an equivalent short resistance $\mathrm{R_{sc}}$. Therefore, for a battery cell whose internal resistance is usually in the level of mΩ , when $\mathrm{R_{sc}}$ lies in the following range 100/10/1 Ω, both ISC and ESC can be regarded as soft SC [8]. In fact, this modification is not baseless. In [166], it is proposed to simulate the battery self-discharge phenomenon, where a very high value of $1 \times 10^4 \Omega$ is used. Besides, this kind of structure has already been used to analyze the battery SC in recent years, including both ISC and ESC [8, 164, 167].

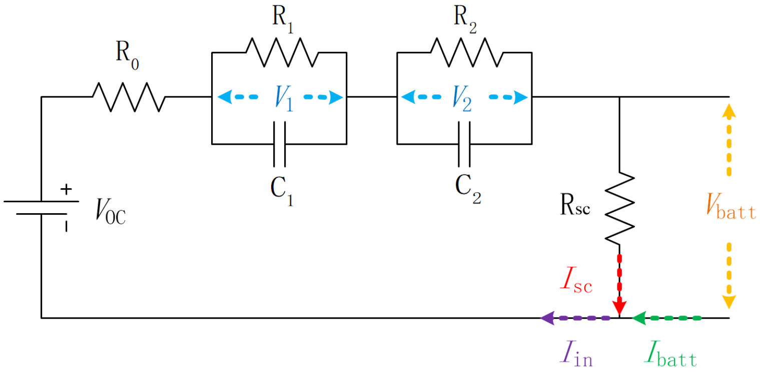

Figure 3.1: Battery ECM with SC resistance.

3.2.1 Model description

1. The resistor $\mathrm{R_0}$, double pair RC and voltage source V_{OC} have been described in the last chapter, and V_1, V_2 and V_{batt} have the same definition as before.

2. I_{batt} is the battery known input current, according to its reference direction in Fig. 3.1, "+" means discharging process, while "-" means charging process.

3. I_{sc} is the SC current through the equivalent SC resistance $\mathrm{R_{sc}}$. It is unidirectional and unknown in reality. Furthermore, its value is $I_{\mathrm{sc}} = \frac{V_{\mathrm{batt}}}{\mathrm{R_{sc}}}$.

4. According to the Kirchhoff's circuit law, $I_{\text{in}} = I_{\text{batt}} + I_{\text{sc}}$, which is the battery real input current with or without the battery fault. If $\mathrm{R_{sc}}$ approaches to infinity, then $I_{\text{sc}} \approx 0$ and $I_{\text{in}} \approx I_{\text{batt}}$. Therefore, the battery works in healthy conditions. Otherwise, the abnormal value of I_{sc} means the battery is exposed to the SC conditions, which could be induced by ISC or ESC.

3.2.2 Battery modeling

Firstly, as presented previously, the battery SOC can be modeled by eq. (1.1).

Therefore, using Kirchhoff's law, the battery dynamic model can be described by the following discrete state-space representation:

$$\begin{bmatrix} V_1(k+1) \\ V_2(k+1) \\ soc(k+1) \end{bmatrix} = \boldsymbol{A} \begin{bmatrix} V_1(k) \\ V_2(k) \\ soc(k) \end{bmatrix} + \boldsymbol{B} I_{\text{in}}(k) \tag{3.1}$$

$$V_{\text{batt}}(k) = V_{\text{OC}}(soc) - V_1(k) - V_2(k) - \mathrm{R}_0 I_{\text{in}}(k)$$

where,

$$\boldsymbol{A} = \begin{bmatrix} \mathrm{e}^{\frac{-T}{\mathrm{R_1C_1}}} & 0 & 0 \\ 0 & \mathrm{e}^{\frac{-T}{\mathrm{R_2C_2}}} & 0 \\ 0 & 0 & 1 \end{bmatrix}, \quad \boldsymbol{B} = \begin{bmatrix} \mathrm{R}_1 \cdot (1 - \mathrm{e}^{\frac{-T}{\mathrm{R_1C_1}}}) \\ \mathrm{R}_2 \cdot (1 - \mathrm{e}^{\frac{-T}{\mathrm{R_2C_2}}}) \\ \frac{-\eta T}{\mathrm{C_n}} \end{bmatrix}$$

Eq. (3.1) is obtained with the zero-order hold approximation under the assumption that the current I_{in} is constant between two adjacent sampling points. The sampling period, $T = 1$ s in this study, which is compliant with the battery internal dynamics and the used setting in the literature [13, 116, 120, 130, 158].

3.3 Robust state and fault estimator design

3.3.1 Linear OCV-SOC case

Firstly, the linear OCV-SOC case is considered. Namely, the OCV-SOC curve can be approximated with $V_{\text{OC}}(soc) = a \cdot soc + b$, where a and b are constant.

Therefore, due to the relationship $I_{\text{in}} = I_{\text{batt}} + I_{\text{sc}}$, the mathematical representation of the battery ECM with SC resistance can be arranged as:

$$\begin{aligned} \boldsymbol{x}(k+1) &= \boldsymbol{A}\boldsymbol{x}(k) + \boldsymbol{B} I_{\text{batt}}(k) + \boldsymbol{B_f} I_{\text{sc}}(k) \\ y(k) &= \boldsymbol{C}\boldsymbol{x}(k) + D I_{\text{batt}}(k) + D_f I_{\text{sc}}(k) \end{aligned} \tag{3.2}$$

where, $\boldsymbol{B_f} = \boldsymbol{B}$; $\boldsymbol{C} = [-1 \quad -1 \quad a]$; $D = D_f = -\mathrm{R}_0$. Besides, state vector is $\boldsymbol{x}(k) = [V_1(k), V_2(k), soc(k)]'$; model output is $y(k) = V_{\text{batt}}(k) - b$.

Hence, based on (3.2), the objective is very clear now. Advanced observer will be employed to achieve the purpose of battery SC detection, namely, estimating the battery unknown fault I_{sc}.

According to (3.2), the design process of battery SC detection observer is discussed based on the existing work [168]. Firstly, as shown in (3.3), battery SC model (3.2) can be further generalized to a state-space representation. Namely, considering the modeling error and the measurement noise in an EV environment, both state equations and output equation will be studied with bounded disturbance.

$$\begin{aligned} \boldsymbol{x}(k+1) &= \boldsymbol{A}\boldsymbol{x}(k) + \boldsymbol{B}u(k) + \boldsymbol{B_f} f(k) + \boldsymbol{B_d} d(k) \\ y(k) &= \boldsymbol{C}\boldsymbol{x}(k) + Du(k) + D_f f(k) + D_d d(k) \end{aligned} \tag{3.3}$$

where, $\boldsymbol{x}(k) \in \mathbb{R}^n$ is the state vector; $y(k) \in \mathbb{R}^p$ is the output; $u(k) \in \mathbb{R}^m$ is the known input, which corresponds to I_{batt}; $f(k) \in \mathbb{R}^{n_f}$ is the so-called fault, which corresponds to I_{sc}; $d(k) \in \mathbb{R}^{n_d}$ is the disturbance that belongs to $\mathrm{L}_2[0, \infty)$; $\boldsymbol{B_d}$ and D_d are constant real matrices of appropriate dimensions.

Furthermore, the SC detection observer (3.4) is designed under the form of a proportional-integral observer. Not only the integral term can guarantee a robust state estimation at fault occurrence, but also it can provide fault estimation simultaneously [169].

$$\begin{aligned} &\hat{\boldsymbol{x}}(k+1) = \boldsymbol{A}\hat{\boldsymbol{x}}(k) + \boldsymbol{B}u(k) + \boldsymbol{B_f}\hat{f}(k) - \boldsymbol{L} \cdot (\hat{y}(k) - y(k)) \\ &\hat{f}(k+1) = \hat{f}(k) - F \cdot (\hat{y}(k) - y(k)) \\ &\hat{y}(k) = \boldsymbol{C}\hat{\boldsymbol{x}}(k) + Du(k) + D_f\hat{f}(k) \end{aligned} \tag{3.4}$$

where $\hat{\boldsymbol{x}}(k) \in \mathbb{R}^n$ is the estimated state vector; $\hat{y}(k) \in \mathbb{R}^p$ is the observer output; $\hat{f}(k) \in \mathbb{R}^{n_f}$ is the estimated $f(k)$; $\boldsymbol{L} \in \mathbb{R}^{n \times p}$ is the gain vector of states; $F \in \mathbb{R}^{n_f \times p}$ is the fault gain.

Therefore, the dynamics error between model (3.3) and observer (3.4) can be described as (3.5), where $\boldsymbol{e_x}(k) = \hat{\boldsymbol{x}}(k) - \boldsymbol{x}(k), e_f(k) = \hat{f}(k) - f(k)$; and $\Delta f(k) = f(k+1) - f(k)$ belongs to $l_2[0, \infty)$. I_i is the symbol of identity matrix with $i \times i$ dimension. 0 is zero matrix with corresponding dimension.

$$\begin{bmatrix} \boldsymbol{e_x}(k+1) \\ e_f(k+1) \end{bmatrix} = \begin{bmatrix} \boldsymbol{A} - \boldsymbol{L}\boldsymbol{C} & \boldsymbol{B_f} - \boldsymbol{L}D_f \\ -F\boldsymbol{C} & I_{n_f} - FD_f \end{bmatrix} \begin{bmatrix} \boldsymbol{e_x}(k) \\ e_f(k) \end{bmatrix} + \begin{bmatrix} \boldsymbol{L}D_d - \boldsymbol{B_d} & 0 \\ FD_d & -I_{n_f} \end{bmatrix} \begin{bmatrix} d(k) \\ \Delta f(k) \end{bmatrix} \tag{3.5}$$

Besides, in order to facilitate the design process. Let

$$\bar{\boldsymbol{A}}_D = \begin{bmatrix} \boldsymbol{A} & \boldsymbol{B_f} \\ 0_{n_f \times n} & I_{n_f} \end{bmatrix}, \bar{\boldsymbol{B}}_d = \begin{bmatrix} \boldsymbol{B_d} & 0_{n \times n_f} \\ 0_{n_f \times n_d} & I_{n_f} \end{bmatrix}$$

$$\bar{\boldsymbol{C}} = \begin{bmatrix} \boldsymbol{C} & D_f \end{bmatrix}, \quad \bar{\boldsymbol{D}}_d = \begin{bmatrix} D_d & 0_{p \times n_f} \end{bmatrix}$$

$$\bar{\boldsymbol{e}}(k) = \begin{bmatrix} \boldsymbol{e_x}(k) \\ e_f(k) \end{bmatrix}, \quad \bar{\boldsymbol{v}}_D(k) = \begin{bmatrix} d(k) \\ \Delta f(k) \end{bmatrix}$$

Hence, (3.5) can be further expressed more generally as (3.6), where $\bar{\boldsymbol{L}} = \begin{bmatrix} \boldsymbol{L} & F \end{bmatrix}'$ contains the proportional and integral gains of the observer.

$$\bar{\boldsymbol{e}}(k+1) = (\bar{\boldsymbol{A}}_D - \bar{\boldsymbol{L}}\bar{\boldsymbol{C}})\bar{\boldsymbol{e}}(k) + (\bar{\boldsymbol{L}}\bar{\boldsymbol{D}}_d - \bar{\boldsymbol{B}}_d)\bar{\boldsymbol{v}}_D(k) \tag{3.6}$$

The key of designing the SC detection observer is how to determine $\bar{\boldsymbol{L}}$, namely, a set of proper gains that will make the error dynamics (3.6) satisfy the following two objectives [168]:

- $(\bar{\boldsymbol{A}}_D - \bar{\boldsymbol{L}}\bar{\boldsymbol{C}})$ is Hurwitz stable, its eigenvalues are inside the unit circle for discrete-time system.
- the fault estimation error $e_f(k)$ is insensitive to the term $\bar{\boldsymbol{v}}_D(k)$, namely, $e_f(k)$ is as small as possible. It can be expressed with H_∞-norm with a given $\gamma > 0$ as:

$$\sup \frac{\|e_f(k)\|_2}{\|\bar{v}_D(k)\|_2} < \gamma \tag{3.7}$$

In order to achieve the aforementioned objectives, a multi-constrained design method is proposed in [168]. The main proof process is rearranged in Annex. However, main results are shown directly in **Theorem 3.3.1**, which will be used to design the SC detection observer.

Theorem 3.3.1. *Let a prescribed H_∞ performance level γ and a circular region $\mathscr{D}(\alpha, r)$ be given. If there exist two symmetric positive definite matrices $\bar{\boldsymbol{P}}_1$, $\bar{\boldsymbol{P}}_2$ $\in \mathbb{R}^{(n+n_f)\times(n+n_f)}$ and two matrices $\bar{\boldsymbol{S}} \in \mathbb{R}^{(n+n_f)\times(n+n_f)}$, $\bar{\boldsymbol{Y}} \in \mathbb{R}^{(n+n_f)\times p}$ such that the following conditions hold:*

$$\begin{bmatrix} \bar{\boldsymbol{M}} & \bar{\boldsymbol{N}} & \bar{\boldsymbol{Y}}\bar{\boldsymbol{D}}_d - \bar{\boldsymbol{S}}\bar{\boldsymbol{B}}_d & 0 \\ * & -\bar{\boldsymbol{P}}_1 & 0 & \bar{I}_{n_f} \\ * & * & -\gamma I_{(n_d+n_f)} & 0 \\ * & * & * & -\gamma I_{n_f} \end{bmatrix} < 0 \tag{3.8}$$

and

$$\begin{bmatrix} -\bar{\boldsymbol{S}} - \bar{\boldsymbol{S}}' + \bar{\boldsymbol{P}}_2 & \bar{\boldsymbol{S}}\bar{\boldsymbol{A}}_D - \bar{\boldsymbol{Y}}\bar{\boldsymbol{C}} - \alpha\bar{\boldsymbol{S}} \\ * & -r^2\bar{\boldsymbol{P}}_2 \end{bmatrix} < 0 \tag{3.9}$$

where $\bar{I}_{n_f} = \begin{bmatrix} 0_{n\times n_f} \\ I_{n_f} \end{bmatrix}$, $\bar{\boldsymbol{M}} = -\bar{\boldsymbol{S}} - \bar{\boldsymbol{S}}' + \bar{\boldsymbol{P}}_1$; $\bar{\boldsymbol{N}} = \bar{\boldsymbol{S}}\bar{\boldsymbol{A}}_D - \bar{\boldsymbol{Y}}\bar{\boldsymbol{C}}$; *"*" represents the matrix's symmetric term. Then error dynamics (3.6) satisfies the* H_∞ *performance index* $\|e_f(k)\|_2 < \gamma\|\bar{v}_D(k)\|_2$, *the eigenvalues of* $(\bar{\boldsymbol{A}}_D - \bar{\boldsymbol{L}}\bar{\boldsymbol{C}})$ *belong to* $\mathscr{D}(\alpha, r)$, *and the gain matrix* $\bar{\boldsymbol{L}}$ *is given by* $\bar{\boldsymbol{L}} = \bar{\boldsymbol{S}}^{-1}\bar{\boldsymbol{Y}}$.

To be short, the SC observer design is subject to two linear-matrix-inequalities (LMIs). The H_∞ performance and regional pole constraint constitute the so-called multi-constrained design method [168]. Besides, the minimum H_∞ attenuation level can be obtained simultaneously by minimizing γ subject to (3.8) and (3.9). The SC detection observer performance is adjusted by tuning the circular region $\mathscr{D}(\alpha, r)$.

3.3.2 Nonlinear OCV-SOC case

Due to the non-linearity of OCV-SOC curve, the battery output can be nonlinear. However, the battery can be described as a linear time-invariant (LTI) model in several SOC intervals. Therefore, inspired by the concept of Takagi-Sugeno (TS) fuzzy system, a systematic way to blend the linear intervals of OCV-SOC curve and build the weighting function self-regulating fault estimator is proposed.

The principle of TS fuzzy system, including modeling and observer/controller design process, is to study nonlinear systems by a set of local LTI models [30]. In the meanwhile, an interpolation mechanism among these models based on nonlinear weighting functions, namely the membership functions (MFs), is used to fuse all the linear subsystems [170]. Hence based on the fuzzy If-Then rules, instead of giving a single output value or an output action as in the traditional Mamdani-type fuzzy inference system, the output of TS fuzzy system is a polynomial function [171]. The concept of TS fuzzy system has been used in various applications such as speed sensor fault tolerant controller design [172], robust controller design for multi-sources energy management [30], classification and regression [171], continuous chaotic system [173] and wind turbines [174]. The general design process in our work is shown in Fig. 3.2, and details will be explained as follows.

3.3.2.1 Fuzzification of OCV-SOC curve

The flowchart presented in Fig. 3.3 illustrates the fuzzification process of battery OCV-SOC curve:

- Fig. 3.3(b): we consider g ($g \in \mathbb{N}$ and $g \geq 2$) linear segments from the OCV-SOC curve and fit the corresponding mathematical expression for each linear

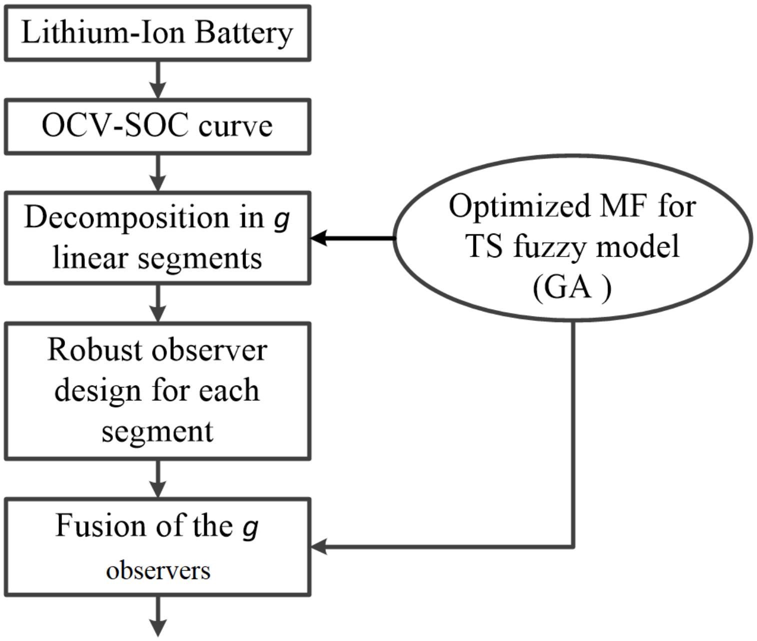

Figure 3.2: Flowchart for robust observer design.

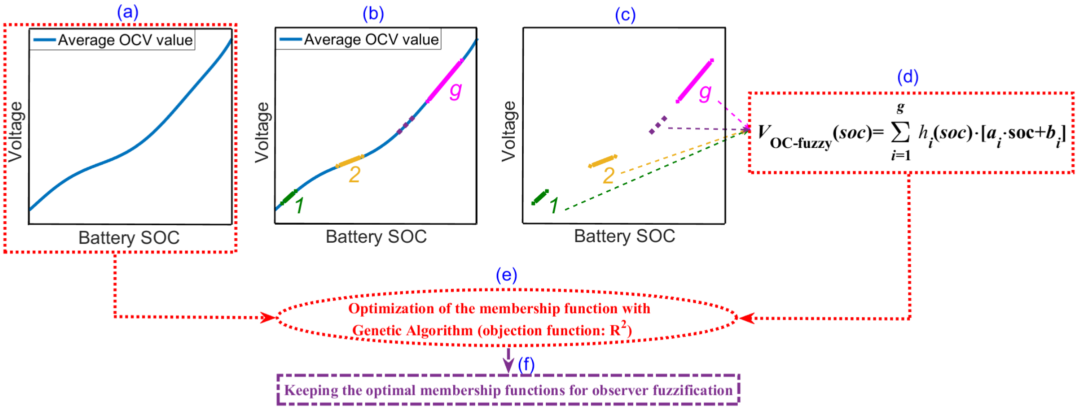

Figure 3.3: Flowchart of the fuzzification process of battery OCV-SOC curve

segment as (3.10). Note that the determination of g depends on the degree of nonlinearity of OCV-SOC curve.

$$V_{\mathrm{OC}i}(soc) = a_i \cdot soc + b_i,\ (i = 1, \dots, g) \tag{3.10}$$

It is important to notice that the linear segments do not need to be contiguous. This approach has two main advantages. Firstly, the model is much simpler compared to the classical one which uses a small discretization step [175]. Secondly, the model is more robust because it does not require strong approximation on the linearity of the whole curve.

- Fig. 3.3(c): a MF should be distributed to each linear segment based on the main idea of TS fuzzy system. In other words, each linear segment contributes to the global nonlinear behavior of OCV-SOC curve through a weighting function $\xi(soc)$ [176]. Furthermore, in order to have a smooth transition among different linear segments, ξ is selected as Gaussian type [177]. As a result, $\xi(soc)$ is determined by the mean μ and the variance σ^2. Hence, for any value of SOC, it is supposed that

$$\xi_i(soc) \geq 0 \text{ and } \sum_{i=1}^{g} \xi_i(soc) > 0,\ (i = 1, \dots, g)$$

- Fig. 3.3(d): after the above two steps, the OCV-SOC curve can be expressed as (3.11).

$$V_{\text{OC-fuzzy}}(soc) = \sum_{i=1}^{g} h_i(soc) \cdot [a_i \cdot soc + b_i] \tag{3.11}$$

where, $h_i(soc) = \frac{\xi_i(soc)}{\sum_{i=1}^{g} \xi_i(soc)}$. Hence, for any value of SOC, $h_i(soc)$ satisfies

$$h_i(soc) \geq 0 \text{ and} \sum_{i=1}^{g} h_i(soc) = 1,\ (i = 1, \dots, g)$$

- Fig. 3.3(e): selecting the optimal parameter pair $(\mu_i, {\sigma_i}^2)$ $(i = 1, \dots, g)$ for each MF ξ_i $(i = 1, \dots, g)$ is necessary. In essence, the optimization problem eventually becomes a problem similar to curve fitting. Therefore, coefficient of determination, R^2, used as the optimization criterion is formulated in (3.12).

$$\mathrm{R}^2 = 1 - \frac{\sum_{i=1}^{n_{\mathrm{ocv}}} \left[V_{\mathrm{OC}}(soc) - V_{\text{OC-fuzzy}}(soc)\right]^2}{\sum_{i=1}^{n_{\mathrm{ocv}}} \left[V_{\mathrm{OC}}(soc) - \bar{V}_{\mathrm{OC}}(soc)\right]^2} \tag{3.12}$$

where: $\bar{V}_{\mathrm{OC}}(soc) = \frac{1}{n_{\mathrm{ocv}}} \sum_{i=1}^{n_{\mathrm{ocv}}} [V_{\mathrm{OC}}(soc)]$;

n_{ocv} is the number of data points used in the optimization process;

$V_{\mathrm{OC}}(soc)$ is the original average OCV-SOC data as shown in Fig. 3.3(a).

Finally, as indicated in Fig. 3.3(f), the obtained optimal membership functions after the optimization process will be used later for the observer fusion.

3.3.2.2 Fuzzification of robust observers

Hence, according to the previously presented method, a robust observer is built firstly for each selected linear segment. Namely, the gain vector $\bar{\boldsymbol{L}}_i = \begin{bmatrix} \boldsymbol{L}_i & F_i \end{bmatrix}'$ $(i = 1, \ldots, g)$ for each sub-observer is determined. Then, based on (3.4), g linear robust observers can be blended directly as (3.13), where the subscript $(\cdot)_{\text{fuzzy}}$ represents the elements of TS fuzzy observer.

$$\begin{aligned} \hat{\boldsymbol{x}}_{\text{fuzzy}}(k+1) &= \textstyle\sum_{i=1}^{g} h_i(\widehat{soc}_{\text{fuzzy}}(k))\,[\boldsymbol{A}\,\hat{\boldsymbol{x}}_{\text{fuzzy}}(k) + \boldsymbol{B}u(k) + \boldsymbol{B_f}\hat{f}_{\text{fuzzy}}(k) \\ &\qquad\qquad\qquad\qquad -\boldsymbol{L}_i \cdot (\hat{y}_{\text{fuzzy}}(k) - y(k))] \\ \hat{f}_{\text{fuzzy}}(k+1) &= \textstyle\sum_{i=1}^{g} h_i(\widehat{soc}_{\text{fuzzy}}(k)) \left[\hat{f}_{\text{fuzzy}}(k) - F_i \cdot (\hat{y}_{\text{fuzzy}}(k) - y(k))\right] \\ \hat{y}_{\text{fuzzy}}(k) &= \textstyle\sum_{i=1}^{g} h_i(\widehat{soc}_{\text{fuzzy}}(k)) \left[\boldsymbol{C}\hat{\boldsymbol{x}}_{\text{fuzzy}}(k) + Du(k) + D_f\hat{f}_{\text{fuzzy}}(k)\right] \end{aligned} \tag{3.13}$$

Two important points should be pointed out. Firstly, according to the TS fuzzy system design method, the optimal MFs for different linear observers are exactly the same one as the fuzzification process of battery OCV-SOC curve [170]. Hence, the schema given in Fig. 3.4 clearly resumes this relationship.

Secondly, $\frac{\mathrm{d}soc}{\mathrm{d}t} \approx 0$ has been proven both in theory and practice [178,179]. Namely, the slowly changing characteristic of SOC makes $\widehat{soc}_{\text{fuzzy}}(k+1) \approx \widehat{soc}_{\text{fuzzy}}(k)$, where $\widehat{soc}_{\text{fuzzy}}(k)$ is included in the estimated state vector $\hat{\boldsymbol{x}}_{\text{fuzzy}}(k)$. Therefore, $\widehat{soc}_{\text{fuzzy}}(k)$ is the so-called fuzzy variable in the TS fuzzy observer for battery ECM, and the obtained TS fuzzy observer is, in essence, a weighting function self-regulating robust observer. The obtained TS fuzzy observer is schematically represented in Fig. 3.5.

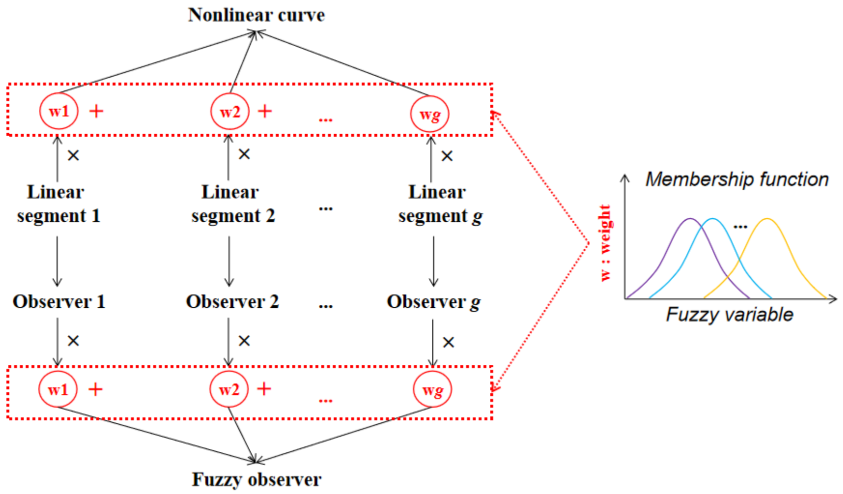

Figure 3.4: Identical MFs for modelling and observer design process.

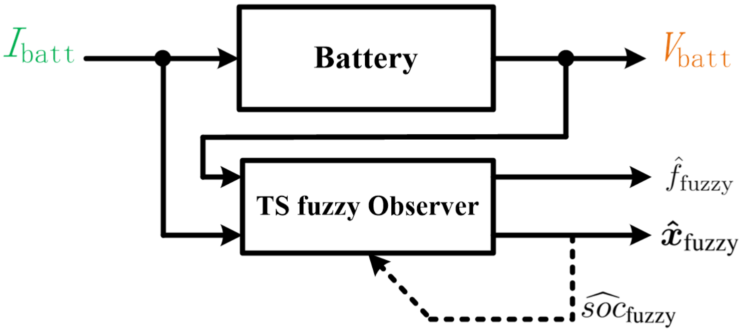

Figure 3.5: Weight function self-regulating state and fault estimator.

3.4 Numerical verification

Numerical simulations of the TS fuzzy fault estimator will be given in this section based on a SAMSUNG ICR 18650-22P LIB cell [15]. Its basic electrical characteristics are summarized in table 3.1.

Table 3.1: Electrical characteristics of SAMSUNG ICR 18650-22P cell

Nominal capacity	2150 mAh
Nominal voltage	3.6 V
Charging cut-off voltage (100% SOC)	4.2±0.05 V
Discharging cut-off voltage (0% SOC)	2.75 V
Maximum charge current	2150 mA
Maximum discharge current	10 A

Furthermore, the used battery ECM parameters for SAMSUNG ICR 18650-22P LIB cell are shown in table 3.2. All the parameters are obtained at 20 ^{o}C, where details can be found in [15].

In addition, according to our research interest and the electrical characteristics of SAMSUNG ICR 18650-22P LIB cell, the input current for battery ECM is taken and adapted from the real experimental EV as shown Fig. 3.6, which has been presented in the first chapter.

However, the details of the powertrain structure is rewritten here. The studied vehicle is a 698 kg (mass without passengers) heavy quadricycle equipped with a single ratio gearbox, a differential and two driven-wheels [14]. The traction subsystem is composed by a three-phase bidirectional converter connected to a 15 kW induction machine which is coupled to the driving wheels [26]. As for the energy storage subsystem, a 16 kW, 40-60 V, PEMFC is connected trough unidirectional DC-DC boost

Table 3.2: SAMSUNG ICR 18650-22P LIB cell parameters

R_0 (Ω)	0.0395
R_1 (Ω)	0.0107
R_2 (Ω)	0.0031
C_1 (F)	4721.2
C_2 (F)	17288
C_n (mAh)	2150
$V_{OC}(soc)$	$-0.6195soc^4 + 1.0899soc^3 - 0.3539soc^2 + 0.6196soc + 3.2354$

Figure 3.6: Tazzari Zero electric vehicle of university of Lille 1 [14]

converter. A 80 V- 40 Ah LFP battery pack is directly connected to the DC bus. The battery pack is composed of 4 series connected battery modules, where each battery module is composed by 6 series connected battery cells. Furthermore, each battery cell has the nominal voltage of 3.6 V, minimal voltage of 2.5 V and maximum voltage of 4.2 V. In addition, a simple EMS thermostat (on/off)) strategy is applied for the presented FC/battery hybrid system.

Ignoring the impact of its energy management strategy, we only focus on the battery current response. Therefore, in order to simulate the typical operating condition of battery, WLTC2 is selected as test cycle for this EV. Its speed profile and the corresponding battery response adapted to SAMSUNG ICR 18650-22P LIB cell are shown in Fig. 3.7.

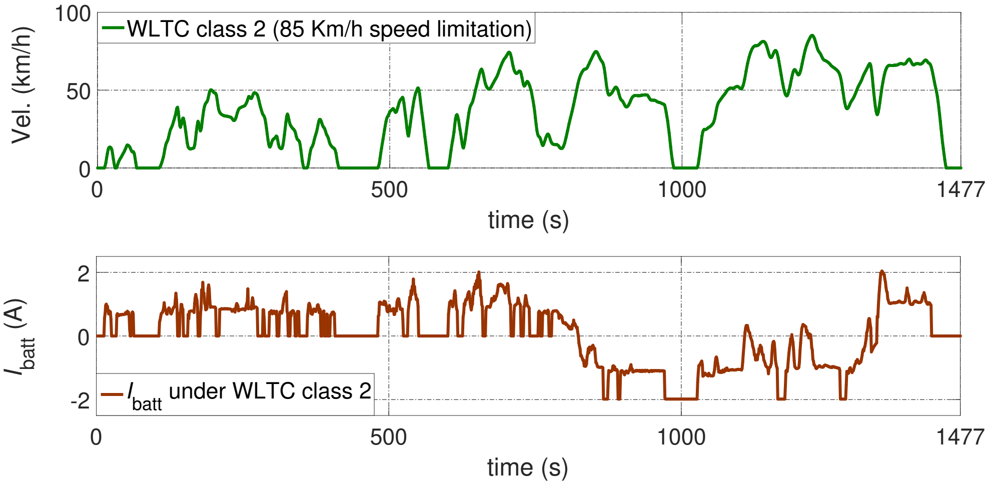

Figure 3.7: EV test cycle and the corresponding adapted EV battery cell current response.

Besides, the statistical information of the disturbance refers to [13]. Namely, the process and measurement noises are independent additive white Gaussian noises. Their variances are 1×10^{-8} and 3.6×10^{-5} respectively. Therefore, in order to determine the disturbance mapping matrices $\boldsymbol{B_d}$ and D_d, the disturbance term d is supposed to follow the standard normal distribution with a variance of 1. Hence, $\boldsymbol{B_d} = \left[1 \times 10^{-4}, 1 \times 10^{-4}, 1 \times 10^{-4}\right]'$ and $D_d = 0.006$ consequently [13].

3.4.1 Short circuit effect

Firstly, with 24 cycles of WLTC 2, the healthy battery electrical response and the battery electrical response under different soft SC conditions are shown in Fig. 3.8. Different soft SC resistances, 10 Ω, 50 Ω and 100 Ω, are respectively introduced to the battery ECM in the middle of the total test time (35448s).

As it can be observed from Fig. 3.8, the battery electrical behavior under soft SC conditions looks like a healthy battery. Because both voltage and SOC are in the normal operation region according to table 3.1. But such electrical abuse does threat the battery's safety and reliability. Especially when the battery is controlled in the close loop EV power supply system, the battery SOC will be forcibly pulled back to the so-called normal range that distributed by the energy management strategy at a higher level. Therefore, the battery in faulty mode will be more deteriorated by the applied charge current, and will finally evolve into serious TR. Hence, how to detect the soft SC is critical, especially when it is hard to distinguish the healthy and degraded modes from the battery electrical behavior is an important issue.

3.4.2 Short circuit current estimation

According to the design process presented previously, the selected linear segments, the corresponding linear robust SC detection observer design results and the optimal MF parameters are shown in table 3.3. Furthermore, the optimized MFs' shape and the fuzzification result of OCV-SOC curve are shown in Fig. 3.9.

Fig. 3.10 and 3.11 are the estimation results of the proposed observer under 10 Ω's SC resistance with 24 cycles of WLTC2. The 10 Ω's SC resistance is introduced to the battery ECM from the 12th test cycle. Although the estimator is deliberately initialized with a smaller SOC value (0.7) than the real one, it is able to converge to the real value. Especially after the abrupt appearance of the SC resistance, the estimator is able to track the dynamic change of the battery SOC. Furthermore, as it can be observed from Fig. 3.11, the simultaneous fault estimation allows to build a good indicator for the SC fault diagnosis.

Table 3.3: Linear robust SOC observer design and MF optimization results

Term / SOC Range	Linearization	$\bar{\boldsymbol{L}}$	γ	$\mathscr{D}(\alpha, r)$	(μ, σ)
[0, 0.2]	0.5841*soc+3.2362	$[-0.0013, 0.0024, 0.0024, -10.1235]'$	2.5046	$(0.8, 0.2)$	$(0.19999, 0.31229)$
[0.65, 0.85]	0.8779*soc+3.1064	$[-0.0020, 0.0017, 0.0023, -10.1241]'$	2.5046	$(0.8, 0.2)$	$(0.8499, 0.24014)$
[0.98, 1]	0.7190*soc+3.2525	$[-0.0017, 0.0020, 0.0024, -10.1233]'$	2.5046	$(0.8, 0.2)$	$(0.99999, 0.33213)$

Furthermore, in order to observe the effect of initial SOC value on the convergence time, various initial SOC values in the observer are tested. The result is shown in Fig. 3.12. We can conclude that the SOC initial value in the proposed observer has limited influence on the convergence time, because the tested results show that observers with different SOC values will converge to the real SOC value in 2000s. It should remember that the initial value of battery SOC can be set after measuring the battery OCV, hence the initial value of the SOC in the observer can be approximately regarded as the correct value. Therefore, the intensive simulation results just show the effective convergence of the proposed observer.

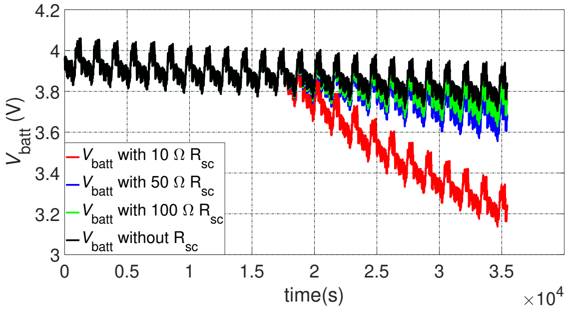

(a) V_{batt}

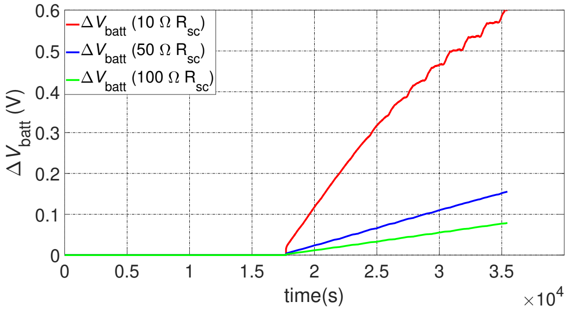

(b) Healthy-Faulty voltage difference

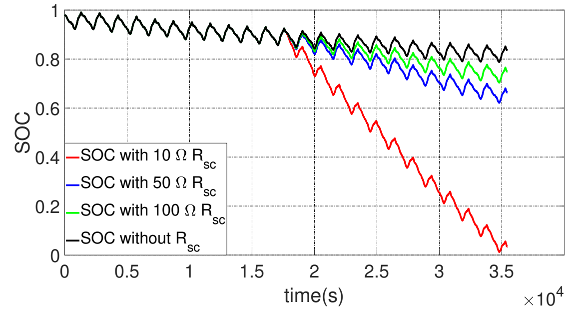

(c) Battery SOC

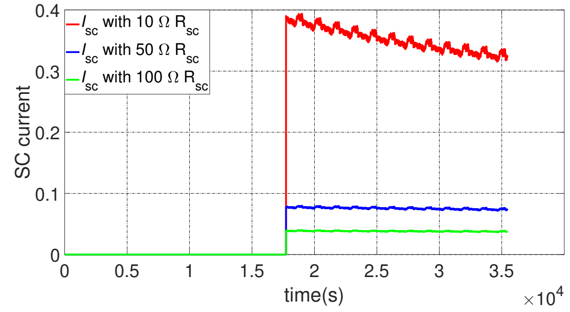

(d) Amplitude of I_{sc}

Figure 3.8: Battery electrical responses under different SC conditions.

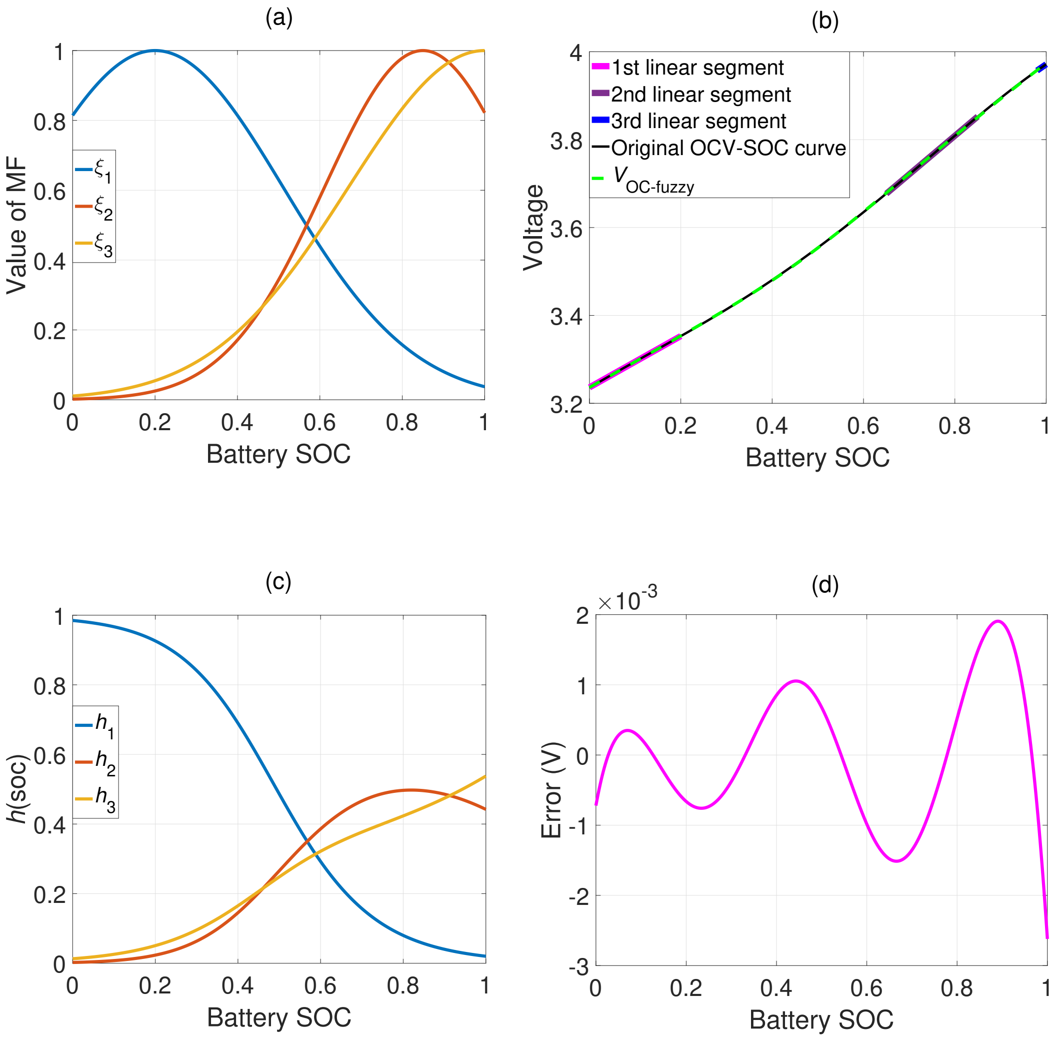

Figure 3.9: (a) optimized MF for each linear segment; (b) fuzzification result of the OCV-SOC curve. (c) weighting factor for each linear segment; (b) fuzzification error.

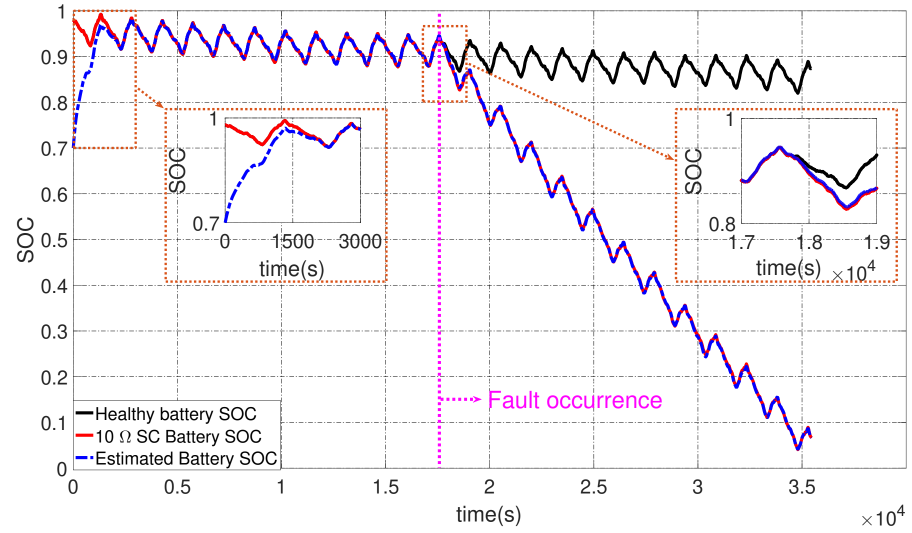

(a) SOC estimation result

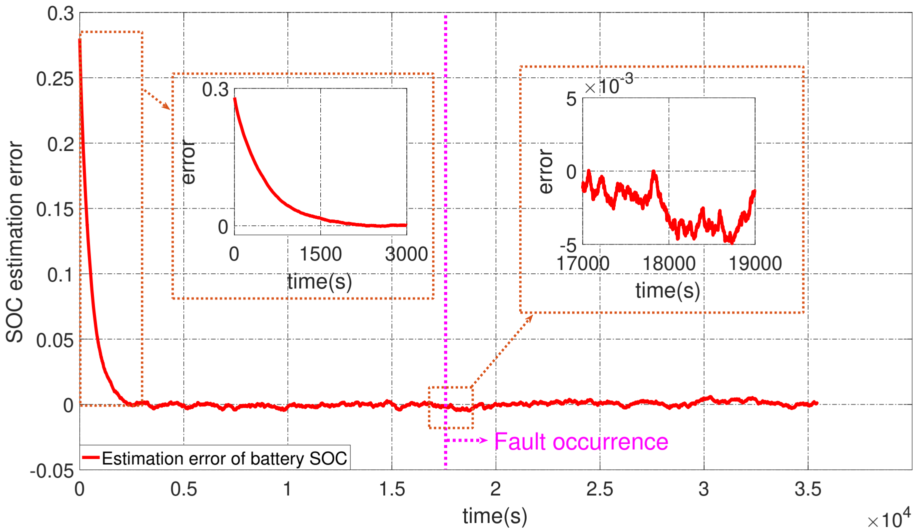

(b) Estimation error

Figure 3.10: SOC estimation before and after the fault occurrence.

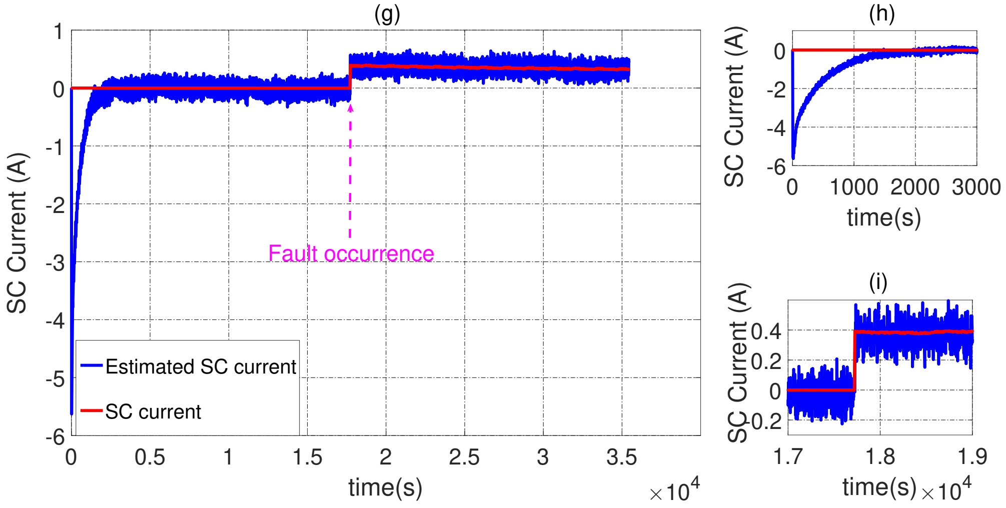

(a) SC current estimation result

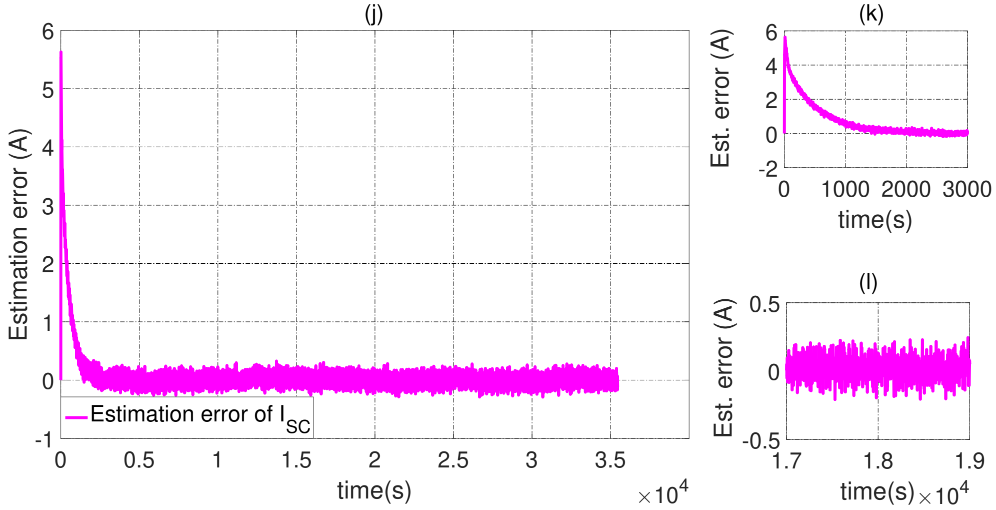

(b) Estimation error

Figure 3.11: SC current estimation before and after the fault occurrence.

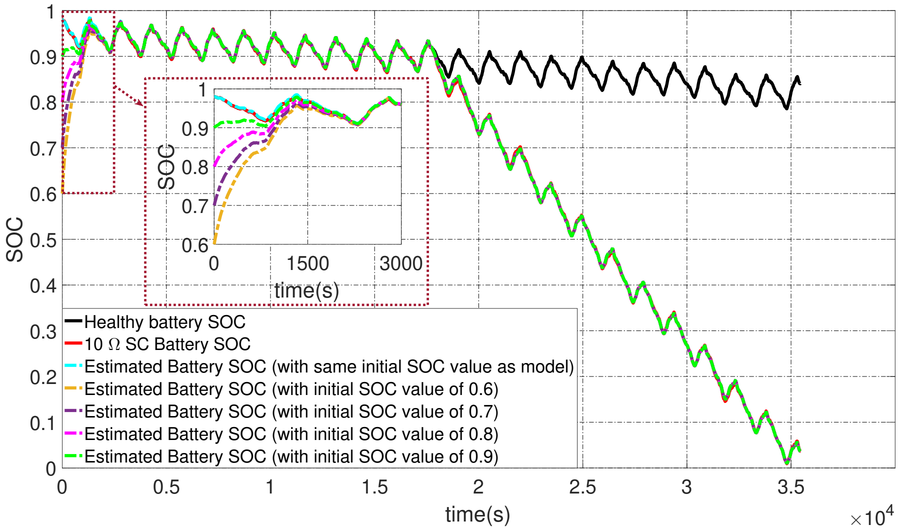

Figure 3.12: SOC estimation with different initial SOC values.

In addition, considering the unknown time point of the SC occurrence, a SC resistance is introduced during the convergence process of the observer. The estimation results are shown in Fig. 3.13 and Fig. 3.14. The SC resistance is introduced at the 500th second, where the observer is still in the convergence process. As can be observed from the estimation results, the SC fault occurrence does not affect the convergence process of the proposed state and fault estimator.

However, as shown in Fig. 3.15, when the SC current amplitude is small, namely the SC fault is small, it is difficult to distinguish the healthy and faulty modes from the estimated I_{sc}. Because the fault signal is corrupted with noise.

According to the definition of Signal-to-noise ratio (SNR) as shown in eq. (3.14):

$$\mathrm{SNR} = 10\log_{10}(\frac{\mu_{signal}^2}{\sigma_{noise}^2}) \tag{3.14}$$

where μ_{signal} is the mean of the non-negative signal, σ_{noise} is the noise standard deviation.

The SNR of the estimated I_{sc} in Fig. 3.15 is given in table 3.4. Hence, in order to improve the fault detection performance, a classical residual evaluation is applied in the following.

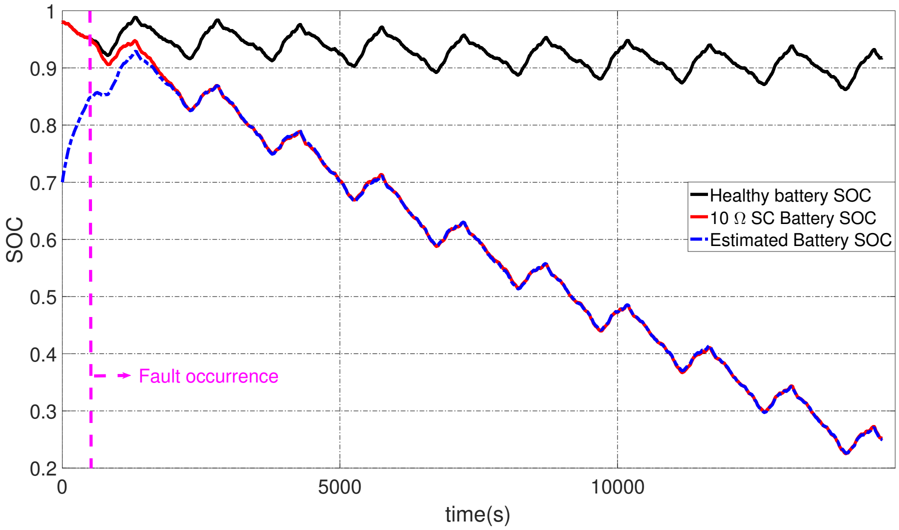

Figure 3.13: SOC estimation result (10 Ω′s SC resistance is introduced at the 500th second).

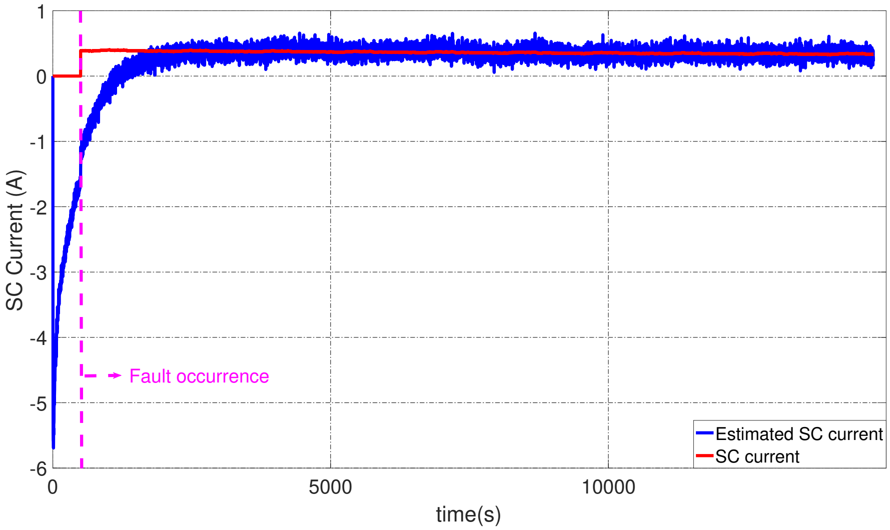

Figure 3.14: SC current estimation result (10 Ω′s SC resistance is introduced at the 500th second).

Table 3.4: SNR of the estimated I_{sc} in Fig. 3.15.

	10Ω	50Ω	100Ω
μ_{signal}	0.3509A	0.0755A	0.0382A
σ_{noise}	0.0760	0.0760	0.0760
SNR	13.2683dB	-0.0753dB	-5.8737dB

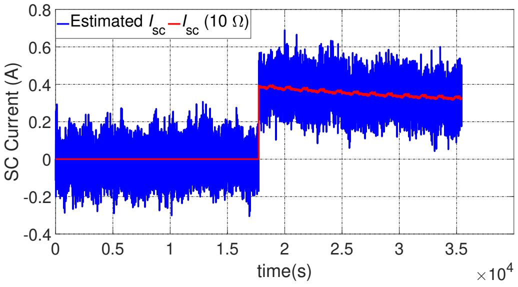

(a) I_{sc} estimation result ($\mathrm{R}_{\mathrm{sc}} = 10\Omega$)

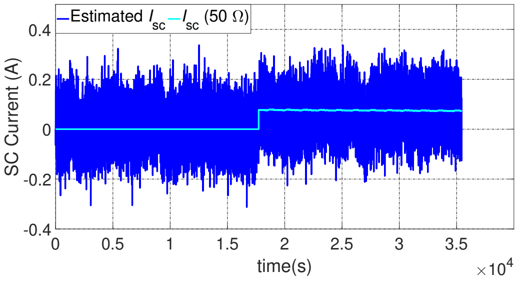

(b) I_{sc} estimation result ($\mathrm{R}_{\mathrm{sc}} = 50\Omega$)

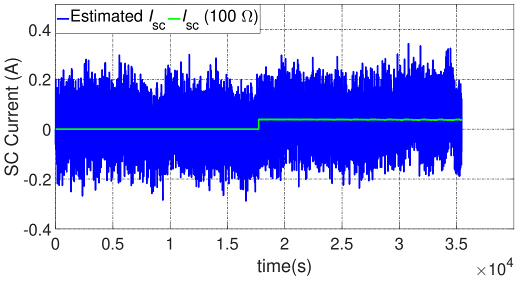

(c) I_{sc} estimation result ($\mathrm{R}_{\mathrm{sc}} = 100\Omega$)

Figure 3.15: I_{sc} estimation result under different SC conditions.

3.5 Cumulative Sum decision

3.5.1 Statistical analysis

As it can be observed from the intensive simulation studies, the obtained estimation result is a typical value-typed data sequence in contrary to the waveform one. Hence, it would be relevant to conduct a statistical analysis of the time-series signal, especially when $\mathrm{R_{sc}} = 100\Omega$.

Therefore, in order to study the statistical features of the estimated signal, we adopt the Monte Carlo methodology with 1000 realizations (500 in healthy case and 500 in faulty case) [180]. Classical statistical indicators, namely mean, variance, skewness and kurtosis of $\hat{I}_{\mathrm{sc}}$, are calculated both for healthy and faulty cases. The definition of these four classical statistical indicators are given as follows [181].

1. Mean: $\mu = \dfrac{1}{N}\sum_{1}^{N} x_j$
2. Variance: $\sigma^2 = \dfrac{1}{N}\sum_{1}^{N} (x_j - \mu)^2$
3. Skewness: $Skw = \dfrac{1}{N}\sum_{1}^{N} (\dfrac{x_j - \mu}{\sigma})^3$
4. Kurtosis: $Kur = \dfrac{1}{N}\sum_{1}^{N} (\dfrac{x_j - \mu}{\sigma})^4$

where, x_j is the jth data value, N is the number of total data points.

As expected, it can be seen from Fig. 3.16 and Fig. 3.17, the change of the mean value before and after the SC fault is evident, while the other three moments have no evident change after the SC fault.

3.5.2 Cumulative Sum fault detection

Based on the obtained statistical analysis result, Cumulative Sum (CUSUM), for the mean value, is applied for the estimated I_{sc}. The aim is to eliminate the diagnostic limitations imposed by a single SC observer, and improve the fault detection performance for incipient fault. Therefore, the flowchart of the battery soft SC detection method proposed is displayed in Fig. 3.18.

CUSUM is a well-known statistical technique that has already been proved to be efficient to detect abrupt changes in signal processing [180]. It allows to detect as quick as possible a change from a healthy to a faulty behavior. The CUSUM function, denoted S in the following, is a simple detection algorithm based on the likelihood process [180]. Namely, the estimated SC current will be treated as time-series signal, and then, the CUSUM method is used to detect the tiny change of the signal due to the incipient fault. CUSUM is computed along with samples of time-series signal.

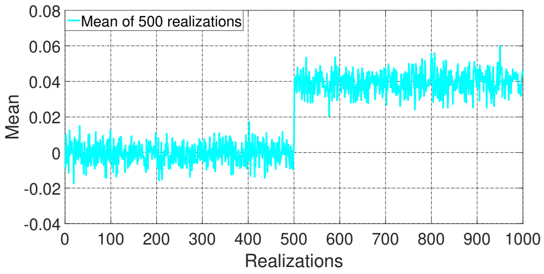

(a) Mean ($\mathrm{R_{sc}} = 100\Omega$)

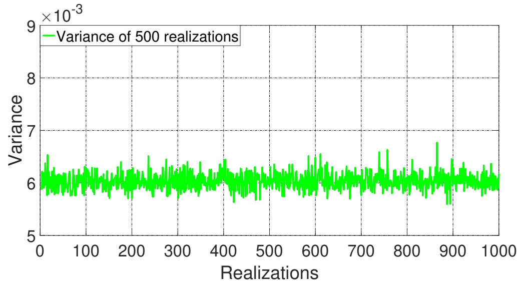

(b) Variance ($\mathrm{R_{sc}} = 100\Omega$)

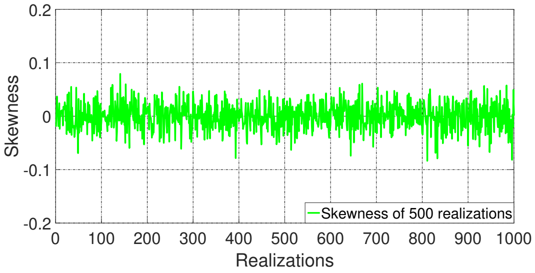

(c) Skewness ($\mathrm{R_{sc}} = 100\Omega$)

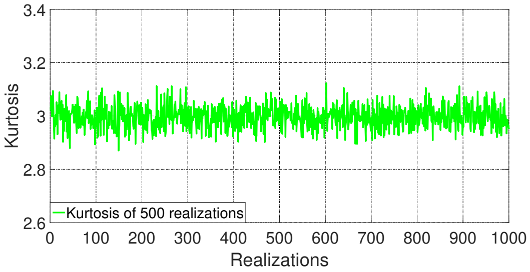

(d) Kurtosis ($\mathrm{R_{sc}} = 100\Omega$)

Figure 3.16: Statistical features of the estimated I_{sc} with 100 Ω's SC resistance.

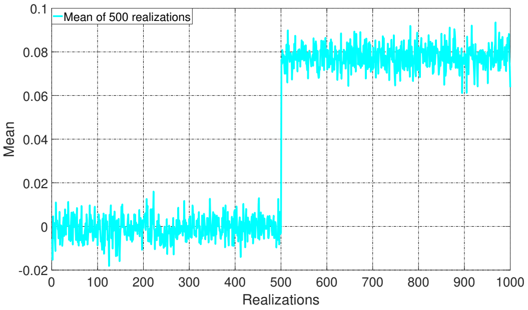

(a) Mean ($R_{sc} = 50\Omega$)

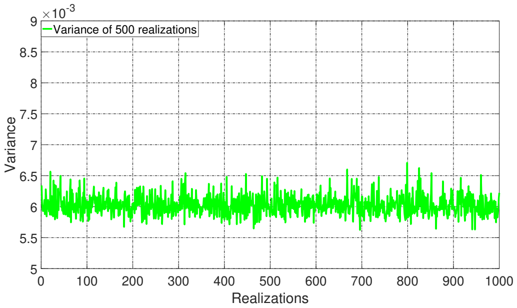

(b) Variance ($R_{sc} = 50\Omega$)

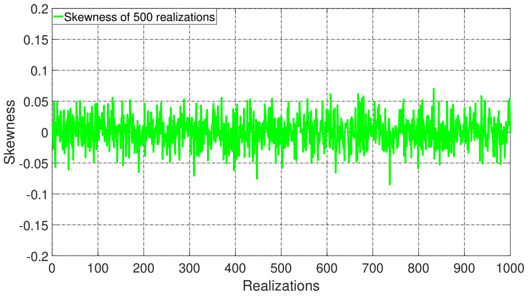

(c) Skewness ($R_{sc} = 50\Omega$)

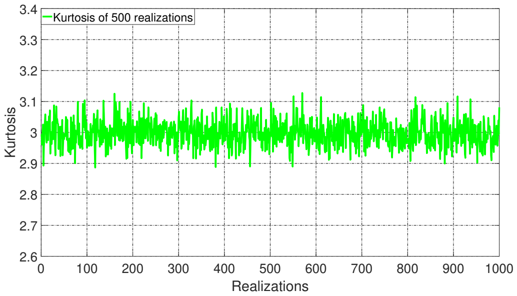

(d) Kurtosis ($R_{sc} = 50\Omega$)

Figure 3.17: Statistical features of the estimated I_{sc} with 50 Ω's SC resistance.

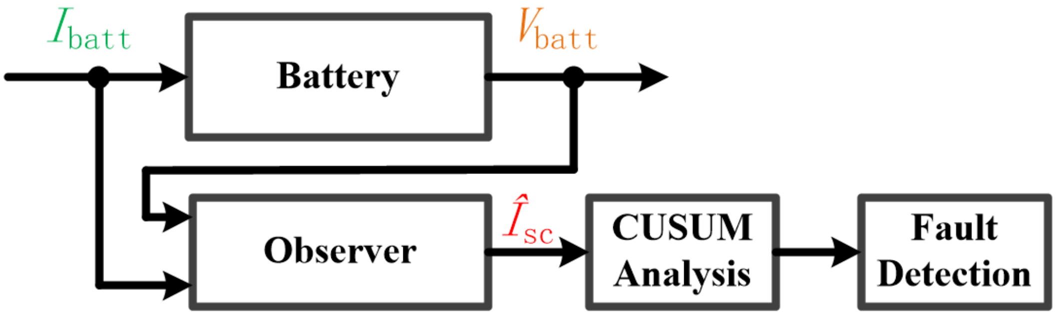

Figure 3.18: Flowchart of battery SC detection.

Theoretically, based on Gaussian distributed process, it is optimally derived as the sufficient statistics s_k such as [180]:

$$S_N = \sum_{k=1}^{N} s_k \tag{3.15}$$

where N is the number of samples. And according to the statical analysis for the estimated I_{sc}, s_k is considered in the case of mean changes in (3.16) [180]:

$$s_k = \left(\frac{\mu_f - \mu_h}{{\sigma_h}^2}\right) \times \left(\hat{I}_{sc}(k) - \frac{\mu_f + \mu_h}{2}\right) \tag{3.16}$$

where, μ_f and μ_h are the mean values of $\hat{I}_{\text{sc}}$ in healthy and faulty cases respectively. σ_h is the standard deviation value of $\hat{I}_{\text{sc}}$ in the healthy condition. According to the previous simulation studies, μ_f and μ_h are selected as 0.03 and 0 respectively. ${\sigma_h}^2 = 0.006$.

Furthermore, the CUSUM decision law can be computed as [180]:

$$D_{S_N} = \left(S_{N_k} - \min_{1\le j\le k}(S_{N_j})\right) \tag{3.17}$$

Hence, fault detection method based on the flowchart in Fig. 3.18 is executed 500 times for $\text{R}_{\text{sc}} = 100\,\Omega, 75\,\Omega, 50\,\Omega, 25\,\Omega$ respectively. As it can be seen from Fig. 3.19, the combination of estimator and CUSUM analysis is effective to carry out the incipient SC detection.

Fig. 3.19(b) represents the average value that can be used for fault detection. The most simple way to detect the fault is to compare the CUSUM to a threshold. One can see from Fig. 3.19(b) that the setting of the threshold will determine the fault detection performance.

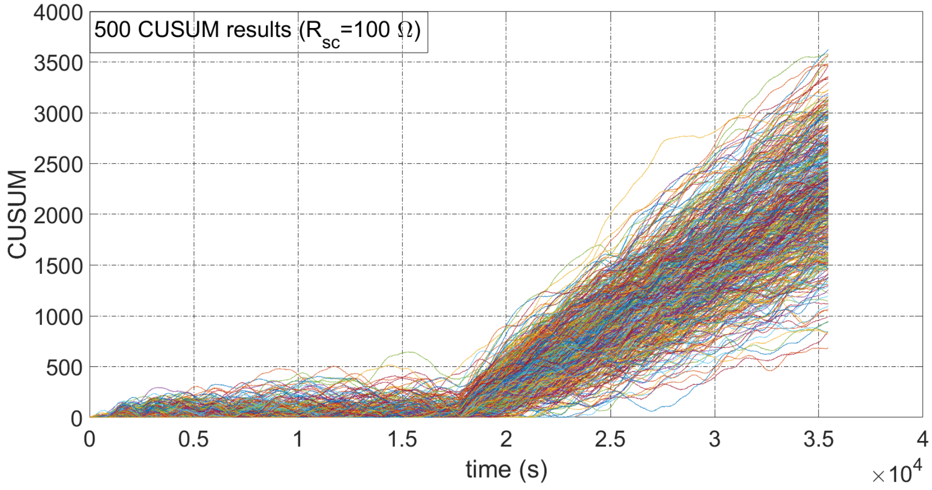

(a) CUSUM detection results under $R_{sc} = 100\Omega$

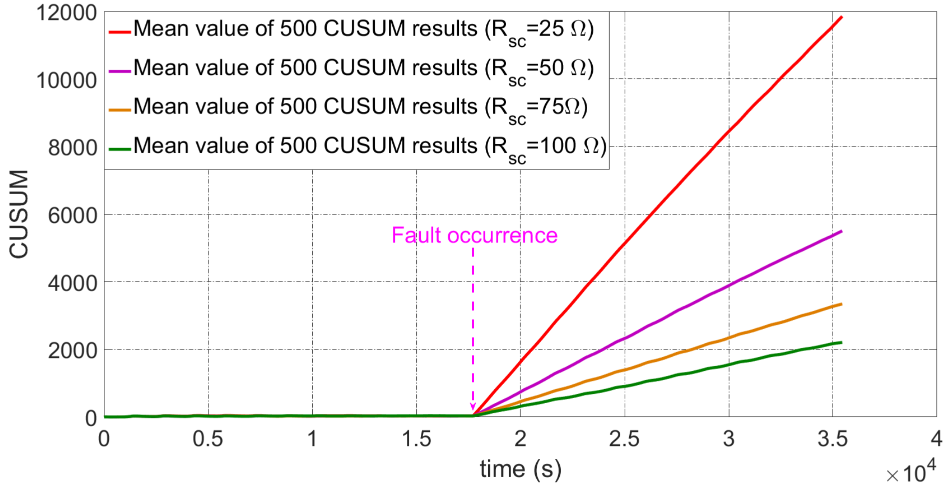

(b) CUSUM detection results under different SC conditions

Figure 3.19: CUSUM detection results.

3.5.3 Threshold setting

3.5.3.1 Threshold 1

The first way to set the detection threshold T_h is to select T_h=0.99$D_{S_N max}$, where $D_{S_N max}$ is the maximum value of D_{S_N} in the healthy case. If the CUSUM decision value is higher than T_h, then it means that a SC abuse condition has been detected [182]. Hence, according to the 500 simulation results, T_h=640.4445.

3.5.3.2 Threshold 2

Furthermore, in order to take advantage of the optimality of the CUSUM algorithm, probability density function (PDF) for the mean $\hat{I}_{sc}$ with or without 100Ω's resistance is shown in Fig. 3.20. Besides, the Kolmogorov-Smirnov test of the obtained PDF confirms that the distribution of the selected variable $\hat{I}_{sc}$ can be considered as Gaussian. Hence, the CUSUM can be the applied optimally [183].

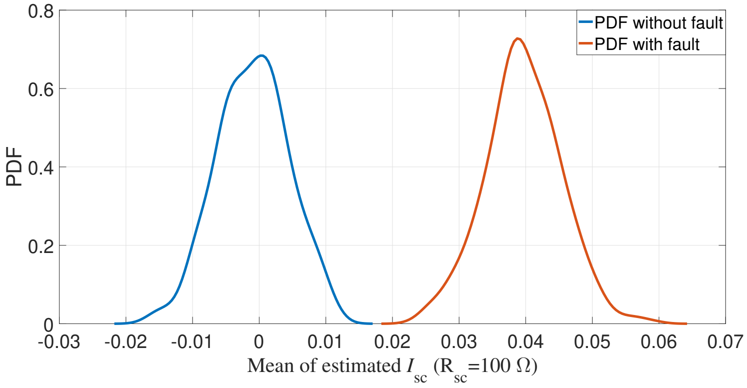

Figure 3.20: PDF of mean value of the estimated I_{sc} ($\text{R}_{\text{sc}} = 100\Omega$)

Therefore, the detection threshold T_h can be set based on the empirical equation T_h=μ_h+3σ_h [184]. In our case, μ_h is the mean value of the 500's CUSUM decision mean value, σ_h is the standard deviation of the 500's CUSUM decision mean value. Therefore, T_h=55.2014 in this case.

3.5.4 Robustness of the fault detection

The robustness of the fault detection for $\text{R}_{\text{sc}} = 100\Omega$ under different disturbance conditions is evaluated probabilistically with:

- The probability of detection (PD), which highlights the ability for correctly detecting a fault when it occurs [182].

- The probability of false alarm (PFA), which measures the probability of considering a healthy situation as a fault [182].

Hence, the receiver operating characteristics (ROC) curve can be plotted based on the PD and PFA. It is used to demonstrate the fault detection performance of the proposed method for different disturbance conditions. The variance of the disturbance term d is changed in order to simulate the different disturbance conditions. As shown in Fig. 3.21, even with the varied disturbance conditions, the proposed CUSUM detection can effectively execute the incipient SC detection.

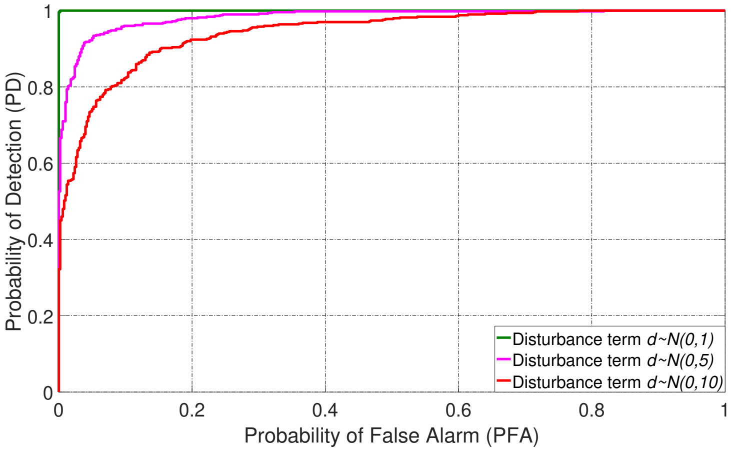

Figure 3.21: Performance of CUSUM under different disturbance conditions ($R_{sc} = 100\Omega$)

3.6 Conclusion

A soft SC diagnosis method that is independent of battery intrinsic properties as much as possible is proposed. Firstly, the traditional battery ECM is modified slightly by adding an equivalent SC resistance. Then, state-space representation for the battery SC model is introduced and used as a basis for designing an observer. Furthermore, the SC detection topic is converted to an estimation of the SC current that flowing through the equivalent SC resistance. The fault estimator is designed for both linear and non-linear OCV curve cases. Especially for the non-linear OCV curve, we propose a weighting function self-regulating robust observer specific to the battery ECM. The slowly changing characteristic of battery state-of-charge is fully used. Besides, a general fuzzification and optimization process for the OCV curve and membership functions are presented. The obtained membership functions are able to provide an optimal combination of the independent linear robust observers. The proposed observer converges to the true SOC value within 2000s regardless the initial SOC value. Moreover, CUSUM, an effective statistical method, is applied to the estimated fault signal in order to complete and improve the fault diagnosis performance. In other words, the proposed soft SC diagnosis method is a combination of model-based and signal-based research work.

General conclusion and perspectives

General conclusion

As mentioned in the general introduction, deep insight of the battery aging process and mechanisms of thermal runaway is still premature nowadays. However, based on the existing experimentally validated battery model and published experimental information, this PhD work has provided some new directions for the battery fault diagnosis, namely the battery state and parameter estimation and battery incipient short circuit diagnosis. The main contributions of this thesis can be divided into two aspects, which will be described respectively as following:

- **From the theoretical aspect**

  The battery extended ECM has been used for battery state and parameter estimation for a long time, however, the relevant observability analysis still needs to be discussed. The research work in [155] can be regarded as the earliest one to present the observability condition for the extended battery ECM. The only clue for demonstrating their conclusion, namely the constant input current cannot guarantee the observability for the extended battery ECM, is interrupted by a reference of private communication. After that, several fragmentary discussions about the observability conditions for the battery ECM and extneded ECM, especially for the nonlinear one, can be found in the research work of [44], [13] and [137]. However, the battery observability conditions based on the extended battery ECM has not been received a direct and complete discussion. Hence, the main theoretical contribution of this thesis is that the necessary observability conditions are clearly listed for the firstly time. The obtained observability conditions can provide an important direction to improve the traditional battery monitoring framework, which will be discussed later.

  Furthermore, regarding the battery short circuit diagnosis, another interesting theoretical contribution is the proposed weighting function self regulating state and fault estimator. Inspired by the TS fuzzy system, including the modelling and controller/observer design process, a new way to integrate the linear OCV-SOC segments is proposed in this thesis. This way does not require the strong linear assumption of the whole OCV-SOC curve as before, hence, the modelling process is much more simple compared to the classical one which uses a small discretization step. Furthermore, the battery internal characteristic is fully used, namely the fuzzy variable SOC allows to constitute a weighting function self regulating mechanism. This can simplify the TS fuzzy system design process, and adapt the TS fuzzy theory to the battery fault diagnosis successfully.

The aforementioned two main theoretical contributions are not baseless. Various experimental validation results in the literature support these two main theoretical contributions.

- **From the practical aspect**

  The traditional battery state and parameter frameworks, namely joint and dual estimation methods, have been recognized as two classical structures to execute the battery on-line monitoring work. Hence, introducing the advanced estimation algorithms to these two classical frameworks is the main research efforts in recent years. However, after finding the observability conditions in this thesis, a new way to group the battery capacity and ECM parameters is naturally proposed. Therefore, a new battery monitoring framework is proposed based on the commonly used KF estimation algorithms. The new structure provides a new direction to improve the battery state and parameter estimation result. Furthermore, results shows that the input current will affect the monitoring result, namely both the dynamic behavior and the altitude of the current will affect the obserability conditions for the extended battery equivalent circuit model, this provides an important practical contribution for the charge control design and health conscious energy management strategy improvement.

  As for the battery short circuit diagnosis, the model based battery fault estimation is combined with the statistical technique. The combination shows an effect fault diagnosis result based on the intensive simulation tests. Besides, classical optimization algorithm, genetic algorithm, is used innovatively to cope with the nonlinear battery OCV-SOC curve. This can shorten the weight function self regulating observer design process in reality. Namely, with the help of genetic algorithm, the proposed weighting function self regulating observer is independent of the battery internal characteristics.

Perspectives

- **Experimental validation**

  Although the obtained results have been verified by intensive simulation tests in this PhD work, experimental validation still need to be conducted to verify once again. Especially for the obtained necessary observability conditions for the extended battery model. The experimentally verified results will be more convincing.

- **Battery remaining useful life prognostic**

  Except for the topic of battery fault diagnosis, battery remaining useful life prediction is also an important part of battery healthy management. If the battery fault diagnosis results decides the actual control decision, while the battery remaining useful life prediction result will plan for future control decision. Hence, it becomes naturally the first perspective after the experimental validation.

- **Battery optimal charging control**

  Currently, the most used battery charging strategy is constant current constant voltage, which is model-free and too conservative for the charging time. Hence, with the battery fault diagnosis module, the optimal battery charging strategy can be envisaged with model predictive control.

- **Health conscious energy management strategy**

  In the high supervisory level, energy management strategy is indispensable. Hence, the battery fault diagnosis result or even the battery prognosis result will be integrated into the energy management strategy. Hence, health conscious energy management strategy is the future research direction.

- **Consideration of electrical sensor faults**

  Electrical sensors, including current and voltage sensors, are of great importance for executing the battery control, diagnosis and energy management. However, the sensor fault cannot be ignored in reality, hence robust energy management strategy with the consideration of sensor fault should be studied.

Résumé en français

La crise énergétique et les problèmes environnementaux posent le plus grand défi pour l'industrie automobile et insistent sur la nécessité de proposer une autre alternative moins polluante que le véhicule thermique. Par conséquent, les véhicules éléctriques (VEs) connaissent un développement en plein essor ces dernières années. Compte tenu de leur haute densité d'énergie/puissance et de leur longue durée de vie, les batteries lithium-ion (LIBs) sont actuellement les sources d'alimentation les plus utilisées et étudiées pour le système de propulsion électrique.

La batterie lithium-ion est un accumulateur électrochimique, elle est composée de quatre éléments principaux, à savoir, d'une cathode, d'une anode, d'un electrolyte et d'un séparateur. En effet, le système de stockage de l'énergie pour un VE est constitué d'un pack de batterie. Ce pack de batterie est formé de plusieurs modules, et chaque module est formé de plusieurs cellules pour avoir plus de pussiance ou plus de l'énergie. La fiabilité des LIBs est sans aucun doute d'une importance fondamentale pour le développement des VEs. Cependant, deux problèmes importants menacent la fiabilité de la batterie.

Tout d'abord, en tant que source d'énergie électrochimique typique, les LIBs présentent des problèmes de vieillissement. A part le temps, qui est le factuer principale de ce vieillissement, la température, la tension de stockage, l'intervalle de l'état de charge (SOC) utilisé et le niveau de courant utilisé pour charger ou décharger la batterie vont aussi affecter ce processus de vieillissement. Durant l'irréversible processus de vieillissement, la batterie progressivement subit une augmentation de la resistance et une diminution de la capacité de stockage causées par la dégradation des électrodes et l'électrolyte. Par conséquent, la durée de vie du système est réduite, cela va donc empêcher le développement de VEs.

En même temps, il y a aussi des contraintes imprévisible comme par exemple la contrainte mécanique, la contrainte électrique et la contrainte thermique. Notamment dans la contrainte électrique, il y a des défauts électriques communs comme la surcharge, la sur-décharge, le court-circuit externe (ESC) et le court-circuit interne (ISC). Ces défauts électriques vont finalement mener la batterie à l'emballement thermique (TR), ce qui est une défaillance catastrophique pour l'application embarquée.

En conséquence, afin de garantir une opération sûre et fiable de la batterie lithium-ion, nous avons besoin d'assurer la surveillance de la batterie avec un contrôle et une gestion d'énergie optimale. Une représentation schematique pour ces trois actions est donnée par la Fig. 1. Afin de prévenir un vieillissement prématuré de la batterie, cette dernière doit être surveillée pour construire la stratégie de gestion d'énergie optimale qui prend en considération son état de santé (SOH) et son état de charge (SOC). Ensuite, le contrôle permet de maintenir les états de la batterie dans une zone optimale, par exemple, tension, courant, SOC, etc. Finalement, la gestion regroupe la gestion de l'énergie avec la partie contrôle. Cela veut dire qu'une stratégie de gestion

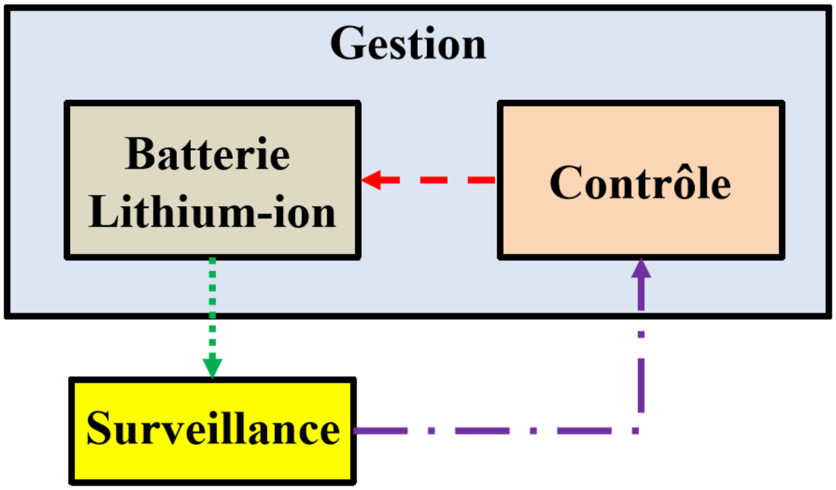

Figure 1: Schéma de surveillance, contrôle et gestion de la batterie.

de haut niveau qui gère l'action du contrôleur en considérant les états de la batterie.

Par ailleurs, la défaillance catastrophique TR peut être la conséquence d'un défaut électrique de court-circuit (SC) naissant. Donc, une alerte préventive de ce type de défaut SC fait aussi partie de la surveillance de la batterie, parce que cela est une action nécessaire qui peut garantir la fiabilité de la batterie pendant son fonctionnement.

De toute évidence, la surveillance joue un rôle primordial pour la suite des actions, qui seront basées sur les résultats obtenus dans l'étape de la surveillance. Pour une application automobile, la tâche de surveillance de batterie est intégrée dans ce que l'on appelle le BMS (Battery management system). BMS n'est pas seulement composé de matériel, le logiciel joue également un rôle important. L'acquisition de données est la fonction principale de BMS, qui recueille le courant, la tension et la température de la cellule à une fréquence et une précision d'échantillonnage appropriées [77]. Les états nonmesurable doivent être estimés à travers ces mesures en ligne et en temps réel [86].

Nous avons donc choisi de nous focaliser sur la surveillance de la batterie. Les travaux de cette thèse portent sur la surveillance en ligne de la batterie ainsi que le diagnostic de SC naissant.

Dans la première partie de la thèse, nous nous somme intéressé à l'estimation des états et les paramètres de la batterie. De plus, considérant la capacité de calcul en temps réel, nous avons choisi d'utiliser les méthodes basées sur le modèle. Bien que les modèles électrochimiques sont plus précis, nous avons préféré les modèles de circuit électrique équivalent (ECM). Parce que les modèles électrochimiques sont constitués des équations aux dérivées partielles, cela ne convient pas à la surveillance des états de la batterie en temps réel. Alors que les modèles de ECM sont constitués des équations différentielles ordianires, ils sont plus facile à calculer en temps réel comparés avec les modèles électrochimiques. Par ailleurs, les modèles de ECM ont des avantages suivants:

1) Simplicité: l'ECM est à la base composé de plusieurs composants idéaux, à savoir d'une résistance, d'un condensateur, d'une inductance et des réseaux RC [112]. Le circuit électrique obtenu peut simuler la tension de la batterie avec le courant comme entrée. L'ECM a été largement utilisé dans le domaine du système de stockage de l'énerigie (Pile à Combustible et supercondensateur) [3,14,44,147] en raison de sa simplicité.

2) Flexibilité: selon les besoins des chercheurs, la complexité de l'ECM peut être ajustée, qui est principalement basée sur l'application spécifique et la précision requise du modèle. A savoir, l'application spécifique décidera : *quel type de composants sera utilisé dans l'ECM ?* La batterie est souvent utilisée dans la gamme de fréquence intermédiaire [44,148], ce qui signifie que l'ECM est généralement composée d'une résistance en série avec plusieurs réseaux RC [112]. Cependant, si nécessaire, l'inductance qui représente les performances dans la basse fréquence et l'élément de phase constante qui simule le phénomène dans la haute fréquence pourraient être ajoutés à l'ECM de base [143]. En outre, la précision requise du modèle répondra également à la question *combien de composants seront utilisés dans l'ECM ?* Par exemple, augmenter le nombre de réseaux RC dans l'ECM augmentera la précision de modèle; cependant, la charge de calcul sera également augmentée en même temps [112]. En bref, un autre réseau RC apportera un état de plus dans la représentation d'état du modèle, ce qui signifie que la conception de l'observateur ou du contrôleur sera plus difficile.

3) Fiabilité: l'ECM a été largement utilisé pour étudier la batterie, et de nombreuses validations expérimentales ont été effectuées pour ECM, notamment sur les problèmes d'optimisation, conception de contrôleur, évaluation d'état [12,75,80,147], etc. Par conséquent, nous pouvons raisonnablement considérer que l'ECM de la batterie a été validé.

4) Composabilité: différente de la flexibilité, ce qui signifie que l'ECM peut être modifié dans sa propre structure et le nombre de composants, l'ECM peut également être étendu par d'autres modèles. L'exemple le plus courant de la composabilité est le modèle multi-physique de batterie [143]. Par rapport aux modèles de batteries électrochimiques, le principal inconvénient de l'ECM est que ses paramètres de l'ECM sont généralement constants. En d'autres termes, ces paramètres ne prennent pas en compte les conditions réelles d'utilisation tels que la direction du courant, le changement de température, le processus de vieillissement. Par conséquent, afin de conserver l'ECM, le modèle thermique ou le modèle de vieillissement peut être fusionné avec l'ECM de base pour simuler

le changement de paramètre comme dans une batterie réelle. En conséquence, le modèle combiné constitue ce que l'on appelle le modèle multi-physique de batterie. La composabilité permet de simuler le comportement électrique de la batterie tout en incluant les effets de température et de vieillissement [149,150].

5) Praticabilité: ce type de modèle convient au calcul EMS en ligne. En particulier, lorsque l'OCV (la tension à vide de la batterie) peut être linéarisé, l'ECM se dégradera en un modèle linéaire, ce qui peut grandement simplifier le processus de calcul. La praticabilité fait de l'ECM un outil précieux pour de nombreux ingénieurs, chercheurs et même entreprise [80].

Basé sur l'analyse ci-dessus, l'ECM est adopté dans cette thèse pour executer l'estimation des états et les paramètres de la batterie, ainsi que le diagnostic du SC naissant de la batterie.

Le chapitre 2 est consacré à l'estimation des états de la batterie. Comme montré dans Fig. 2, la méthode générale dans la litterature pour surveiller la batterie est basée sur le modèle étendu. A savoir, les paramètres de la batterie sont intégrés dans le ECM avec l'hypothèse qu'ils changent doucement. Cette hypothèse est largement validée par plusieurs travaux expérimentaux sur la batterie [134,137,155]. Le modèle ECM, comme montré dans la Fig. 3, est donc étendu avec ces paramètres telles que la résistance ou la capacité actuelle de batterie.

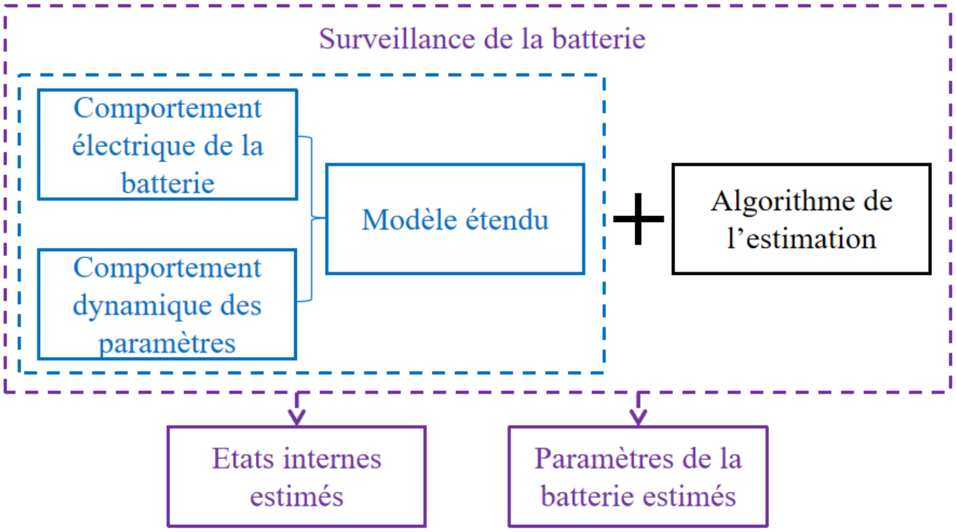

Figure 2: Schéma de surveillance de la batterie.

L'algorithme de l'estimation peut être utilisé pour estimer les états internes et les paramètres de la batterie. Cette idée générale a conduit à deux structures pour surveiller la batterie, à savoir "joint estimation" et "dual estimation", des perspectives d'amélioration sont présentées auparavant dans ces structures traditionnelles,

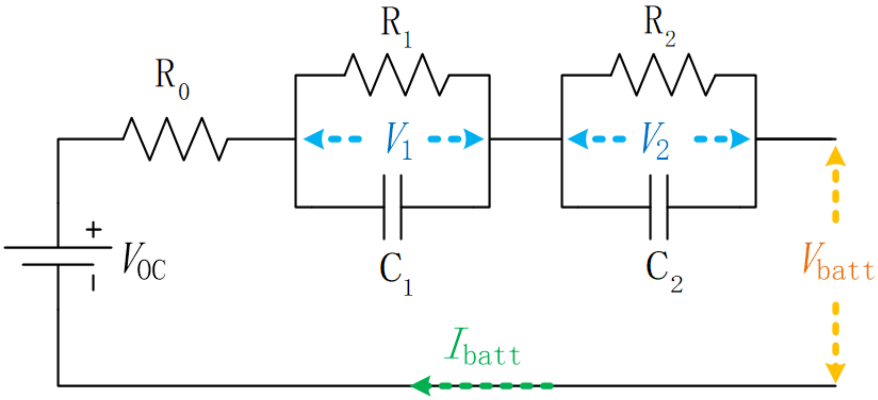

Figure 3: Modèle ECM de la batterie.

les conditions nécessaires pour estimer les états et les paramètres de la batterie ne sont pas encore claires. Donc, notre principale contribution théorique est l'analyse de l'observabilité pour la batterie ECM non-linéaire étendu. Avec une décomposition du modèle, les conditions d'observabilité nécessaires sont clairement répertoriées. Cela fournit un support théorique important pour proposer un nouveau cadre de surveillance de batterie basé sur le filtre de Kalman en cascade.

Les conditions nécessaires que nous avons trouvées pour estimer les paramètres d'après le modèle étendu sont listées dans la Fig. 4. Tout d'abord, les deux conditons connues telles que la dérivée de OCV (tension en circuit ouvert) par rapport au SOC et le courant de la batterie ne soient pas nuls, sont des conditions basiques pour guarantir l'observabilité du modèle étendu de la batterie. Ces deux conditions sont déjà présentées dans la littérature [13, 137]. De plus, dans cette thèse, nous avons trouvé trois autres conditions pour mieux estimer les paramètres de la batterie à travers l'analyse de l'observabilité. Afin d'avoir une meilleure estimation pour les paramètres d'ECM, la dérivée de courant de la batterie ne doit pas être nulle. Cela veut dire que le comportement dynamique du courant de la batterie peut affecter le résultat de l'estimation. Deux nouvelles conditions pour estimer la capacité actuelles sont aussi ajoutées. Nous avons montré que l'amplitude de courant de la batterie ainsi que la valeur initiale de capacité actuelle peuvent aussi impacter les performances de l'estimation.

Les résultats trouvés présentent un support théorique important afin de proposer une nouvelle structure pour la surveillance de la batterie basée sur un filtre Kalman en cascade. Cette structure est donnée par la Fig. 5 où les paramètres sont à estimer d'une nouvelle manière. Cette structure est différente par rapport aux structures traditionnelles où l'estimation des paramètres d'ECM et l'estimation de la capacité actuelle sont complètement séparées. Ajouter à cela la partie dédiée à l'estimation de la tension à vide de la batterie qui est utilisée pour l'estimation des paramètres

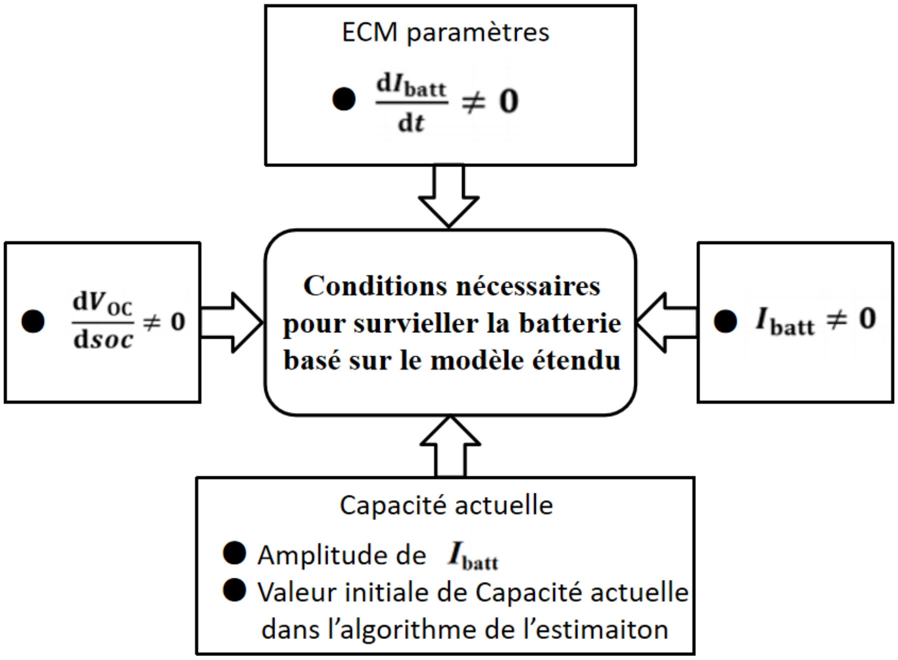

Figure 4: Les conditions nécessaires pour l'estimation d'après le modèle étendu.

d'ECM et l'estimation de la capacité actuelle. Cette nouvelle structure a donné des meilleures estimations avec des résultats moins fluctués par rapport aux structures traditionnelles ce qui présente un avantage pour une meilleure surveillance de la batterie.

Comme mentionné précédemment, la détection de défauts de SC naissant de la batterie fait aussi partie de la surveillance. Ceci est malheureusement difficile, car pendant la période d'incubation de TR, il n'y a pas de symptômes significatifs dans la batterie [5, 160]. Par conséquent, le diagnostic du SC naissant de la batterie est devenue récemment un sujet important. En fait, le SC dans la condition contrainte électrique, y compris ISC et ESC, est une étape importante avant TR. Alors que le SC dur (la résistance de SC réside dans la région de $m\Omega$) induira directement un grave danger thermique. Donc, le résultat de détection sera sans signification en raison du manque de temps pour prendre la décision [8]. Au contraire, un SC naissant (la valeur de la résistance SC doit être évaluée en fonction de la résistance interne de la batterie, par exemple des résistances de SC comme $100/10/1\ \Omega$) a besoin de temps pour mener la batterie au TR [8, 87]. De toute évidence, la détection SC pour le SC naissant est plus significative.

La détection de SC peut être, par exemple, réalisée par l'analyse thermique. Dans [161], un modèle électrochimico-thermique 3D est construit pour simuler les divers scénarios du ISC et la détection du ISC est abordée par un paramétrage du modèle et

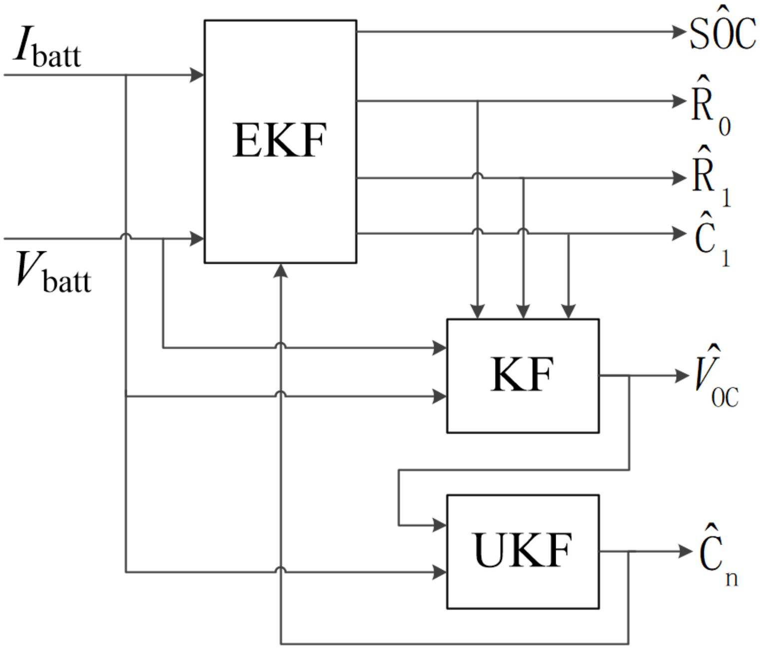

Figure 5: La nouvelle structure proposeé pour la surveillance de batterie.

l'estimation des paramètres. Dans [162], la détection de défaut thermique de batterie est basée sur un observateur, qui est synthétisé à la base d'un modèle thermique à deux états non-linéaire. Cependant, du point de vue de la sécurité, le changement brutal de la température signifie souvent que TR a été formé [160]. Par conséquent, le diagnostic de SC basé sur des signaux électriques, à savoir le courant et la tension de batterie mesurés, est plus populaire. Dans [89, 163], un schéma de détection pour ESC basé sur le modèle est proposé en utilisant différents modèles pour des conditions défectueuses et saines, qui sont obtenus à partir de leurs expériences d'abus menées. Dans [160], le diagnostic du SC naissant est exécuté à l'aide de la variation de capacité de charge restante à l'intérieur de la batterie. Dans [8], une méthode de détection du ISC est proposée en identifiant les paramètres du modèle, où la différence de tension entre chaque cellule est décrite avec un modèle ECM simplifié. De plus, une analyse quantitative sur le SC naissant est développée avec le modèle de différence de cellule et l'algorithme d'estimation d'état dans [165].

Bien que les travaux de recherche ont récemment fait des progrès remarquables dans le diagnostic et la détection du SC naissant de batterie, des solutions plus générales du point de vue du travail axé sur le contrôle doivent encore être étudiées. Autrement dit, nous voulons profiter de la littérature existante, y compris le modèle validé et les informations expérimentales, pour proposer une méthode générale de diagnostic de SC naissant.

Le chapitre 3 est dédiée à l'étude de la détection du défaut de SC naissant de la batterie. La détection du SC naissant est traitée à l'aide d'un algorithme d'estimation robuste de défaut en utilisant le modèle ECM modifié. Un observateur autorégulateur à fonction de pondération est proposé pour détecter le défaut SC. Dans le même temps, une approche systématique est proposée pour construire le mécanisme d'autorégulation afin de mieux gérer la courbe non-linéaire, de la batterie, de OCV en fonction de SOC. Cette estimation de courant de SC est suivie par une analyse statistique avec la fonction CUSUM (Cumulative Sum). Cette technique d'analyse a permis la détection du SC naissant de la batterie.

La Fig. 6 montre l'approche systématique que nous avons proposée pour construire un estimateur dédié à la détection SC naissant de la batterie. En raison de la non-linéarité de la courbe OCV-SOC, la sortie de la batterie peut être non linéaire. Cependant, la batterie peut être décrite par un modèle LTI (Linear time invariant) dans plusieurs intervalles de SOC. Par conséquent, inspiré par le concept de système flou Takagi-Sugeno (TS), une manière systématique de fusionner les intervalles linéaires de la courbe OCV-SOC et de construire l'estimateur de défaut autorégulant de la fonction de pondération est proposé.

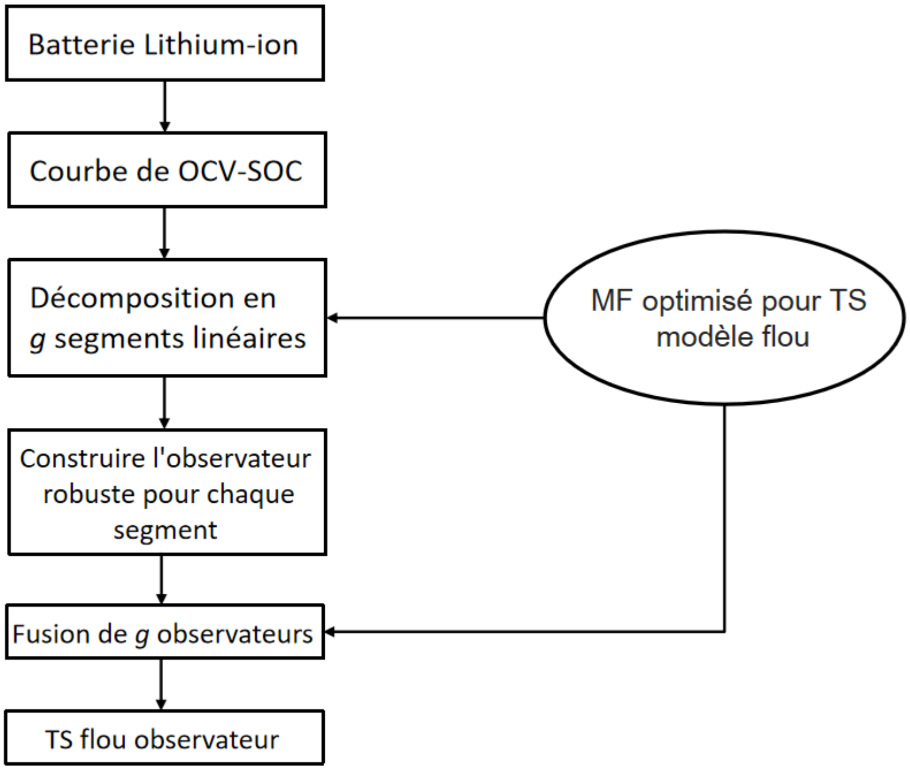

Figure 6: Approche systématique pour l'estimation de SC.

Le principe du système flou TS, incluant le processus de modélisation et de conception d'observateur/contrôleur, est d'étudier les systèmes non-linéaires par un ensemble de modèles LTI locaux [30]. Ensuite, un mécanisme d'interpolation parmi ces modèles basé sur des fonctions de pondération non-linéaires, à savoir les fonctions d'appartenance (MFs), est utilisé pour fusionner tous les sous-systèmes linéaires [170]. Par conséquent, basé sur des règles floues If-Then, au lieu de donner une valeur de sortie unique ou une action de sortie comme dans le système d'inférence floue traditionnel de type Mamdani. La sortie du système flou TS est une fonction polynomiale [171]. Le concept de système flou TS a été utilisé dans diverses applications telles que la conception de contrôleurs tolérants aux défauts de capteur de vitesse [172], la conception de contrôleur robuste pour la gestion d'énergie multi-sources [30], la classification et la régression [171], système chaotique continu [173] et éoliennes [174].

Afin de traiter la courbe non-linéaire de OCV-SOC, des segments linéaires sont choisis d'abord en fonction de la non-linéarité de cette courbe. Par la suite, un observateur robuste est construit pour chaque segment en se basant sur une approche de système flou Takagi-Sugeno (TS). L'optimisation des "membership function" est obligatoire pour fusionner les observateurs robustes construits. Pour cet objectif, nous avons utilisé l'algorithme génétique pour obtenir cette optimisation. Finalement, la caractéristique de changement lent de SOC nous a permis d'avoir un mécanisme d'autorégulation pour cet estimateur.

Ensuite, le CUSUM (Cumulative Sum), pour la valeur moyenne, est appliquée pour le défaut estimé. L'objectif est d'éliminer les limitations de diagnostic imposées par un seul observateur et d'améliorer les performances de détection de défaut pour un défaut naissant. Par conséquent, le schéma de notre méthode proposée pour le diagnostic du SC naissant est donné par la Fig 7.

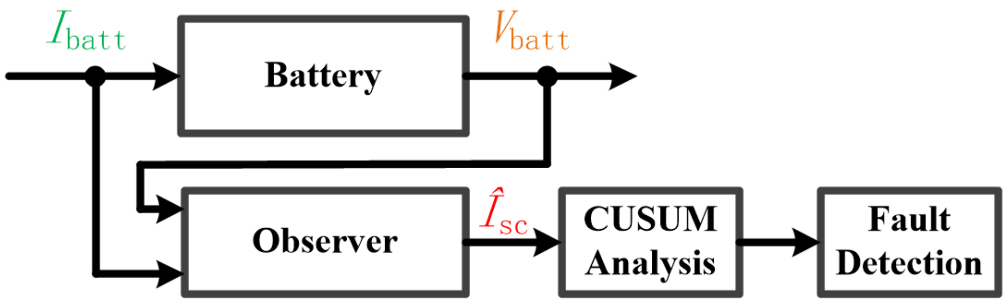

Figure 7: Schéma sur le diagnostic du SC naissant avec le CUSUM.

CUSUM est une technique statistique bien connue qui s'est déjà avérée efficace pour détecter des changements brusques dans le traitement du signal [180]. Il permet de détecter le plus rapidement possible un passage d'un comportement sain à un comportement défectueux. Le courant SC estimé sera traité comme un signal de série temporelle, puis la méthode CUSUM est utilisée pour détecter les petits changements du signal dû au défaut naissant. CUSUM est calculé avec des échantillons de signal de série temporelle.

Des études de simulation intensives basées sur des données expérimentales réelles ont vérifié notre contribution sur les aspects théoriques et méthodologiques dans le domaine de la surveillance de la batterie et du diagnostic SC naissant. Les résultats de la Fig. 8 montrent que le SC naissant est détecté en passant par la technique statistique (Somme Cumulative) du courant SC estimé afin d'assurer un meilleur résultat du diagnostic.

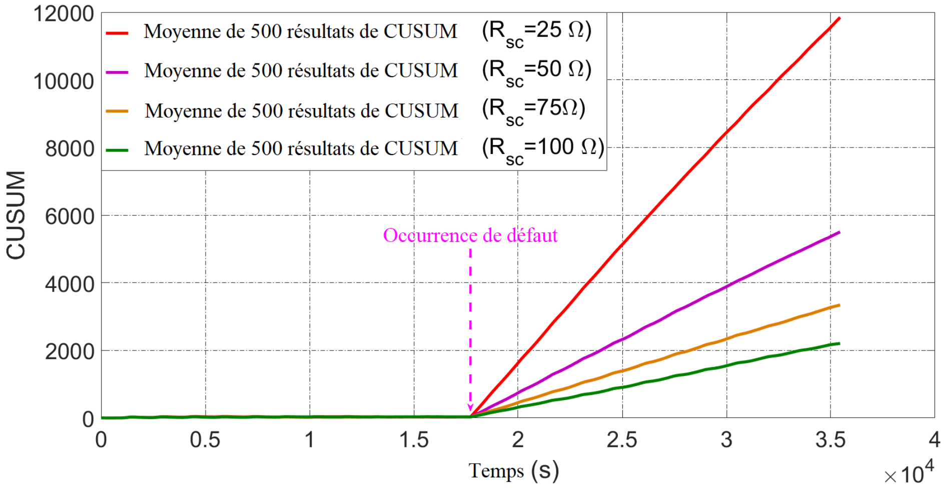

Figure 8: Le résultat du diagnostic de SC naissant avec CUSUM.

Annex

Proof of Theorem 3.3.1

Lemma 1: Discrete-time Bounded Real Lemma [168, 185]
Consider a discrete-time LTI system, $\boldsymbol{G}$, with state-space realization ($\boldsymbol{A_d}$, $\boldsymbol{B_d}$, $\boldsymbol{C_d}$, $\boldsymbol{D_d}$,), where $\boldsymbol{A_d} \in \mathbb{R}^{n\times n}$, $\boldsymbol{B_d} \in \mathbb{R}^{n\times m}$, $\boldsymbol{C_d} \in \mathbb{R}^{p\times n}$ and $\boldsymbol{D_d} \in \mathbb{R}^{p\times m}$. The H_∞ norm of $\boldsymbol{G}$ is:

$$\|\boldsymbol{G}\|_\infty = \sup_u \frac{\|\boldsymbol{G}_\mathbf{u}\|_2}{\|\boldsymbol{u}\|_2} \tag{A.1}$$

where, $\boldsymbol{u} \in \mathrm{L}_2[0,\infty)$ is the input signal, $\boldsymbol{G}_\mathbf{u}$ is the system's output with the input $\boldsymbol{u}$.

The inequality $\|\boldsymbol{G}\|_\infty < \gamma$ holds under the following necessary and sufficient condition:

$$\begin{bmatrix} -\boldsymbol{X} & \boldsymbol{X}\boldsymbol{A_d} & \boldsymbol{X}\boldsymbol{B_d} & 0 \\ * & -\boldsymbol{X} & 0 & \boldsymbol{C_d}' \\ * & * & -\gamma\boldsymbol{I} & \boldsymbol{D_d}' \\ * & * & * & -\gamma\boldsymbol{I} \end{bmatrix} < 0 \tag{A.2}$$

where $\boldsymbol{X} \in \mathbb{R}^{n\times n}$ is a symmetric positive definite matrix and $\gamma \in \mathbb{R}_{>0}$, 0 and $\boldsymbol{I}$ are respectively the zero matrix and unit matrix with corresponding dimensions. Here and everywhere in the sequel, $*$ denotes the symmetric elements in a symmetric matrix.

Lemma 2 [168]:
For a given matrix $\boldsymbol{A} \in \mathbb{R}^{n\times n}$, the eigenvalues of $\boldsymbol{A}$ belong to the circuit region $\mathscr{D}(\alpha, r)$ with center $\alpha + j0$ and radius r if and only if there exists a symmetric positive definite matrix $\boldsymbol{P} \in \mathbb{R}^{n\times n}$ such that

$$\begin{bmatrix} -\boldsymbol{P} & \boldsymbol{P}\boldsymbol{A}_r \\ * & -\boldsymbol{P} \end{bmatrix} < 0 \tag{A.3}$$

where $\boldsymbol{A_r} = \frac{\boldsymbol{A}-\alpha\boldsymbol{I}}{r}$, $\boldsymbol{I}$ is the unit matrix with corresponding dimension.

Remark 1 [168]:
For the sake of calculation convenience, *Lemma 2* can be changed into the following equivalent form:

$$\begin{bmatrix} -\boldsymbol{P} & \boldsymbol{P}(\boldsymbol{A}-\alpha\boldsymbol{I}) \\ * & -r^2\boldsymbol{P} \end{bmatrix} < 0 \tag{A.4}$$

The studied error system in section 3.3.1, namely eq. (3.6), is rewritten as follows:

$$\begin{cases} \bar{\boldsymbol{e}}(k+1) = (\bar{\boldsymbol{A}}_D - \bar{\boldsymbol{L}}\bar{\boldsymbol{C}})\bar{\boldsymbol{e}}(k) + (\bar{\boldsymbol{L}}\bar{\boldsymbol{D}}_d - \bar{\boldsymbol{B}}_d)\bar{\boldsymbol{v}}_D(k) \\ e_f(k) = [\ 0_{n_f\times n} \quad I_{n_f}\ ]\bar{\boldsymbol{e}}(k) \end{cases} \tag{A.5}$$

where the definitions of all the terms in eq. (A.5) have been given clearly in section 3.3.1.

Therefore, using the bounded real lemma for discrete-time system as shown in *Lemma 1* and the pole placement constraint in *Remark 1*, the following theorem can be obtained directly:

Theorem A.1 [168]

Let a prescribed H_∞ performance level γ and a circular region $\mathscr{D}(\alpha, r)$ be given. Error dynamics eq. (A.5) satisfies the H_∞ performance index $\|e_f(k)\|_2 < \gamma\|\bar{v}_D(k)\|_2$, and the eigenvalues of $(\bar{\boldsymbol{A}}_D - \bar{\boldsymbol{L}}\bar{\boldsymbol{C}})$ belong to $\mathscr{D}(\alpha, r)$ if and only if there exist two symmetric positive definite matrices $\bar{\boldsymbol{P}}_1$, $\bar{\boldsymbol{P}}_2 \in \mathbb{R}^{(n+n_f)\times(n+n_f)}$ and a matrix $\bar{\boldsymbol{L}} \in \mathbb{R}^{(n+n_f)\times p}$ such that the following conditions hold:

$$\begin{bmatrix} -\bar{\boldsymbol{P}}_1 & \bar{\boldsymbol{P}}_1(\bar{\boldsymbol{A}}_D - \bar{\boldsymbol{L}}\bar{\boldsymbol{C}}) & \bar{\boldsymbol{P}}_1(\bar{\boldsymbol{L}}\bar{\boldsymbol{D}}_d - \bar{\boldsymbol{B}}_d) & 0 \\ * & -\bar{\boldsymbol{P}}_1 & 0 & \bar{\boldsymbol{I}}_{n_f} \\ * & * & -\gamma \boldsymbol{I}_{(n_d+n_f)} & 0 \\ * & * & * & -\gamma I_{n_f} \end{bmatrix} < 0 \tag{A.6}$$

and

$$\begin{bmatrix} -\bar{\boldsymbol{P}}_2 & \bar{\boldsymbol{P}}_2(\bar{\boldsymbol{A}}_D - \bar{\boldsymbol{L}}\bar{\boldsymbol{C}}) - \alpha\bar{\boldsymbol{P}}_2 \\ * & -r^2\bar{\boldsymbol{P}}_2 \end{bmatrix} < 0 \tag{A.7}$$

where $\bar{\boldsymbol{I}}_{n_f} = \begin{bmatrix} 0_{n\times n_f} \\ I_{n_f} \end{bmatrix}$.

Remark 2 [168]:

Introducing two different Lyapunov matrices $\bar{\boldsymbol{P}}_1$, $\bar{\boldsymbol{P}}_2$ rather than a single one provides some degrees of design freedom and allows *Theorem A.1 [168]* to be a necessary and sufficient condition. However, the coupling of the observer gain matrix $\bar{\boldsymbol{L}}$ between eq. (A.6) and eq. (A.7) results in a nonconvex problem, which cannot be handled by linear optimization procedures. To recover convexity, we must require that all specifications are enforced by a common Lyapunov matrix, that is, $\bar{\boldsymbol{P}}=\bar{\boldsymbol{P}}_1=\bar{\boldsymbol{P}}_2$, therefore resulting in the following corollary.

Corollary 1 [168]

Let a prescribed H_∞ performance level γ and a circular region $\mathscr{D}(\alpha, r)$ be given. If there exists a symmetric positive definite matrix $\bar{\boldsymbol{P}} \in \mathbb{R}^{(n+n_f)\times(n+n_f)}$ and a matrix $\bar{\boldsymbol{Y}} \in \mathbb{R}^{(n+n_f)\times p}$ such that the following conditions hold:

$$\begin{bmatrix} -\bar{\boldsymbol{P}} & \bar{\boldsymbol{P}}\bar{\boldsymbol{A}}_D - \bar{\boldsymbol{Y}}\bar{\boldsymbol{C}} & \bar{\boldsymbol{Y}}\bar{\boldsymbol{D}}_d - \bar{\boldsymbol{P}}\bar{\boldsymbol{B}}_d & 0 \\ * & -\bar{\boldsymbol{P}} & 0 & \bar{\boldsymbol{I}}_{n_f} \\ * & * & -\gamma\bar{\boldsymbol{I}}_{(n_d+n_f)} & 0 \\ * & * & * & -\gamma I_{n_f} \end{bmatrix} < 0 \tag{A.8}$$

and

$$\begin{bmatrix} -\bar{\boldsymbol{P}} & \bar{\boldsymbol{P}}\bar{\boldsymbol{A}}_D - \bar{\boldsymbol{Y}}\bar{\boldsymbol{C}} - \alpha\bar{\boldsymbol{P}} \\ * & -r^2\bar{\boldsymbol{P}} \end{bmatrix} < 0 \tag{A.9}$$

where $\bar{\boldsymbol{I}}_{n_f} = \begin{bmatrix} 0_{n\times n_f} \\ I_{n_f} \end{bmatrix}$*, then error dynamics eq. (A.5) satisfies the H_∞ performance index $\|e_f(k)\|_2 < \gamma\|\bar{v}_D(k)\|_2$, and the eigenvalues of $(\bar{\boldsymbol{A}}_D - \bar{\boldsymbol{L}}\bar{\boldsymbol{C}})$ belong to $\mathscr{D}(\alpha, r)$, and the observer gain can be calculated by $\bar{\boldsymbol{L}}=\bar{\boldsymbol{P}}^{-1}\bar{\boldsymbol{Y}}$.*

Remark 3 [168]:

To guarantee the convergence performance of the state and fault estimation observer, the multiconstrained design is involved, leading to possible conservatism, because of the common Lyapunov matrix $\bar{\boldsymbol{P}}$ in *Corollary 1.* Multiconstrained design problems may have no solution because of the increase number of constraints that are considered. Hence, in order to guarantee the feasibility, different Lyapunov matrices $\bar{\boldsymbol{P}}_1$ and $\bar{\boldsymbol{P}}_2$ can be designed by introducing slack variables. This finally leads to the following theorem, which is used in this thesis.

Theorem A.2 [168]

Let a prescribed H_∞ performance level γ and a circular region $\mathscr{D}(\alpha, r)$ be given. If there exist two symmetric positive definite matrices $\bar{\boldsymbol{P}}_1$, $\bar{\boldsymbol{P}}_2 \in \mathbb{R}^{(n+n_f)\times(n+n_f)}$ and two matrices $\bar{\boldsymbol{S}} \in \mathbb{R}^{(n+n_f)\times(n+n_f)}$, $\bar{\boldsymbol{Y}} \in \mathbb{R}^{(n+n_f)\times p}$ such that the following conditions hold:

$$\begin{bmatrix} -\bar{\boldsymbol{S}} - \bar{\boldsymbol{S}}' + \bar{\boldsymbol{P}}_1 & \bar{\boldsymbol{S}}\bar{\boldsymbol{A}}_D - \bar{\boldsymbol{Y}}\bar{\boldsymbol{C}} & \bar{\boldsymbol{Y}}\bar{\boldsymbol{D}}_d - \bar{\boldsymbol{S}}\bar{\boldsymbol{B}}_d & 0 \\ * & -\bar{\boldsymbol{P}}_1 & 0 & \bar{I}_{n_f} \\ * & * & -\gamma I_{(n_d+n_f)} & 0 \\ * & * & * & -\gamma I_{n_f} \end{bmatrix} < 0 \tag{A.10}$$

and

$$\begin{bmatrix} -\bar{\boldsymbol{S}} - \bar{\boldsymbol{S}}' + \bar{\boldsymbol{P}}_2 & \bar{\boldsymbol{S}}\bar{\boldsymbol{A}}_D - \bar{\boldsymbol{Y}}\bar{\boldsymbol{C}} - \alpha\bar{\boldsymbol{S}} \\ * & -r^2\bar{\boldsymbol{P}}_2 \end{bmatrix} < 0 \tag{A.11}$$

where $\bar{I}_{n_f} = \begin{bmatrix} 0_{n\times n_f} \\ I_{n_f} \end{bmatrix}$*. Then error dynamics (A.5) satisfies the* H_∞ *performance index* $\|e_f(k)\|_2 < \gamma\|\bar{v}_D(k)\|_2$*, the eigenvalues of* $(\bar{\boldsymbol{A}}_D - \bar{\boldsymbol{L}}\bar{\boldsymbol{C}})$ *belong to* $\mathscr{D}(\alpha, r)$*, and the gain matrix* $\bar{\boldsymbol{L}}$ *is given by* $\bar{\boldsymbol{L}} = \bar{\boldsymbol{S}}^{-1}\bar{\boldsymbol{Y}}$*.*

Proof [168]

By introducing a slack matrix $\bar{\boldsymbol{S}}$, different Lyapunov matrices $\bar{\boldsymbol{P}}_1$ and $\bar{\boldsymbol{P}}_2$ can be designed. Based on the deducing process of eq. (A.6) and eq. (A.7), we need to prove the equivalence of eq. (A.6) and eq. (A.10) and the equivalence of eq. (A.7) and eq. (A.11).

The equivalence of eq. (A.6) and eq. (A.10):

eq. (A.6) → eq. (A.10): when choosing $\bar{\boldsymbol{P}}_1 = \bar{\boldsymbol{S}} = \bar{\boldsymbol{S}}'$ in eq. (A.10), we can obtain eq. (A.6), and then eq. (A.6) implies eq. (A.10).

eq. (A.10) → eq. (A.6): In eq. (A.10), we can obtain $\bar{\boldsymbol{S}} + \bar{\boldsymbol{S}}' > \bar{\boldsymbol{P}}_1 > 0$, which implies that $\bar{\boldsymbol{S}}$ is nonsingular. Because $\bar{\boldsymbol{P}}_1$ is symmetric positive definite, the inequality $(\bar{\boldsymbol{P}}_1 - \bar{\boldsymbol{S}})\bar{\boldsymbol{P}}_1^{-1}(\bar{\boldsymbol{P}}_1 - \bar{\boldsymbol{S}})' \geq 0$ holds, and it can also be expressed as $-\bar{\boldsymbol{S}} - \bar{\boldsymbol{S}}' + \bar{\boldsymbol{P}}_1 \geq -\bar{\boldsymbol{S}}\bar{\boldsymbol{P}}_1^{-1}\bar{\boldsymbol{S}}'$. Therefore, it follows from eq. (A.10) that

$$\begin{bmatrix} -\bar{\boldsymbol{S}}\bar{\boldsymbol{P}}_1^{-1}\bar{\boldsymbol{S}}' & \bar{\boldsymbol{S}}(\bar{\boldsymbol{A}}_D - \bar{\boldsymbol{L}}\bar{\boldsymbol{C}}) & \bar{\boldsymbol{S}}(\bar{\boldsymbol{L}}\bar{\boldsymbol{D}}_d - \bar{\boldsymbol{B}}_d) & 0 \\ * & -\bar{\boldsymbol{P}}_1 & 0 & \bar{I}_{n_f} \\ * & * & -\gamma I_{(n_d+n_f)} & 0 \\ * & * & * & -\gamma I_{n_f} \end{bmatrix} < 0 \tag{A.12}$$

and then premultiplying and postmultiplying by diag($\bar{\boldsymbol{P}}_1\bar{\boldsymbol{S}}^{-1}$, $I_{(n+n_f)}$, $I_{(n_d+n_f)}$, I_{n_f}) and its transpose, we obtain eq. (A.6), which establishes that eq. (A.10) implies eq. (A.6).

The equivalence of eq. (A.7) and eq. (A.11):

eq. (A.7) → eq. (A.11): when choosing $\bar{\boldsymbol{P}}_2 = \bar{\boldsymbol{S}} = \bar{\boldsymbol{S}}'$ in eq. (A.11), we can obtain eq. (A.7), and then eq. (A.7) implies eq. (A.11).

eq. (A.11) → eq. (A.7): In eq. (A.11), we can obtain $\bar{\boldsymbol{S}} + \bar{\boldsymbol{S}}' > \bar{\boldsymbol{P}}_2 > 0$, which implies that $\bar{\boldsymbol{S}}$ is nonsingular. Because $\bar{\boldsymbol{P}}_2$ is symmetric positive definite, the inequality $(\bar{\boldsymbol{P}}_2 - \bar{\boldsymbol{S}})\bar{\boldsymbol{P}}_2^{-1}(\bar{\boldsymbol{P}}_2 - \bar{\boldsymbol{S}})' \geq 0$ holds, and it can also be expressed as $-\bar{\boldsymbol{S}} - \bar{\boldsymbol{S}}' + \bar{\boldsymbol{P}}_2 \geq -\bar{\boldsymbol{S}}\bar{\boldsymbol{P}}_2^{-1}\bar{\boldsymbol{S}}'$. Therefore, it follows from eq. (A.11) that

$$\begin{bmatrix} -\bar{\boldsymbol{S}}\bar{\boldsymbol{P}}_2^{-1}\bar{\boldsymbol{S}}' & \bar{\boldsymbol{S}}(\bar{\boldsymbol{A}}_D - \bar{\boldsymbol{L}}\bar{\boldsymbol{C}}) - \alpha\bar{\boldsymbol{S}} \\ * & -r^2\bar{\boldsymbol{P}}_2 \end{bmatrix} < 0 \tag{A.13}$$

and then premultiplying and postmultiplying by $\mathrm{diag}(\bar{\boldsymbol{P}}_2\bar{\boldsymbol{S}}^{-1}, I_{(n+n_f)})$ and its transpose, we obtain eq. (A.7), which establishes that eq. (A.11) implies eq. (A.7). ■

The LMI constraints presented in this thesis are solved by the YALMIP function in the Matlab environment [186]. The used solver is SEDUMI.

Bibliography

[1] H. Li. *Energy consumption minimization strategy for fuel cell hybrid electric vehicles.* PhD thesis, Bourgogne Franche-Comté, 2018.

[2] T. Bunsen, P. Cazzola, M. Gorner, L. Paoli, S. Scheffer, R. Schuitmaker, J. Tattini, and J. Teter. Global ev outlook 2018: Towards cross-modal electrification. 2018.

[3] M. Yue, S. Jemei, R. Gouriveau, and N. Zerhouni. Review on health-conscious energy management strategies for fuel cell hybrid electric vehicles: Degradation models and strategies. *International Journal of Hydrogen Energy*, 2019.

[4] W. Waag, C. Fleischer, and D. U. Sauer. Critical review of the methods for monitoring of lithium-ion batteries in electric and hybrid vehicles. *Journal of Power Sources*, 258:321 – 339, 2014.

[5] A. Sidhu, A. Izadian, and S. Anwar. Adaptive nonlinear model-based fault diagnosis of li-ion batteries. *IEEE Transactions on Industrial Electronics*, 62(2):1002–1011, 2014.

[6] H. Wang, E. Lara-Curzio, E. T. Rule, and C. S. Winchester. Mechanical abuse simulation and thermal runaway risks of large-format li-ion batteries. *Journal of Power Sources*, 342:913–920, 2017.

[7] A. Kriston, A. Pfrang, H. Döring, B. Fritsch, V. Ruiz, I. Adanouj, T. Kosmidou, J. Ungeheuer, and L. Boon-Brett. External short circuit performance of graphite-lini1/3co1/3mn1/3o2 and graphite-lini0. 8co0. 15al0. 05o2 cells at different external resistances. *Journal of Power Sources*, 361:170–181, 2017.

[8] M. Ouyang, M. Zhang, X. Feng, L. Lu, J. Li, X. He, and Y. Zheng. Internal short circuit detection for battery pack using equivalent parameter and consistency method. *Journal of Power Sources*, 294:272–283, 2015.

[9] X. Feng, Y. Pan, X. He, L. Wang, and M. Ouyang. Detecting the internal short circuit in large-format lithium-ion battery using model-based fault-diagnosis algorithm. *Journal of Energy Storage*, 18:26 – 39, 2018.

[10] R. Guo, L. Lu, M. Ouyang, and X. Feng. Mechanism of the entire overdischarge process and overdischarge-induced internal short circuit in lithium-ion batteries. *Scientific reports*, 6:30248, 2016.

[11] H. Luo, Y. Xia, and Q. Zhou. Mechanical damage in a lithium-ion pouch cell under indentation loads. *Journal of Power Sources*, 357:61–70, 2017.

[12] Z. Chen, Y. Fu, and C. C. Mi. State of charge estimation of lithium-ion batteries in electric drive vehicles using extended kalman filtering. *IEEE Transactions on Vehicular Technology*, 62(3):1020–1030, 2012.

[13] S. Zhao, S. R. Duncan, and D. A. Howey. Observability analysis and state estimation of lithium-ion batteries in the presence of sensor biases. *IEEE Transactions on Control Systems Technology*, 25(1):326–333, 2016.

[14] C. Depature, S. Jemei, L. Boulon, A. Bouscayrol, N. Marx, S. Morando, and A. Castaings. Ieee vts motor vehicles challenge 2017-energy management of a fuel cell/battery vehicle. In *2016 IEEE Vehicle Power and Propulsion Conference (VPPC)*, pages 1–6. IEEE, 2016.

[15] B. Xia, Z. Zhang, Z. Lao, W. Wang, W. Sun, Y. Lai, and M. Wang. Strong tracking of a h-infinity filter in lithium-ion battery state of charge estimation. *Energies*, 11(6):1481, 2018.

[16] M. Crippa, G. Oreggioni, D. Guizzardi, M. Muntean, E. Schaaf, E. Lo Vullo, E. Solazzo, F. Monforti-Ferrario, J.G.J. Olivier, and E. Vignati. Fossil co2 and ghg emissions of all world countries. *Publications Office of the European Union: Luxembourg*, 2019.

[17] A. González, E. Goikolea, J. A. Barrena, and R. Mysyk. Review on supercapacitors: technologies and materials. *Renewable and Sustainable Energy Reviews*, 58:1189–1206, 2016.

[18] H. Chen, T. Cong, W. Yang, C. Tan, Y. Li, and Y. Ding. Progress in electrical energy storage system: A critical review. *Progress in natural science*, 19(3):291–312, 2009.

[19] X. Luo, J. Wang, M. Dooner, and J. Clarke. Overview of current development in electrical energy storage technologies and the application potential in power system operation. *Applied energy*, 137:511–536, 2015.

[20] S. Rehman, L. M. Al-Hadhrami, and M. M. Alam. Pumped hydro energy storage system: A technological review. *Renewable and Sustainable Energy Reviews*, 44:586–598, 2015.

[21] M. Budt, D. Wolf, R. Span, and J. Yan. A review on compressed air energy storage: Basic principles, past milestones and recent developments. *Applied Energy*, 170:250–268, 2016.

[22] B. Bendjedia, N. Rizoug, M. Boukhnifer, F. Bouchafaa, and M. Benbouzid. Influence of secondary source technologies and energy management strategies on energy storage system sizing for fuel cell electric vehicles. *International Journal of Hydrogen Energy*, 43(25):11614–11628, 2018.

[23] The four components of a li-ion battery. `https://www.samsungsdi.com/column/technology/detail/55272.html?pageIndex=1&idx=55272&brdCode=001&listType=list&searchKeyword=`, 2018.

[24] Y. Hua, A. Cordoba-Arenas, N. Warner, and G. Rizzoni. A multi time-scale state-of-charge and state-of-health estimation framework using nonlinear predictive filter for lithium-ion battery pack with passive balance control. *Journal of Power Sources*, 280:293–312, 2015.

[25] Christoph R. Birkl, Matthew R. Roberts, Euan McTurk, Peter G. Bruce, and David A. Howey. Degradation diagnostics for lithium ion cells. *Journal of Power Sources*, 341:373 – 386, 2017.

[26] E. G. Amaya, H. Chiacchiarini, C. De Angelo, and M. Asensio. The energy management strategy of fc/battery vehicles winner of the 2017 ieee vts motor vehicles challenge. In *2017 IEEE Vehicle Power and Propulsion Conference (VPPC)*, pages 1–6. IEEE, 2017.

[27] Eric A Wan and Rudolph Van Der Merwe. The unscented kalman filter for nonlinear estimation. In *Proceedings of the IEEE 2000 Adaptive Systems for Signal Processing, Communications, and Control Symposium (Cat. No. 00EX373)*, pages 153–158. Ieee, 2000.

[28] C. Hu, B. D. Youn, and J. Chung. A multiscale framework with extended kalman filter for lithium-ion battery soc and capacity estimation. *Applied Energy*, 92:694–704, 2012.

[29] K. Shivarama Krishna and K. Sathish Kumar. A review on hybrid renewable energy systems. *Renewable and Sustainable Energy Reviews*, 52:907–916, 2015.

[30] E. Ibrahim. *Commande intelligente tolérante aux fautes des systèmes multi-sources d'énergie*. PhD thesis, Lille 1, 2013.

[31] H. Zhao, Q. Wu, S. Hu, H. Xu, and R. C. Nygaard. Review of energy storage system for wind power integration support. *Applied energy*, 137:545–553, 2015.

[32] Y. Ma, A. Kelman, A. Daly, and F. Borrelli. Predictive control for energy efficient buildings with thermal storage: Modeling, stimulation, and experiments. *IEEE control systems magazine*, 32(1):44–64, 2012.

[33] V. Dorer, R. Weber, and A. Weber. Performance assessment of fuel cell micro-cogeneration systems for residential buildings. *Energy and Buildings*, 37(11):1132–1146, 2005.

[34] A.A. Khodadoost Arani, G.B. Gharehpetian, and M. Abedi. Review on energy storage systems control methods in microgrids. *International journal of electrical power & energy systems*, 107:745–757, 2019.

[35] S. Vazquez, S. M. Lukic, E. Galvan, L. G. Franquelo, and J. M. Carrasco. Energy storage systems for transport and grid applications. *IEEE Transactions on Industrial Electronics*, 57(12):3881–3895, 2010.

[36] N. Ghaviha, J. Campillo, M. Bohlin, and E. Dahlquist. Review of application of energy storage devices in railway transportation. *Energy Procedia*, 105:4561–4568, 2017.

[37] J. Han, J. Charpentier, and T. Tang. An energy management system of a fuel cell/battery hybrid boat. *Energies*, 7(5):2799–2820, 2014.

[38] H. Zhang, F. Mollet, C. Saudemont, and B. Robyns. Experimental validation of energy storage system management strategies for a local dc distribution system of more electric aircraft. *IEEE Transactions on Industrial Electronics*, 57(12):3905–3916, 2010.

[39] M. Aamir, K. A. Kalwar, and S. Mekhilef. Uninterruptible power supply (ups) system. *Renewable and sustainable energy reviews*, 58:1395–1410, 2016.

[40] K. Goebel, B. Saha, A. Saxena, J. R. Celaya, and J. P. Christophersen. Prognostics in battery health management. *IEEE instrumentation & measurement magazine*, 11(4):33–40, 2008.

[41] J. S. Martínez, J. Mulot, F. Harel, D. Hissel, M. Pera, R. I. John, and M. Amiet. Experimental validation of a type-2 fuzzy logic controller for energy management in hybrid electrical vehicles. *Engineering Applications of Artificial Intelligence*, 26(7):1772–1779, 2013.

[42] J. K. Woodacre, R. J. Bauer, and R. A. Irani. A review of vertical motion heave compensation systems. *Ocean Engineering*, 104:140–154, 2015.

[43] R. Hemmati and H. Saboori. Emergence of hybrid energy storage systems in renewable energy and transport applications–a review. *Renewable and Sustainable Energy Reviews*, 65:11–23, 2016.

[44] Z. Shi. *Modeling and online aging monitoring of supercapacitors.* PhD thesis, Nantes, 2014.

[45] G. Vulusala, S. Venkata, and S. Madichetty. Application of superconducting magnetic energy storage in electrical power and energy systems: a review. *International Journal of Energy Research*, 42(2):358–368, 2018.

[46] W. Buckles and Wi. V. Hassenzahl. Superconducting magnetic energy storage. *IEEE Power Engineering Review*, 20(5):16–20, 2000.

[47] H. Liu and J. Jiang. Flywheel energy storage—an upswing technology for energy sustainability. *Energy and buildings*, 39(5):599–604, 2007.

[48] M. H. Nehrir, C. Wang, K. Strunz, H. Aki, R. Ramakumar, J. Bing, Z. Miao, and Z. Salameh. A review of hybrid renewable/alternative energy systems for electric power generation: configurations, control, and applications. *IEEE Transactions on Sustainable Energy*, 2(4):392–403, 2011.

[49] T. M. I. Mahlia, T. J. Saktisahdan, A. Jannifar, M. H. Hasan, and H. S. C. Matseelar. A review of available methods and development on energy storage; technology update. *Renewable and Sustainable Energy Reviews*, 33:532–545, 2014.

[50] H. Budde-Meiwes, J. Drillkens, B. Lunz, J. Muennix, S. Rothgang, J. Kowal, and D. U. Sauer. A review of current automotive battery technology and future prospects. *Proceedings of the Institution of Mechanical Engineers, Part D: Journal of Automobile Engineering*, 227(5):761–776, 2013.

[51] J. M. Tarascon and M. Armand. Issues and challenges facing rechargeable lithium batteries. *Nature*, 414:359–367, 2001.

[52] H. L. Ferreira, R. Garde, G. Fulli, W. Kling, and J. P. Lopes. Characterisation of electrical energy storage technologies. *Energy*, 53:288–298, 2013.

[53] W Wang. Vanadium redox flow batteries – improving the performance and reducing the cost of vanadium redox flow batteries for large-scale energy storage. *Electricity Delivery and Energy Reliability*, 2012.

[54] W. Tong. *Wind power generation and wind turbine design.* WIT press, 2010.

[55] S. Mekhilef, R. Saidur, and A. Safari. Comparative study of different fuel cell technologies. *Renewable and Sustainable Energy Reviews*, 16(1):981–989, 2012.

[56] A. Kirubakaran, S. Jain, and R. K. Nema. A review on fuel cell technologies and power electronic interface. *Renewable and Sustainable Energy Reviews*, 13(9):2430–2440, 2009.

[57] S. Hajiaghasi, A. Salemnia, and M. Hamzeh. Hybrid energy storage system for microgrids applications: A review. *Journal of Energy Storage*, 21(1):543–570, 2019.

[58] A. Khaligh and Z. Li. Battery, ultracapacitor, fuel cell, and hybrid energy storage systems for electric, hybrid electric, fuel cell, and plug-in hybrid electric vehicles: State of the art. *IEEE transactions on Vehicular Technology*, 59(6):2806–2814, 2010.

[59] B. Bendjedia. *Gestion et optimisation d'énergie électrique avec tolérance aux défauts d'un système hybride PàC/batterie.* PhD thesis, Paris Saclay, 2018.

[60] J. Cao and A. Emadi. A new battery/ultracapacitor hybrid energy storage system for electric, hybrid, and plug-in hybrid electric vehicles. *IEEE Transactions on power electronics*, 27(1):122–132, 2011.

[61] P. Zhang, F. Yan, and C. Du. A comprehensive analysis of energy management strategies for hybrid electric vehicles based on bibliometrics. *Renewable and Sustainable Energy Reviews*, 48:88–104, 2015.

[62] Q. Li, H. Yang, Y. Han, M. Li, and W. Chen. A state machine strategy based on droop control for an energy management system of pemfc-battery-supercapacitor hybrid tramway. *International Journal of Hydrogen Energy*, 41(36):16148–16159, 2016.

[63] Y. Zhou, A. Ravey, and M. Péra. Multi-mode predictive energy management for fuel cell hybrid electric vehicles using markov driving pattern recognizer. *Applied Energy*, 258:114057, 2020.

[64] M. A. Xavier and M. S. Trimboli. Lithium-ion battery cell-level control using constrained model predictive control and equivalent circuit models. *Journal of Power Sources*, 285:374–384, 2015.

[65] D. D. Sarma and A. K. Shukla. Building better batteries: A travel back in time. *ACS Energy Letters*, 3(11):2841–2845, 2018.

[66] J. Tarascon. Is lithium the new gold? *Nature Chemistry*, 2:510, 2010.

[67] M.A. Hannan, M.S.H. Lipu, A. Hussain, and A. Mohamed. A review of lithium-ion battery state of charge estimation and management system in electric vehicle applications: Challenges and recommendations. *Renewable and Sustainable Energy Reviews*, 78:834 – 854, 2017.

[68] Q. Wang, B. Jiang, B. Li, and Yan Y. A critical review of thermal management models and solutions of lithium-ion batteries for the development of pure electric vehicles. *Renewable and Sustainable Energy Reviews*, 64:106 – 128, 2016.

[69] M. R. Palacín. Understanding ageing in li-ion batteries: a chemical issue. *Chem. Soc. Rev.*, 47:4924–4933, 2018.

[70] N. Nitta, F. Wu, J. T. Lee, and G. Yushin. Li-ion battery materials: present and future. *Materials Today*, 18(5):252 – 264, 2015.

[71] A. Mauger and C. M. Julien. Critical review on lithium-ion batteries: are they safe? sustainable? *Ionics*, 23(8):1933–1947, Aug 2017.

[72] R. Zhang, B. Xia, B. Li, L. Cao, Y. Lai, W. Zheng, H. Wang, and W. Wang. State of the art of lithium-ion battery soc estimation for electrical vehicles. *Energies*, 11(7), 2018.

[73] H. G. Foad, J. Joris, G. Shovon, G. Rahul, F. Yousef, K. Theodoros, O. Noshin, and V. M. Joeri. Concept of reliability and safety assessment of lithium-ion batteries in electric vehicles: Basics, progress, and challenges. *Applied Energy*, 251:113343, 2019.

[74] A. Farmann, W. Waag, A. Marongiu, and D. U. Sauer. Critical review of on-board capacity estimation techniques for lithium-ion batteries in electric and hybrid electric vehicles. *Journal of Power Sources*, 281:114 – 130, 2015.

[75] Tinghong Wang. *Commande robuste pour une gestion énergétique fonction de l'état de santé de la batterie au sein des véhicules hybrides*. PhD thesis, Grenoble, 2013.

[76] A. Barré, B. Deguilhem, S. Grolleau, M. Gérard, F. Suard, and D. Riu. A review on lithium-ion battery ageing mechanisms and estimations for automotive applications. *Journal of Power Sources*, 241:680 – 689, 2013.

[77] L. Lu, X. Han, J. Li, J. Hua, and M. Ouyang. A review on the key issues for lithium-ion battery management in electric vehicles. *Journal of Power Sources*, 226:272 – 288, 2013.

[78] J. Meng, M. Boukhnifer, and D. Diallo. Comparative study of lithium-ion battery open-circuit-voltage online estimation methods. *IET Electrical Systems in Transportation*, 2019.

[79] W. Waag and D. U. Sauer. Adaptive estimation of the electromotive force of the lithium-ion battery after current interruption for an accurate state-of-charge and capacity determination. *Applied Energy*, 111:416–427, 2013.

[80] Aurélien Lièvre. *Développement d'un système de gestion de batterie lithium-ion à destination de véhicules" mild hybrid": détermination des indicateurs d'état (SoC, SoH et SoF)*. PhD thesis, 2015.

[81] M. A Roscher and D. U. Sauer. Dynamic electric behavior and open-circuit-voltage modeling of lifepo4-based lithium ion secondary batteries. *Journal of Power Sources*, 196(1):331–336, 2011.

[82] Andrea C., Simona O., and Giorgio R. A control-oriented lithium-ion battery pack model for plug-in hybrid electric vehicle cycle-life studies and system design with consideration of health management. *Journal of Power Sources*, 279:791 – 808, 2015.

[83] Asmae EL MEJDOUBI. *Diagnostic de l'état de vieillissement des systemes de stockage de l'énergie électrique*. PhD thesis, Université de Caen Normandie, 2015.

[84] S. M. Rezvanizaniani, Z. Liu, Y. Chen, and J. Lee. Review and recent advances in battery health monitoring and prognostics technologies for electric vehicle (ev) safety and mobility. *Journal of Power Sources*, 256:110 – 124, 2014.

[85] J. Vetter, P. Novák, Wagner. M.R., C. Veit, K. C. Möller, J.O. Besenhard, M. Winter, M. Wohlfahrt-Mehrens, C. Vogler, and A. Hammouche. Ageing mechanisms in lithium-ion batteries. *Journal of Power Sources*, 147(1):269 – 281, 2005.

[86] R. Xiong, L. Li, and J. Tian. Towards a smarter battery management system: A critical review on battery state of health monitoring methods. *Journal of Power Sources*, 405:18 – 29, 2018.

[87] X. Feng, M. Ouyang, X. Liu, L. Lu, Y. Xia, and X. He. Thermal runaway mechanism of lithium ion battery for electric vehicles: A review. *Energy Storage Materials*, 10:246 – 267, 2018.

[88] J. Wen, Y. Yu, and C. Chen. A review on lithium-ion batteries safety issues: existing problems and possible solutions. *Materials express*, 2(3):197–212, 2012.

[89] R. Xiong, R. Yang, Z. Chen, W. Shen, and F. Sun. Online fault diagnosis of external short circuit for lithium-ion battery pack. *IEEE Transactions on Industrial Electronics*, 67(2):1081–1091, Feb 2020.

[90] Z. Zhang, X. Kong, Y. Zheng, L. Zhou, and X. Lai. Real-time diagnosis of micro-short circuit for li-ion batteries utilizing low-pass filters. *Energy*, 166:1013 – 1024, 2019.

[91] J. Jaguemont, L. Boulon, and Y. Dubé. A comprehensive review of lithium-ion batteries used in hybrid and electric vehicles at cold temperatures. *Applied Energy*, 164:99–114, 2016.

[92] Y. Zheng, X. Han, L. Lu, J. Li, and M. Ouyang. Lithium ion battery pack power fade fault identification based on shannon entropy in electric vehicles. *Journal of Power Sources*, 223:136 – 146, 2013.

[93] Y. Zou, X. Hu, H. Ma, and S. Li. Combined state of charge and state of health estimation over lithium-ion battery cell cycle lifespan for electric vehicles. *Journal of Power Sources*, 273:793 – 803, 2015.

[94] H. Rahimi-Eichi, U. Ojha, F. Baronti, and M. Chow. Battery management system: An overview of its application in the smart grid and electric vehicles. *IEEE Industrial Electronics Magazine*, 7(2):4–16, 2013.

[95] J. Meng, M. Boukhnifer, and D. Diallo. A new model-based lithium-ion battery online monitoring structure. In *2019 Prognostics and System Health Management Conference (PHM-Paris)*, pages 24–29. IEEE, 2019.

[96] Q. Wang, B. Jiang, B. Li, and Y. Yan. A critical review of thermal management models and solutions of lithium-ion batteries for the development of pure electric vehicles. *Renewable and Sustainable Energy Reviews*, 64:106–128, 2016.

[97] H. Liu, Z. Wei, W. He, and J. Zhao. Thermal issues about li-ion batteries and recent progress in battery thermal management systems: A review. *Energy conversion and management*, 150:304–330, 2017.

[98] A. Hussein and I. Batarseh. A review of charging algorithms for nickel and lithium battery chargers. *IEEE Transactions on Vehicular Technology*, 60(3):830–838, 2011.

[99] C. Zou, C. Manzie, and D. Nešić. Model predictive control for lithium-ion battery optimal charging. *IEEE/ASME Transactions on Mechatronics*, 23(2):947–957, 2018.

[100] J. Harmouche. *Statistical Incipient Fault Detection and Diagnosis with Kullback-Leibler Divergence: From Theory to Applications*. PhD thesis, Supélec, 2014.

[101] A. Raisemche. *Commande tolérante aux défauts d'une chaine de traction d'un véhicule électrique: Fault tolerant control of electric vehicle power train*. PhD thesis, Université Paris-Sud–Paris XI, 2014.

[102] V. Venkatasubramanian, R. Rengaswamy, K. Yin, and S. N. Kavuri. A review of process fault detection and diagnosis: Part i: Quantitative model-based methods. *Computers & chemical engineering*, 27(3):293–311, 2003.

[103] Florin Stoican. *Fault tolerant control based on set-theoretic methods*. PhD thesis, 2011.

[104] Y. Zhang and J. Jiang. Bibliographical review on reconfigurable fault-tolerant control systems. *Annual reviews in control*, 32(2):229–252, 2008.

[105] V. Venkatasubramanian, R. Rengaswamy, and S. N. Kavuri. A review of process fault detection and diagnosis: Part ii: Qualitative models and search strategies. *Computers & chemical engineering*, 27(3):313–326, 2003.

[106] V. Venkatasubramanian, R. Rengaswamy, S. N. Kavuri, and K. Yin. A review of process fault detection and diagnosis: Part iii: Process history based methods. *Computers & chemical engineering*, 27(3):327–346, 2003.

[107] S. Nejad, D. T. Gladwin, and D. A. Stone. A systematic review of lumped-parameter equivalent circuit models for real-time estimation of lithium-ion battery states. *Journal of Power Sources*, 316:183–196, 2016.

[108] G. L. Plett. High-performance battery-pack power estimation using a dynamic cell model. *IEEE Transactions on vehicular technology*, 53(5):1586–1593, 2004.

[109] R. Xiong, F. Sun, H. He, and T. D. Nguyen. A data-driven adaptive state of charge and power capability joint estimator of lithium-ion polymer battery used in electric vehicles. *Energy*, 63:295–308, 2013.

[110] Q. Miao, L. Xie, H. Cui, W. Liang, and M. Pecht. Remaining useful life prediction of lithium-ion battery with unscented particle filter technique. *Microelectronics Reliability*, 53(6):805–810, 2013.

[111] A. Guha and A. Patra. State of health estimation of lithium-ion batteries using capacity fade and internal resistance growth models. *IEEE Transactions on Transportation Electrification*, 4(1):135–146, 2017.

[112] X Hu, S. Li, and H. Peng. A comparative study of equivalent circuit models for li-ion batteries. *Journal of Power Sources*, 198:359 – 367, 2012.

[113] Joaquín Klee Barillas, Jiahao Li, Clemens Günther, and Michael A Danzer. A comparative study and validation of state estimation algorithms for li-ion batteries in battery management systems. *Applied Energy*, 155:455–462, 2015.

[114] J. Xu, C. C. Mi, B. Cao, J. Deng, Z. Chen, and S. Li. The state of charge estimation of lithium-ion batteries based on a proportional-integral observer. *IEEE Transactions on Vehicular Technology*, 63(4):1614–1621, 2013.

[115] I. Kim. The novel state of charge estimation method for lithium battery using sliding mode observer. *Journal of Power Sources*, 163(1):584–590, 2006.

[116] B. Xia, W. Zheng, R. Zhang, Z. Lao, and Z. Sun. A novel observer for lithium-ion battery state of charge estimation in electric vehicles based on a second-order equivalent circuit model. *Energies*, 10(8):1150, 2017.

[117] F. Zhang, G. Liu, L. Fang, and H. Wang. Estimation of battery state of charge with hinfinity observer: applied to a robot for inspecting power transmission lines. *IEEE Transactions on Industrial Electronics*, 59(2):1086–1095, 2011.

[118] Z. Yu, R. Huai, and L. Xiao. State-of-charge estimation for lithium-ion batteries using a kalman filter based on local linearization. *Energies*, 8(8):7854–7873, 2015.

[119] G. L. Plett. Extended kalman filtering for battery management systems of lipb-based hev battery packs: Part 3. state and parameter estimation. *Journal of Power sources*, 134(2):277–292, 2004.

[120] G. L. Plett. Sigma-point kalman filtering for battery management systems of lipb-based hev battery packs: Part 2: Simultaneous state and parameter estimation. *Journal of power sources*, 161(2):1369–1384, 2006.

[121] B. Xia, H. Wang, Y. Tian, M. Wang, W. Sun, and Z. Xu. State of charge estimation of lithium-ion batteries using an adaptive cubature kalman filter. *Energies*, 8(6):5916–5936, 2015.

[122] F. Sun, X. Hu, Y. Zou, and S. Li. Adaptive unscented kalman filtering for state of charge estimation of a lithium-ion battery for electric vehicles. *Energy*, 36(5):3531–3540, 2011.

[123] D. Zhou, K. Zhang, A. Ravey, F. Gao, and A. Miraoui. Online estimation of lithium polymer batteries state-of-charge using particle filter-based data fusion with multimodels approach. *IEEE Transactions on Industry Applications*, 52(3):2582–2595, 2016.

[124] D. How, M. A. Hannan, M. Lipu, and P. J. Ker. State of charge estimation for lithium-ion batteries using model-based and data-driven methods: A review. *IEEE Access*, 7:136116–136136, 2019.

[125] E. Chemali, P. J. Kollmeyer, M. Preindl, and A. Emadi. State-of-charge estimation of li-ion batteries using deep neural networks: A machine learning approach. *Journal of Power Sources*, 400:242–255, 2018.

[126] J. Hu, J. Hu, H. Lin, X. Li, C. Jiang, X. Qiu, and W. Li. State-of-charge estimation for battery management system using optimized support vector machine for regression. *Journal of Power Sources*, 269:682–693, 2014.

[127] T. Zahid, K. Xu, W. Li, C. Li, and H. Li. State of charge estimation for electric vehicle power battery using advanced machine learning algorithm under diversified drive cycles. *Energy*, 162:871–882, 2018.

[128] M. Einhorn, F. V. Conte, C. Kral, and J. Fleig. A method for online capacity estimation of lithium ion battery cells using the state of charge and the transferred charge. *IEEE Transactions on Industry Applications*, 48(2):736–741, 2011.

[129] M. A. Roscher, J. Assfalg, and O. S. Bohlen. Detection of utilizable capacity deterioration in battery systems. *IEEE Transactions on vehicular technology*, 60(1):98–103, 2010.

[130] H. He, R. Xiong, and H. Guo. Online estimation of model parameters and state-of-charge of lifepo4 batteries in electric vehicles. *Applied Energy*, 89(1):413–420, 2012.

[131] L Plett Gregory. Extended kalman filtering for battery management systems of lipb-based hev battery packs: Part 1. background. *Journal of Power Sources*, 134(2):252–261, 2004.

[132] F. Auger, M. Hilairet, J. M. Guerrero, E. Monmasson, T. Orlowska-Kowalska, and S. Katsura. Industrial applications of the kalman filter: A review. *IEEE Transactions on Industrial Electronics*, 60(12):5458–5471, 2013.

[133] V. Duong, H. Bastawrous, K. Lim, K. See, P. Zhang, and S. Dou. Online state of charge and model parameters estimation of the lifepo4 battery in electric vehicles using multiple adaptive forgetting factors recursive least-squares. *Journal of Power Sources*, 296:215–224, 2015.

[134] Q. Yu, R. Xiong, C. Lin, W. Shen, and J. Deng. Lithium-ion battery parameters and state-of-charge joint estimation based on h-infinity and unscented kalman filters. *IEEE Transactions on Vehicular Technology*, 66(10):8693–8701, 2017.

[135] P. Shen, M. Ouyang, L. Lu, J. Li, and X. Feng. The co-estimation of state of charge, state of health, and state of function for lithium-ion batteries in electric vehicles. *IEEE Transactions on vehicular technology*, 67(1):92–103, 2017.

[136] G. L. Plett. Dual and joint ekf for simultaneous soc and soh estimation. In *Proceedings of the 21st Electric Vehicle Symposium (EVS21), Monaco*, pages 1–12, 2005.

[137] L. Zhao, Z. Liu, and G. Ji. Lithium-ion battery state of charge estimation with model parameters adaptation using h infinity extended kalman filter. *Control Engineering Practice*, 81:114–128, 2018.

[138] I. Kim. A technique for estimating the state of health of lithium batteries through a dual-sliding-mode observer. *IEEE Transactions on Power Electronics*, 25(4):1013–1022, 2009.

[139] C. Chen, R. Xiong, and W. Shen. A lithium-ion battery-in-the-loop approach to test and validate multiscale dual h infinity filters for state-of-charge and capacity estimation. *IEEE Transactions on power Electronics*, 33(1):332–342, 2017.

[140] Rui Xiong, Yongzhi Zhang, Hongwen He, Xuan Zhou, and Michael G Pecht. A double-scale, particle-filtering, energy state prediction algorithm for lithium-ion batteries. *IEEE Transactions on Industrial Electronics*, 65(2):1526–1538, 2017.

[141] A. Fotouhi, D. J. Auger, K. Propp, S. Longo, and M. Wild. A review on electric vehicle battery modelling: From lithium-ion toward lithium–sulphur. *Renewable and Sustainable Energy Reviews*, 56:1008–1021, 2016.

[142] M. El Lakkis, O. Sename, M. Corno, and D. B. Pietri. Combined battery soc/soh estimation using a nonlinear adaptive observer. In *2015 European Control Conference (ECC)*, pages 1522–1527. IEEE, 2015.

[143] Tedjani Mesbahi. *Influence des stratégies de gestion d'une source hybride de véhicule électrique sur son dimensionnement et sa durée de vie par intégration d'un modèle multi-physique*. PhD thesis, 2016.

[144] M. Ecker, J. B. Gerschler, J. Vogel, S. Käbitz, F. Hust, P. Dechent, and D. U. Sauer. Development of a lifetime prediction model for lithium-ion batteries based on extended accelerated aging test data. *Journal of Power Sources*, 215:248–257, 2012.

[145] J. Schmalstieg, S. Käbitz, M. Ecker, and D. U. Sauer. A holistic aging model for li (nimnco) o2 based 18650 lithium-ion batteries. *Journal of Power Sources*, 257:325–334, 2014.

[146] J. Wang, P. Liu, J. Hicks-Garner, E. Sherman, S. Soukiazian, M. Verbrugge, H. Tataria, J. Musser, and P. Finamore. Cycle-life model for graphite-lifepo4 cells. *Journal of power sources*, 196(8):3942–3948, 2011.

[147] David Hernandez Torres. *Commande robuste de générateurs électrochimiques hybrides*. PhD thesis, Grenoble, 2011.

[148] T. Azib, C. Larouci, A. Chaibet, and M. Boukhnifer. Online energy management strategy of a hybrid fuel cell/battery/ultracapacitor vehicular power system. *IEEJ Transactions on Electrical and Electronic Engineering*, 9(5):548–554, 2014.

[149] X. Lin, H. E. Perez, S. Mohan, J. B. Siegel, A. G. Stefanopoulou, Y. Ding, and M. P. Castanier. A lumped-parameter electro-thermal model for cylindrical batteries. *Journal of Power Sources*, 257:1–11, 2014.

[150] A. Cordoba-Arenas, S. Onori, and G. Rizzoni. A control-oriented lithium-ion battery pack model for plug-in hybrid electric vehicle cycle-life studies and system design with consideration of health management. *Journal of Power Sources*, 279:791–808, 2015.

[151] M. Einhorn, F. V. Conte, C. Kral, and J. Fleig. Comparison, selection, and parameterization of electrical battery models for automotive applications. *IEEE Transactions on Power Electronics*, 28(3):1429–1437, 2012.

[152] X. Lin. Theoretical analysis of battery soc estimation errors under sensor bias and variance. *IEEE Transactions on Industrial Electronics*, 65(9):7138–7148, 2018.

[153] Q. Yu, R. Xiong, L. Wang, and C. Lin. A comparative study on open circuit voltage models for lithium-ion batteries. *Chinese Journal of Mechanical Engineering*, 31(1):65, 2018.

[154] Y. Chiang, W. Sean, and J. Ke. Online estimation of internal resistance and open-circuit voltage of lithium-ion batteries in electric vehicles. *Journal of Power Sources*, 196(8):3921–3932, 2011.

[155] J. Chiasson and B. Vairamohan. Estimating the state of charge of a battery. In *Proceedings of the 2003 American Control Conference, 2003.*, volume 4, pages 2863–2868. IEEE, 2003.

[156] A. Hauser and R. Kuhn. High-voltage battery management systems (bms) for electric vehicles. In *Advances in Battery Technologies for Electric Vehicles*, pages 265–282. Elsevier, 2015.

[157] Gregory L Plett. *Battery management systems, Volume I: Battery modeling*, volume 1. Artech House, 2015.

[158] R. Xiong, Q. Yu, C. Lin, et al. A novel method to obtain the open circuit voltage for the state of charge of lithium ion batteries in electric vehicles by using h infinity filter. *Applied energy*, 207:346–353, 2017.

[159] F. Sun, R. Xiong, H. He, W. Li, and J. E. E. Aussems. Model-based dynamic multi-parameter method for peak power estimation of lithium–ion batteries. *Applied Energy*, 96:378–386, 2012.

[160] X. Kong, Y. Zheng, M. Ouyang, L. Lu, J. Li, and Z. Zhang. Fault diagnosis and quantitative analysis of micro-short circuits for lithium-ion batteries in battery packs. *Journal of Power Sources*, 395:358–368, 2018.

[161] X. Feng, C. Weng, M. Ouyang, and J. Sun. Online internal short circuit detection for a large format lithium ion battery. *Applied Energy*, 161:168–180, 2016.

[162] S. Dey, Z. A. Biron, S. Tatipamula, N. Das, S. Mohon, B. Ayalew, and P. Pisu. Model-based real-time thermal fault diagnosis of lithium-ion batteries. *Control Engineering Practice*, 56:37–48, 2016.

[163] Z. Chen, R. Xiong, J. Tian, X. Shang, and J. Lu. Model-based fault diagnosis approach on external short circuit of lithium-ion battery used in electric vehicles. *Applied energy*, 184:365–374, 2016.

[164] M. Seo, T. Goh, M. Park, G. Koo, and S. W. Kim. Detection of internal short circuit in lithium ion battery using model-based switching model method. *Energies*, 10(1):76, 2017.

[165] W. Gao, Y. Zheng, M. Ouyang, J. Li, X. Lai, and X. Hu. Micro-short-circuit diagnosis for series-connected lithium-ion battery packs using mean-difference model. *IEEE Transactions on Industrial Electronics*, 66(3):2132–2142, 2018.

[166] S. Sankararaman, M. J. Daigle, and K. Goebel. Uncertainty quantification in remaining useful life prediction using first-order reliability methods. *IEEE Transactions on Reliability*, 63(2):603–619, 2014.

[167] A. Naha, A. Khandelwal, K. S. Hariharan, A. Kaushik, A. Yadu, and S. M. Kolake. On-board short-circuit detection of li-ion batteries undergoing fixed charging profile as in smartphone applications. *IEEE Transactions on Industrial Electronics*, 66(11):8782–8791, 2019.

[168] K. Zhang, B. Jiang, V. Cocquempot, and H. Zhang. A framework of robust fault estimation observer design for continuous-time/discrete-time systems. *Optimal control applications and methods*, 34(4):442–457, 2013.

[169] Bahram Shafai and Mehrdad Saif. Proportional-integral observer in robust control, fault detection, and decentralized control of dynamic systems. In *Control and Systems Engineering*, pages 13–43. Springer, 2015.

[170] K. Zhang, B. Jiang, and V. Cocquempot. Fuzzy unknown input observer-based robust fault estimation design for discrete-time fuzzy systems. *Signal Processing*, 128:40–47, 2016.

[171] Michela Fazzolari, Rafael Alcala, Yusuke Nojima, Hisao Ishibuchi, and Francisco Herrera. A review of the application of multiobjective evolutionary fuzzy systems: Current status and further directions. *IEEE Transactions on Fuzzy systems*, 21(1):45–65, 2012.

[172] Sabrina Aouaouda, Mohammed Chadli, and Moussa Boukhnifer. Speed sensor fault tolerant controller design for induction motor drive in ev. *Neurocomputing*, 214:32–43, 2016.

[173] Yan-Wu Wang, Zhi-Hong Guan, and Hua O Wang. Impulsive synchronization for takagi–sugeno fuzzy model and its application to continuous chaotic system. *Physics letters A*, 339(3-5):325–332, 2005.

[174] Xiaoxu Liu, Zhiwei Gao, and Michael ZQ Chen. Takagi–sugeno fuzzy model based fault estimation and signal compensation with application to wind turbines. *IEEE Transactions on Industrial Electronics*, 64(7):5678–5689, 2017.

[175] H. Rahimi-Eichi, F. Baronti, and M. Chow. Online adaptive parameter identification and state-of-charge coestimation for lithium-polymer battery cells. *IEEE Transactions on Industrial Electronics*, 61(4):2053–2061, 2013.

[176] Sabrina Aouaouda and Moussa Boukhnifer. Observer-based fault tolerant controller design for induction motor drive in ev. In *2014 IEEE Conference on Control Applications (CCA)*, pages 1190–1195. IEEE, 2014.

[177] Robert Babuška. *Fuzzy modeling for control*, volume 12. Springer Science & Business Media, 2012.

[178] G. Du, W. Cao, S. Hu, Z. Lin, and T. Yuan. Design and assessment of an electric vehicle powertrain model based on real-world driving and charging cycles. *IEEE Transactions on Vehicular Technology*, 68(2):1178–1187, 2018.

[179] Y. Chiang, W. Sean, and J. Ke. Online estimation of internal resistance and open-circuit voltage of lithium-ion batteries in electric vehicles. *Journal of Power Sources*, 196(8):3921–3932, 2011.

[180] C. Delpha, D. Diallo, H. Al Samrout, and N. Moubayed. Multiple incipient fault diagnosis in three-phase electrical systems using multivariate statistical signal processing. *Engineering Applications of Artificial Intelligence*, 73:68–79, 2018.

[181] Demba Diallo and Claude Delpha. Incipient offset current sensor fault detection and diagnosis using statistical analysis and the kullback leibler divergence for ac drive. In *IECON 2017-43rd Annual Conference of the IEEE Industrial Electronics Society*, pages 8070–8075. IEEE, 2017.

[182] M. Baghli, C. Delpha, D. Diallo, A. Hallouche, D. Mba, and T. Wang. Three-level npc inverter incipient fault detection and classification using output current statistical analysis. *Energies*, 12(7):1372, 2019.

[183] Michèle Basseville, Igor V Nikiforov, et al. *Detection of abrupt changes: theory and application*, volume 104. prentice Hall Englewood Cliffs, 1993.

[184] A. Youssef, C. Delpha, and D. Diallo. An optimal fault detection threshold for early detection using kullback–leibler divergence for unknown distribution data. *Signal Processing*, 120:266–279, 2016.

[185] Ryan James Caverly and James Richard Forbes. Lmi properties and applications in systems, stability, and control theory. *arXiv preprint arXiv:1903.08599*, 2019.

[186] Johan Lofberg. Yalmip: A toolbox for modeling and optimization in matlab. In *2004 IEEE international conference on robotics and automation (IEEE Cat. No. 04CH37508)*, pages 284–289. IEEE, 2004.

université
PARIS-SACLAY

ÉCOLE DOCTORALE
Physique et ingénierie :
Electrons, Photons,
Sciences du vivant (EOBE)

Titre : Diagnostic de la batterie et gestion de l’énergie pour applications embarquées

Mots clés : Véhicule électrique, Batterie Lithium-Ion, Vieillissement, Court-circuit naissant, Estimation de l’état, Estimation des paramètres, Traitement du signal.

Résumé : Les véhicules électriques (VEs) connaissent un développement en plein essor ces dernières années pour faire face aux problèmes environnementaux et aux dérèglements climatiques. Du point de vue du stockage de l'énergie, c’est essentiellement la technologie des batteries lithium-ion (LIB) qui est la plus utilisée pour d’alimentation des véhicules électriques compte tenu de leur haute densité d'énergie / puissance et de leur longue durée de vie. La fiabilité des LIBs est sans aucun doute d'une importance fondamentale pour le développement des VE. Dans cet objectif, les travaux de thèse s’inscrivent dans le développement des algorithmes dédiés à l’estimation des états de la batterie ainsi qu’au diagnostic de courts-circuits naissants. L’estimation des états de la batterie, qui peut également être qualifiée de surveillance de la batterie, est un élément indispensable de la stratégie de gestion de l’énergie d'un véhicule électrique ou hybride. Par ailleurs, le vieillissement prématuré peut être évité grâce à la surveillance des états de batterie telles que l'état de charge (SOC) et l'état de santé (SOH). De plus, étant donné que l'emballement thermique (TR) peut être la conséquence d’un défaut de court-circuit (SC) électrique, de ce fait, une détection efficace de SC naissant de la batterie peut donc donner une alerte protectrice de TR. La principale contribution de cette thèse réside dans les aspects théoriques et méthodologiques dans le domaine de la surveillance de la batterie et du diagnostic SC naissant.

Title : Battery fault diagnosis and energy management for embedded applications

Keywords : Electric vehicle, Lithium-Ion battery, Aging, Incipient short-circuit, State estimation, Parameter estimation, Signal processing.

Abstract : In order to cope with environmental problems and climate change, electric vehicles (EVs) gain the ever booming development in recent years. From the point of view of energy storage, because of their high energy / power density and their extended lifespan, it is essentially the lithium-ion battery (LIB) technology which is the most used power unit for EVs. Doubtlessly, reliability of LIBs is of vital importance for the development of EVs. To this end, this thesis is dedicated to the algorithmic development of battery state and parameter estimation as well as incipient short-circuit diagnosis.

The battery state and parameter estimation, which can also be termed as battery monitoring, is a critical part in the so-called health conscious energy management strategy for electric or hybrid electric vehicle. Premature aging can be avoided through the accurate battery state estimation such as state of charge (SOC) and state of health (SOH). Furthermore, as the thermal runaway (TR) can be ultimately attributed to short-circuit (SC) electrical abuse, therefore, effective battery incipient SC detection can give an early warning of TR. The main contribution of this thesis lies in the theoretical and methodological aspects in the domain of battery monitoring and incipient SC diagnosis.

Université Paris-Saclay
Espace Technologique / Immeuble Discovery
Route de l’Orme aux Merisiers RD 128 / 91190 Saint-Aubin, France